Toxicological Profile of Microcystins:

Determination of the Toxicokinetic and Toxicodynamic Mechanisms of Microcystins in Human Cells

Dissertation zur Erlangung des

akademischen Grades

eines Doktors der Naturwissenschaften (Dr. rer. nat.)

vorgelegt von

Fotler, Regina

an der

Universität Konstanz

Mathematisch-Naturwissenschaftliche Sektion

Fachbereich Biologie

Konstanz, 2023

Tag der mündlichen Prüfung: 25. April 2024

1. Referent: Prof. Dr. Daniel Dietrich

2. Referent: Prof. Dr. Valentin Wittmann

3. Referent: Prof. Dr. Aswin Mangerich

After all this time?

Always.

Danksagung

Zunächst möchte ich mich bei Daniel Dietrich für die Bereitstellung des Dissertationsthemas bedanken. Danke für das Schreiben der zahlreichen Stipendienanträge und die allgemeine Unterstützung in jeder Hinsicht. Eine Doktorarbeit habe ich mir selbst nicht zugetraut, danke für das Ermutigen und die stetige Motivation und Zuversicht!

Mein weiterer Dank gilt Valentin Wittmann für die Übernahme des Zweitgutachtens, aber auch für die großartige Zusammenarbeit und die Bereitstellung so vieler Microcystine, ohne die ein Großteil meiner Arbeit nicht möglich gewesen wäre. Dabei möchte ich mich vor allem bei Marius Wrona für die schnelle und zuverlässige Synthese der zahlreichen Microcystine bedanken! Danke!!!

Danke auch an Falk Schreiber für die Bereitschaft den Prüfungsvorsitzt zu übernehmen. Auch hier möchte ich mich für die gute Zusammenarbeit bedanken. Ein besonderer Dank geht an Sabrina Jäger-Honz. Ein ganz, ganz, ganz, ganz großes Dankeschön! Danke für deine fachliche Unterstützung! Dafür, dass du mir jederzeit alle Fragen beantwortet hast. Aber ganz besonders: Danke für dein offenes Ohr, für das Anhören meiner Sorgen, für die stetige Motivation weiterzumachen und für die lebensnotwendige Versorgung mit Kaffee und Schokolade!

Ein besonderer Dank gilt der gesamten AG Dietrich! Danke, dass ihr mich von Anfang an so herzlich aufgenommen habt! Danke Steff, für das Einarbeiten ins Thema. Hätte mir jemand in der Bachelorzeit erzählt, dass ich alles, was ich bei dir lerne für meine eigene Doktorarbeit brauche, hätte ich das niemals geglaubt (so viel zum Thema ich mach nie wieder Phosphatase Assays :D). Dabei gilt ein ganz großes Dankeschön der Mädelsgang! Danke Nadja, Eva, Barbie und Feli für die zahlreich Abende der Ablenkung, Motivation und Zuspruch – Beschte! Und Alex! Danke für die zahlreichen Gespräche im Büro, bester Sitznachbar! An dieser Stelle sei erwähnt, dass ich mich an keine bestimmte Reihenfolge gehalten habe!

Während meiner Doktorandenzeit durfte ich eine Vielzahl an Studenten betreuen. Ein großes Dankeschön gilt dabei an jeden einzelnen Studi, ob mein eigener oder von mir adoptiert! Niemals hätte ich gedacht, dass das Betreuen so viel Spaß macht und mir die Studis so sehr ans Herz wachsen. Dabei möchte ich natürlich Elena Schönfeld für die Bearbeitung des Kapitel IV als Masterarbeit danken! Ein ganz besonderer Dank gilt hierbei Julia Dressler! Danke, dass ich dich über deine Studienzeit als Betreuer begleiten durfte. Du warst nicht nur mein erster Bachelorstudi, sondern auch meine letzter Masterstudi! Ohne dich wären viele Projekte gar nicht möglich gewesen! Danke für alles, vor allem für die letzten Monate!!! Ich bin unendlich stolz auf dich, du packst deine Doktorarbeit genauso gut wie du deine anderen Abschlussarbeiten gemeistert hast.

Des Weiteren möchte ich meinem Mini-me Asisa danken! Auch wenn du nie mein Studi warst: Danke für alles! Danke für das Motivationspaket, dass ich innerhalb kurzer Zeit leergefuttert hab, danke für

den Zuspruch und Zuhören! Danke, danke, danke!! Dasselbe gilt auch für Carla! Danke für die vielen Macarons, für das auf mich achten und zur Seite nehmen und auf mich aufpassen, und die zahlreichen Kaffeepausen! Danke für all die großartigen Gespräche und einfach fürs Dasein!

Ein ganz, ganz großes Dankeschön geht auch an Simon! Vielen lieben Dank für die unfassbare Unterstützung vor allem während der sehr aufregenden Defense Vorbereitungszeit! Ich glaube ohne dich hätte ich mich während dieser Zeit nur noch verrückter gemacht! Einfach danke für alles!

Ein besonderer Dank geht auch an einen ganz besonderen Menschen – meinem Partner in Crime Claudi! Danke Claudi, dass du mich die letzte Zeit begleitet hast! Für das Anhören meiner Sorgen, für das Mitaufregen, wenn ich es am meisten gebraucht hab, aber auch für das Beruhigen, wenn ich mich wieder in Nichtigkeiten verzettelt hab! Danke für jede einzelne Sprachnachricht, wovon jede einzelne ein eigener Podcast sein könnte :D So viel Platz hab ich gar nicht auf der Seite um zu sagen wie dankbar ich dir bin!

Selbes gilt für meine Familie!

Danke an jeden einzelnen fürs an mich glauben und da sein. Vor allem für das Ablenken! Danke, dass ich bei euch einfach ich sein kann.

Mein allergrößter Dank geht an Fabi.

Freund – danke für die letzten 16 wundervolle Jahre! Für das immer da sein, das Zuhören und einfach alles. Ich kann gar nicht in Worte fassen, wie dankbar ich bin dich zu haben! Danke für deine Geduld und Zuversicht. Du bist mein bester Freund, mein Leben, mein Herz. Du bist mein „After all this time? Always.“.

Danke!

Table of Contents

Danksagung ..... **I**
Table of Contents ..... **III**
Record of Achievements ..... **V**
Notes to the Reader ..... **VII**
Abstract ..... **IX**
Zusammenfassung ..... **X**
1. General Introduction **1**
1.1. Cyanobacteria **1**
1.1.1. Ecology of Cyanobacteria 1
1.1.2. Cyanotoxins 2
1.1.3. Microcystins 4
1.2. Toxicodynamics of Microcystins **5**
1.2.1. Phosphatases 5
1.2.2. Microcystin Mode of Action 8
1.3. Toxicokinetics of Microcystins **10**
1.3.1. Absorption 11
1.3.2. Distribution 12
1.3.3. Metabolism and Excretion 17
1.4. Risk Assessment **20**
1.5. Aim of the Study **21**
2. Chapter I **23**
2.1. Hydrophobic Adda Determines Toxicity **23**
2.1.1. Introduction 23
2.1.2. Results 26
2.1.3. Discussion 34
3. Chapter II **38**
3.1. L-Amino Acid at Position (2) Determines OATP-Mediated Microcystin Uptake **38**
3.1.1. Introduction 38
3.1.2. Results 41
3.1.3. Discussion 51
4. Chapter III **57**
4.1. Role of Glutathione in the Microcystin Toxicity Mechanism **57**
4.1.1. Introduction 57
4.1.2. Results 60
4.1.3. Discussion 67
5. Chapter IV **73**
5.1. Protein Half-Lives of PPPs and Glutathione Synthesizing Enzymes **73**
5.1.1. Introduction 73
5.1.2. Results 76
5.1.3. Discussion 83

6. Chapter V 87
6.1. Immortalized Human Hepatocyte Cell Line Characterization 87
6.1.1. Introduction 87
6.1.2. Results 90
6.1.3. Discussion 100
7. Concluding Discussion 105
8. Materials and Methods 111
8.1. Cell Systems 111
8.1.1. Cell Lines 111
8.1.2. Microscopic Assessment 113
8.1.3. Growth Analysis 114
8.2. Microcystins 115
8.3. Assays 115
8.3.1. Cytotoxicity Assays 115
8.3.2. Metabolic Assays 117
8.3.3. Phosphatase Assays 117
8.3.4. Glutathione Assays 119
8.3.5. Multiplexing of Assays 121
8.4. Protein Half-Life Analysis 122
8.4.1. Cycloheximide Chase Assay 122
8.4.2. Determination of Glutathione Half-Life and Protein Stability 123
8.5. Protein Analysis 123
8.5.1. Membrane Protein Isolation 123
8.5.2. SDS PAGE 123
8.5.3. Western Blot Analysis 124
8.5.4. Proteomics 125
8.6. Gene Expression Analysis 125
8.6.1. Primer 125
8.6.2. Quantitative Real-Time PCR (RT-qPCR) 129
8.7. Cell Cycle Analysis 129
8.7.1. Cell Cycle Synchronization 129
9. Supplementary 131
9.1. Chapter I 131
9.2. Chapter II 133
9.3. Chapter III 135
9.4. Chapter IV 136
9.5. Chapter V 141
10. Authors Contributions 142
11. List of Figures 144
12. List of Tables 146
13. List of Abbreviations 147
14. Bibliography 149

Record of Achievements

Journal Articles:

Altaner, S., Jaeger, S., **Fotler, R.**, Zemskov, I., Wittmann, V., Schreiber, F., & Dietrich, D. R. (2020). Machine learning prediction of cyanobacterial toxin (microcystin) toxicodynamics in humans. *ALTEX, 37*(1), 24-36. (https://doi.org/10.14573/altex.1904031)

Awards

Toxins Award 2022 handed over by the German Society of Toxicology for the poster "Machine Learning Prediction of Cyanobacterial Toxin (Microcystin) Toxicodynamics in Humans".

Poster Presentations

- **Fotler, R.** Wrona M., Dressler J., Jaeger-Honz S., Wittmann T., Schreiber F., and Dietrich D.*, „L-Amino Acid Hydrophobicity in Position (2) Determines OATP1B1 but not OATP1B3 Mediated Transport of Microcystins in Humans", presented at the 62nd Annual Society of Toxicology Conference 03/2023 in Nashville, Tennessee, United States of America

- **Fotler, R***., Altaner S., Jaeger-Honz S., Zemskov I., Wittmann T., Schreiber F., and Dietrich D., „Machine Learning Prediction of Cyanobacterial Toxin (Microcystin) Toxicodynamics in Humans", Presented at the 61st Annual Society of Toxicology Conference 03/2022 San Diego, California, United States of America

- **Fotler, R***., Altaner S., Jaeger-Honz S., Zemskov I., Wittmann T., Schreiber F., and Dietrich D., „Machine Learning Prediction of Cyanobacterial Toxin (Microcystin) Toxicodynamics in Humans", Presented at the 88th Annual Meeting of the German Society for Experimental and Clinical Pharmacology and Toxicology (DGPT) 03/2022 Digital in Bonn, Germany

- **Fotler, R***., Riehle E., Altaner S., Dietrich, D.R., „Microcystin inhibition of human ser/thr protein phosphatases and impact on the eukaryotic glutathione detoxification system", Presented at the 11th International Conference on Toxic Cyanobacteria 05/2019 Krakow, Poland.

** presenting author*

Talks

Toxicological Profile of Microcystins, 2 h lecture as part of the 'Advanced Course Human-and Environmental Toxicology', annually 2019 – 2022

Supervision

Master Thesis

- Master Thesis Julia Dressler 2022 “Characterization of Human and Mouse Hepatocytes Under Physiological Oxygen Condition and Their Cellular Response to Cyanobacterial Toxin Microcystin”

- Master Thesis Elena Schönfeld 2021/2022 “Determination of Protein Half-Lives and Protein Stabilities of Human Serine/Threonine Phosphatases and Glutathione Relevant Enzymes”

Bachelor Thesis

- Bachelor Thesis Maja Kadel 2022 “Determination of the Toxic Properties of Microcystin Extract of Microcystis aeruginosa in Stably Transfected Human Embryonic Kidney Cells (HEK293)”

- Bachelor Thesis Julia Dressler 2020 “Determination of Microcystin Toxicity in Stably Transfected Embryonic Kidney Cells (HEK293)”

Internship and Advanced Course:

Supervision of 2 research assistants and interns, 4 students during the annual advanced course.

Scholarship and Funding

Full scholarship by the ‘Arthur- and-Aenne-Feindt-Stiftung’ (Hamburg, Germany).

Member of the ‘Graduate School Biological Sciences’ (GBS) of the university of Konstanz during the whole time of the PhD work.

Notes to the Reader

Dear Reader,

This dissertation is divided into five chapters, each of which can be read independently, including an introduction with detailed aim of the study, results, and a comprehensive discussion part.

Since all chapters deal with microcystin toxicity, but focus on specific aspects, possible repetitions in the introduction part are to be excused. Although each chapter can be read independently, cross-references are provided to facilitate further reading on individual aspects of microcystin toxicity.

All five chapters are framed by a detailed general introduction, including the general aim of this dissertation, and a concluding discussion that briefly contextualizes all chapters. All the materials and methods used, as well as all supplementary figures and tables, are summarized at the end in an additional chapter.

Since this dissertation is the result of a highly productive interdisciplinary collaboration between different departments (Biology, Chemistry, and Informatics), as well as several master's theses and students, all contributions are explicitly summarized at the end of this dissertation.

With this, I would like to take this opportunity to thank all the collaborators and students involved for the not only productive, but also highly valuable three years of collaboration!

Thank you!

Abstract

Although more than 250 microcystin congeners have been described, the toxicity of only a few are known and have been assessed using purified proteins, including only limited aspects of toxicity. Comparative studies including both toxicodynamic (serine/threonine phosphatase (PPP) inhibition and glutathione (GSH) conjugation) and toxicokinetic (cellular uptake via organic anion transporting polypeptides, OATPs) parameters are lacking so far. However, the mechanism of microcystin toxicity can only be fully understood by evaluating and combining both parameters. Therefore, the aim of this dissertation was to contribute to the understanding of each parameter, first in simplified but then in more complex but biologically more relevant cell systems. Using specifically synthesized microcystin congeners and purified PPPs, this study clearly demonstrated that the presence, length, and orientation of the unique and hydrophobic side chain Adda played a critical role in the microcystin-induced PPP inhibition mechanism. While the covalent bond formation, although inducing irreversibility, played a minor role in purified PPPs as well as in stably transfected HEK293 cell lines. Additionally, the individual transporting properties of OATP1B1 and OATP1B3 were studied. Therefore, stably transfected HEK293-OATP1B1, -OATP1B3, and control vector (CV) were exposed to 21 structurally different microcystin congeners covering the known spectrum of hydrophobicity, molecular weights and common as well as unusual modifications of the consensus structure. In this study, the positions (2) and (4) were demonstrated to determine the hydrophobicity of the microcystin molecule, thereby defining its OATP-mediated uptake. In this study, a clear correlation between the total hydrophobicity and OATP-mediated uptake was demonstrated and thereby allowing the classification of microcystins into three distinct groups: less toxic, moderately toxic, and very toxic. Moreover, position (2) was shown to be critical for OATP1B1-mediated, but not OATP1B3-mediated, microcystin uptake. Furthermore, it was shown that microcystin congener-specific toxicity *in vivo* is due to OATP-mediated uptake rather than to the different PPP inhibition capacities. This study provided preliminary insights into the potential role of GSH conjugation to microcystins by establishing three independent assays to simultaneously monitor cell viability (cytotoxicity), PPP activity and GSH response. The commonly accepted assumption that GSH conjugation to microcystin results in detoxification due to reduced toxicity was not supported as evidenced by total GSH depletion with subsequent microcystin exposure, while no significant changes in cytotoxicities and PPP activities were observed. These results were confirmed not only in simplified HEK293, but also in complex and biologically relevant human and mouse hepatocytes. Thereby, the microcystin-induced GSH response was shown to be significantly different between human and mouse hepatocytes, challenging the current risk assessment based solely on a mouse study. So far, microcystin toxicity studies have been limited to single exposures to high microcystin concentrations, mostly in either rodent or human but carcinogenic hepatocyte cell lines with questionable OATP expression and therefore critical biological relevance. This study demonstrated that the IHH cell line is a reliable and suitable cell line for (chronic) microcystin toxicity testing, as evidenced by the expression of hepatocyte-specific transporters, including the microcystin-relevant OATP1B1, OATP1B3, and MRP2.

Zusammenfassung

Obwohl mehr als 250 Microcystine beschrieben wurden, ist die Toxizität nur für wenige bekannt und wurde nur mit gereinigten Proteinen unter Verwendung begrenzter Toxizitätsaspekte untersucht. Vergleichbare Studien, die sowohl toxikodynamische (Inhibierung der Serin/Threonin Phosphatasen (PPPs) und Glutathion (GSH) Konjugation) als auch toxikokinetische Parameter (zelluläre Aufnahme über organische Anionen transportierende Polypeptide, OATPs) umfassen, fehlen bislang. Der vollständige Toxizitätsmechanismus von Microcystin kann jedoch nur durch die Auswertung und Kombination beider Parameter verstanden werden. Daher war es das Ziel dieser Dissertation, einen Beitrag zum Verständnis beider Parameter zu leisten, zunächst in vereinfachten, dann in komplexeren, aber biologisch relevanteren Zellsystemen. Die Ausbildung kovalenter Bindungen spielt dagegen nur eine untergeordnete Rolle. Zusätzlich wurden die individuellen Transporteigenschaften von OATP1B1 und OATP1B3 untersucht. Dazu wurden stabil transfizierte HEK293-OATP1B1, -OATP1B3 und -CV mit 21 verschiedenen Microcystinen behandelt. In dieser Studie konnte gezeigt werden, dass die Positionen (2) und (4) die Gesamthydrophobizität der Microcystine bestimmen und somit auch deren OATP-vermittelte Aufnahme definieren. In dieser Studie konnte eine klare Korrelation zwischen Hydrophobizität und OATP-vermittelter Aufnahme gezeigt werden, die eine Klassifizierung der Microcystine in drei Gruppen erlaubt: weniger toxisch, mäßig toxisch und sehr toxisch. Weiterhin konnte gezeigt werden, dass die Position (2) für die OATP1B1-vermittelte Aufnahme von Microcystinen entscheidend ist, jedoch nicht für die OATP1B3-vermittelte Aufnahme. Anschließend konnte gezeigt werden, dass die Microcystin-Kongener-spezifische Toxizität eher durch die OATP-vermittelte Aufnahme als durch Unterschiede in der PPP-Inhibitionskapazität induziert wird. Darüber hinaus wurden erste Erkenntnisse über die mögliche Rolle der GSH-Konjugation an Microcystine gewonnen, indem drei unabhängige Assays zur gleichzeitigen Überwachung der Zellviabilität (Zytotoxizität), der PPP-Aktivität und der GSH-Reaktion etabliert wurden. Die Hypothese, dass die Konjugation von GSH an Microcystin zu einer Verringerung der Toxizität führt, wurde verworfen. Dies konnte nicht nur in HEK293, sondern auch in den komplexeren Hepatozyten von Mensch und Maus gezeigt werden. Es zeigte sich auch, dass sich die durch Microcystin induzierte GSH-Reaktion zwischen Mensch und Maus signifikant unterscheidet, was die derzeitige Risikobewertung, die ausschließlich auf einer Studie an Mäusen beruht, in Frage stellt. Bisherige Studien beschränkten sich auf eine einmalige Exposition mit hohen Microcystinkonzentrationen und verwendeten meist Nagetierzelllinien, oder humane, aber karzinogene Hepatozytenzelllinen mit zweifelhafter OATP-Expression und daher kritischer biologischer Relevanz. Diese Studie zeigte, dass die IHH-Zelllinie eine zuverlässige und geeignete Zelllinie für (chronische) Microcystin-Toxizitätstests ist, was durch die Expression hepatozytenspezifischer Transporter, einschließlich der für Microcystin relevanten OATP1B1-, OATP1B3- und MRP2-Transporter, belegt wurde. Darüber hinaus konnte in dieser Studie gezeigt werden, dass es sich bei den PPPs um intermediär stabile Proteine handelt und die Halbwertszeit dieser Proteine auf einen Bereich von 16-24 Stunden eingegrenzt werden konnte.

1. General Introduction

1.1. Cyanobacteria

1.1.1. Ecology of Cyanobacteria

Cyanobacteria are a phylogenetic group of gram-negative and photoautotrophic bacteria. Due to their high tolerance to changing environments and successful combination of various pathways, cyanobacteria are among the oldest organisms on Earth (Tomitani et al., 2006; Whitton & Potts, 2007). Moreover, their ability to use two photosystems to split H_2O instead of H_2S enriched the atmosphere with oxygen, changing life on Earth from anaerobic to aerobic living conditions (Olson, 2006). Cyanobacteria (ancient Greek *kuanós* = blue) are enriched with (photosynthetic) pigments such as phycoerythrocyanin, carotenoids, and chlorophyll a, giving bacterial cultures an intense green or blue color (Colyer et al., 2005). This resulted in the use of the inaccurate, but commonly used term 'blue-green algae'. Despite the fact that cyanobacteria are procaryotes, their only similarity to eukaryotic algae is their ability to perform oxygenic photosynthesis. But instead of starch, they store a nitrogen-containing biopolymer, so called cyanophycin (Vermaas, 2001).

Figure 1: Cyanobacterial Blooms

Recurring cyanobacterial blooms in the northern region of the United States (Lake Erie). Severe bloom formations were detected in July 2015 (left) and July 2019 (right). Pictures were obtained from the NASA Earth Observatory.

Due to their high resilience and broad diversity, cyanobacteria can withstand harsh environmental conditions and are therefore found in many different and extreme environments, ranging from various salinities (freshwater and marine environments), various pH levels (from acidic hot springs to alkaline lakes), or extreme temperatures, such as hot springs or Antarctica (Kleinteich et al., 2012). Thereby, their organization forms are as diverse as their habitants, ranging from unicellular organisms to filamentous or colonial living forms. Cyanobacteria can be found in nature as either symbiotic or endosymbiotic organisms (Whitton & Potts, 2007). Moreover, the 'endosymbiotic theory' states that chloroplasts in higher plants and algae originate from the endosymbiosis of cyanobacteria incorporated by another unicellular organism. However, whether cyanobacteria are the origin of mitochondria remains controversial (Martin et al., 2015). Cyanobacteria possess a unique and remarkable ability to overcome nutrient limitations, which contributes

to their resilience. Some filamentous cyanobacteria such as Anabaena or Nostoc, have evolved the ability to differentiate individual cells into heterocysts under nitrogen-limited conditions (Whitton & Potts, 2007). Heterocysts are enlarged cells with micro-anaerobic conditions, allowing the activation of nitrogenase and fixation of atmospheric N_2 to provide the cells with nitrogen for biosynthesis (Broda & Peschek, 1983). This ability allows them not only to grow under nutrient-poor conditions but also to spread in large numbers, resulting in visible biofilms on the surface of water bodies, so called cyanobacterial blooms or harmful algal blooms (HABs), see **Figure 1**. Thus, bloom formation is favored by increasing water temperatures and high nitrogen and phosphorous water bodies (Paerl & Otten, 2013). With increasing eutrophication and rising temperatures due to climate change and global warming, bloom formation and bloom duration are expected to increase (Kleinteich et al., 2012; Paerl & Huisman, 2008). Alarmingly, studies have shown that warmer water temperatures not only favor bloom formation, but especially favor toxin-producing cyanobacteria species over non-toxic strains (Davis et al., 2009).

1.1.2. Cyanotoxins

Cyanobacteria produce numerous bioactive metabolites, including a variety of intracellular cyanotoxins. These cell-bound toxins are released into the water during cyanobacterial lysis due to cell death or the process of drinking water treatment (Hoeger et al., 2002). Cyanotoxins accumulate in aquatic organisms and reach higher trophic levels through the food chain, posing a threat not only to the environment but also to human and animal health (Chen et al., 2016). However, the natural functions of cyanotoxins remain unclear. A commonly accepted hypothesis is that cyanotoxins enhance competition with other bacteria or fungi in resource-limited environments (Svirčev et al., 2019). More recent studies suggest that in addition to the competitive advantage, some cyanotoxins may also function as cyanobacterial physiological aides, such as protecting against oxidative stress or assisting in nutrient uptake (Holland & Kinnear, 2013; Makower et al., 2015). Since the composition and toxicity of cyanotoxins are nearly as diverse as cyanobacterial genera, it seems most likely that no common function can account for all cyanotoxins (Codd et al., 2005). Generally, cyanotoxins have been classified according to their primary toxic effects on mammals as hepatotoxins, neurotoxins, dermatoxins, and endotoxins.

Hepatotoxins play a crucial role and are mainly associated with cyanotoxins. These include small cyclic peptides (microcystin, nodularin) but also alkaloids (cylindrospermopsin). The cyclic pentapeptide nodularin is structurally related to microcystin. Based on their structural homology, both hepatotoxins indicate similar mode of action: the inhibition of serine/threonine phosphoprotein phosphatases (MacKintosh et al., 1990; MacKintosh et al., 1995; Pearson et al., 2010). Both toxins primarily target the liver, but also accumulate in the intestine and kidneys. Acute intoxication with high toxin concentrations results in hepatocyte necrosis, hepatic vascular damage, and consequently death from hemorrhagic shock (McLellan & Manderville, 2017). Similar target, but different chemical structure and therefore different mode of action indicates cylindrospermopsin. Cylindrospermopsin is a tricyclic alkaloid and an uracil

analogue. It exerts its toxic properties by binding to DNA, leading to DNA fragmentation and subsequently inhibiting protein synthesis (Buratti et al., 2017).

The class of neurotoxins represent another group of highly potent toxins. Anatoxin, commonly known as very fast death factor (VFDF), is a bicyclic amine alkaloid. It binds to the nicotinic acetylcholine receptor by mimicking natural acetylcholine. Saxitoxin, also known as paralytic shellfish toxin, blocks voltage-gated sodium channels, and disrupts neuronal signaling. In both cases, acute intoxication with high toxin concentrations results in death from respiratory failure (Carmichael et al., 1975; Carmichael et al., 1979).

A recent study summarized and analyzed all published data from the beginning of all records until 2018 on the global occurrence of cyanotoxins and cyanotoxin-related intoxications in humans and animals. The geographical distribution in Europe revealed microcystin as the most abundant cyanotoxin found (58 %, 198 out of 341 reports), followed by cylindrospermopsin (18 %), saxitoxin (10 %), anatoxin (10 %), and nodularin (1 %), see **Figure 2**. Likewise, in the United States, microcystin was the most frequently reported toxin (57 %, 135 out of 238 reports), followed by anatoxin (15 %), cylindrospermopsin (4 %) and saxitoxin (3 %) (Svirčev et al., 2019).

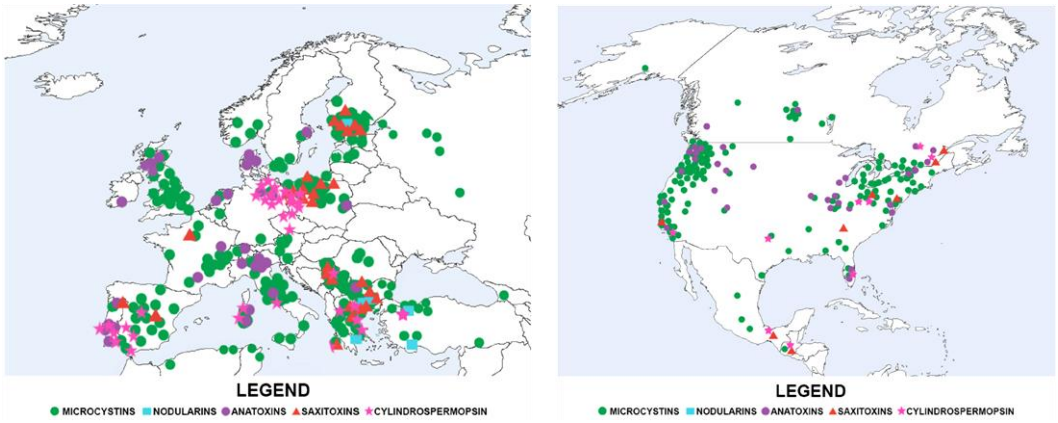

Figure 2: Geographical Distribution of Cyanotoxin Reports

Geographical distribution of cyanotoxins occurrence reported in Europe (left) and North and Central America (right), demonstrating microcystins as the most abundant cyanotoxin. Images have been adapted from Svirčev et al., 2019.

In this global review of global cyanobacterial blooms, microcystins were clearly identified as the most commonly occurring cyanotoxin in freshwater. But despite being extensively studied, the toxicokinetic and toxicodynamic aspects of microcystins in humans remain poorly understood. However, microcystins comprise a group of more than 250 different variants with specific kinetic and dynamic properties and varying toxicity. This emphasizes the urgency of understanding the toxic mechanisms and consequently assessing the associated risks.

1.1.3. Microcystins

Microcystins are one of the most abundant cyanobacterial toxins and are named after Microcystis aeruginosa, a species of cyanobacteria in which the toxin was first identified. In fact, other genera such as Nostoc or Anabaena, are also capable of producing microcystins (Dawson, 1998; Falconer et al., 1980; Runnegar et al., 1987).

Microcystins comprise a complex group of cyclic peptides consisting of seven common but also unique amino acids, see **Figure 3**. The consensus structure of microcystins include: D-alanine at position (1), two variable L-amino acids at positions (2) and (4), ß-D-methylaspartate at position (3), D-glutamine at position (6), D-methyldehydroalanine (Mdha) at position (7) and a unique hydrophobic amino acid Adda (3-amino-9-methoxy-10-phenyl-2,6,8-trimethyl-deca-4(E),6(E)-dienoic acid) at position (5) that is characteristic of microcystins and nodularins (Malik et al., 2020). While positions (1), (5) and (6) are quite conserved, positions (3) and (7) show variations, such as (de)methylation. However, positions (2) and (4), which are mostly incorporated L-amino acids, are hypervariable positions and specify the nomenclature of microcystins. The variable positions combined with other minor alterations result in many possible microcystin variants, so called congeners. To date, more than 250 microcystin congeners have been described (Spoof & Catherine, 2016). Thereby, the nomenclature is derived from the amino acid one-letter code at the positions (2) and (4). The most studied congener, and generally often described to be the most toxic congener, is MC-LR (L = leucine, R = arginine). The congeners differ in their polarity, some contain hydrophobic amino acid residues such as MC-LF (F = phenylalanine) and MC-LW (W = tryptophan), while MC-RR is more hydrophilic (McLellan & Manderville, 2017; Vichi et al., 2016).

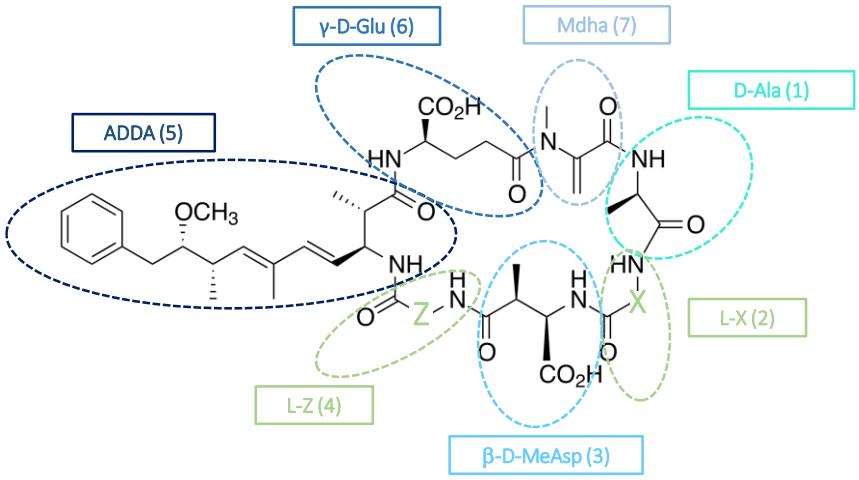

Figure 3: Consensus Structure of Microcystins

The monocyclic heptapeptide consists of five D-amino acids and two variable L-amino acids. All microcystins share a common consensus structure: at position (1) D-alanine (D-Ala), followed by two variable L-amino acids (L-X, L-Y) at positions (2) and (4), ß-D-methylaspartate (ß-D-MeAsp) at position (3), unique Adda chain at position (5), γ-D-glutamine (γ -D-Glu) at position (6) and at position (7) D-methyldehydroalanine (Mdha).

The cyclic structure increases their chemical stability and resistance to chemical degradation such as hydrolysis or oxidation, despite low pH levels or high temperatures (Drobac et al., 2013). Regardless of UV irradiation, microcystins can persist in water for months or even years (Chorus & Welker, 2021; Harada et al., 1996). Considering the consumption of contaminated food, microcystins have been found to withstand boiling for several hours and never could be completely removed (Schmidt et al., 2014). Once ingested, the toxin is resistant to enzymatic breakdown by digestive enzymes such as pepsin, trypsin, or chymotrypsin (Smith et al., 2010).

In general, the toxicological effects of foreign substances, such as microcystins are determined by their toxicodynamic and toxicokinetic properties. Toxicodynamics describes the effect and mode of action of a substance, i.e., 'what the toxin does to the body'. Toxicokinetics, on the other hand, describes the extent and time course of a substance resulting from the interaction of absorption, distribution, metabolism, and excretion, essentially 'what the body does to the toxin' (Marquardt et al., 2019).

1.2. Toxicodynamics of Microcystins

Toxicodynamics studies the dynamic interaction of a toxin with its biological target, resulting in adverse effects at the cellular level. The subcellular biological targets of microcystins are serine/threonine phosphoprotein phosphatases (PPPs). By forming a covalent bond with the catalytic subunit and through hydrophobic interactions, microcystins irreversibly inhibit PPPs and completely abolish their function, resulting in hyperphosphorylation and disruption of protein homeostasis and signaling pathways.

1.2.1. Phosphatases

Protein (de)phosphorylation is a highly dynamic process that tightly regulates enzyme (de)activation. Post-translational modifications, such as phosphorylation, are crucial for the induction and regulation of intracellular signaling pathways and the maintenance of cellular protein homeostasis. Hence, the balance between phosphatases (dephosphorylation) and kinases (phosphorylation) is essential. In humans, 2 % of the genome is encoded for kinases (518 protein kinases of which 428 (82 %) are serine/threonine kinases, whereas only 200 phosphatases exist, of which only 30 (15 %) account to the class of serine/threonine phosphatases) (Shi, 2009). While all kinases share a common three-dimensional structure and biochemistry, phosphatases are much more complex, with a variety of different structures and hydrolysis mechanisms. Accordingly, phosphatases are clustered into four classes based on their target dephosphorylation residue: serine/threonine phosphatases, tyrosine phosphatases and dual specificity phosphatases (capable of dephosphorylating tyrosine as well as serine and threonine residues) and the rare class of histidine phosphatases (Brautigan, 2013).

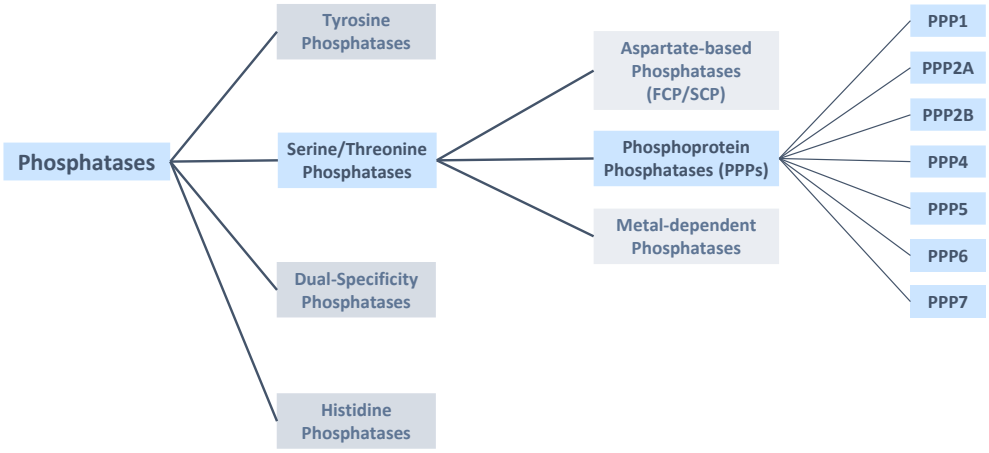

Figure 4: Phosphatase Classification

Phosphatases can be divided into four classes: tyrosine phosphatases, serine/threonine phosphatases, dual specificity phosphatases and the rare class of histidine phosphatases. Serine/threonine phosphatases are further subdivided into families and each family consists of several family members. Phosphatases relevant to microcystin-induced toxicity mechanisms are highlighted in blue.

Serine/Threonine Phosphoprotein Phosphatases (PPPs)

In eukaryotic cells, phosphorylation occurs mainly on three hydroxyl-containing amino acids: serine, threonine, tyrosine, and rarely on histidine. Proteomic analysis of 6600 phosphorylation sites on 2244 human proteins revealed that serine is the most dominant target of all phosphorylation sites (86.4 %), followed by threonine (11.8 %) and tyrosine (1.8 %) (Olsen et al., 2006). Although histidine phosphorylations are well studied in plants, fungi and bacteria, phosphorylation on histidine residues in mammalian cells is still poorly understood, so are their biological roles (Besant & Attwood, 2005). Due to the predominance of serine and threonine phosphorylation sites, serine/threonine phosphatases represent the largest and best studied class of phosphatases and have been further specified into three families: phosphoprotein phosphatases (PPPs), aspartate-based protein phosphatases (FCP/SCP), and metal-dependent phosphatases (PPM), see **Figure 4** (Shi, 2009). In contrast to the FCP/SCP members, PPMs and PPPs require metal ions for their catalytic activity. While PPPs require manganese (Mn^{2+}), zinc (Zn^{2+}) or ion (Fe^{2+}), PPM members prefer manganese (Mn^{2+}) and magnesium (Mg^{2+}) (Barford et al., 1998; Egloff et al., 1995; Shi, 2009).

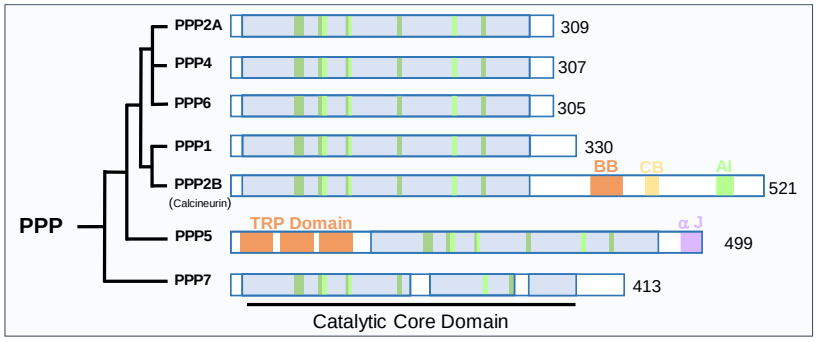

Figure 5: PPP Catalytic Domains

PPP family members exhibit a common catalytic core domain, while PPP2B and PPP5 demonstrate additional domains for protein regulation. The most closely related PPPs are PPP2A, PPP4 and PPP6. Figure was adapted and modified from Shi 2009.

PPPs represent the largest family in the class of serine/threonine phosphatases. The PPP family is mainly characterized by the association of the catalytic subunit with various regulatory subunits according to their function and target tissue. Based on the sequence of the catalytic subunits, PPPs have been further classified into seven subtypes: PPP1, PPP2A, PPP2B (Calcineurin), PPP4, PPP5, PPP6 and PPP7, see Figure 5. Although the catalytic subunits of the PPPs are highly conserved with a sequence homology of approximately 65 % (Altaner, 2019), each subtype exhibits remarkable substrate specificity due to the interaction with specific regulatory subunits as well as scaffolding subunits, as summarized in Table 1.

Although PPPs are typically expressed ubiquitously, their expression level vary depending on organ and tissue. Solely the expression of PPP7 is restricted to the retina and brain region (Cohen, 2004; Shi, 2009). While PPP1 only binds to a regulatory subunit, PPP2A, PPP4, and PPP6 require a scaffold subunit for complete activation (Brautigan, 2013). This could be attributed to the fact that PPP2A, PPP4, and PPP6 are more closely related (Cohen, 2004; Shi, 2009). Among all PPPs, PPP5 is the most unique one. PPP5 neither binds to a scaffolding nor to a regulatory subunit. Its enzymatic function is regulated by an autoregulatory tetratricopeptide repeat (TPR) domain located on the same peptide as the catalytic subunit (Chen et al., 1994; Yang et al., 2005). The mechanism of dephosphorylation takes place in a single step reaction: a water molecule activated by two metal ions positioned at the catalytic site of the PPPs, acts as a nucleophile initiating hydrolysis of the substrate phosphomonoester bond (Shi, 2009).

Table 1: Members and Functions of PPP Family

The main functions, subcellular expression, and tissue distribution of members of the PPP family are summarized. Table was compiled from various sources, including (Altaner, 2019; Brautigan, 2013; Cohen, 2004; Shi, 2009).

Enzyme	Subunits	Involved in	Subcellular Expression	Tissue Distribution
PPP1	> 100	Dopamine response Lipid metabolism Circadian rhythm Glycogen metabolism	Primarily nuclear, but also present in the cytosol, highly mobile	Ubiquitously expressed, interacts with over 200 regulatory proteins
PPP2A	> 15	Cell survival Cell Cycle/DNA replication Apoptosis	Cytosol Mitochondria Nucleus	Ubiquitously expressed, highly conserved
PPP2B	2	Memory Long-term potentiation Neuro-and muscle development	Cytosol T-tubules	High levels in the brain regions; activated by high Ca^{2+} concentrations
PPP4	> 5	Organization of microtubules (centrosomes) Histone-phosphorylation	Cytoskeleton Cytosol Nucleus	Ubiquitously expressed
PPP5	None	Stress response Cell cycle arrest Regulation of DNA damage kinases	Predominantly expressed in nucleus, but also cytoplasm	Ubiquitously expressed with higher levels in brain region; regulation through autoinhibition
PPP6	> 4	G1/S transition Transcription Translation Morphogenesis	Cytosol Mitochondria	Ubiquitously expressed
PPP7	Unknown	Regulation of retinal function	Cytosol Nucleus	Brain regions

1.2.2. Microcystin Mode of Action

The primary effect of microcystins is the inhibition of the catalytic subunit of serine/threonine phosphoprotein phosphatases (PPPs), resulting in hyperphosphorylation. To date, the inhibition mechanism of MC-LR has mostly been studied in the catalytic subunits of either PPP1 or PPP2A.

Inhibition Mechanism

In general, microcystins inhibit PPPs by binding to the catalytic subunit and thereby abolishing their functionality in a two-step process:

(1) First, a non-covalent binding of the hydrophobic Adda side chain to the hydrophobic active site of PPPs allows the correct positioning of microcystins in the catalytic center.

(2) Second, a covalent bond is formed between the terminal carbon atom of Mdha and a cysteine residue of the PPP catalytic center.

Thereby, the inhibitory capacity can be observed prior to covalent attachment, although covalent binding takes only approximately two hours (Pereira et al., 2013). The precise interaction sites between microcystins and PPPs have been determined by co-crystallization of the catalytic subunit of PPP1 complexed with MC-LR (Goldberg et al., 1995) or radiolabeled PPP1 complexed with MC-LR (MacKintosh et al., 1990; MacKintosh et al., 1995). Since all PPPs share a highly conserved catalytic subunit, the two-step process of enzyme inhibition is thought to be similar for all PPPs (Pereira et al., 2013). Crystallized structures of PPP1 and PPP2A complexed with MC-LR suggest a very similar conformation of the toxin within the active sites (Altaner, 2019). More recent and advanced *in silico* modeling methods provided insights into the dynamics of the binding interactions. Molecular dynamics simulation was used to study the conformation of MC-LR and its binding to PPP1. It was shown that MC-LR could adapt to a folded conformation that allowed a formation of stable hydrogen bonds with PPP1. Additionally, the simulation suggested that the binding of MC-LR induced a conformational change in PPP1, potentially explaining its inhibitory effect on enzymes (Jaeger-Honz et al., 2022).

Cellular Consequences Using PPP2A as Example

The determination of the toxic effects of microcystins has been extensively studied in a variety of model systems, including cellular model systems, as well as in whole animal model organisms. Once absorbed, microcystins are rapidly taken up via transporters, so called organic anion transporting polypeptides (OATPs) and cause enzyme inhibition due to their high affinity for PPPs. As a result, affected cells remain in a hyperphosphorylated state, disrupting multiple signal transduction pathways. In Figure 6, some of the most striking and interrelated cellular consequences induced by mainly PPP2A inhibition are presented. It is important to note that these indicated cellular effects represent only a limited part of the total cellular consequences induced by microcystin exposure.

The cytoskeleton of eukaryotic cells is a highly complex and well-organized network of microfilaments, microtubules, and intermediate filaments. Its functions not only include the maintenance of cell shape but it's also crucial in the process of cell division, migration, adhesion, and signal transduction (Hohmann & Dehghani, 2019). Dynamic changes in (de)phosphorylation are required to maintain cytoskeletal homeostasis. Microcystin-induced hyperphosphorylation affects all three cytoskeletal components (Zhou et al., 2015). Cytokeratin 8 and 18, which are important intermediate filaments, become hyperphosphorylated when PPP2A is inhibited. This contributes not only to cytoskeletal disruption but is also associated with tumor-promoting effects (Ohta et al., 1992). Microcystins cause severe microfilament disorganization, by promoting actin fibers in depolymerization, subsequent, aggregation and collapse. This is mainly mediated by mitogen-activated kinase (MAPK), which are typically dephosphorylated by PPP2A leading to their inactivation and consequently initiating apoptosis (McLellan & Manderville, 2017; Zhou et al., 2015). Additionally, the activation of the tumor suppressor protein p53 has been directly linked to microcystin toxicity (McLellan & Manderville, 2017; Takumi et al., 2010; Vichi et al., 2016). As a substrate of PPP2A, hyperphosphorylation leads to the stabilization and accumulation of activated p53, which induces the expression of the pro-apoptotic Bax. In turn, Bax triggers the release of cytochrome C, leading to the activation of the apoptotic pathway via caspases (Aubrey et al., 2018).

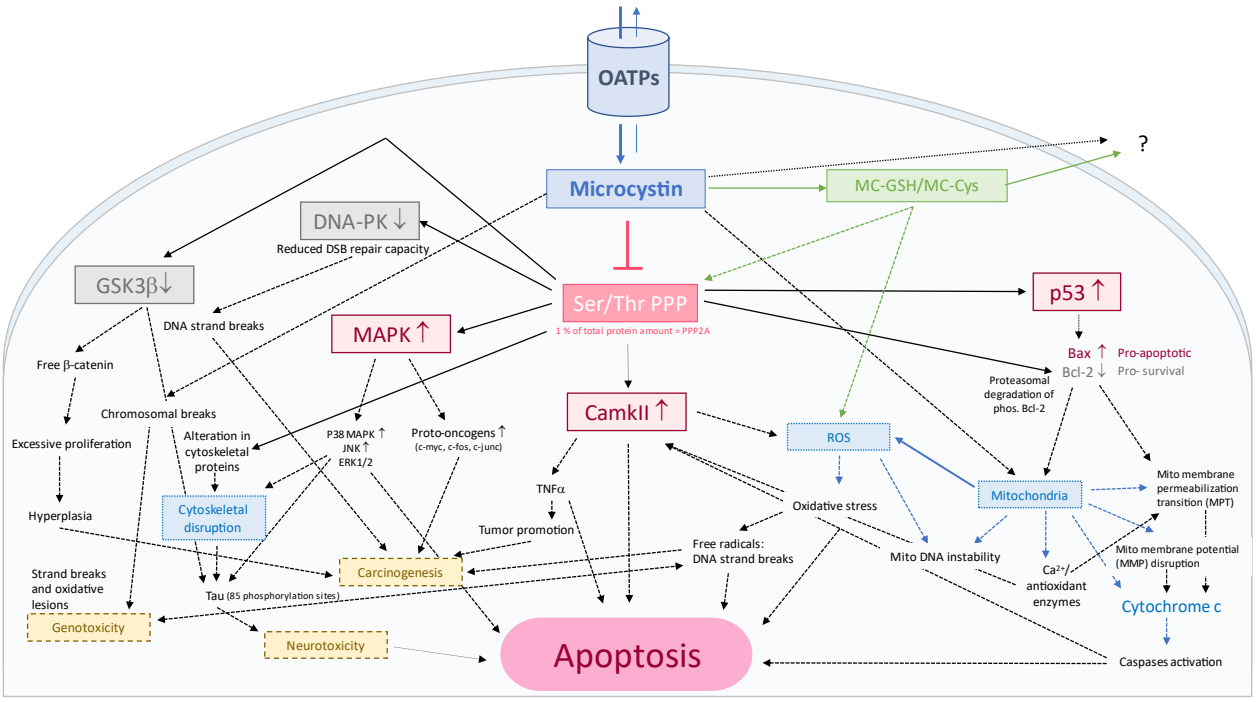

Figure 6: Cellular Consequences of Microcystin-Induced PPP2A Inhibition

Summarized are the main cellular consequences of microcystin-induced PPP2A inhibition. Microcystins are actively taken up via OATPs and primarily target PPPs. Through covalent binding, microcystins induce irreversible PPP inhibition, leading to a cascade of adverse effects, as indicated in the blue boxes. Substrates of PPP2A activated by hyperphosphorylation are marked with red boxes, resulting in severe cellular toxic effects, as highlighted in yellow boxes. Consequently, cell death is induced mostly by apoptosis. Schematic illustration was compiled using various sources (McLellan & Manderville, 2017; Shi, 2009; Vichi et al., 2016; Zhou et al., 2015).

Furthermore, the pro-survival protein Bcl-2 is directly phosphorylated by PPP2A (Li et al., 2016). In its phosphorylated form, it is tagged for ubiquitylation and consequently degraded via the proteasome. Finally, microcystins induce cell death not only by activating p53 and inducing pro-apoptotic Bax expression, but also by suppressing pro-survival Bcl-2 activity by proteasomal degradation. The generation of reactive oxygen species (ROS) by microcystins, leading to increased oxidative stress, is thought to be the result of two mechanisms. Firstly, elevated ROS levels via disruption of the glutathione (GSH) homeostasis due to GSH conjugation with microcystins, leaving no free GSH for ROS scavenging function (Bouaïcha & Maatouk, 2004). Secondly, elevated ROS levels via the activation of Ca^{2+}/calmodulin-dependent protein kinase II (CamKII), which is known to increase ROS and induce oxidative stress through multiple pathways (Campos & Vasconcelos, 2010; Fladmark et al., 2002). Oxidative stress is known to induce apoptosis through multiple ways, including the activation of caspase enzymes, mitochondrial dysfunction, and DNA damage (Marnett, 2000).

In summary, all cellular consequences are highly interrelated. Despite the individual damage caused by each cellular event, their cumulative effect is dramatic and ultimately leads to the induction of cell death.

1.3. Toxicokinetics of Microcystins

Toxicokinetics describes the **a**bsorption, **d**istribution, **m**etabolism, and **e**xcretion (ADME) of a toxin as a function of dose and time. Decisive factors are the route of exposure and the toxin concentration, see **Figure 7**. The toxicokinetic properties of microcystins are characterized by moderate intestinal absorption but rapid distribution to the primary target organ (liver), low metabolism including glutathione conjugation, and low urinary and fecal excretion (Arman & Clarke, 2021).

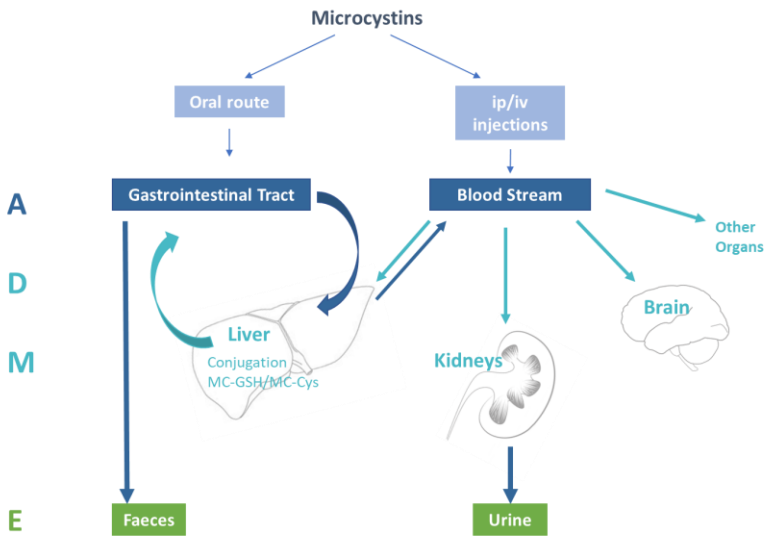

Figure 7: Toxicokinetics of Microcystins

Schematic ADME (absorption, distribution, metabolism, and excretion) pathways of microcystins. Toxicity and toxicokinetic properties are highly dependent on the route of exposure and bioavailability. Illustration was modified and adapted (Vichi et al., 2016).

1.3.1. Absorption

The route of exposure determines the route of absorption. Microcystins can be absorbed through the gastrointestinal tract (e.g., oral ingestion of contaminated water or food), directly into the bloodstream (e.g., intravenous exposure), through dermal absorption, or by inhalation of microcystin aerosols during recreational activities (McLellan & Manderville, 2017). However, inhalation of microcystin aerosols is not considered to be of significant concern since the calculated aerosol concentrations generated by wind would not reach critical concentrations (Wood & Dietrich, 2011). By far the most reported route of exposure is the oral route. With increasing health awareness, but also due to the shift from synthetic to more natural alternatives to pharmaceutical products, the demand for dietary supplements and health products, including a variety of 'blue-green-algae' products, is increasing dramatically. However, these often contain toxin-producing cyanobacterial materials (Bautista et al., 2015; Gilroy et al., 2000; Heussner et al., 2012; Vichi et al., 2012). Although rare, intravenous exposure to microcystins is the most serious and harmful route of exposure. To date, only two cases of intravenous human exposure to microcystins have been reported. These two cases involved microcystin-contaminated water as part of dialysis treatment for patients with pre-existing kidney disease. The most dramatic case occurred in 1996 in Caruaru, Brazil. A total of 131 patients were treated with contaminated water, resulting in 76 deaths directly linked to microcystin toxicity (Azevedo et al., 2002; Carmichael et al., 2001; Pouria et al., 1998). Five years later, in 2001, a similar accidental use of microcystin-contaminated water occurred in Rio de Janeiro, Brazil. A total of 44 patients were exposed to microcystin-contaminated water during dialysis treatments, this time at sublethal concentrations (Soares et al., 2006).

Excurse: Lipinski's Rule of Five

The toxicokinetics of a chemical substance is highly dependent on its bioavailability. Bioavailability is the ability of a chemical to be absorbed into the blood and utilized by the body. Due to chemical properties (e.g., solubility, hydrophobicity), first-pass effect in the liver, or degradation by enzymes in the intestine, the route of exposure is critical in determining bioavailability (Marquardt et al., 2019). Lipinski's rule describes the molecular properties of a chemical substance (drug or toxin), reflecting its kinetic properties and bioavailability in the human body (Benet et al., 2016). According to the rule, a substance has a high bioavailability when administered orally if it has following properties: (1) Not more than ten hydrogen bond acceptors. (2) Not more than five hydrogen bond donors. (3) A molecular weight of less than 500 g/mol. (4) An octanol-water partition coefficient (LogP) not exceeding 5 (Benet et al., 2016). SwissADME, an *in silico* web tool for evaluating and predicting pharmaco- and toxicokinetic properties of small molecules (Daina et al., 2017), was used for microcystins. Using the chemical structure of the most frequently detected microcystins, the *in silico* predicted bioavailability was relatively low, since three of Lipinski's rules were violated. Regardless of the congener, the molecular weight of microcystins is above 500 g/mol, more than ten hydrogen bond acceptors and more than five hydrogen donors could be

detected. Despite low bioavailability and the moderate absorption, the challenge with microcystin toxicity is its poor excretion and high affinity for albumin, resulting in its potential persistence in the body for an extended time.

1.3.2. Distribution

Compared to other organisms (bovine, porcine and fish), human albumin demonstrated the highest binding rate to microcystins (Zhang et al., 2013). Because of its high binding affinity to albumin, microcystins are rapidly distributed through the systemic circulation, primarily to the liver, but also to other organs. The distribution of the toxin to organs other than the liver depends on the availability of the transporters and the level of blood perfusion of the organ.

Liver

Located in the upper abdominal cavity, the liver is a crucial organ with a unique structure. It is divided into two main lobes, which are further subdivided into eight segments, comprising various smaller lobules. The liver is supplied with blood by two main sources: the hepatic artery, which provides oxygenated blood (accounting for only 25 % of the total liver blood supply), and the portal vein, which brings nutrient-rich blood from the digestive tract (75 % of the liver blood supply). The liver performs essential functions, such as detoxification, bile synthesis, glycogen storage, and blood glucose regulation. Over 12 % of our total blood volume is found in the liver (Schulze et al., 2019; Stanger, 2015).

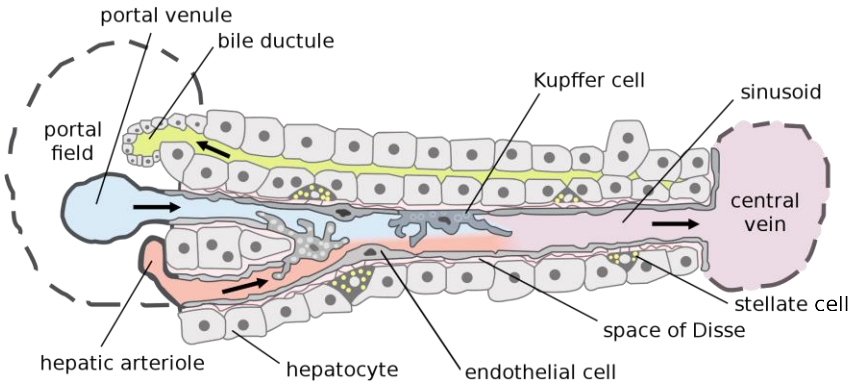

Figure 8: Hepatic Lobule

The hepatic lobule consists of hepatocytes, the primary functional cell type of the liver, arranged in plates separated by sinusoids. Endothelial cells encase primary blood vessels, called sinusoids, and are in close contact with hepatocytes, although they are separated by an interstitial space (space of Disse). Bile canaliculi transport bile to the bile ducts. The portal triad is located at each corner of the lobule. Schematic illustration was reproduced and adapted (Frevert et al., 2005).

All liver functions take place in the microscopic functional units, so called lobules, see **Figure 8**. Each lobule consists of hepatocytes arranged in a distinctive hexagonal pattern around a central vein, with each corner of the hexagon being a portal triad consisting of a bile duct, hepatic artery, and a portal vein. Hepatocytes are the most abundant cell type found in the lobules, representing 60 % of the total cell number and 80 % of the total cell mass (Stanger, 2015). Hepatocytes perform key functions, including detoxification and the synthesis and secretion of albumin and bile. Synthesized bile is collected and transported through

the bile canaliculi to the bile duct, where it is released into the duodenum. Endothelial cells encase primary blood vessels, called sinusoids, and are in close contact with hepatocytes, although they are separated by an interstitial space, known as space of Disse. This interstitial space enables the exchange of substances between the blood and the hepatocytes, through fenestrated endothelial cells, such as the uptake of nutrients. Moreover, Kupffer cells can be found in the Space of Disse. These are the liver resident macrophages, specialized immune cells that remove waste products and harmful substances from the blood (Schulze et al., 2019; Stanger, 2015).

Liver Zonation

The liver is a complex and multifunctional organ. One of its key features is its ability to display functional heterogeneity. Despite similar morphology, hepatocytes located in the portal vein and central vein regions exhibit different functions. The division of the liver into distinct functional zones based on the distribution of blood, oxygen, nutrients and metabolic activity is called liver zonation (Stanger, 2015). The liver is divided into three zones:

(1) Zone 1 (or periportal zone) is located around the portal triads and is directly supplied with blood and oxygen. It has the highest oxygen content with 10 – 15 % oxygen. This zone includes energetically demanding functions, such as gluconeogenesis, and protein secretion.

(2) Zone 2 (or intermediary zone) is in the midlobular zone, and its oxygen content is gradually decreased from 10 % to 5 % O_2.

(3) Zone 3 (perivenous or centrilobular zone) is located around the central vein that drains the blood from the liver and has the lowest oxygen content (< 5 %). With decreasing oxygen, less energy-demanding processes such as xenobiotic metabolism and detoxification, bile acid biosynthesis, and glycolysis are engaged (Kietzmann, 2017; Stanger, 2015).

Microcystin Pathophysiology

Although microcystins primarily target the liver, there is evidence that microcystins accumulate in other tissues and organs and cause similar damage (McLellan & Manderville, 2017). While most of the available data are derived from rodent studies, an increasing number of epidemiologic studies are providing data linking microcystin exposure to specific human pathologies (Arman & Clarke, 2021). Acute exposure simulation in rats by intravenous injection of microcystins showed that in addition to the liver, microcystins were found in the kidneys, followed by the lungs and stomach. Low concentrations were also found in the heart, intestine, spleen, brain, and gonads (Wang et al., 2008). Organ distribution and pathophysiological effects are highly dependent on the type of toxicity. Toxicity can be either acute (a single exposure with a high toxin concentration) or chronic (multiple exposures with a low concentration over time). Overall, the organ distribution of microcystins is complex and influenced by a variety of factors, including route of exposure, dose, and individual susceptibility, see Figure 9.

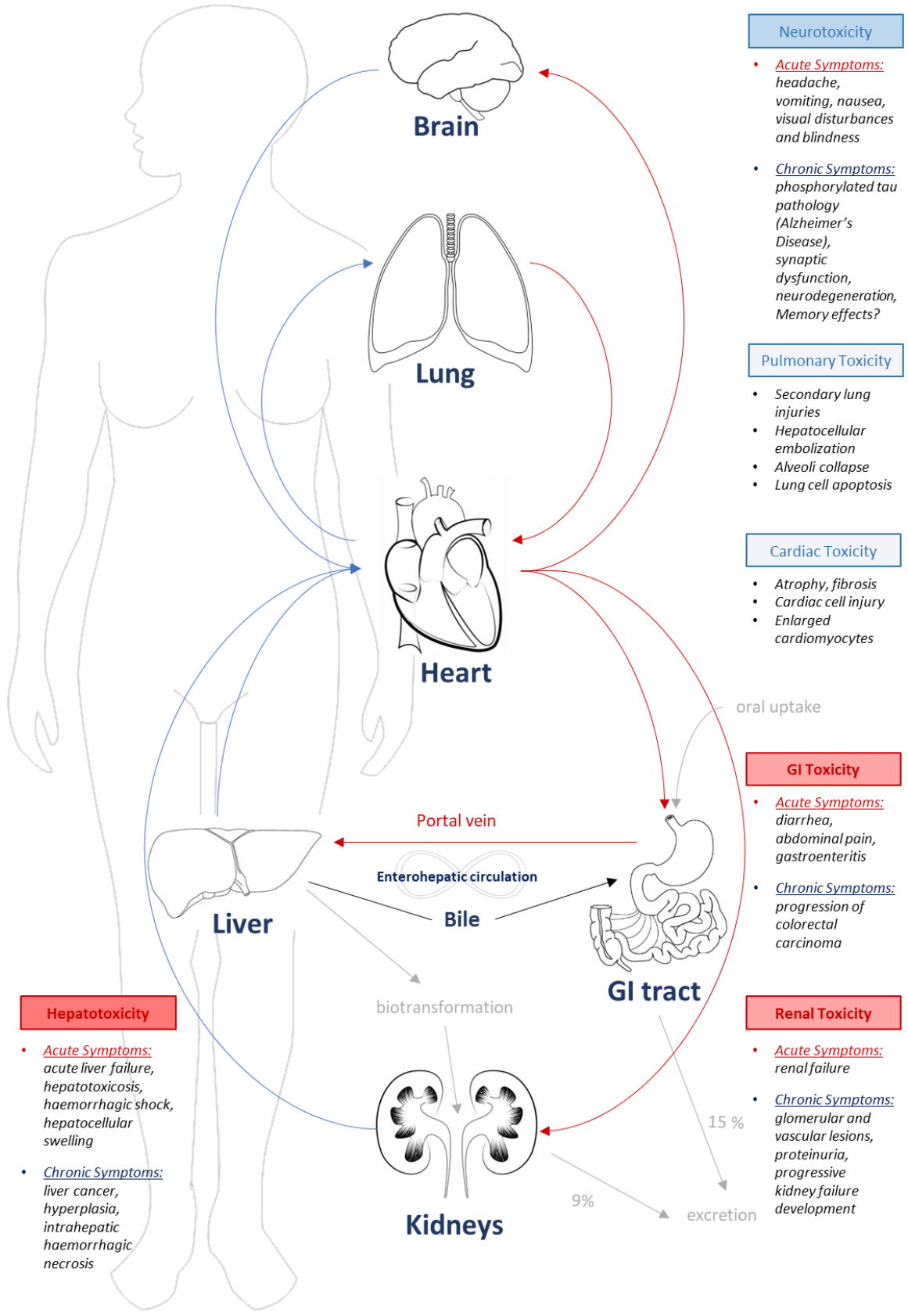

Figure 9: Systemic Circulation and Organ Distribution of Microcystins

Schematic illustration of the human systemic blood circulation. Red arrows indicate oxygen-rich blood flow, blue arrows indicate oxygen-deficient blood flow. Boxes describe microcystin-induced toxicity, symptoms, and tissue damage. Red boxes indicate severe toxicity, followed by blue boxes indicating moderate toxic effects. Schematic representation contains primarily rodent data and has been compiled of various sources.

Liver Toxicity

Microcystins are distributed via the portal circulation to the liver, where they are rapidly taken up by hepatocytes through influx transporters known as organic anion transporting polypeptides (OATPs). It is not only the accumulation of microcystins in the liver that is challenging, as OATP expression is particularly high in hepatocytes. It is also the continuous distribution within the enterohepatic circulation that causes repeated damage to the liver. Through the enterohepatic circulation, microcystins can be released from the liver through the bile into the duodenum, then reabsorbed into the bloodstream and transported back to the liver for an indefinite period of time.

Rodent studies of acute microcystin exposure resulted in centrilobular inflammation and fibrosis, disruption of hepatic plates, apoptosis, and necrosis (Clarke et al., 2019; Yoshida et al., 1998). These results are consistent with observations from accidental human exposures during dialysis in Caruaru, Brazil in 1996 (Azevedo et al., 2002). Acute human exposure to microcystins has been associated with serum biomarkers of liver damage, including aspartate aminotransferase (AST), alanine aminotransferase (ALT), γ-glutamyltransferase (Chen et al., 2009; Svirčev et al., 2017). But the acute liver failure in a 20-month-old child with subsequent liver transplantation after acute microcystin exposure due to recreational activities in highly contaminated waters, seems to be an exceptional case (Vidal et al., 2017). While acute effects such as acute liver failure, hemorrhagic necrosis and hepatic swelling have been consistently observed in several species, including rats, mice, dogs, cattle, and sea otters, reported acute effects in humans are rare (Backer et al., 2013; Miller et al., 2010). Environmental exposures do not appear to exceed the threshold for acute human toxicity, so that microcystin-induced liver damage is mainly reflected by chronic exposure (Shi et al., 2021).

Chronic exposure to microcystins has been linked to the risk of hepatocellular cancer induced by the tumor-promoting properties of microcystins. Microcystins are classified as 'possibly carcinogenic to humans' by the International Agency for Research on Cancer (Iarc, 2010). This classification is based on rodent studies, but also on epidemiological data of hepatocellular carcinoma directly related to microcystin exposure in fishermen, mainly in the southwestern region of China (Yu, 1995). The tumor-promoting properties induced by repeated exposure to low concentrations of microcystins may be due to several mechanisms. By disrupting cellular homeostasis through hyperphosphorylation, microcystins may contribute to cell growth and, in contrast to acute microcystin-induced toxicity, result in the inhibition of apoptosis. However, the constant cell death induced by the toxic potential of microcystins could promote cell proliferation to main organ function. But since, proper cell cycle checkpoints are not available due to PPP inhibition, cells proliferate without control, making cells susceptible to mutations and thus increasing the likelihood of cancerous lesions (Zegura, 2016).

Furthermore, at the molecular level, microcystins inactivate glycogen synthase kinase-3β (GSK3β), which is involved in the Wnt signaling pathway and is responsible for β-catenin phosphorylation, leading

to β-catenin ubiquitylation. Accumulation of non-phosphorylated β-catenin induces its translocation into the nucleus where it induces the expression of proliferative genes, resulting in hyperplasia and carcinogenesis (Thompson & Williams, 2018).

Renal Toxicity

Toxicity in other organs than the liver is typically the result of chronic exposure to relatively low concentrations of microcystins. Nevertheless, chronic microcystin exposure poses a risk to renal toxicity. Chronic exposure of microcystins was shown to damage the cortex and medulla of the kidneys (Milutinović et al., 2002). Vascular alterations and intense number of proteins found in the urinary space induced glomerular leakage, decreased glomerular filtration rates and incremented urinary flow. Results of rodent studies indicated that microcystins are assumed to lead to progressive kidney failure (Lin et al., 2016; Xu et al., 2020).

Gastrointestinal Toxicity

Microcystins enter the gastrointestinal tract through oral ingestion, but also through release of microcystins from the liver via the enterohepatic circulation. Symptoms of acute microcystin intoxication include diarrhea, abdominal pain, nausea, vomiting and gastroenteritis, triggered by microcystin-induced apoptotic damages to the ileum, jejunum, and duodenum (Botha et al., 2004; Pilotto et al., 1997). Chronic exposure is assumed to contribute colorectal carcinoma by stimulating epithelial to mesenchymal transition (EMT) and inducing motility and invasive properties, leading to distant metastasis (Ren et al., 2017; Zhou et al., 2002).

Neurotoxicity

The blood-brain-barrier expresses OATP1A2, which is capable of transporting microcystins from the body to the brain (Fischer et al., 2005). Disruption of the cytoskeleton, increased ROS levels, apoptosis, and inflammation result from hyperphosphorylation, indicating similar effects as expected from other cell and tissue types (Massey et al., 2018). Microcystin-induced neurotoxicity includes neurostructural, -functional and behavioral changes. Studies in rodents showed that neurons in the hippocampus were damaged, affecting the long-term potential and thereby impairing learning and memory (Li et al., 2015; Maidana et al., 2006; Wang et al., 2013). Microcystin has also been shown to induce blood-brain-barrier dysfunction by causing astrocyte and microglial impairment and neuroinflammatory responses (Wang et al., 2019). Another *in vivo* study showed that microcystin induces tau hyperphosphorylation, resulting in impaired function in the neuronal axonal transport, synaptic dysfunction, and neurodegeneration, contributing to Alzheimer's disease (Li et al., 2012; Zhang et al., 2018). Furthermore, microcystin was shown to induce neurite degeneration via neurite shortening in a concentration- and congener-dependent manner (Feurstein et al., 2011).

1.3.3. Metabolism and Excretion

Metabolism is the process by which xenobiotics are converted to more hydrophilic metabolites that can be eliminated from the body through excretion. Metabolism involves four distinct phases:

Phase 0: Uptake

Uptake via influx transporters.

Phase I: Functionalization

Involves the introduction of a functional group into the xenobiotic, usually through oxidation, reduction, or hydrolysis.

Phase II: Conjugation

Involves the conjugation of a functional group to a substance, forming a water-soluble compound that is easily excreted by the body, usually through glucuronidation, sulfation, acetylation, or methylation.

Phase III: Elimination

Elimination via efflux transporters.

Microcystins are actively taken up via organic anion transporting polypeptides (phase 0), conjugated to glutathione (phase II), and most likely eliminated via multidrug resistance-associated protein 2 (MRP2) efflux transporter (phase III). Microcystins are not known to be involved in phase I metabolism (Clarke et al., 2019; Kaur et al., 2019; Vichi et al., 2016).

Phase 0: Uptake via Organic Anion Transporting Polypeptides

Due to their chemical structure and amino acid composition, microcystins are rather hydrophilic and spatially large molecules and require active transport to cross cell membranes. The transmembrane transport of microcystins is mainly mediated by organic anion transporting polypeptides (OATPs) in humans (Fischer et al., 2005), but also in rodents (Feurstein et al., 2009; Feurstein et al., 2010). Organic anion transporting polypeptides (human: OATPs, rodents Oatps) belong to the solute carrier organic anion (SLCO) gene family and are multi-specific transporters and mediate the sodium-independent transport of a wide range of amphipathic organic compounds, e.g., bile salts, thyroid hormones, or steroid conjugates (Hagenbuch & Meier, 2003; Hagenbuch & Meier, 2004; Stieger & Hagenbuch, 2014). Besides the characteristic 12 transmembrane domain, see **Figure 10**, all OATPs share common structural features as:

(1) Large extracellular domain between transmembrane domains 9 and 10 with many conserved cysteine residues.
(2) N-glycosylation sites in the extracellular loops 2 and 5.
(3) Consensus superfamily signature DX-RW-(I,V)-GAWW-X-G-(F,L)-L at the border between extracellular loop 3 and transmembrane domain 6 (Hagenbuch & Meier, 2004).

OATPs are clustered into families. One family involved in the microcystin-mediated transport is the OATP1 family, with its three subfamilies: OATP1A, OATP1B, and OAT1C, as summarized in **Table 2**.

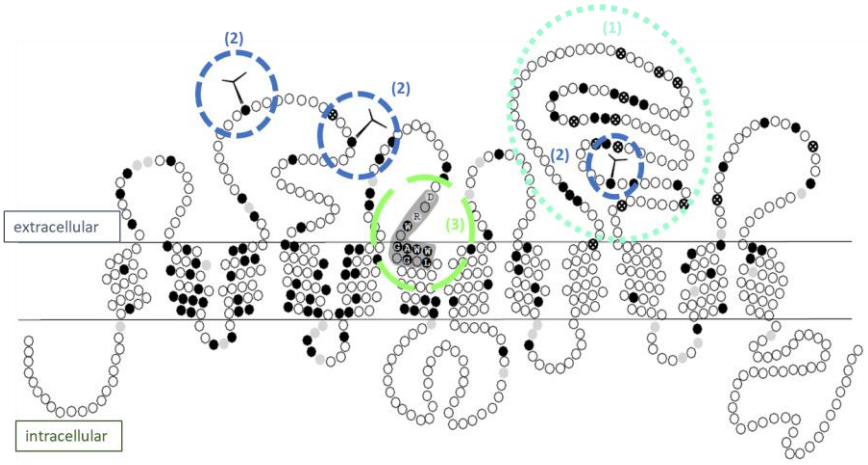

Figure 10: Schematic Structure of Organic Anion Transporting Polypeptides

Illustrated are the 12 transmembrane domains of the organic anion transporting polypeptides (OATPs). Indicated in black are the conserved amino acids, whereas the conserved and charged amino acids are tagged in grey and the conserved cysteine residues are marked with asterisks. The common structure features are indicated in turquoise (1) large extracellular transmembrane domain with many conserved cysteine residues, (2) in blue the N-glycosylation sites and (3) in green the conserved consensus sequence. Illustration was adapted and modified (Hagenbuch & Meier, 2003).

Although similar in structure, OATPs exhibit substrate specificity and distinct expression patterns in organ and tissue distribution. For instance, OATP1B1 and OATP1B3 are mainly found in the liver, whereas OATP1A2 is mainly expressed in the endothelial cells of the blood-brain-barrier (Stieger & Hagenbuch, 2014).

Table 2: OATP1 Subfamily Members

Listed are the members of the human OATP1 subfamily, including their size, tissue distribution, predominant substrates, and ability to transport microcystins. Table was compiled from various sources, including (Fischer et al., 2005; Hagenbuch & Meier, 2004).

Transporter	Size	Tissue Distribution	Substrates	Microcystin Transport
OATP1A2	670 amino acids	Brain (BBB), kidney, liver	Bile salts, organic anions, organic cations	Yes (Feurstein et al., 2009; Fischer et al., 2005)
OATP1B1	691 amino acids	Liver	Bile salts, organic anions	Yes (Fischer et al., 2010; Fischer et al., 2005)
OATP1B3	702 amino acids	Liver	Bile salts, organic anions	Yes (Fischer et al., 2010; Fischer et al., 2005)
OATP1C1	712 amino acids	Brain, Leydig cells (testis)	Thyroid hormones T4, rT3	Unknown

Using *Xenopus laevis* oocytes as an expression system, microcystin-mediated uptake was studied with different members of the OATPs/Oatps family. No microcystin transport was detected in Oatp1a1, Oatp1a4 and OATP2B1, but in OATP1B1, OATP1B3, Oatp1b2 and OATP1A2 (Fischer et al., 2005). Since OATP1B1 and OATP1B3 are highly expressed in the liver, this result contributed significantly to the understanding of the observed organ-specific toxicity of microcystins.

Phase II: Microcystin Conjugation to Glutathione

Glutathione (GSH) is one of the most important antioxidants synthesized in cells. It is a tripeptide, consisting of glutamate, cysteine, and glycine with an unusual γ-peptide bond between glutamate and cysteine that prevents it from being hydrolyzed by most peptidases (Anderson, 1998). Due to its key function in detoxification and ROS scavenger, GSH is found in high concentrations in cells, ranging from 1-2 mM in the cytosol, but can reach up to 10 mM in hepatocytes (Forman et al., 2009; Meister, 1988). GSH exists in both the thiol-reduced (GSH) and the disulfide-oxidized from (GSSG), with GSH being the predominant and active form, accounting for > 98 % of total cellular GSH. Glutathione reductase is responsible for mainlining GSH in its active thiol form. Biological activity is mediated by the reactive thiol group of the cysteinyl moiety and includes oxidation-reduction (redox) and nucleophilic addition-type reactions (Forman et al., 2009).

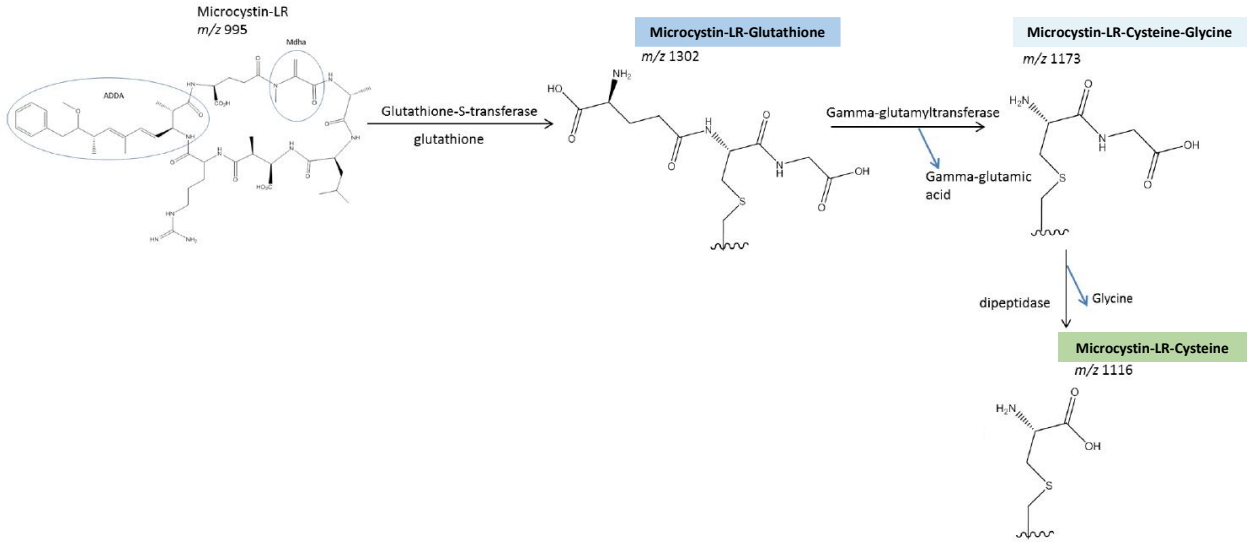

Figure 11: Glutathione Conjugation to Microcystin-LR

Glutathione is conjugated to microcystin-LR via glutathione-S-transferase (GST), resulting in microcystin-LR-glutathione (MC-LR-GSH). Cleavage of the γ-glutamic acid group catalyzed by γ-glutamyl-transferase results in microcystin-LR-cysteine-glycine intermediate. In the presence of dipeptidase, glycine is cleaved, and microcystin-LR-cysteine (MC-LR-Cys) is formed. Image was adapted and modified (Schmidt et al., 2014).

GSH conjugation to microcystins can occur either spontaneously at alkaline pH (Kondo et al., 1992) or enzymatically via the phase II enzyme glutathione-S-transferase (GST), see Figure 11. GSH conjugation was reported for several species, including humans. Recent studies have characterized GSH conjugation in human systems using recombinant GST and liver cytosol. Similar to OATPs, a congener selectivity for GST and microcystin congeners has been reported (Buratti et al., 2011; Santori et al., 2020). The conjugation reaction is a two-step process. In the first step, the thiol group of the cysteine residue (GSH) nucleophilically attacks the microcystin α,β-unsaturated carbonyl of Mdha, resulting in the first conjugation product, microcystin-GSH (MC-GSH). In a second step, glutamic acid is cleaved by γ-

glutamyltransferase to form the intermediate microcystin-cysteine-glycine (MC-Cys-Gly). The glycine residue of this intermediate is rapidly cleaved by a dipeptidase to yield second conjugate, microcystin-cysteine (MC-Cys) (Schmidt et al., 2014).

Phase III: Microcystin Elimination

Microcystins are primarily excreted as the parent compound via urine and feces, although several studies have shown that only a small percentage of the administered dose is excreted from the body. ADME studies performed on mice showed that only 24 % of the injected microcystin dose was excreted via urine (9 %) and feces (15 %). Of this, 60 % of the excreted microcystins were present as the parent compound (Robinson et al., 1991). Despite the high levels of unbound microcystins found, initial indications showed that MC-GSH was concentrated in the feces, while MC-Cys was more abundant in the kidneys, possibly indicating the excretion pathways (Schmidt et al., 2014). Since the amount of microcystin conjugates excreted is very low, the actual function of GSH conjugation to microcystins remains unclear. Moreover, the role of glutathione conjugation to microcystins as 'detoxification' is still highly controversial, as there are no valid data on MC-GSH or MC-Cys toxicities. Similarly, cellular elimination via efflux transporters is not fully understood. Recent studies have demonstrated microcystin-mediated export via multidrug resistance associated protein 2 (MRP2) transporters, albeit only for unbound microcystins and not for their conjugates (Kaur et al., 2019).

1.4. Risk Assessment

A guideline value of 1 µg/l has been published by the World Health Organization (WHO) as a safe concentration of microcystin for drinking water and recreational waters (World Health, 2020). This guideline value is thereby derived from the tolerable daily intake (TDI) value of 0.04 µg/kg body weight (Dietrich & Hoeger, 2005), which is based on the no-observed-effect-level (NOEL) determined in two animal studies, involving mice (Fawell et al., 1999) and pigs (Falconer et al., 1994).

In a first study, mice were exposed to MC-LR by intraperitoneal injection. Subsequently, biomarkers of liver damage, such as glutamyl transaminase (GGT), aspartate aminotransferase (AST) and alanine aminotransferase (ALT) were detected at an injected dose of 200 µg/kg body weight, but not at a dose of 40 µg/kg body weight (Fawell et al., 1999). In a second study, pigs were exposed to microcystins through free access to drinking water containing cyanobacterial material. The pigs ingested a total of 180 µg/kg bodyweight microcystins per day. Only one of the five pigs exhibited mild symptoms and the NOEL was therefore considered to be modestly below 180 µg/kg body weight (Falconer et al., 1994). Risk assessment based on this study is difficult since the identity of the microcystin congeners present was not clearly determined. According to the authors, at least nine different microcystin congeners were present, but not MC-LR or MC-RR. Hence, the NOEL (40 µg/kg body weight) calculated from the mice study was used to determine the TDI using the following equation: $TDI = \frac{NOEL}{UF}$, including an uncertainty factor (UF)

of 1,000, resulting in a TDI value of 0.04 µg/kg body weight (Dietrich & Hoeger, 2005). The uncertainty factor includes the extrapolation from animal to human (factor 10), population variability (factor 10), and various factors (tumor promotion, extrapolation due to chronic effects, data set inadequacies, factor 10). This TDI value was then used to calculate a guideline value (GV) for the assessment of safe microcystin concentrations in water using the following equation $GV = \frac{TDI * body\ weight * AF}{C}$, assuming an allocation factor (AF) of 0.8, a body weight of an 'international standard adult' of 70 kg and a total volume of the source (C) of 2 liters, resulting in a GV for microcystins of 0.96 µg/l (= 1 µg/l) (Dietrich & Hoeger, 2005; World Health, 2020). In the same way, a value for dietary supplements (10 µg/g MC-LR in 2 g tablets, AF 1) was calculated (Dietrich & Hoeger, 2005). Consequently, the current risk assessment is based solely on a rodent study performed in 1999 with a single microcystin congener (MC-LR) and has remained unchanged since then, even though more than 250 congeners have been described (Spoof & Catherine, 2016) and congener-specific toxicity has been demonstrated (Feurstein et al., 2011; Fischer et al., 2010). However, studies have shown that rodents vary widely in the expression of OATPs, as well in the affinity and capacity for microcystin-mediated transport, thus being poor surrogates for human microcystin toxicity testing (Fischer et al., 2010; Fischer et al., 2005). Hence, first steps towards congener-specific risk assessment, including first *in silico* toxicity prediction models, have been postulated (Altaner et al., 2020). Nevertheless, these only cover the toxicodynamic aspects of microcystin toxicity and do not include the specific toxicokinetic properties.

1.5. Aim of the Study

Although more than 250 microcystin congeners have been described so far, the toxicity of only a few is known and has been assessed only with purified PPPs, including only limited aspects of toxicity. Comparative studies including both toxicodynamic and toxicokinetic parameters are lacking. Here, time-dependent cellular uptake is defined as toxicokinetics, while binding and dynamic interactions in the cytosol, focusing on the microcystin molecule, are defined as toxicodynamic parameters, although GSH conjugation strictly speaking falls under whole organism toxicokinetics. However, the mechanism of microcystin toxicity can only be fully understood by evaluating and combining both parameters, see Figure 12. Therefore, the overall aim of this dissertation was to contribute to the understanding of each parameter, first in simplified but then in more complex but biologically more relevant cell systems. Basically, the aims of this dissertation can be roughly divided into the following parts (note: each chapter provides a detailed aim of the study focusing on specific parts of the microcystin toxicity mechanism):

- Determination of Toxicodynamic Parameters.

  Identification of microcystin features responsible for efficient PPP inhibition. Thereby the roles of covalent bond and the unique Adda side chain will be investigated using purified PPPs but also whole cell systems.

- Determination of Toxicokinetic Parameters.

  Identification of the microcystin features responsible for efficient OATP-mediated uptake. Thereby, the individual transporting properties of hepatocyte specific OATP1B1 and OATP1B3 will be determined using structurally different microcystin congeners, covering the known spectrum of hydrophobicity, molecular weights, and modifications.

- Analysis of Microcystin Toxicity Mechanism by Combining Toxicodynamic and Toxicokinetic Parameters.

  Evaluation of congener-specific toxicity and the role of cellular GSH conjugation as a potential microcystin detoxification mechanism by establishing of three independent assays that simultaneously monitor cytotoxicity, PPP activity and GSH response. First in simple HEK293 cell models, but then further in more physiologically relevant and complex hepatocytes cell systems.

- Preliminary Experiments for Chronic Microcystin Toxicity Studies.

  Prior to simulating chronic exposure, which reflects most reported human intoxications, the protein stabilities and half-lives of the PPPs will be determined to appropriately contextualize turnover rates with subsequent protein degradation. Moreover, a suitable human and non-carcinogenic hepatocyte cell line is required. Therefore, the not widely known immortalized human hepatocyte (IHH) cell line will be characterized and evaluated as a suitable and reliable hepatocyte cell line. Consequently, the basis for the following chronic exposure studies should be manifested. In addition, since the risk assessment is based solely on mouse studies, human hepatocytes should be compared with mouse hepatocytes, to challenge and evaluate the current risk assessment.

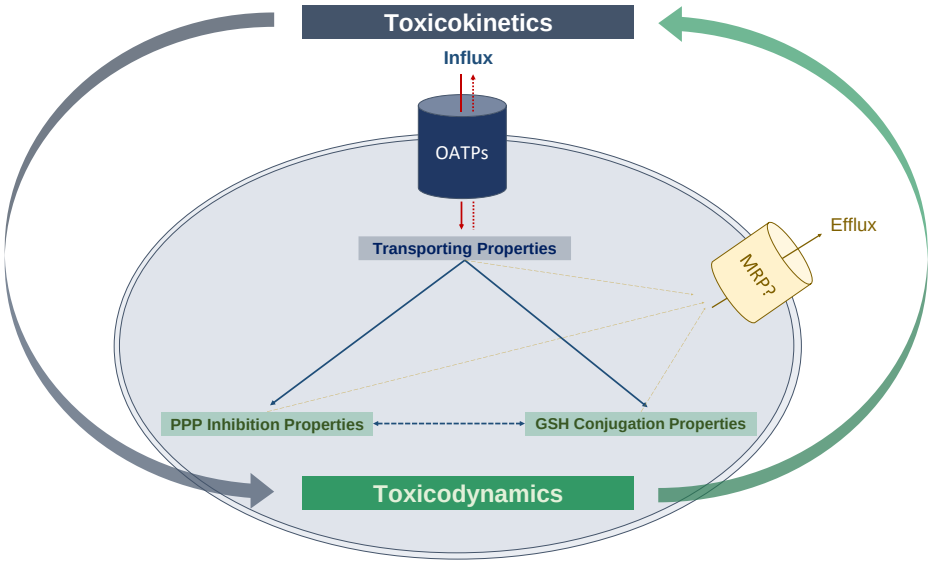

Figure 12: Graphical Abstract of the Dissertation

Microcystin toxicity is reflected by toxicokinetic (blue) and toxicokinetic (green) parameters. Cellular uptake is mediated by organic anion transporting polypeptides (OATPs). Once inside the cell, microcystins bind to serine/threonine phosphatases (PPPs), leading to severe cellular damage, e.g., induction of cell death via apoptosis. The cellular detoxification system, including glutathione, is involved in the microcystin conjugation pathway with unknown effects. The mechanism of microcystin toxicity can only be elucidated when all components are understood individually and in combination. It is noteworthy that the efflux of microcystin, possibly through MRP2, was not included in this study and is therefore shown in yellow.

2. Chapter I

2.1. Hydrophobic Adda Determines Toxicity

2.1.1. Introduction

Microcystins are complex cyclic peptides composed of seven amino acids, including D-alanine at position (1), two variable L-amino acids at positions (2) and (4), ß-D-methylaspartate at position (3), D-glutamine at position (6), D-methyldehydroalanine (Mdha) at position (7), and a unique hydrophobic amino acid Adda (3-amino-9-methoxy-10-phenyl-2,6,8-trimethyl-deca-4(E),6(E)-dienoic acid) at position (5), which is characteristic of microcystins and nodularins. While positions (1), (5), and (6) are quite conserved, positions (2) and (4) are hypervariable positions, and specify the nomenclature of microcystins (Malik et al., 2020). Microcystins are classified as hepatotoxins and are highly potent serine/threonine phosphoprotein phosphatases (PPPs) inhibitors (MacKintosh et al., 1990; MacKintosh et al., 1995). Protein (de)phosphorylation is a highly dynamic and essential process, regulating enzyme (de)activation, cellular protein homeostasis, and various signaling pathways. Inhibition of PPPs leads to hyperphosphorylation and deregulation of fundamental cellular processes and may consequently lead to cell death (Brautigan, 2013; Shi, 2009). Members of the PPP family share a highly conserved catalytic subunit and based on their sequence, PPPs have been further classified into seven subtypes: PPP1, PPP2A, PPP2B (Calcineurin), PPP4, PPP5, PPP6 and PPP7. Among all known phosphatases, PPP1 and PPP2A are the most crucial ones, accounting for more than 90 % of protein dephosphorylation in eukaryotic cells (Bollen et al., 2010), as evidenced by their key function in the cell cycle, DNA regulation, and glycogen metabolism (Shi, 2009). In contrast to other members of the PPP family, PPP5 is unique since no regulatory or scaffolding domain is required for its enzymatic activation. PPP5 is regulated by an autoregulatory tetratricopeptide repeat (TPR) domain located on the same peptide as the catalytic subunit (Shi, 2009).

Interaction of Microcystins with the Catalytic Subunit of PPPs

Direct interaction sites between microcystins and PPPs have been studied by co-crystallization of the catalytic subunits of PPP1 and PPP2A complex with MC-LR (Goldberg et al., 1995; Xing et al., 2006). Besides the finding that the cyclic structures are not planar, but rather flexible and twisted, it was also observed that microcystins bind directly to the catalytic center, completely blocking access to the active site for other substrates (Fontanillo & Köhn, 2018; Pereira et al., 2013). Several interaction sites have been identified that are theorized to contribute significantly to the inhibitory properties of microcystins, see Figure 13. Hydrogen bonds were formed at position (7) and especially at position (3) of the carboxylic acid group of ß-D-methylaspartate with Arg96 and Tyr134 in PPP1 and Arg89 and Tyr127 in PPP2A. The hydrophobic Adda side chain, located at position (5), was found to interact with the hydrophobic groove formed by Cys127, Ile130, Ile133, Tyr134 and Trp206 in PPP1 and by Gln122, Ille123, His191 and Trp200 in PPP2A. The carboxylic acid group of D-glutamine at position (6) was found to bind to the metal binding

sites of PPP1 via two water molecules, stabilizing Adda hydrophobic interactions. Mdha at position (7) was found to bind covalently to Cys273 in PPP1 and Cys269 in PPP2A via a Michael-type addition reaction (Fontanillo & Köhn, 2018; Pereira et al., 2013).

A

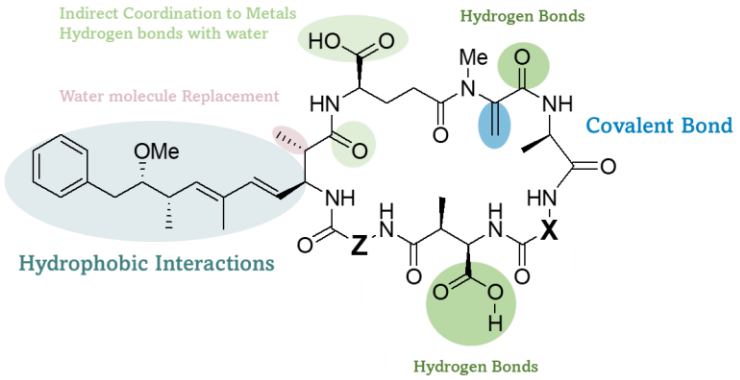

B

												ß12/ß13 loop residues			
PPP1cα	**R96**	C127	S129	**I130**	**Y134**	**V195**	D197	**W206**	**R221**	V250	**Y272**	**C273**	E275	F276
PPP2Acα	**R89**	**S120**	**Q122**	**I123**	**Y127**	**V189**	**H191**	**W200**	**R214**	**L243**	**Y265**	**C266**	**R268**	**C269**
PPP2Bcα	**R122**	C153	H155	L156	F160	P221	A223	**W232**	**R254**	A283	**Y311**	L312	V314	Y315
PPP4c	**R86**	**S117**	**Q119**	**I120**	**Y124**	**V186**	**H188**	**W197**	**R211**	**L240**	**Y262**	**C263**	**R265**	**C266**
PPP5c	**R275**	T306	N308	M306	**Y313**	P375	D377	**W386**	**R400**	V429	**Y451**	**C452**	Q454	M455
PPP6c	**R85**	**S116**	**Q118**	**I119**	**Y123**	I185	**H187**	**W196**	**R210**	**L239**	**Y261**	**C262**	**R264**	**C265**
PPP7cα	**R205**	D236	M238	M239	**Y243**	E350	E352	**W361**	**R376**	C405	**Y427**	Y428	E430	G431

H-bond forming residues | Hydrophobic groove residues | Covalent bond forming residues

Figure 13: Interaction Sites of Microcystins and Catalytic Subunit of PPPs

Representation of **(A)** the general microcystin structure including all interaction sites and **(B)** partial sequence alignment of the PPP catalytic subunits with corresponding microcystin interaction sites. Figures were modified from (Fontanillo & Köhn, 2018; Pereira et al., 2013).

Inhibition Mechanism

Based on these findings, including both experimental and *in silico* studies, microcystin-induced PPP inhibition was theorized to be facilitated by mainly two key processes:

(1) **Non-covalent** binding of the hydrophobic Adda side chain to the hydrophobic groove of the PPP active site.

(2) **Covalent bond** formation between the α,β-unsaturated terminal carbonyl group of Mdha and a cysteine moiety of the PPP active site.

Initial studies showed that the non-covalent interaction of Adda led to inhibitory effects in PPP1 and PPP2A already within minutes (Craig et al., 1996), while *in silico* studies analyzed that the formation of the covalent bond between the cysteine and the Mdha methylene group was shown to take approximately 2 hours (Pereira et al., 2013) and did not seem to be essential for inhibition (Craig et al., 1996; Pereira et al., 2013). The formation of the covalent bond is hypothesized not to contribute to the PPPs inhibition ability, but rather to enhance the inhibition by inducing irreversibility. Thus, covalent binding may play an important part in the biological role of microcystins (Fontanillo & Köhn, 2018; Pereira et al., 2013). Interestingly, all PPPs known to be inhibited by microcystins, indicate at least one cysteine residue in the ß12/13 loop of

the catalytic subunit to form a covalent bond with the Mdha methylene group, whereas PPPs known to be less sensitive to microcystins (PPP2B and PPP7) don't (Pereira et al., 2013), contributing to the question of the actual role of the covalent bond formation.

Aim of the Study

To date, more than 250 microcystin variants, so called congeners, have been described. However, the high number of congeners is mainly due to the hypervariable positions (2) and (4) and to minor alterations (i.e., (de)methylation), which allowed mainly the study of the influence of L-amino acids in the inhibition mechanism. The establishment of the total synthesis of microcystins in the laboratory allowed the incorporation of specific modifications, providing access to the missing diversity of variants and thus allowing the study of different binding sites (Fontanillo et al., 2016; Zemskov et al., 2017). These synthetically induced variations derived from a parental microcystin molecule are called derivates.

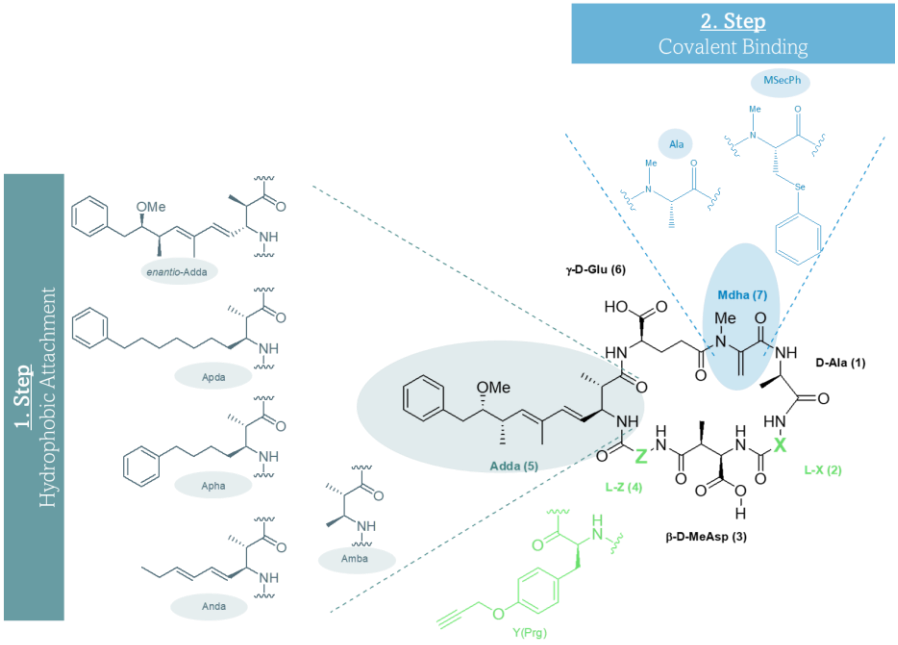

Figure 14: Graphical Abstract of Chapter I

Summarized are the structural changes within the synthetic microcystin derivates, including five Adda derivates and two Mdha derivates. Anda = (2S,3S,4E,6E)-3-amino-2-methylnona-4,6-dienoic acid, Amba = (2S,3S)-3-amino-2-methylbutanoic acid, Apda = (2S,3S)-3-amino-2-methyl-10-phenyldecanoic acid, Apha = (2S,3S)-3-amino-2-methyl-7-phenylheptanoic acid, MSecPh = N-methyl-Se-phenyl-L-seleno-cysteine, Prg = propargyl.

To study the impact of (i) the hydrophobic and non-covalent binding site and (ii) the covalent binding, various microcystin derivates were synthesized. Five Adda derivates were used that differed in the length of the Adda backbone or in the presence and orientation of residues, as summarized in **Figure 14**. Additionally, two different microcystin derivates, both lacking the Mdha methylene group, were analyzed. The aim of this study was to elucidate the mechanism of microcystin-induced PPP inhibition both *in vitro* in purified but active PPPs and in whole biological cellular systems. Thereby, the role of Adda components, as well as the role of reversible and irreversible PPP inhibition abilities, were studied in detail.

2.1.2. Results

Microcystin-induced PPP inhibition is theorized to be facilitated by mainly two key processes: the non-covalent binding of the hydrophobic Adda side chain at position (5) to the hydrophobic groove of the PPPs, followed by the formation of a covalent bond between the α,β-unsaturated carbonyl group of the Mdha at position (7) and the cysteine moiety of the PPPs. To understand the mechanism of microcystin-induced PPP inhibition, the study of both processes is critical. Therefore, purified but enzymatically active rPPP1 and hPPP5 were exposed to various microcystin derivates with specific modifications at position (5) or (7). Since microcystin toxicity comprises both toxicodynamic (i.e., PPP inhibition) and toxicokinetic (i.e., active uptake via organic anion transporting polypeptides, OATPs) aspects, the OATP-mediated uptake and subsequent induced cytotoxicity in stably transfected HEK293 cell lines were analyzed to assess the overall microcystin toxicity.

Role of Covalent Binding, Induced Irreversibility and Enhanced Microcystin Toxicity

Initial studies indicated that the formation of the covalent bond does not appear to be critical for microcystin-induced PPP inhibition. Rather than initiating PPP inhibition, it is thought to enhance microcystin toxicity. To test whether the covalent bond is (i) necessary or (ii) enhances PPP inhibition by accompanying irreversibility, two *de novo* synthesized microcystin derivates lacking the α,β-unsaturated carbon atom (methylene group) in the Mdha residue at position (7) were used, resulting in no covalent bond formation. While in [Ala^{7}]MC-L(DAz)-Y(Prg) the unsaturated carbon atom was replaced by a saturated one, simply by changing the incorporated amino acid from dehydroalanine to alanine, in [MSecPh^{7}]MC-LY(Prg) the Mdha binding site was blocked by the incorporation of the amino acid phenyl-selenocysteine, an analogue of cysteine with selenium in place of sulfur. This additional residue should not only prevent the formation of a covalent bond, but also contribute to steric effects by disrupting the interaction sites between the PPP and position (7). Both derivates indicate a propargyloxy residue (Prg) at position (4) since MC-LY(Prg) was used as parental molecule. Therefore, for both derivates MC-LY(Prg) was used as reference molecule. All derivates were kindly provided by Prof. Dr. Valentin Wittmann (Bioorganic Chemistry Department, University of Konstanz), synthesized by Ivan Zemskov ([MSecPh^{7}]MC-LY(Prg), MC-LY(Prg) and Marius Wrona ([Ala^{7}]MC-L(DAz)-Y(Prg)).

Using *in vitro* phosphatase inhibition assays with catalytically active rPPP1 (rabbit skeletal muscle) and hPPP5 (human), both Mdha derivates were shown to induce PPP inhibition in a concentration-dependent manner, as demonstrated in **Figure 15**. To analyze microcystin-induced PPP inhibition, the half-maximal inhibitory concentrations (IC_{50}) were calculated and compared to the IC_{50} of the parental microcystin MC-LY(Prg), see **Table 3**. Interestingly, solely [Ala^{7}]MC-L(DAz)-Y(Prg) was significantly less toxic in rPPP1 compared to MC-LY(Prg), as indicated by a 6-fold higher IC_{50} (10.85 nM and 1.692 nM, respectively), see **Figure 15 A-B**. Moreover, hPPP5 exposed to neither [Ala^{7}]MC-L(DAz)-Y(Prg) nor [MSecPh^{7}]MC-LY(Prg) showed significant differences compared to MC-LY(Prg) (0.935 nM, 6.825 nM, and

1.717 nM, respectively), as demonstrated in **Figure 15 C-D**. Comparing both PPPs, significant differences were found for both derivates, but not for the parental microcystin, see **Supplementary Figure 1**. While hPPP5 was significantly more sensitive to [Ala^7]MC-L(DAz)-L(Prg) than rPPP1, contrary effect was observed for [MSecPh^7]MC-LY(Prg).

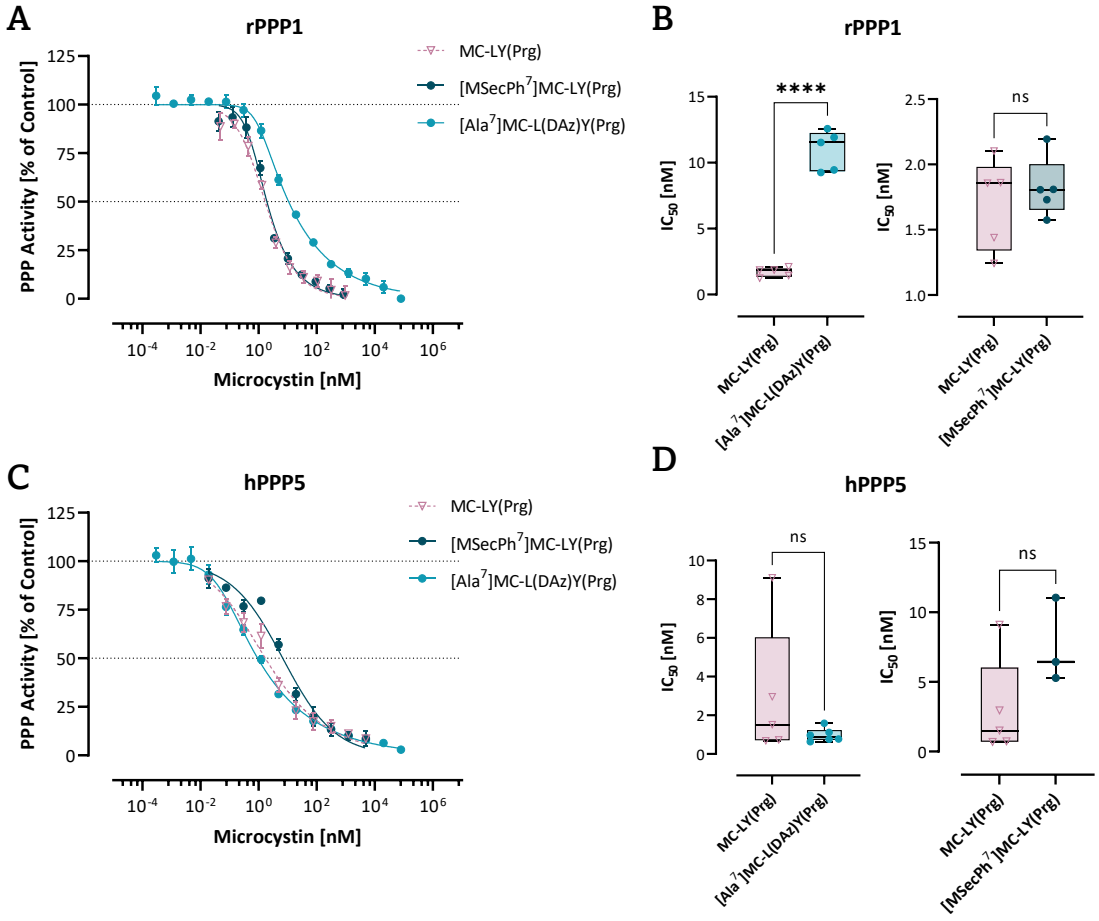

Figure 15: Phosphatase Inhibition Properties of Mdha Derivates

Graphed are PPP activities measured in **(A-B)** rPPP1 and **(C-D)** hPPP5 exposed to Mdha derivates and compared to MC-LY(Prg) for analyses. Inhibition curves: each point represents the mean of 3-6 independent biological replicates, pipetted in triplicates ± SEM (n=3-6). IC_{50} values were calculated using asymmetric nonlinear regression. Statistical analyses were performed using two-tailed unpaired t-test with p-values summarized in **Table 3**.

To test the biological activities of the Mdha derivates, toxin exposure assays were performed on stably transfected HEK293-OATP1B1, -OATP1B3 and control (CV) cells. Cells were exposed to microcystin derivates for 48 hours and subsequently cell viability was measured. Analogous to the PPP dataset, Mdha derivates induced a concentration-dependent decrease in cell viability in OATP1B1- and OATP1B3-expressing HEK293 cells. No decrease in cell viability was measured in HEK293-CV cells, indicating active OATP-mediated microcystin uptake across the cell membrane, see **Figure 16**. For cytotoxicity analysis, the half-maximal effective concentrations (EC_{50}) were calculated and compared to the EC_{50} of the parental microcystin MC-LY(Prg), as summarized in **Table 4**.

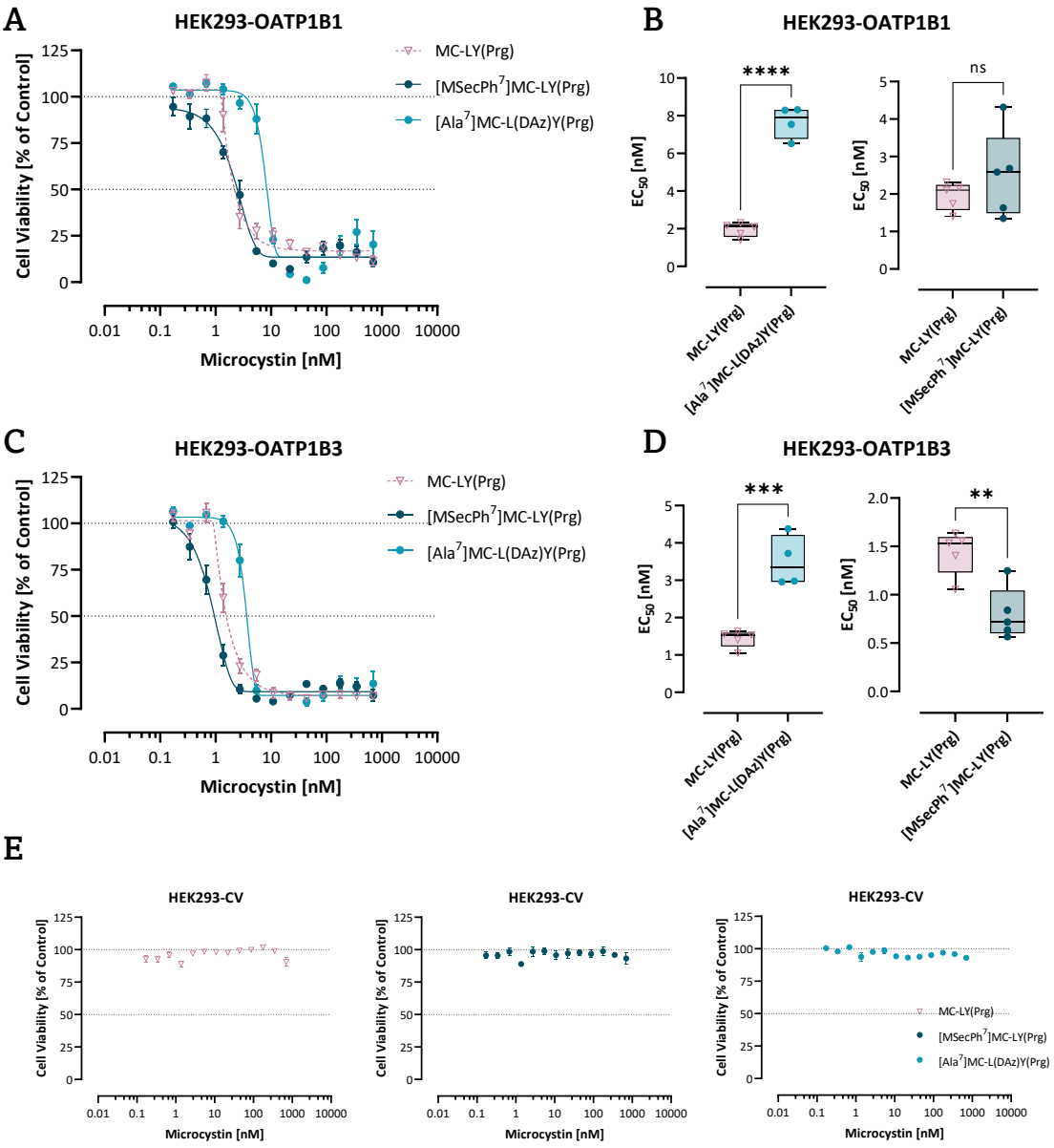

Figure 16: OATP-mediated Uptake of Mdha Derivates

Cell viabilities measured in **(A-B)** HEK293-OATP1B1, **(C-D)** HEK293-OATP1B3 and **(E)** HEK293-CV cells exposed to Mdha derivates and compared to MC-LY(Prg) are illustrated. Inhibition curves: each point represents the mean of 4-5 independent biological replicates, pipetted in triplicates ± SEM (n=4-5). EC_{50} were calculated using asymmetric nonlinear regression. Statistical analyses were performed using two-tailed unpaired t-test with p-values summarized in **Table 4**.

Consistent with previous results, [Ala^7]MC-L(DAz)Y(Prg) showed the highest significant difference between the parental microcystin and the derivate. In HEK293-OATP1B1 cells, the measured EC_{50} for [Ala^7]MC-L(DAz)Y(Prg) was 4-fold higher than the EC_{50} of MC-LY(Prg) (7.981 nM and 1.857 nM, respectively), see **Figure 16 A-B**. A similar effect was observed in OATP1B3-expressing cells, where the EC_{50} value was 3-fold higher (3.495 nM) compared to the parental microcystin (1.467 nM), see **Figure 16 C-D**. [MSecPh^7]MC-LY(Prg) showed only slightly increased toxicity in HEK293-OATP1B3 (0.849 nM), but not in HEK293-OATP1B1 (2.251 nM). Noteworthy, cellular systems include various factors that influence the cellular outcome. The introduction of an additional phenylselenenyl residue increased

hydrophobicity and thus the OATP-mediated transport. This factor was not included in this study, therefore the differences between OATP1B1 and OATP1B3 were not analyzed further. This aspect of microcystin induced toxicity will be further discussed and analyzed in Chapter II.

Hydrophobic Adda Side Chain Determines Microcystin Toxicity

Since the formation of the covalent bond neither seemed to be critical for microcystin-induced PPP inhibition, nor clearly enhanced PPP inhibition *in vitro*, further studies were focused on the hydrophobic Adda side chain. To test whether the hydrophobic Adda side chain is (i) essential and facilitates PPP inhibition, (ii) the presence and orientation of Adda residues are crucial, and if (iii) the Adda backbone length is critical, five different *de novo* synthesized Adda derivates were used:

(1) **[Apda^5]MC-LF:** Adda backbone without residues but terminal phenyl group, includes only saturated bonds.

(2) **[Anda^5]MC-LY(Prg):** Adda backbone without any residues (6 C atoms), includes unsaturated bonds.

(3) **[Apha^5]MC-LF:** Shorter Adda backbone (only 4 C atoms long instead of 7), no residues but terminal phenyl group, includes only saturated bonds.

(4) **[Amba^5]MC-LY(Prg):** Methyl group instead of Adda side chain.

(5) **[enantio-Adda^5]MC-LF:** Complete Adda chain but with residues facing opposite orientation.

All derivates were kindly provided by Prof. Dr. Valentin Wittmann, synthesized by Ivan Zemskov ([Anda^5]MC-LY(Prg), [Amba^5]MC-LY(Prg) and (enantio-Adda^5]MC-LF)) and Marius Wrona ([Apda^5]MC-LF, [Apha^5]MC-LF)).

Compared to the reference microcystins, all tested Adda derivates showed a significant decrease in PPP inhibition ability. Here, two reference microcystins were used since either MC-LF or MC-LY(Prg) was used as parental microcystin. Interestingly, except for [enantio-Adda^5]MC-LF, all Adda derivates induced concentration dependent inhibition in rPPP1 and hPPP5, albeit with highly different toxicities, as shown in **Figure 17**. All IC_{50} values and corresponding statistical analyses were summarized in **Table 3** and **Supplementary Figure 2**.

First, the PPP inhibition ability of [Apda5]MC-LF was evaluated in rPPP1 and hPPP5. The removal of all residues except the terminal phenyl group increased the IC_{50} from 0.3622 nM to 1,459 nM (4,000-fold increase) for rPPP1 and from 2.014 nM to 1,189 nM (600-fold increase) for hPPP5, see **Figure 17 A.** [Anda^5]MC-LY(Prg), which differs from [Apda5]MC-LF mainly by the absence of the terminal phenyl group and the presence of unsaturated bonds, showed comparable high IC_{50} values for rPPP1 (1,727 nM) and hPPP5 (2,421 nM), see **Figure 17 C**. Reducing the length of the Adda backbone, [Apha^5]MC-LF, resulted in a dramatic 150,000-fold increase in IC_{50} for rPPP1 (57,317 nM) and a 9,000-fold increase for hPPP5 (19,614nM), see **Figure 17 B**. This was exceeded only by [Amba^5]MC-LY(Prg), which lacks the entire Adda side chain, as demonstrated in **Figure 17 D**.

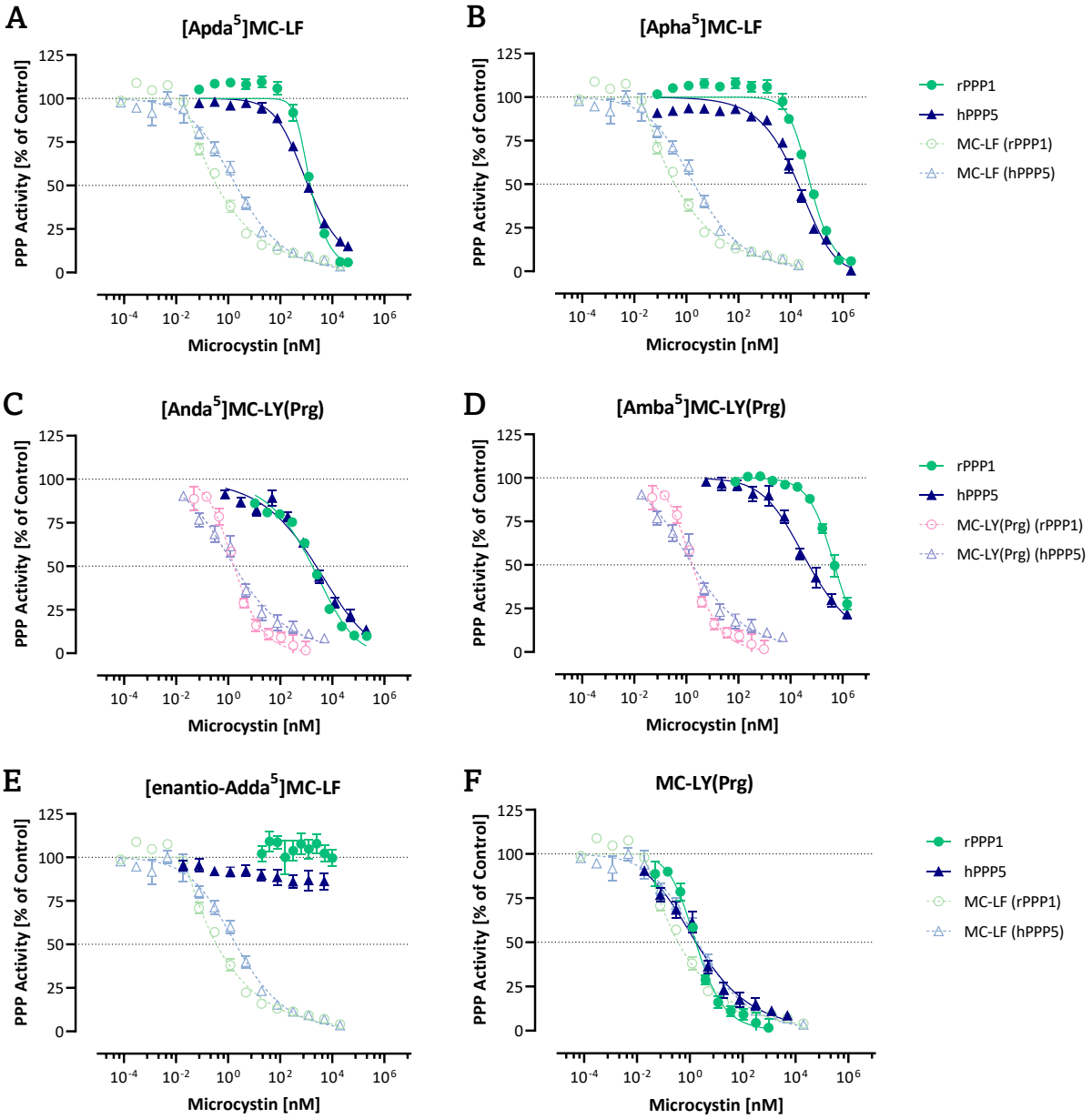

Figure 17: Phosphatase Inhibition Properties of Adda Derivates

Graphed are PPP activities of rPPP1 (green) and hPPP5 (blue) exposed to the five Adda derivates. For reference, the parental microcystins either MC-LF **(A-B** and **E-F)** or MC-LY(Prg) **(C-D)** were shown in lighter color. Each point represents the mean of 3-6 independent biological replicates, pipetted in triplicates ± SEM (n=3-6). IC_{50} were calculated using asymmetric nonlinear regression.

In rPPP1, 486,891 nM and in hPPP5 51,056 nM were required to reduce the PPP activity by 50 %, which corresponds to a 290,000- and 30,000-fold reduction in toxicity, respectively. The ability to inhibit PPPs was completely abolished in the enantiomeric Adda derivate, which failed to reduce PPP activity in rPPP1 and hPPP5, at least in the concentration range used, see **Figure 17 E**. Among all tested derivates, both reference molecules MC-LF and MC-LY(Prg) showed the highest PPP inhibition capacity (here referred to as toxicity) with comparable toxicity, as indicated by the lowest IC_{50}, see **Figure 17 F**.

Table 3: Summary of the IC_{50} Values and Statistical Analyses

IC_{50} values were calculated using asymmetric nonlinear regression. For reference, the derivates were compared to their parent microcystin and statistical analyses were performed using two-tailed unpaired t-test. Since [enantio-Adda[5]]MC-LF did not inhibit either rPPP1 or hPPP5, no IC_{50} values were calculated. n.d. = not determined, ns = not significant.

Microcystin	rPPP1					hPPP5				
	IC_{50} [nM]	CI_{95} [nM]	R^2	Statistics MC-LF	P-Value	IC_{50} [nM]	CI_{95} [nM]	R^2	Statistics MC-LF	P-Value
[Apda[5]]MC-LF	1,459	1,105-1,891	0.9725	****	<0.0001	1,187	1,014-1391	0.9927	****	<0.0001
[Apha[5]]MC-LF	57,317	48,352-67,713	0.9783	****	<0.0001	19,614	15,429-n.d.	0.9724	***	0.0009
[enantio-Adda[5]]MC-LF	n.d.	n.d.	n.d.	n.d.	n.d.	n.d.	n.d.	n.d.	n.d.	n.d.
MC-LY(Prg)	1.692	1.291-2.217	0.9335	***	0.0001	1.717	1.118-2.606	0.9212	ns	-
MC-LF	0.3622	0.3007-0.4371	0.9804	-	-	2.014	1.525-2.648	0.9783	-	-
	IC_{50} [nM]	CI_{95} [nM]	R^2	Statistics MC-LY(Prg)	P-Value	IC_{50} [nM]	CI_{95} [nM]	R^2	Statistics MC-LY(Prg)	P-Value
[Anda[5]]MC-LY(Prg)	1,727	1,435-n.d.	0.9671	****	<0.0001	2,421	1,675-n.d.	0.9387	**	0.0048
[Amba[5]]MC-LY(Prg)	486,891	404,437-586,013	0.9524	****	<0.0001	51,056	34,053-77,659	0.9182	*	0.0419
[MSecPh[7]]MC-LY(Prg)	1.943	1.568-2.419	0.9548	ns	-	6.825	n.d.-10.09	0.9568	ns	-
[Ala[7]]MC-L(DAz)-Y(Prg)	10.85	8.756-13.60	0.9833	****	<0.0001	0.935	0.7862-1.109	0.9856	ns	-

Table 4: Summary of the EC_{50} Values and Statistical Analyses

EC_{50} values were calculated using asymmetric nonlinear regression. For reference, the derivates were compared to their parent microcystin and statistical analyses were performed using two-tailed unpaired t-test. ns = not significant.

Microcystin	HEK293-OATP1B1				HEK293-OATP1B3			
	EC_{50} [nM]	R^2	Statistics MC-LF	P-Value	EC_{50} [nM]	R^2	Statistics MC-LF	P-Value
[Apda[5]]MC-LF	0.951	0.9877	ns	-	0.295	0.9728	*	0.0169
[Apha[5]]MC-LF	47.94	0.9834	****	<0.0001	17.67	0.9827	****	<0.0001
[enantio-Adda[5]]MC-LF	156.7	0.9750	****	<0.0001	95.98	0.9806	****	<0.0001
MC-LY(Prg)	1.857	0.9494	ns	-	1.467	0.9650	ns	-
MC-LF	1.281	0.9219	-	-	0.921	0.9377	-	-
	EC_{50} [nM]	R^2	Statistics MC-LY(Prg)	P-Value	EC_{50} [nM]	R^2	Statistics MC-LY(Prg)	P-Value
[Anda[5]]MC-LY(Prg)	34.44	0.9685	****	<0.0001	14.90	0.9581	****	<0.0001
[Amba[5]]MC-LY(Prg)	2629	0,8948	****	<0.0001	94.66	0.9493	***	0.0007
[MSecPh[7]]MC-LY(Prg)	2.251	0.9323	ns	-	0.849	0.9400	**	0.0038
[Ala[7]]MC-L(DAz)-Y(Prg)	7.981	0.9493	****	<0.0001	3.495	0.9684	***	0.0003

Interestingly, all Adda derivates, including [enantio-Adda[5]]MC-LF, showed OATP-mediated transport, as demonstrated in **Figure 18**. No reduction in cell viability was measured in HEK293-CV cells, indicating for active microcystin transport into the cells, see **Supplementary Figure 3**. However, the measured toxicity of all Adda derivates differed from the parental microcystin toxicity, although not as clearly as in the *in vitro* PPP experimental setup. All EC_{50} values and corresponding statistical analyses were summarized in **Table 4** and **Supplementary Figure 4**.

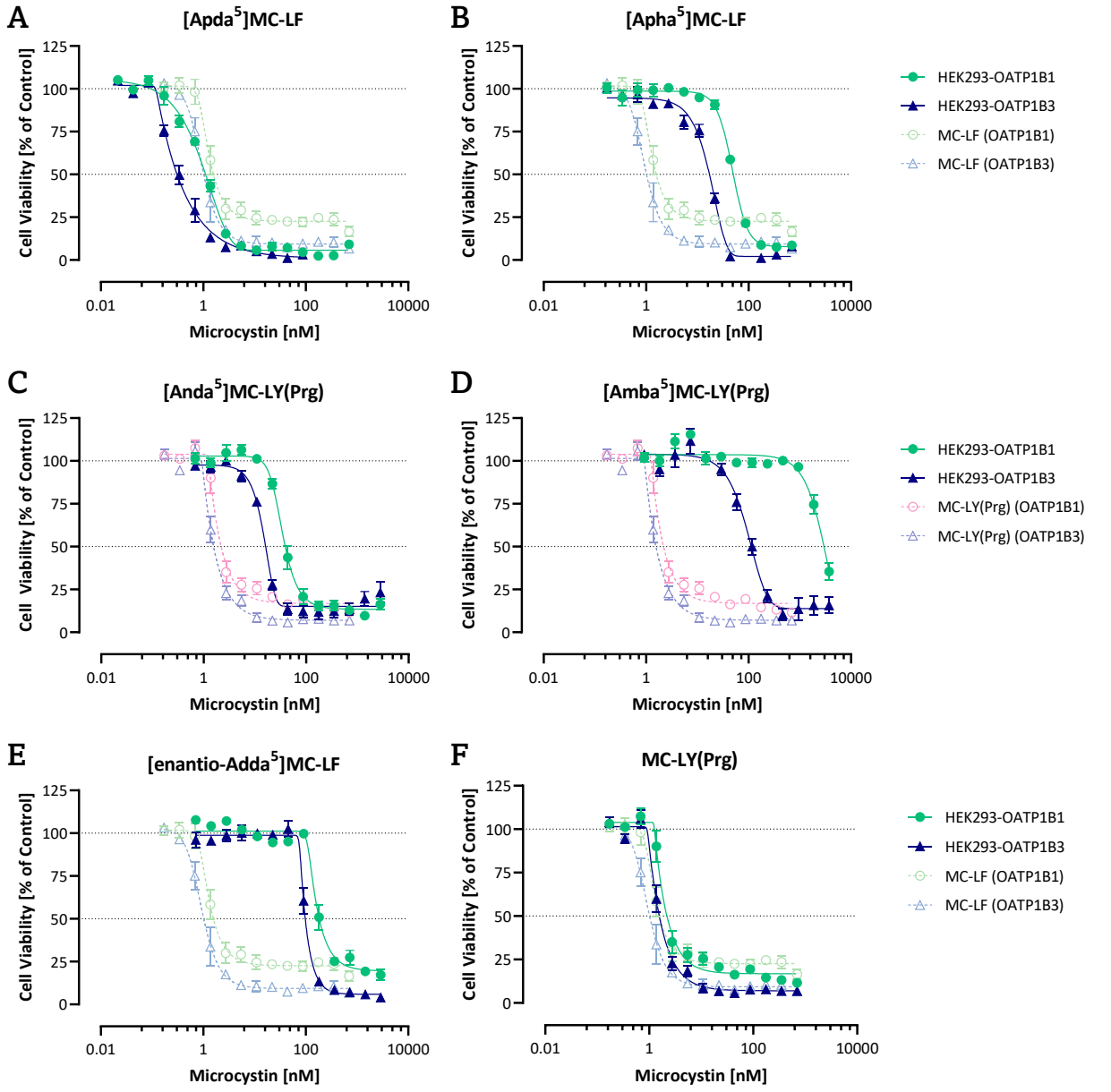

Figure 18: OATP-mediated Uptake of Adda Derivates

Cell viabilities measured in HEK293-OATP1B1 (green) and HEK293-OATP1B3 (blue) after 48 h exposure to the five Adda derivates are graphed. For reference, the parental microcystins either MC-LF **(A-B** and **E-F)** or MC-LY(Prg) **(C-D)** were shown in lighter color. Each point represents the mean of 3-5 independent biological replicates, pipetted in triplicates ± SEM (n=3-5). EC_{50} were calculated using asymmetric nonlinear regression.

Compared to the other Adda derivates, [Apda^5]MC-LF showed only slight differences in HEK293-OATP1B1 (0.951 nM) and HEK293-OATP1B3 (0.295 nM) in reference to the parental MC-LF (1.281 nM and 0.921 nM, respectively), **Figure 18 A**. In contrast, [Apha^5]MC-LF showed significantly lower cytotoxicity and increased EC_{50} values in HEK293-OATP1B1 (47.94 nM) and HEK293-OATP1B3 (17.67 nM), see **Figure 18 B**, comparable to the EC_{50} values measured for [Anda^5]MC-LY(Prg) (34.44 nM and 14.90 nM, respectively), see **Figure 18 C**. No Adda side chain resulted in a substantial 1,400-fold increase in EC_{50} in OATP1B1-expressing cells (2629 nM), but only in a moderate 60-fold increase in OATP1B3-expressing cells (94.66 nM), see **Figure 18 D**. Although [enantio-Adda^5]MC-LF failed to inhibit

rPPP1 and hPPP5 *in vitro*, a sigmoidal concentration-dependent decrease in cell viability was measured in both cell lines, see **Figure 18 E**. Again, the highest toxicity was induced by MC-LF and MC-LY(Prg). Both reference microcystins showed comparable toxicities, see **Figure 18 F**.

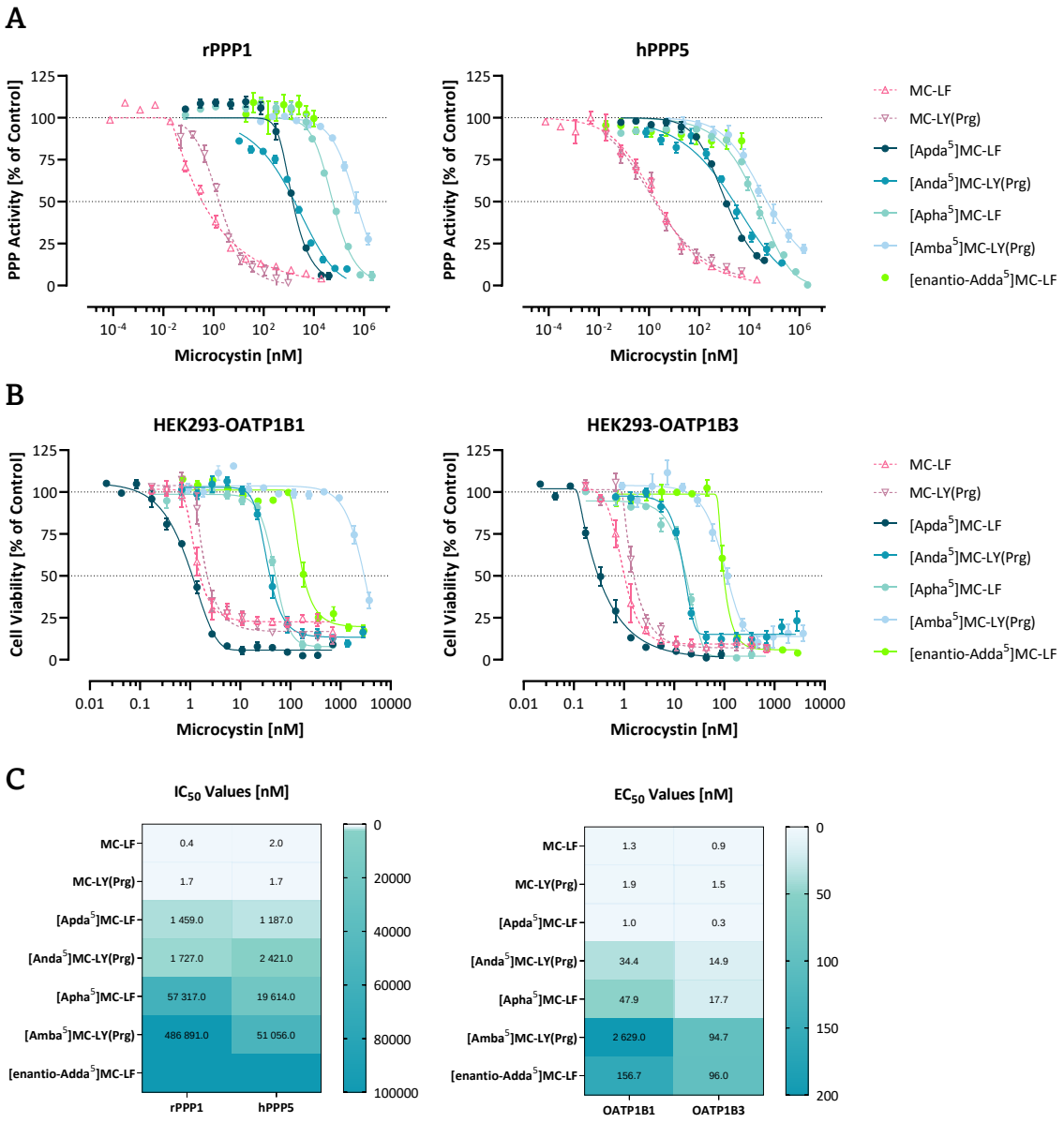

Figure 19: Comparison of Adda Derivates

Adda derivates were compared in **(A)** rPPP1, hPPP5, and **(B)** OATP1B1- and OATP1B3-expressing cell lines, with the corresponding **(C)** IC_{50} and EC_{50} values visualized as heatmaps.

By combining all Adda derivates into one graph for either rPPP1 or hPPP5, the contribution of Adda in the microcystin-induced PPP inhibition mechanism can be clearly determined, as demonstrated in **Figure 19 A**. Starting with smaller alterations in [Adpa[5]]MC-LF, followed by [Anda[5]]MC-LY(Prg) over the incorporation of greater alterations in [Apha[5]]MC-LF, [Amba[5]]MC-LY(Prg) and finally [enantio-Adda[5]]MC-LF, a distinct pattern in the gradual increase of IC_{50} values can be observed, as visualized in **Figure 19 C**. A similar pattern, although not as clear as in the PPP *in vitro* dataset, can be seen in the OATP-expressing cells, see **Figure 19 B-C**.

2.1.3. Discussion

The highly dynamic process of protein phosphorylation is an essential post-translational modification in eukaryotic cells that regulates enzyme (de)activation, protein homeostasis, and various signaling pathways, and contributes significantly to cell survival (Brautigan, 2013; Shi, 2009). Owing to the predominance of serine and threonine phosphorylation sites (86.4 % and 11.8 %, respectively), serine/threonine phosphatases represent the largest class of phosphatases (Shi, 2009). Based on their catalytic subunit sequence, this large class of phosphatases can be subdivided into several families, including the most prominent family of phosphoprotein phosphatases (PPPs). Members of the PPPs family share a highly conserved catalytic subunit and represent one of the oldest families of enzymes (Cohen, 2004). The most abundant PPPs include PPP1 and PPP2A, which account for more than 90 % of the total protein dephosphorylation in eukaryotic cells (Bollen et al., 2010). Besides the catalytic subunit, PPP1 requires a regulatory subunit to fully activate its enzymatic function. Among all PPPs, PPP5 is unique since no regulatory or scaffolding subunit is needed for its enzymatic activation. PPP5 is expressed as a single peptide with a TPR domain acting as an autoinhibitory domain (Yang et al., 2005). Therefore, PPP1 as one of the most essential eukaryotic PPPs, and PPP5 as one of the most unique PPPs, were used in this study. Since enzymatically active human PPP1 was not available, PPP1 isolated from rabbit skeletal muscle (rPPP1) was used, due to its 100 % protein sequence identity with hPPP5. Whereas hPPP1 and hPPP5 share 37 % sequence homology (Altaner et al., 2020).

Considering their essential role in cell maintenance, it is not surprising that PPPs are targets of several potent toxins such as okadaic acid, cantharidin, nodularin or microcystins. Microcystins inhibit PPPs by binding directly to the catalytic center, thereby blocking substrate access to the active site (MacKintosh et al., 1990; MacKintosh et al., 1995). Consequently, dephosphorylation is no longer catalyzed, leading to a hyperphosphorylated state of cellular proteins, and among various cellular events, the induction of cell death (McLellan & Manderville, 2017). The inhibition mechanism is theorized to be facilitated by mainly two key processes. First, the non-covalent binding of the hydrophobic Adda side chain to the hydrophobic groove of the PPP active site. Second, the formation of a covalent bond between the α,β-unsaturated terminal carbonyl group of Mdha and the cysteine moiety of the PPP active site (Fontanillo & Köhn, 2018). Although the binding chemistry has been reported using crystal structures complexed with MC-LR (Goldberg et al., 1995; Xing et al., 2006) or computational studies (Jaeger-Honz et al., 2022; Pereira et al., 2013), the data presented here are unique as they show a direct comparison of the covalent and non-covalent interactions of microcystins *in vitro*. Using synthesized microcystin derivates, either lacking the covalent binding site (Mdha derivates) or alteration in the hydrophobic Adda side chain (Adda derivates), the inhibition mechanism could be retraced, elucidating the direct influence of the interactions in two different PPPs, as well as their biological relevance in cell systems.

Previous studies proposed that the formation of the covalent bond may not be critical for microcystin-induced PPP inhibition, since inhibitory effects in PPP1 and PPP2A were observed within minutes, whereas the formation of the covalent bond between the cysteine and the Mdha methylene group required hours (Craig et al., 1996). Rather than initiating PPP inhibition, it is considered to enhance microcystin toxicity (Pereira et al., 2013). Noteworthy, the additional diazirine (DAz) moiety at position (2) in [Ala^{7}]MC-L(DAz)Y(Prg), whose photoinduced crosslinking function is induced at a wavelength between 330 nm and 370 nm, has been shown not to interfere with the assays used in preliminary experiments. Indeed, both Mdha derivates [Ala^{7}]MC-L(DAz)Y(Prg) and [MSecPh^{7}]MC-LY(Prg), were able to inhibit rPPP1 and hPPP5, indicating that the formation of the covalent bond is not essential to induce sufficient PPP inhibition. These results align with the fact that nodularins show similar structures and toxicities as microcystins but are unable to bind covalently to PPPs due to the lack of the Mdha methylene group (Rinehart et al., 1988), indicating a subordinate role in the inhibition mechanism. Interestingly, no significant difference in PPP inhibition ability was observed for both Mdha derivates in rPPP1 and hPPP5 compared to the parental microcystin, raising the question of whether the formation enhances toxicity by accompanying irreversibility. Although this reaction seems to be accessory for PPP inhibition, it is hypothesized to play a more important part in the biological role of microcystins including its function in the conjugation to glutathione (Pereira et al., 2013; Santori et al., 2020; Vichi et al., 2016). Indeed, this study demonstrated that the Mdha derivates tended to be less toxic in biological systems (OATP-expressing cell lines) than their parental microcystins with the ability to bind covalently. However, this could be explained by the experimental setup used. While no substrates other than microcystins were available in the *in vitro* PPP assay, various potential substrates were present in the cytosol. Despite the high affinity of microcystins for PPPs, these hydrophobic interactions are only short-lived (Fontanillo & Köhn, 2018; Pereira et al., 2013) and cellular processes are highly dynamic, allowing the catalytic subunit to be occupied by another substrate, blocking access for microcystins. Nevertheless, the question of the glutathione conjugation in terms of toxicity remains unclear. So far, no comparable studies have been performed on microcystin conjugates (MC-GSH, MC-Cys) that clearly demonstrate conjugate-induced PPP inhibition, i.e., toxicity. But considering that covalent binding is not essential to induce PPP inhibition, and thus the steric effects of the introduced phenylselenenyl residue at position (7) in [MSecPh^{7}]MC-LY(Prg) was not particularly hindering, it seems very likely that the conjugates will still show PPP inhibition abilities. This raises the question of whether increased elimination via efflux transporters is more important than the role of GSH in reducing microcystin toxicity. It is noteworthy, that glutathione, consisting of three amino acids, is much larger and therefore difficult to compare with the phenylselenenyl residue, highlighting the need for additional data at this point.

Short insertion: Focus of this study was solely on the microcystin-induced PPP inhibition mechanism, therefore no further data on the role of glutathione toxicity were shown. A detailed study of

this topic is presented in Chapter III. Similar, differences between OATP1B1 and OATP1B3 mediated uptake were not discussed here, but in detail in Chapter II.

Since the formation of the covalent bond did not appear to be critical for PPP inhibition either *in vitro* or in cell systems, Adda was assumed to be the driving force of the inhibition mechanism. To support this hypothesis, the requirement of the Adda side chain had to be clarified. In fact, the Adda derivate, completely lacking the Adda side chain [Amba^5]MC-LY(Prg), showed a dramatic reduction in toxicity, with a 290,000-fold and 30,000-fold increase in the IC_{50} values measured in rPPP1 and hPPP5, respectively. Whereas the presence of the Adda backbone only, [Anda^5]MC-LY(Prg), partially restored PPP inhibition capabilities (1,727 nM in rPPP1 and 2,421 nM in hPPP5). Nevertheless, toxicity was still reduced by 1,000-fold in rPPP1 and 1,4000-fold in hPPP5 compared to the parental MC-LY(Prg), raising the question of what backbone length is necessary for sufficient PPP inhibition. Therefore, two additional Adda derivates were used, which differed only in backbone length. While [Apda^5]MC-LF represents the usual Adda backbone of seven carbon atoms, with no residues except for the terminal phenyl group, [Apha^5]MC-LF has a shortened backbone of four carbon atoms, with no residues except for the terminal phenyl group. Shortening the Adda backbone to only four instead of seven carbon atoms resulted in a significant reduction in PPP inhibitory capacity, as indicated by a 40-fold increase in rPPP1 and a 20-fold increase in hPPP5 IC_{50} values compared to [Apda^5]MC-LF, and a dramatic 160,000-fold and 10,000-fold increase compared to the parental microcystin, respectively. Besides the presence of saturated bonds in [Apda^5]MC-LF, the Adda side chain of [Anda^5]MC-LY(Prg) differed from [Apda^5]MC-LF mainly in the absence of the terminal phenyl group. Interestingly, both showed IC_{50} values in a comparable concentration range (1,459 nM and 1,727 nM in rPPP1; 1,187 nM and 2,421 nM in hPPP5, respectively), showing no significant difference. Therefore, it was concluded that the terminal phenyl group, which contributed to the hydrophobicity of the Adda side chain, was not decisive for the PPP inhibition mechanism. Thereby, the calculated LogP values for the Adda side chain was 5.44 for [Apda^5]MC-LF and 2.78 for [Anda^5]MC-LY(Prg) (calculated by using the chemical structure and ChemDraw). Intriguingly, more than the presence of the terminal residue, the orientation of the Adda backbone residues played a role, as indicated in the failure of [enantio-Adda^5]MC-LF to inhibit rPPP1 and hPPP5. The results are consistent with structural analysis, which revealed that the Adda side chain is extremely tight accommodated in the hydrophobic groove of the PPPs (Harada et al., 1990; Pereira et al., 2013). Conformational changes within the residues, no stable binding to the corresponding protein residues in the hydrophobic groove (Cys127, Ile130, Ile133, Tyr134, Trp206) can be formed (Fontanillo & Köhn, 2018). Similar results were reported using molecular dynamics simulations using [enantio-Adda^5]MC-LF in PPP1. In contrast to MC-LF, [enantio-Adda^5]MC-LF was unable to bind sufficiently to the hydrophobic groove and instead of binding, it moved out of the binding site, then returned and flipped reversed. This effect was observed only for the enantiomeric form and not for the other congeners tested (Jaeger-Honz et al., 2022). Surprisingly, these results were not supported by those obtained from the OATP-expressing HEK293 cell lines. In contrast to the *in vitro* PPP assay, [enantio-

Adda[5]]MC-LF induced cytotoxic effects in both OATP-expressing cell lines, although the induced cytotoxicities were comparably weak. Except for [enantio-Adda[5]]MC-LF, the OATP1B1- and OATP1B3-expressing cell lines showed basically the same trend as observed in the *in vitro* dataset, as visualized in the heatmap in **Figure 19**. Moreover, all Adda derivates showed OATP-mediated transport, even though OATP1B1-expressing cells had difficulties in the transport of [Amba[5]]MC-LY(Prg) compared to OATP1B3-expressing cells, indicated in the high difference in EC_{50} (2,629 nM and 94,7 nM, respectively). While both cell lines displayed similar PPP expression levels (see Chapter II), this effect is likely due to the hydrophobicity of the microcystins, as OATP1B1-expressing cells were less efficient in transporting rather hydrophilic microcystins than the OATP1B3 transporter. It is important to mention that OATP-mediated uptake is highly dependent on the hydrophobicity of the whole microcystin molecule, and since the Adda derivates differ widely in their LogP values, no clear conclusion can be drawn here. The influence of hydrophobicity, especially in OATP1B1- and OATP1B3-expressing cells, is discussed in detail in Chapter II.

While this study included only positions (5) and (7) to study the inhibitory mechanism, other positions should not be ignored. The viable positions (2) and (4) are known to contribute, but do not determine toxicity like Adda. Although the crystal structures of PPP1 and PPP2A complexed with MC-LR showed only minor interactions at position (2) but no apparent interaction of the position (4) with the phosphatases, both positions contribute to the overall hydrophobicity of the molecule. Overall, positions (2) and (4) appear to play only a minor role in the PPP inhibition mechanism, as a previous study of 18 congeners in PPP1, PPP2A and PPP5 revealed (Altaner et al., 2020). Moreover, the free carboxylic acid group of D-glutamine at position (6), as well as the carbonyl group of the Adda side chain, have been shown to contribute significantly by introducing hydrogen bonds to metal-bound water molecules and thereby stabilizing hydrophobic interactions (Fontanillo & Köhn, 2018; Pereira et al., 2013; Stotts et al., 1993).

Conclusion

Albeit Adda itself was shown to be non-toxic (Namikoshi et al., 1989), this study clearly demonstrated that the presence, length, and orientation of the hydrophobic side chain play a decisive role in the microcystin-induced PPP inhibition mechanism. While the formation of the covalent bond, although inducing irreversibility, only plays a subordinate role. More importantly, is the correct positioning of the microcystin molecule, which is controlled by the high hydrophobic affinity of the Adda side chain. Since the hydrophobic groove of the PPPs in the catalytic subunit is extremely tight, no other orientation of the Adda residues is possible. Moreover, the length of the Adda backbone is critical to facilitate sufficient hydrophobic interaction sites, shortening of the Adda backbone induces loss of affinity.

3. Chapter II

3.1. L-Amino Acid at Position (2) Determines OATP-Mediated Microcystin Uptake

3.1.1. Introduction

Microcystins are complex cyclic peptides composed of seven amino acids, including D-alanine at position (1), two variable L-amino acids at positions (2) and (4), ß-D-methylaspartate at position (3), D-glutamine at position (6), D-methyldehydroalanine (Mdha) at position (7), and a unique hydrophobic amino acid Adda (3-amino-9-methoxy-10-phenyl-2,6,8-trimethyl-deca-4(E),6(E)-dienoic acid) at position (5), see **Figure 21**. The variety of L-amino acids and smaller alterations (e.g., (de)methylations) currently results in more than 250 microcystin congeners (Spoof & Catherine, 2016), albeit the toxicity is known for only a few. Microcystins are classified as hepatotoxins and are highly potent serine/threonine phosphoprotein phosphatases (PPPs) inhibitors (MacKintosh et al., 1990; MacKintosh et al., 1995). PPPs are the most important phosphatases in eukaryotic cells, contributing significantly to essential cellular events and cell survival. Inhibition of PPPs leads to hyperphosphorylation and disruption of fundamental cellular processes, resulting in the induction of cell death (McLellan & Manderville, 2017). Members of the PPP family share a highly conserved catalytic subunit and based on the sequence, PPPs have been further classified into seven subtypes: PPP1, PPP2A, PPP2B (Calcineurin), PPP4, PPP5, PPP6 and PPP7 (Brautigan, 2013; Cohen, 2004; Shi, 2009). Among all known phosphatases, PPP1 and PPP2A are the most essential ones, accounting for more than 90 % of protein dephosphorylation in eukaryotic cells (Bollen et al., 2010). Due to the hydrophobic Adda side chain, microcystins display a high affinity for the hydrophobic groove in the catalytic center of PPPs (MacKintosh et al., 1990; MacKintosh et al., 1995). This non-covalent but highly hydrophobic interaction allows the correct positioning of the toxin to form a covalent bond between the α,β-unsaturated terminal carbonyl group of Mdha and the cysteine moiety of the PPP active site (Craig et al., 1996; Pereira et al., 2013). Thereby, the inhibitory capacities of naturally occurring microcystins, which differ mainly in the L-amino acid positions (2) and (4), are comparable with similar IC_{50} values in the nanomolar range (Altaner et al., 2020; Fischer et al., 2010; Fontanillo & Köhn, 2018; Pereira et al., 2013), suggesting a highly conserved molecular mode of action. Indeed, the study presented in Chapter I clearly demonstrated that the presence, length, and orientation of the hydrophobic Adda side chain played a critical role in the microcystin-induced PPP inhibition mechanism. While the formation of the covalent bond, although inducing irreversibility, played a minor role. Comparable results were obtained by studying 18 different microcystin congeners using purified and active rPPP1, hPPP2A, and hPPP5 (Altaner et al., 2020). However, the study of microcystin-induced PPP inhibition *in vitro* using PPPs covers only a very limited aspect of microcystin toxicity. In fact, microcystin toxicity includes both toxicodynamic (e.g., PPP inhibition) and toxicokinetic (e.g., cellular uptake) parameters. To contextualize the toxicodynamic dataset presented in Altaner et. al. (2020) appropriately, a comparable toxicokinetic dataset including biologically relevant systems is needed.

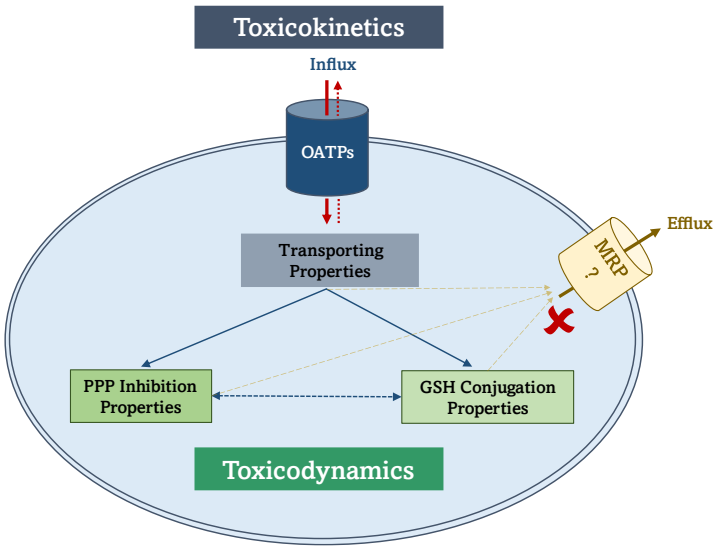

Figure 20: Chapter II Graphical Abstract

The toxicokinetic parameters of microcystins are highlighted in blue and include active uptake via organic anion transporting polypeptides (OATPs). While the cellular toxicodynamic parameters are highlighted in green, including serine/threonine phosphoprotein phosphatase (PPP) inhibition and glutathione (GSH) conjugation properties. Since the OATP1B1- and OATP1B3-expressing HEK293 cell lines do not express microcystin-relevant efflux transporters (e.g., MRPs), the yellow-marked pathways were excluded in this study. Notably, OATPs are assumed to be directional transporters.

Cellular systems are complex due to the many variables involved, see **Figure 20**. In addition to the PPP inhibition capabilities of microcystins, the toxicodynamic aspect includes the possible conjugation to glutathione (GSH). GSH conjugation to microcystins can occur spontaneously at alkaline pH or enzymatically via the phase II enzyme glutathione-S-transferase (GST) (Kondo et al., 1992; Vichi et al., 2016). Using recombinant GSTs and human hepatic cytosol with MC-LR and MC-RR showed that the conjugation appeared to be congener-dependent, although MC-RR was conjugated more efficiently than MC-LR (Buratti et al., 2017; Buratti & Testai, 2015). However, it is still unclear whether the resulting conjugates (MC-GSH, MC-Cys) are toxic (PPP inhibitory capacity) or not. Due to their chemical structure and amino acid composition, microcystins are rather hydrophilic and spatially large molecules and require active transport to cross cell membranes. Transmembrane transport is thereby mediated by organic anion transporting polypeptides (OATPs). Using *Xenopus laevis* oocytes as an expression system, microcystin-mediated uptake was studied and the liver-specific OATP1B1 and OATP1B3 were identified as main microcystin transporters (Fischer et al., 2005). Although both transporters exhibit 80 % amino acid homology and share a number of common substrates (such as statins, rifampicin, or bromosulfophthalein), differences in transport kinetics were observed (Hagenbuch & Meier, 2004). Indeed, previous studies using MC-LR, MC-LF and MC-RR have identified congener-specific uptake in OATP1B1- and OATP1B3-expressing HEK293 cells (Fischer et al., 2010). So far, cellular elimination via efflux transporters is not fully understood. Recent studies have demonstrated microcystin-mediated export via multidrug resistance-associated protein 2 (MRP2) transporters, albeit only for unbound microcystins and not for their conjugates (Kaur et al., 2019).

Aim of the Study

Although more than 250 microcystin congeners have been described, the toxicity of only a few are known and have only been assessed in simplified *in vitro* PPP experiments. So far, a comparable dataset including toxicodynamic and toxicokinetic parameters, see **Figure 20**, is lacking. To reduce all included variables to a basic limit, a simplified biological cell system was used instead of complex hepatocytes to combine toxicodynamic and toxicokinetic parameters. Human embryonic kidney 293 (HEK293) cells are a robust but simple cell line, as they were isolated at a very early stage of fetal development. Owing to the absence of influx and efflux transporters and their high transfection efficiency for membrane proteins, HEK293 cells are widely used to study individual transporter capabilities and kinetics. To study the individual transporting properties, stably transfected HEK293-OATP1B1, -OATP1B3, and control vector (CV) cells were exposed to 21 structurally different microcystin congeners, covering the known spectrum of hydrophobicity, molecular weights and common as well as unusual modifications of the consensus structure, see **Figure 21** and summarized in **Supplementary Table 1**. Although no known microcystin efflux transporters are expressed in HEK293 cells, it is important to note that OATPs are assumed to be bidirectional, even though influx is assumed to be highly preferential (Mahagita et al., 2007).

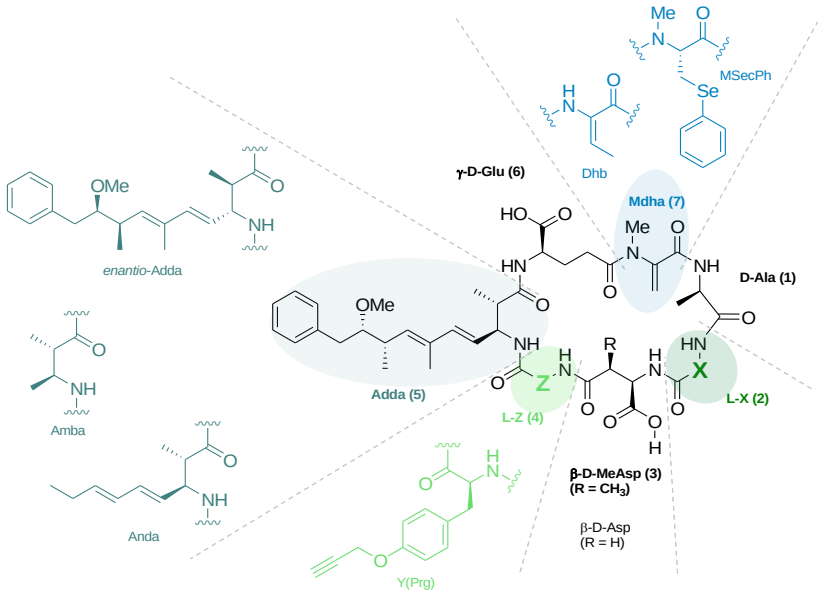

Figure 21: Summary of the Used Microcystin Variants

The consensus structure of microcystins and modifications in the synthetic variants are illustrated. The dashed lines represent individual amino acids, further details are summarized in **Supplementary Table 1**. Figure was modified and adapted (Altaner et al., 2020). Anda = (2*S*,3*S*,4*E*,6*E*)-3-amino-2-methylnona-4,6-dienoic acid, Amba = (2*S*,3*S*)-3-amino-2-methylbutanoic acid, Dhb = (E)-2-amino-2-butenoic acid, MSecPh = N-methyl-Se-phenyl-L-selenocysteine, Prg = propargyl.

This study aimed to elucidate the toxicokinetic parameters of microcystin toxicity. Thereby, features responsible for (i) sufficient microcystin uptake, and (ii) differences between OATP1B1- and OATP1B3-mediated uptake were studied. Moreover, the initial hypothesis that congener-dependent toxicity is primarily induced by OATP-mediated uptake (toxicokinetics) rather than PPP inhibitory capacities (toxicodynamics) was evaluated.

3.1.2. Results

Transporter Expression and Toxicodynamic Parameters

Stably transfected HEK293-OATP1B1 and HEK293-OATP1B3 cells were used to study the cellular OATP-mediated microcystin uptake. HEK293 cells, transfected with the respective control vector plasmid (CV), were used as transport control. To adequately compare the transport properties of OATP1B1- and OATP1B3-expressing cells, the actual transporter expression, localization, and quantity were determined and compared. Immunocytochemistry (ICC) staining was used to visualize the actual transporter expression and localization, whereas western blot analysis of the isolated membrane fractions was used to confirm similar expression levels.

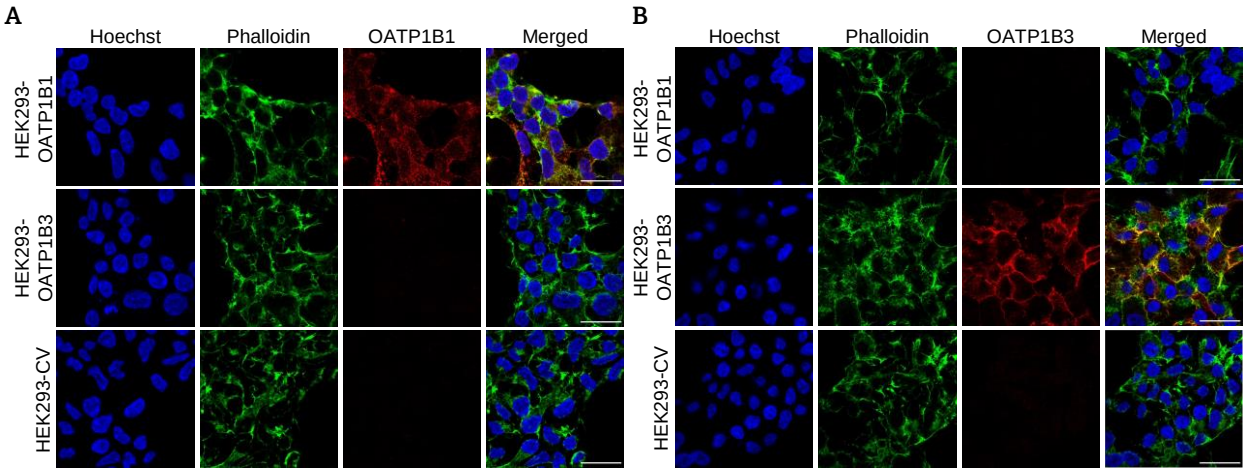

Figure 22: Immunocytochemistry Staining

Immunocytochemistry staining was performed on HEK293-OATP1B1, -OATP1B3- and -CV cells using **(A)** OATP1B1 or **(B)** OATP1B3 antibodies. Cells were counterstained with Hoechst33342 (blue) to visualize cell nuclei and phalloidin (green) to visualize actin. The scale bars indicate 30 µm.

ICC staining clearly showed the exclusive expression of OATP1B1 and OATP1B3 in the corresponding cell lines, see **Figure 22 A-B**. Both transporters appeared to be localized and concentrated at the cell membrane, as indicated by higher antibody density. No antibody staining was observed in the cell nuclei. HEK293-CV cells showed no sensitivity to either OATP1B1 or OATP1B3 antibodies. The exclusive expression of OATP1B1 and OATP1B3 was additionally confirmed by western blot analysis, see **Figure 23 A-B**. Subsequent blot quantification and statistical comparison confirmed similar expression levels of OATP1B1 and OATP1B3 transporters, see **Figure 23 C**. To exclude any effects due to varying toxicodynamic parameters in the cell lines used, the baselines of the cellular GSH content and PPP activities were determined. Similar concentrations of cytosolic GSH were measured in HEK293-OATP1B1, HEK293-OATP1B3 and HEK293-CV cells (1.9 mM, 1.8 mM, 1.7 mM, respectively), see **Figure 23 D**. Thus, differences in the conjugation capacities of the cell lines were excluded. The similarity of all cell lines was also confirmed by measuring cellular PPP activities. Adapted phosphatase activity assay was performed using a defined enzymatic activity of rPPP1 (3 units, U) and corresponding cell lysates, see **Figure 23 E**.

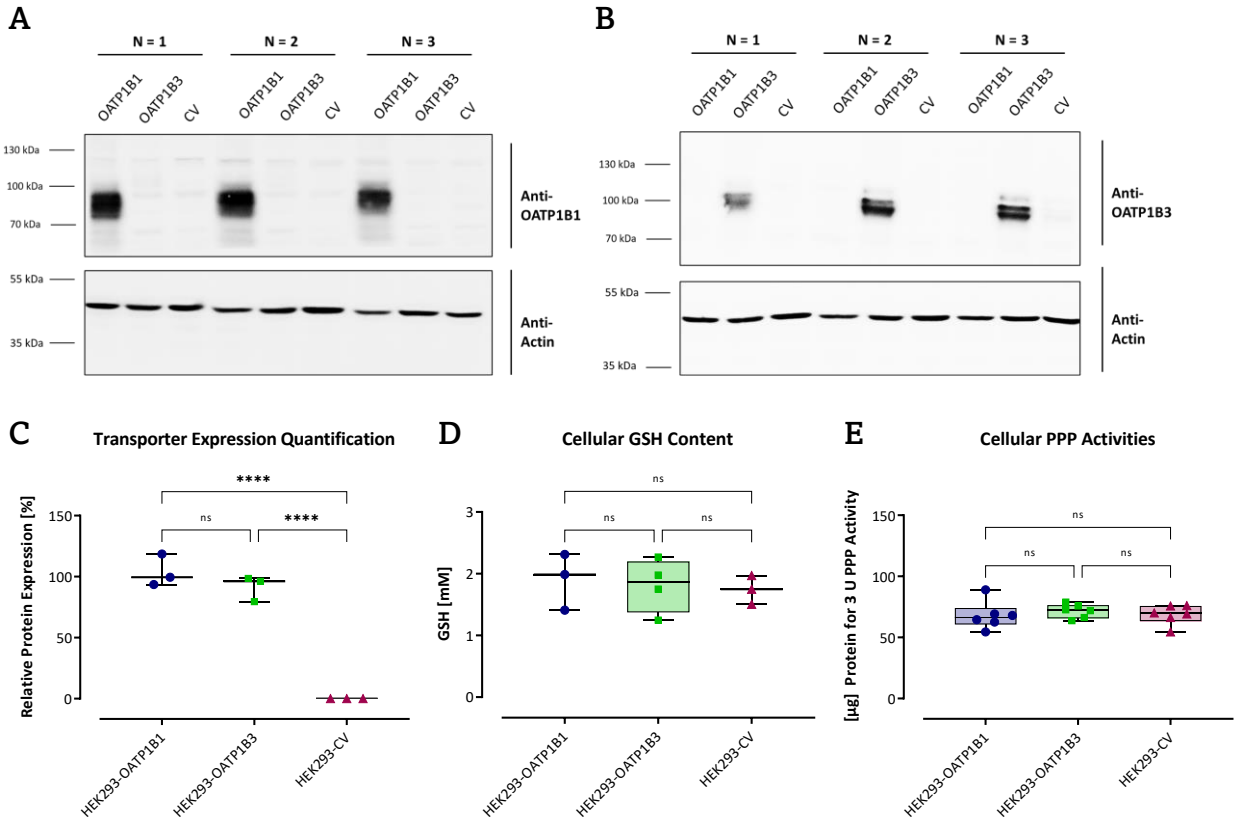

Figure 23: Transporter Expression, GSH Content and PPP Activities

Western blot analysis was performed using either **(A)** OATP1B1 or **(B)** OATP1B3 antibodies, with actin as loading control (30 µg/lane). Blots were **(C)** quantified using ImageJ software. Toxicodynamic parameters including **(D)** cellular GSH concentration and **(E)** PPP activities were determined in HEK293-OATP1B1 (blue), HEK293-OATP1B3 (green), and HEK293-CV (red) cells. Statistical analyses were performed using one-way ANOVA followed by Tukey's multiple comparison post-test ($p<0.0001$); ns = not significant. Each point represents one biological replicate (n=3-6).

Similar amounts of cell lysates were required to induce 3 U PPP enzyme activity in HEK293-OATP1B1, -OATP1B3 and -CV cells (68 µg, 72 µg and 69 µg, respectively). To validate the experimental setup and measured activities, experiments using phosphatase inhibitors (10 mM sodium orthovanadate or 50 mM sodium fluoride) were performed using defined enzyme activities of HEK293-OATP1B1 or -OATP1B3 cell lysates, see **Supplementary Figure 5.** As no significant differences were found in either GSH content or PPP activity, the basic toxicodynamic parameters of all cells were assumed to be the same.

Expression Level of Serine/Threonine Phosphatases

Proteomic analysis using nano LC-MS/MS was performed to determine the relative abundance of PPPs in HEK293 cells, see **Figure 24**. As no significant differences were found within the toxicodynamic parameters, PPP expression was analyzed in HEK293-CV cells. Among all proteins, 1.5 % were identified as phosphatases, of which only 0.02 % were tyrosine phosphatases, and 0.7 % were serine/threonine phosphatases, see **Figure 24 A**. These 0.7 % serine/threonine phosphatases were composed of 0.21 % PPP1, 0.39 % PPP2A, 0.01 % PPP2B, 0.03 % PPP4, 0.03 % PPP5 and 0.04 % PPP6, see **Figure 24 B**. For visualization, the distribution of all PPP members was graphed as a percentage of the total abundance of

serine/threonine phosphatases, see **Figure 24 C**. As a result, PPP2A was identified as the most dominantly expressed PPP in HEK293 cells, accounting for 54.4 % of all PPPs, followed by PPP1 (29.6 %). The expression levels of PPP4, PPP5 and PPP6 were similarly low (4.1 %, 4.3 % and 5.9 %, respectively). PPP2B was barely expressed, accounting for only 1.1 % of all PPPs. PPP7 was not detected in HEK293-CV cells.

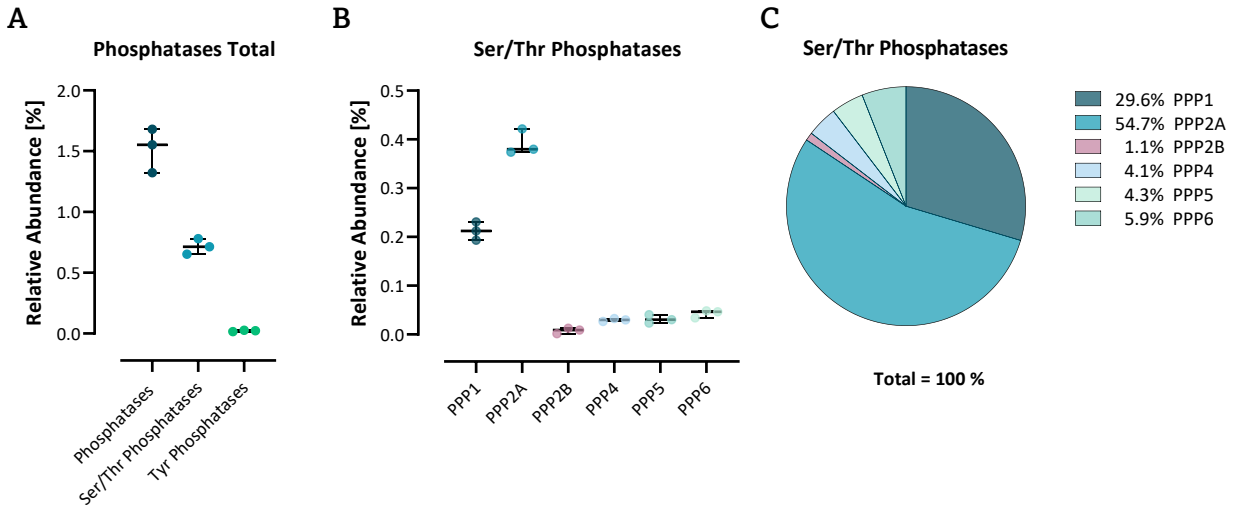

Figure 24: Proteomic Analysis of PPP Expression Levels

Proteomic analysis revealed the relative abundance of **(A)** all phosphatases and **(B)** PPP members in HEK293-CV cells. For visualization, the distribution of all PPP members was graphed as a percentage of the total abundance of serine/threonine phosphatases **(C).** Proteomic analysis was performed using three independent replicates (n=3).

Microcystin Congener-Dependent OATP Uptake

To study OATP1B1- and OATP1B3-mediated uptake, firstly 17 microcystin congeners were used. These 17 structurally different congeners covered the known spectrum of hydrophobicity, had various molecular weights, and included both common and unusual modifications of the consensus structure. While twelve congeners were naturally occurring microcystins including MC-LR, MC-RR, MC-LF, MC-LW, MC-YR, MC-HilR, MC-LA, MC-WR, MC-LY, MC-HtyR, [ß-D-Asp^3]MC-LR and [ß-D-Asp^3, Dhb^7]MC-RR. Five microcystin congeners were synthesized *de novo* with modifications to either the Adda side chain [enantio-Adda^5]MC-LF, [Anda^5]MC-LY(Prg), and [Amba^5]MC-LY(Prg)) or the Mdha group ([MSecPh^7]MC-LY(Prg)). Since some of the synthetic microcystins contained a propargylated tyrosine residue at position (4), MC-LY(Prg) was used as a reference substance to exclude any effects due to propargylation.

Cells were exposed to microcystins for 48 hours, followed by cell viability measurements. The exposure assay provided well-fitted (R^2) concentration-dependent response curves. To efficiently compare microcystin-induced cytotoxicities, the half-maximal effective concentrations (EC_{50}) were calculated using non-linear regression analysis, see **Figure 25**. All calculated EC_{50} values were summarized in **Table 5**. No transport, as indicated by no decrease in cell viability, was measured in HEK293-CV, see **Supplementary Figure 6**.

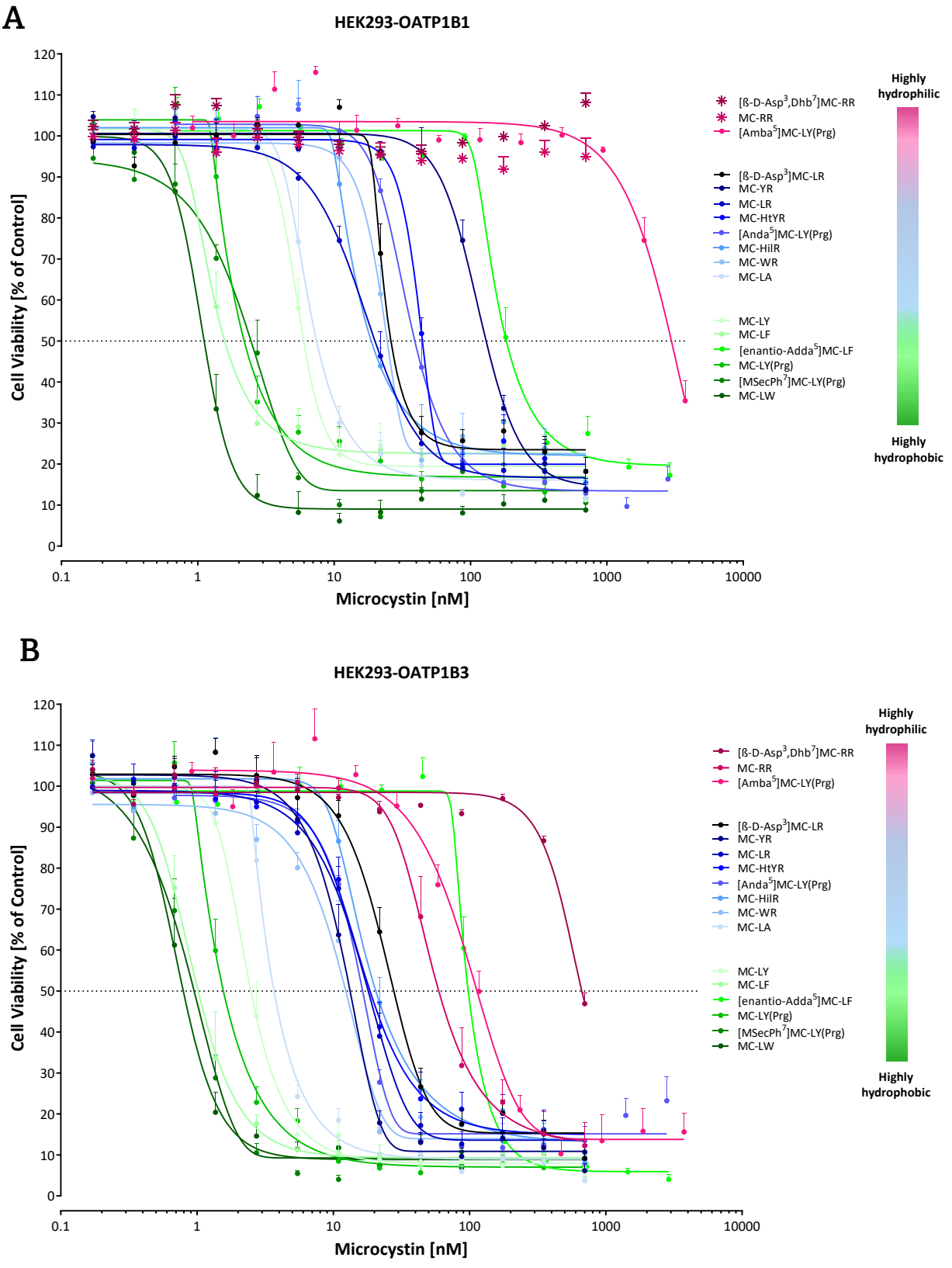

Figure 25: OATP1B1- and OATP1B3-Mediated Microcystin Cytotoxicity

Cell viability was measured in **(A)** HEK293-OATP1B1 and **(B)** HEK293-OATP1B3 cells after exposure to 17 structurally different microcystin congeners. Each point represents the mean of 3-8 independent biological replicates pipetted in triplicates ± SEM (n=3-8). Only upper error bars are shown for reasons of clarity.

OATP1B1-Mediated Microcystin Uptake

Despite the most hydrophilic microcystin congeners, MC-RR and [ß-D-Asp^3, Dhb^7]MC-RR, all congeners induced a concentration-dependent response curve, see **Figure 25 A**. However, no OATP1B1-mediated uptake was measured for either MC-RR congener, at least not in the concentration range used. Compared to the most frequently detected MC-LR with an EC_{50} of 16.78 nM, almost all congeners showed significant differences in the induced toxicities. No significant differences were found for MC-HilR and MC-WR, with EC_{50} values of 15.00 nM and 22.04 nM, respectively.

While MC-LR showed EC_{50} in the moderate range, significantly lower EC_{50} values were measured for MC-LW and MC-LF, indicating significantly higher cytotoxic effects. In this dataset, MC-LW and MC-LF were the most toxic microcystin variants tested, with EC_{50} values of 1.058 nM and 1.281 nM, respectively. Since MC-LY(Prg) differs from MC-LF only in the propargyloxy moiety, it is not surprising that the synthetic derivate has a comparatively low EC_{50} value (1.857 nM), as the same applies to [MSecPh^7]MC-LY(Prg) (2.250 nM), as already shown and discussed in Chapter I.

Moderate toxicity with elevated EC_{50} values was measured for MC-WR, [ß-D-Asp^3]MC-LR, [Anda^5]Mc-LY(Prg), and MC-HtyR (22.04 nM, 23.37 nM, 34.44 nM, and 41.10 nM, respectively). Whereas low cytotoxic effects were induced by MC-YR, [enantio-Adda^5]MC-LF and [Amba^5]MC-LY(Prg) with EC_{50} values of 115.2 nM, 156.7 nM, and 2,695 nM, respectively.

Table 5: Summary of EC_{50} Values and Statistical Analyses

Calculated EC_{50} values and corresponding coefficients of determination (R^2) for 17 microcystin congeners exposed to HEK293-OATP1B1 and HEK293-OATP1B3 cells are summarized. No transport was observed for MC-RR and [ß-D-Asp^3, Dhb^7]MC-RR in OATP1B1-expressing cells. Therefore, values are indicated as not defined (n.d.). Statistical analyses were performed using unpaired t-tests, p-values are summarized in the table; ns = not significant.

Congener	HEK293-OATP1B1				HEK293-OATP1B3				OATP1B1 - OATP1B3	
	EC_{50} [nM]	R^2	Statistical Comparison to MC-LR		EC_{50} [nM]	R^2	Statistical Comparison to MC-LR		Statistical Comparison	
MC-LR	16.78	0.9467	-	-	15.99	0.9437	-	-	ns	0.5294
MC-RR	n.d.	n.d.	n.d.	n.d.	52.97	0.9315	***	0.0005	n.d.	n.d.
MC-LF	1.281	0.9219	****	<0.0001	0.921	0.9377	****	<0.0001	ns	0.1541
MC-LW	1.058	0.9177	****	<0.0001	0.722	0.9462	****	<0.0001	ns	0.1649
MC-YR	115.2	0.9505	****	<0.0001	12.10	0.9640	ns	0.1513	****	<0.0001
MC-HilR	15.00	0.9391	ns	0.6437	17.71	0.9497	ns	0.4835	ns	0.5884
MC-LA	6.551	0.9099	***	0.0006	3.476	0.9755	***	0.0003	*	0.0134
MC-WR	22.04	0.9353	ns	0.1505	11.24	0.9263	ns	0.2916	**	0.0043
MC-LY	5.317	0.9473	***	0.0002	2.352	0.9557	***	0.0002	***	0.0002
MC-HtyR	41.10	0.9575	****	<0.0001	16.08	0.9440	ns	0.5965	****	<0.0001
[ß-D-Asp^3]MC-LR	23.37	0.9375	*	0.0110	23.87	0.9411	*	0.0196	ns	0.6646
[MSecPh^7]MC-LY(Prg)	2.250	0.9323	****	<0.0001	0.842	0.9400	****	<0.0001	*	0.0125
MC-LY(Prg)	1.857	0.9494	****	<0.0001	1.467	0.9650	***	0.0001	*	0.0306
[enantio-Adda^5]MC-LF	156.7	0.9750	****	<0.0001	95.98	0.9806	****	<0.0001	**	0.0019
[ß-D-Asp^3, Dhb^7]MC-RR	n.d.	n.d.	n.d.	n.d.	511.9	0.9023	***	0.0005	n.d.	n.d.
[Anda^5]MC-LY(Prg)	34.44	0.9685	**	0.0013	15.00	0.9579	ns	0.6743	***	0.0005
[Amba^5]MC-LY(Prg)	2,695	0.8951	****	<0.0001	94.66	0.9493	***	0.0007	****	<0.0001

OATP1B3-Mediated Microcystin Uptake

In contrast to HEK293-OATP1B1, OATP1B3-expressing HEK293 cells showed concentration-dependent response curves for all congeners, indicating OATP1B3-mediated uptake of all MC-RR congeners, see **Figure 25 B**.

Similar to OATP1B1-expressing cells, the highest cytotoxicity in OATP1B3-transfected cells was induced by MC-LW, MC-LF, MC-LY(Prg) and [MSecPh^{7}]MC-LY(Prg) with the lowest half-maximal concentrations of 0.722 nM, 0.921 nM, 1.467 nM, and 0.842 nM, respectively. Compared to MC-LR (15.99 nM), no significant differences were observed in HEK293-OATP1B3 cells exposed to MC-WR, MC-YR, [Anda^{5}]MC-LY(Prg), MC-HtYR, MC-HilR and [ß-D-Asp^{3}]MC-LR, which covered a moderate toxicity range (12-24 nM). The highest effective half-maximal concentrations were measured for the synthetic derivates [enantio-Adda^{5}]MC-LF and [Amba^{5}]MC-LY(Prg), 95.98 nM and 94.66 nM, respectively. This was exceeded only by [ß-D-Asp^{3}, Dhb^{7}]MC-RR (511.9 nM).

Hydrophobicity of the Whole Microcystin Molecule Determines OATP-Mediated Transport

By analyzing both graphs in **Figure 25**, it became apparent that the observed cytotoxicities could be clustered into three groups: less toxic, moderately toxic, and very toxic, as highlighted in the graphs as red, blue, and green clusters, respectively. Since no experimentally determined LogP values were available for all 17 microcystins, *in silico* calculated LogP values were used to compare the overall hydrophobicities of the congeners. All LogP calculations were kindly performed by Sabrina Jaeger-Honz (Life Science Informatics Department, University of Konstanz) using previously published protocols (Wildman & Crippen, 1999).

The obtained LogP values of the whole microcystin molecules were sorted and visualized in **Figure 26 A**. Accordingly, a gradual decrease in EC_{50} values was observed when all congeners were sorted from highly hydrophilic to highly hydrophobic, see **Figure 26 B**. Thereby revealing the pattern of OATP1B1- and OATP1B3-mediated uptake in which hydrophobic microcystins were preferentially transported over hydrophilic ones. As the Adda side chain is essential in the mechanism of PPP-inhibition, these congeners were not included in this analysis but are shown in **Supplementary Figure 7**. In contrast to HEK293-OATP1B3, the hydrophobicity pattern for arginine-containing microcystin congeners was disrupted in OATP1B1-expressing cells (MC-YR, MC-HtyR, and MC-WR). Interestingly, these were those with the highest significant differences when comparing OATP1B1- and OATP1B3-mediated uptake. While OATP1B3 showed sufficient transport of these arginine-containing congeners, OAT1B1 failed (MC-RR congeners) or showed difficulties (MC-YR, MC-HtyR, and MC-WR) in the transport of these microcystin variants.

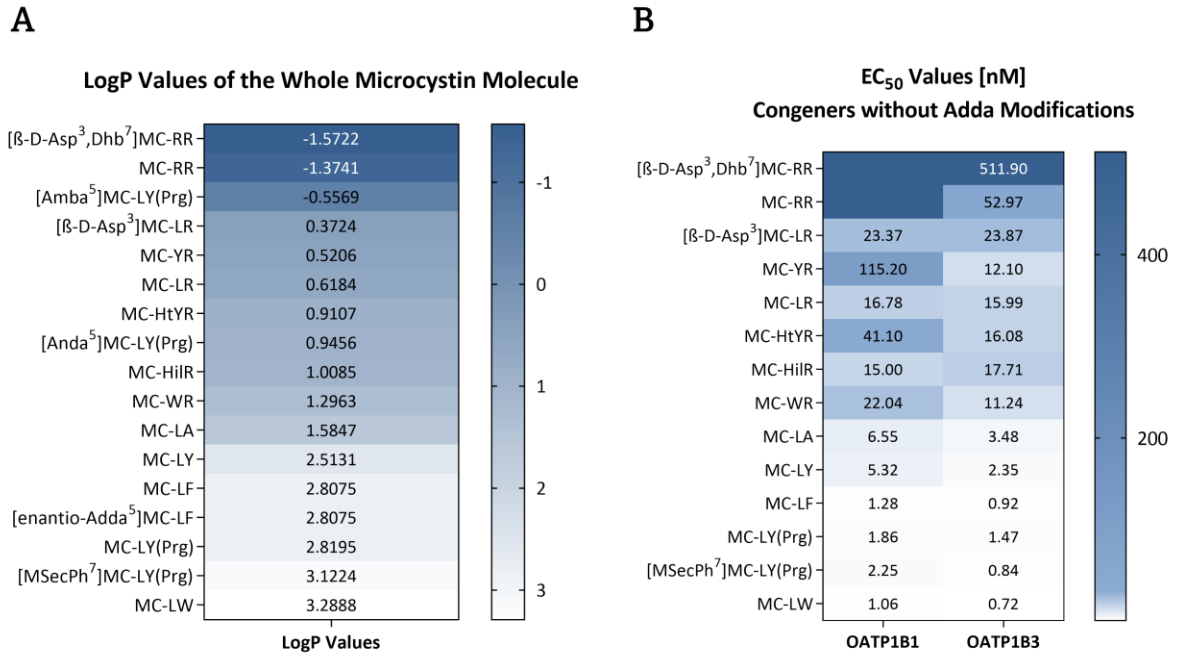

Figure 26: Correlation Between Microcystin Hydrophobicity and OATP-Mediated Uptake

Microcystin congeners were sorted based on their hydrophobicity. Therefore, **(A)** *in silico* calculated LogP values were used (negative LogP values = hydrophilicity, positive LogP values = hydrophobicity). Accordingly, EC_{50} data obtained for **(B)** OATP1B1- and OATP1B3-expressing cells were visualized.

Position (2) Determines OATP1B1- but not OATP1B3-Mediated Uptake

Based on these results, further analyses were performed in OATP1B1-expressing cells. Starting with one of the most hydrophilic congeners MC-RR, which was not found to be transported in OATP1B1, the transport properties could be significantly increased by replacing the arginine residue at position (2) with a slightly less hydrophilic tyrosine residue (MC-YR, EC_{50} 115.2 nM), although the whole microcystin molecule is still classified as highly hydrophilic. Replacement of tyrosine with homotyrosine, which differs from tyrosine by an additional methyl group and therefore slightly increased hydrophobicity, resulted in a 3-fold lower EC_{50} (MC-HtyR, EC_{50} 41.10 nM). To verify the emerging hypothesis that position (2) is critical for the OATP1B1-mediated uptake, synthetic microcystin congeners in which positions (2) and (4) were transposed were studied. Therefore, microcystin pairs with a highly hydrophobic and a highly hydrophilic amino acid residues located at the variable positions were used: MC-F_{D5}R and MC-RF_{D5}; MC-YR and MC-RY; MC-LR and MC-KL_{D7}. All synthesized microcystin derivates were kindly provided by Prof. Dr. Valentin Wittmann (Bioorganic Chemistry Department, University of Konstanz) and synthesized by Marius Wrona (D = deuterated). The direct comparison of these microcystin pairs had the advantage that the overall hydrophobicity of the molecule remained the same, as indicated by identical LogP values, whereas only the roles of positions (2) and (4) were studied. As the sensitivity for MC-LR was comparable for both OATP1B1 and OATP1B3 (16.78 nM and 15.99 nM, respectively), the first step was to analyze whether the switch in the positions (2) and (4) would result in an altered transport ability. Unfortunately, MC-RL was not available, therefore an amino acid with comparable chemical properties was used. Hence, the first

experimental setup included MC-LR, MC-KL_{D7}, and MC-RR as reference, as shown in **Figure 27 A**. While the positional change from the hydrophilic residue at position (4) to position (2) in MC-KL_{D7} resulted in a significant increase in the EC_{50} value in OATP1B1-expressing cells (141.50 nM), no significant differences were observed in OATP1B3-expressing cells (23.27 nM) compared to MC-LR (16.78 nM and 15.99 nM, respectively). A summary of the EC_{50} values obtained and the statistical analyses performed are summarized in **Figure 28** and **Table 6**.

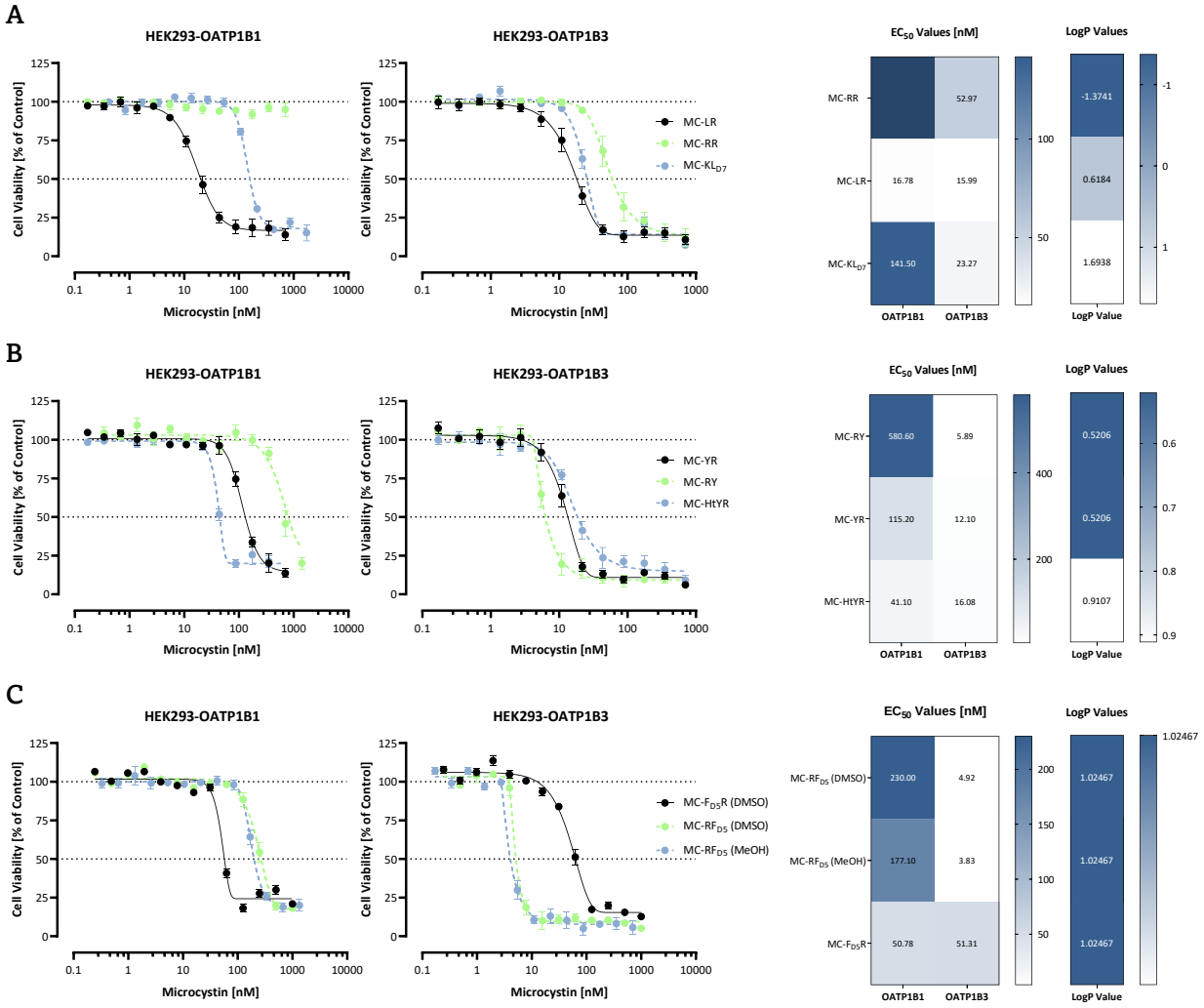

Figure 27: Comparison of Positions (2) and (4) in OATP-Mediated Microcystin Uptake

Microcystin pairs with transposed positions (2) and (4) were studied in OATP1B1- and OATP1B3-expressing HEK293 cells. Comparative cytotoxic response curves were generated for **(A)** MC-LR, MC-RR and MC-KL_{D7}, **(B)** MC-YR, MC-RY and MC-HtyR and **(C)** MC-$F_{D5}R$ (DMSO), MC-RF_{D5} (DMSO) and MC-RF_{D5} (MeOH). For better comparison, heatmaps with the obtained EC_{50} values and calculated LogP values are shown on the corresponding right side. Each point represents the mean ± SEM (n=3-9).

Since MC-YR demonstrated one of the highest differences in OATP1B1- and OATP1B3-mediated transport, the second experimental setup included MC-YR and MC-RY, as shown in **Figure 27 B**. Although the overall hydrophobicity of both molecules was identical, significant differences were observed within the OATP1B1-mediated transport. While MC-YR has already been classified as a less toxic congener in this dataset (115.2 nM), transposition of the arginine residue from position (4) to position (2) resulted in a

5-fold increase in EC_{50} concentration (580.6 nM), but only in the OATP1B1-expressing cells. Whereas MC-HtyR, which differs from MC-YR by only one additional methyl group and a slightly higher hydrophobicity, showed increased toxicity (41.10 nM). No significant differences in OATP1B3-mediated transport were observed for either congener.

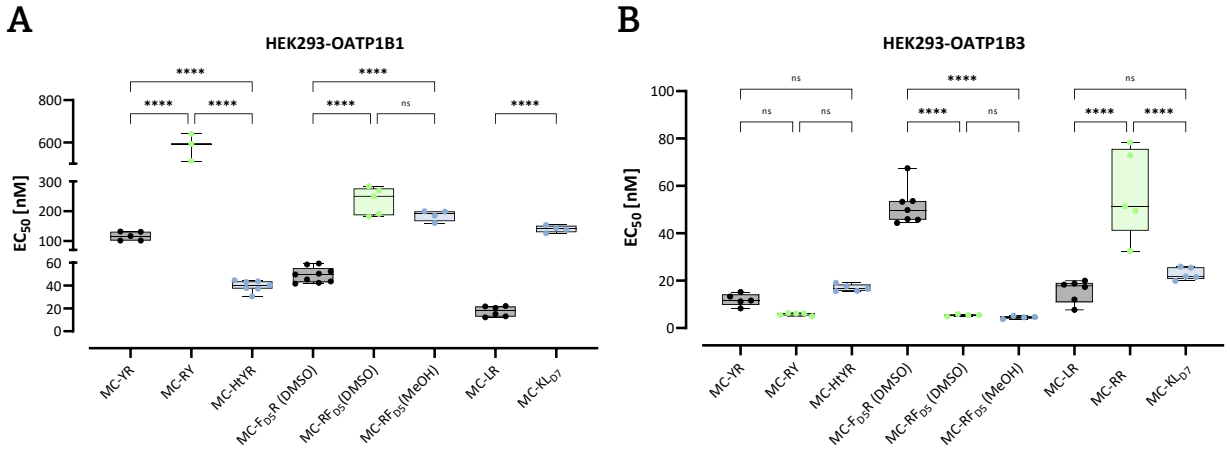

Figure 28: Statistical Analysis of Transposed Positions

The EC_{50} values obtained for the microcystin pairs in **(A)** HEK293-OATP1B1 and **(B)** HEK293-OATP1B3 cells are summarized. Each point represents one independent biological replicate ± SD (n=3-9). Statistical analyses were performed using one-way ANOVA followed by Tukey's multiple comparison post-test (p<0.0001).

Since arginine-containing congeners showed the most striking results, an amino acid with opposite chemical properties was used to further evaluate the impact of position (2) on the OATP1B1-mediated microcystin uptake. Due to the high hydrophobicity of phenylalanine, MC-LF was clearly classified as highly toxic despite its bulky chemical structure. Therefore, MC-F_{D5}R and MC-RF_{D5} were used to study the OATP-mediated uptake, see **Figure 27 C**. Exceptionally, MC-F_{D5}R and MC-RF_{D5} were dissolved in DMSO for solubility reasons. To rule out any effects due to DMSO, EC_{50} were additionally determined using similar amounts of MC-RF_{D5} dissolved in MeOH. In both cell lines, no significant difference was observed for MC-RF_{D5} dissolved in either DMSO or MeOH, see **Table 6**. For all congeners tested, no transport was measured in the control cells (HEK293-CV), see **Supplementary Figure 6**.

Table 6: Summary of EC_{50} Values of Transposed Microcystin Pairs

Summarized are the EC_{50} values obtained in **Figure 28** OATP1B1- and OATP1B3- expressing cells. Statistical analyses were performed using one-way ANOVA followed by Tukey's multiple comparison post-test (p<0.0001); n.d.= not defined, ns = not significant.

Congener Pairs	HEK293-OATP1B1			HEK293-OATP1B3		
	EC_{50} [nM]	Statistics		EC_{50} [nM]	Statistics	
MC-YR vs. MC-RY	115.2 vs. 580.6	****	<0.0001	12.10 vs. 5.890	ns	0.9191
MC-YR vs. MC-HtYR	115.2 vs. 41.10	****	<0.0001	12.10 vs. 16.08	ns	0.9726
MC-RY vs. MC-HtYR	619.1 vs. 41.10	****	<0.0001	5.890 vs. 16.08	ns	0.3105
MC-F_{D5}R (DMSO) vs. MC-RF_{D5} (DMSO)	50.78 vs. 230.0	****	<0.0001	51.31 vs. 4.920	****	<0.0001
MC-F_{D5}R (DMSO) vs. MC-RF_{D5} (MeOH)	50.78 vs. 177.1	****	<0.0001	51.31 vs. 3.833	****	<0.0001
MC-RF_{D5} (DMSO) vs. MC-RF_{D5} (MeOH)	230.0 vs. 177.1	ns	0.0706	4.920 vs. 3.833	ns	>0.9999
MC-LR vs. MC-RR	n.d.	n.d.	n.d.	15.99 vs. 52.97	****	<0.0001
MC-LR vs. MC-KL_{D7}	16.78 vs. 141.5	****	<0.0001	15.99 vs. 23.27	ns	0.7770
MC-RR vs. MC-KL_{D7}	n.d.	n.d.	n.d.	52.97 vs. 23.27	****	<0.0001

Interestingly, MC-F_{D5}R showed similar EC_{50} values in OATP1B1- and OATP1B3-expressing cells (50.78 nM and 51.21 nM, respectively). However, while transposition of the arginine residue from position (4) to position (2) resulted in decreased cytotoxicity (177.1 nM in MeOH, 230.0 nM in DMSO) in OATP1B1-expressing cells, cytotoxicity in OATP1B3-expressing cells dramatically increased by approximately 10-fold (3.833 nM in MeOH, 4.920 nM in DMSO). Hence, a bulky, albeit hydrophobic, phenylalanine residue at position (2) significantly impaired OATP1B3-mediated uptake, whereas an arginine residue at position (2) was beneficial. While an arginine residue at position (2) significantly impaired microcystin uptake in OATP1B1-expressing cells.

Toxicokinetic vs. Toxicodynamic Properties

The aim of this study was to contextualize the toxicodynamic *in vitro* PPP dataset by providing toxicokinetic parameters in biologically relevant systems, a direct comparison of the obtained EC_{50} with the published IC_{50} data was indispensable, see **Figure 29**. As the essential role of Adda was clarified in Chapter I, only naturally occurring microcystins are shown for clarity, but a detailed comparison of all congeners, including synthetic ones, is provided in **Supplementary Figure 7**. Interestingly, while a distinct pattern according to the hydrophobicity can be observed for the EC_{50} values for both, OATP1B1 and OATP1B3, no trend was apparent for the IC_{50} values obtained in rPPP1, hPPP2A or hPPP5. A gradual increase in cytotoxicity was measured with increasing hydrophobicity in HEK293-OATP1B1 and -OATP1B3, as highlighted in **Figure 29 A**, but the corresponding IC_{50} values remained in similar concentration ranges (0.3-2 nM), see **Figure 29 B**. Solely [ß-D-Asp^3, Dhb^7]MC-RR showed a drastic reduction in toxicity, e.g., PPP inhibition capability.

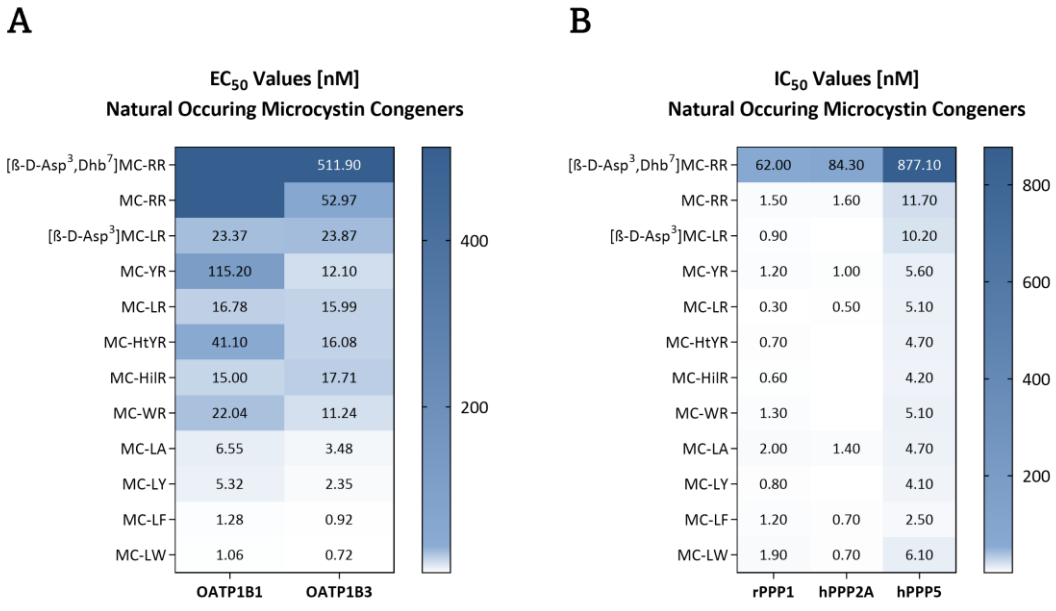

Figure 29: Toxicokinetics vs. Toxicodynamics

Visualized is the comparison of **(A)** EC_{50} values measured in OATP1B1- and OATP1B3-expressing HEK293 cells and **(B)** IC_{50} values determined for rPPP1, hPPP2A and hPPP5 after the exposure to 12 naturally occurring microcystin congeners. IC_{50} values were obtained from Altaner et al. (2020). Empty boxes (hPPP2A) indicate missing data due to product discontinuation.

3.1.3. Discussion

Microcystins are chemically stable and highly potent hepatotoxins. Due to their wide distribution and high toxicity, microcystins are among the most frequently detected cyanotoxins (Svirčev et al., 2019), associated with drinking water or food contamination and have caused morbidity and mortality in humans (Arman & Clarke, 2021; McLellan & Manderville, 2017). All microcystins share a common consensus structure as cyclic heptapeptides, consisting of five unusual D-amino acids including a unique Adda side chain, and two variable L-amino acids. The hypervariable positions (2) and (4) and smaller alterations, such as (de)methylations, provide for currently over 250 microcystin congeners (Spoof & Catherine, 2016), albeit toxicity is known for only few.

Microcystin toxicity has primarily been assessed and characterized by its ability to inhibit serine/threonine phosphoprotein phosphatases (PPPs) (MacKintosh et al., 1990; MacKintosh et al., 1995). Due to its unique Adda side chain, microcystins display a high affinity for the hydrophobic groove of the PPP catalytic subunit. This non-covalent but highly hydrophobic interaction allows the correct positioning of the toxin to form a covalent bond between the α,β-unsaturated carbonyl group of the Mdha residue and the cysteine moiety of the PPP active site (Craig et al., 1996; Goldberg et al., 1995). While the formation of the covalent bond was shown to be accessory and not essential for PPP inhibition, the presence, length, and orientation of the hydrophobic Adda side chain were shown to be critical. Co-crystallization of PPP1 and PPP2A complexed with MC-LR further revealed that variable positions (2) and (4) do not contribute to a required or direct PPP interaction, suggesting that positions (2) and (4), although hypervariable, play a minor role in the microcystin-induced PPP inhibition mechanism (Craig et al., 1996; Fontanillo & Köhn, 2018; Goldberg et al., 1995; Pereira et al., 2013). Indeed, the *in vitro* determined inhibition capacities of naturally occurring microcystins, which differed mainly in the variable positions (2) and (4), were comparable in the lower nanomolar range (Altaner et al., 2020; Hoeger et al., 2007). In contrast, *in vivo* rodent studies showed distinct congener-specificity (Chernoff et al., 2020; Fischer et al., 2010; Sivonen & Jones, 1999), raising the question whether this discrepancy arises due to toxicodynamic or toxicokinetic parameters, since *in vivo* microcystin toxicity comprises both parameters. Due to their chemical structure, microcystins are rather hydrophilic and spatially large molecules and require OATP-mediated uptake to cross cell membranes. Thereby, OATP1B1 and OATP1B3 have been identified as the main transporters in hepatocytes (Fischer et al., 2005).

Although OATP1B1- and OATP1B3-mediated microcystin uptake has been reported to be congener-dependent (MC-LR, MC-RR, MC-LF, and MC-LW), the data presented here are unique in that they combine PPP inhibitory capacities (toxicodynamics) with OATP1B1- and OATP1B3-mediated uptake (toxicokinetics) in biologically relevant systems using 17 structurally different microcystin congeners. To study the basic principles of OATP-mediated uptake, the HEK293 expression system was used instead of highly complex hepatocytes. Although these would provide greater physiological relevance, but due to

immediate transporter retention (Jigorel et al., 2005) as well as high donor variation (Fischer et al., 2010), a more robust but simpler system was preferred. The clear advantage of HEK293 as an expression system was the absence of all influx and efflux transporters, thus ensuring the causality of OATP1B1- and OATP1B3-mediated uptake with the associated cytotoxicity. However, one of the prerequisites for such a study is a comparable expression of the transporters and equal baselines of all toxicodynamic parameters, including PPP activities and cellular GSH concentrations. Indeed, similarity of HEK293-OATP1B1, -OATP1B3 and -CV cells regarding their toxicodynamic parameters was clearly confirmed. Thereby, the GSH concentrations measured (1.9 mM, 1.8 mM, and 1.7 mM, respectively) were consistent with data found in the literature (Forman et al., 2009; Meister, 1988). Thus, differences in the conjugation capacities of the cell lines were excluded. Nevertheless, microcystin-conjugation to GSH was shown to be congener-dependent (Buratti et al., 2011; Buratti & Testai, 2015; Santori et al., 2020). Although the toxicities of microcystin conjugates (MC-GSH, MC-Cys) remain unclear, conjugation as a possible detoxification mechanism must be considered when comparing toxicokinetic and toxicodynamic parameters. *Short insertion:* Microcystin-induced GSH response will be discussed in detail in Chapter III.

More substantially, the overall PPP activities were similar in all three cell lines. As the PPP activity assay does not correspond to specific PPP members, proteomic analyses were performed to quantify the expression levels of PPPs to contextualize the *in vitro* PPP toxicodynamic dataset with PPP found in HEK293. Interestingly, PPP2A was identified as the most abundant expressed PPP (54.7 % of all serine/threonine phosphatases), followed by PPP1 (29.6 %) and lower expression levels of PPP4, PPP5 and PPP6 (4.1 %, 4.3 %, and 5.9 %, respectively). These results are consistent with their essential functions in the regulation of the cell cycle and cell survival (Shi, 2009). PPP1 and PPP2A are known to be the most essential phosphatases, accounting for more than 90 % of protein dephosphorylation in eukaryotic cells (Bollen et al., 2010). It is not surprising that no PPP7, whose expression is highly restricted to the retina, and very low levels of PPP2B (1.1 %), which is ubiquitously expressed, but at significantly higher levels in neuronal tissues, were detected (Brautigan, 2013; Cohen, 2004; Shi, 2009).

As the OATP-expressing HEK293 cells were generated by the transfection of OATP cDNAs into the pcDNA3.1(+) expression vector and were thus under the control of the same promoter (cytomegaly virus), it is reasonable to assume that the HEK293 cells stably expressed comparable levels of recombinant human OATP1B1 and OATP1B3 transporters (Fischer et al., 2010; König et al., 2000a, 2000b). This assumption was qualitatively supported by immunocytochemistry and western blot analysis, confirming the exclusive expression of each transporter, as well as comparable levels of expression. These results are supported by previously described data using the same cell lines (Fischer et al., 2010). Hence, differences in the measured congener-specific cytotoxicity can be assumed to be a result of OATP1B1- or OATP1B3-mediated transport properties, and not due to any differences in the expression levels of PPPs or OATPs.

In this study, microcystin-induced toxicity was defined as the combination of efficient OATP-mediated uptake and subsequent cellular PPP inhibition, resulting in decreased cell viability (cytotoxicity).

The most striking difference was observed for both MC-RR congeners. While OATP1B1-expressing cells failed to transport either MC-RR or [ß-D-Asp^3, Dhb^7]MC-RR, OATP1B3-expressing cells were able to transport both, albeit with the lowest affinities, as indicated by the highest EC_{50} values (52.97 nM and 511.9 nM, respectively). Based on similar findings describing congener-selective transport in OATP1B1 and OATP1B3 (Fischer et al., 2010), it was hypothesized that OATP-mediated microcystin uptake is congener-specific due to selective hydrophobic features. Therefore, the EC_{50} values obtained were sorted according to their hydrophobicity (LogP values). Indeed, a correlation between increasing hydrophobicity and increasing toxicity was observed. Both transporters preferentially transported hydrophobic over hydrophilic microcystins. Thereby, revealing that the microcystins used could be clustered into distinct groups: less toxic, moderately toxic, and very toxic. While highly hydrophilic microcystin congeners [ß-D-Asp^3, Dhb^7]MC-RR and MC-RR, showed low toxicity, highly hydrophobic congeners MC-LF and MC-LW showed the highest measured toxicities (1.28 nM and 1.06 nM in OATP1B1- and 0.92 nM and 0.72 nM in OATP1B3-expressing cells, respectively). Comparing the most hydrophilic congener [ß-D-Asp^3, Dhb^7]MC-RR with the most hydrophobic congener MC-LW in OATP1B3-expressing cells, a dramatic 700-fold difference in toxicity was observed, underlining the congener-specific toxicity. Interestingly, the most commonly detected and still proposed to be the most toxic congener, MC-LR (Arman & Clarke, 2021; McLellan & Manderville, 2017), showed only moderate toxicity in both OATP1B1- and OATP1B3-expressing cells (16.78 nM and 15.99 nM, respectively). Compared to the more hydrophobic congeners, MC-LF and MC-LW, MC-LR showed an approximately 20-fold decrease in toxicity. These results were consistent with previously described results, revealing MC-LF and MC-LW as significantly more toxic in HEK293 expression systems as well as in primary human hepatocytes (Fischer et al., 2010).

Although the general congener-specific OATP-mediated uptake could be clearly explained, distinct differences were found when analyzing and comparing OATP1B1- and OATP1B3-mediated transport. While OATP1B3 showed sufficient transport of arginine-containing microcystins, OATP1B1 failed (MC-RR congeners) or showed impaired transport abilities (MC-YR, MC-HtyR, and MC-WR). This raised the question of whether hydrophobicity at position (2) defines OATP1B1-mediated transport. Therefore, pairs of microcystins with a highly hydrophobic and a highly hydrophilic amino acid residue located at the variable positions were used: MC-F_{D5}R and MC-RF_{D5}; MC-YR and MC-RY; MC-LR and MC-KL_{D7}. Direct comparison of these pairs had the advantage of similar overall hydrophobicity, as indicated by identical LogP values, while solely the role of the positions (2) and (4) could be determined. Noteworthy, synthetic derivates included deuterated atoms, which were assumed to have no impact on their chemical properties or LogP values (Prakash et al., 2022). Truly, highly hydrophilic residues at position (2), including MC-KL_{D7}, MC-RY and MC-RF_{D5}, showed significantly impaired OATP1B1-mediated uptake (141.5 nM, 580.6 nM, 177.1 nM in MeOH and 230.0 nM in DMSO, respectively). While the toxicity and thus OATP-mediated uptake affinity was restored when positions (2) and (4) were transposed to MC-LR, MC-YR, MC-F_{D5}R (16.78 nM, 12.10 nM, and 51.31 nM, respectively). Transposition from position (2) to position (4) could

increase OATP1B1-mediated uptake by up to 50-fold. In contrast, hydrophobic arginine residues at position (2) showed to be beneficial in OATP1B3-expressing cells, as indicated by decreased EC_{50} values in MC-RY (5.89 nM) and MC-RF_{D5} (4.92 nM in MeOH and 3.833 nM in DMSO) compared to MC-YR and MC-F_{D5}R (12.10 nM and 51.31 nM, respectively). Although no statistical significance was calculated for MC-YR/MC-RY, transposition of the arginine residue to position (2) induced a 2-fold increase in toxicity, whereas transposition of the arginine residue to position (2) in MC-RF_{D5}/MC-F_{D5}R resulted in a 10-fold increase in toxicity. Indeed, studies using OATP1B1- or OATP1B3- transfected cancer cell lines (HeLa and RKO) have demonstrated similar findings. They not only demonstrated a 150-fold range in transporter selectivity, but also showed that the amino acids at positions (2) and (4) appeared to be important for the potency and selectivity of the transporters. They concluded that the presence of arginine residues at position (2) reduced the observed cytotoxicity in OATP1B1-expressing cells. While a slightly more aromatic amino acid, such as tyrosine, homotyrosine or as presented in this study phenylalanine at position (4) in addition to arginine at position (2) seemed to be beneficial for OATP1B3-expressing cells (Niedermeyer et al., 2014).

Despite the common OATP consensus sequence, OATP1B1 and OATP1B3 share 80 % amino acid sequence homology (König et al., 2000a, 2000b). However, the two transporters differ in their molecular weight and size (OATP1B1 = 84 kDa and OATP1B3 = 120 kDa), which may result in differences in the folding structures and pore sizes. Therefore, OATP1B3 transporters may be more tolerant to the cationic nature of arginine residues, whereas OATP1B1 may be more sensitive. As the OATP-mediated transport mechanism is not fully understood, differences in the transport properties of OATP1B1 and OATP1B3 cannot be excluded, as demonstrated in previous studies using OATP1B1- and OATP1B3-expressing HEK293 cells. Coincubation of bromosulfophthalein (BSP) with MC-LR was shown to inhibit MC-LR uptake by OATP1B1, while no comparable substrate competition was observed for OATP1B3 (Fischer et al., 2010). Indeed, it has been reported that specific amino acids in the transmembrane domains 2, 6, 8, 9, and 10 and extracellular loop 6 are critical for the transport function of both transporters. Accordingly, changes within specific amino acid residues in the corresponding transmembrane domain or extracellular loop result in variations in substrate-specific transport (Alam et al., 2018; Hagenbuch & Meier, 2004). Differences in the transport properties were also observed by studying the kinetic properties, using Xenopus oocytes as an expression system and MC-LR. Although quite related K_m values were determined for OATP1B1 (7 ± 3 µM) and OATP1B3 (9 ± 3 µM), both transporters differed in their maximal microcystin uptake capacity (V_{max}). The OATP1B3 transporter was observed to transport MC-LR with an approximately 4-fold higher capacity than OATP1B1 (Fischer et al., 2005). Whether this is also true for OATP1B1 and OATP1B3 transporters expressed in HEK293 cells, remains to be determined.

This study aimed to contextualize toxicodynamic parameters of the *in vitro* PPP dataset (Altaner et al., 2020) by providing toxicokinetic parameters in biologically relevant systems. Speaking of toxicokinetic parameters in this context indicates OATP-mediated uptake with subsequent cellular PPP

inhibition, resulting in cytotoxicity. Therefore, an exclusive dataset of OATP-mediated uptake alone could not be provided. Furthermore, it is important to note that OATP-mediated transport is theorized to be bidirectional. This aspect of transport was not considered and determined in this study. Due to the chemical gradient and the lack of efflux transporters, influx was assumed to be highly preferential. Nevertheless, the comparison of the EC_{50} dataset obtained in this study with the IC_{50} dataset obtained in the *in vitro* PPP study (Altaner et al., 2020) not only identified the role of the variable positions, but also explained the congener-specific toxicity. While both transporters clearly showed congener-dependent toxicity, the most abundantly expressed phosphatases, PPP1 and PPP2A, did not show similar effect. Solely [ß-D-Asp^3, Dhb^7]MC-RR showed a drastic reduction in toxicity, e.g., PPP inhibition capability. Therefore, congener-specific toxicity is assumed to be rather due to OATP-mediated transport than to PPP inhibition.

Conclusion

In this study, the so far underestimated roles of the hypervariable positions (2) and (4) in the microcystin-induced toxicity mechanism were explained by combining both toxicodynamic and toxicokinetic parameters. While the hydrophobic Adda side chain was clearly shown to be essential for microcystin's mode of action in inhibiting PPPs, the formation of the covalent bond between the Mdha group and the cysteine residue of the PPPs was shown to play only a minor role, albeit inducing irreversibility. While the variable positions (2) and (4) were shown to be negligible in the PPP-mechanism, this study identified their importance in the OATP-mediated microcystin uptake, see **Figure 30**.

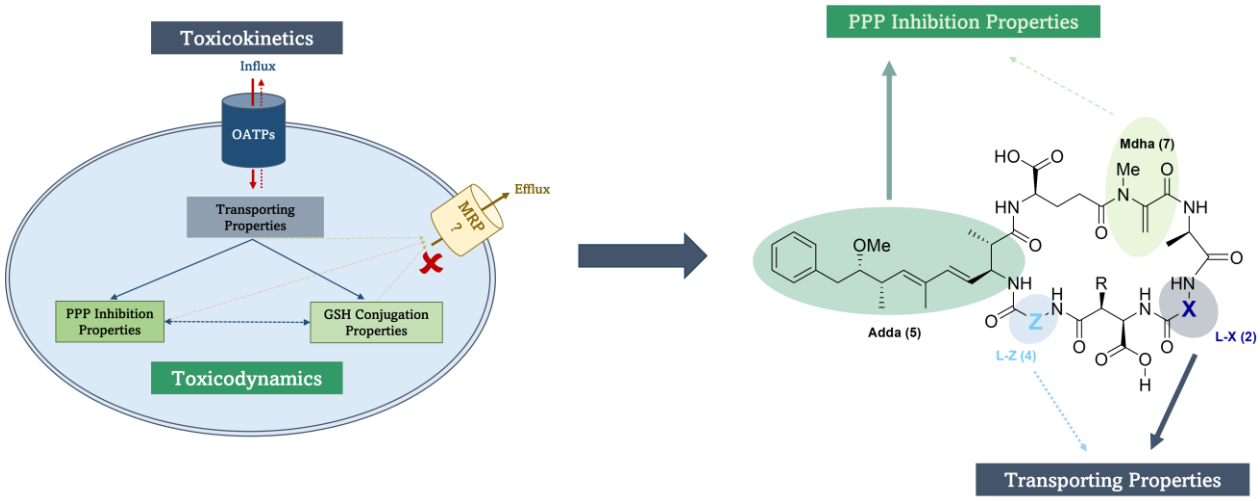

Figure 30: Role of Microcystin Positions in the Toxicity Mechanism

While the hydrophobic Adda side chain is primarily responsible for the PPP inhibition properties (green), the formation of the covalent bond (Mdha) is not required but induces the irreversibility of the inhibition. The hypervariable positions (2) and (4) define the OATP-mediated transporting properties (blue). Thereby, position (2) appears to be more essential than position (4). The importance of the individual position is marked in a darker color and indicated by the strength of the arrows.

Positions (2) and (4) determine the total hydrophobicity of the microcystin molecule, thereby defining its OATP-mediated uptake. In this study, a clear correlation between the total hydrophobicity and OATP-mediated uptake was demonstrated. According to their hydrophobicity, microcystins were classified into three groups: less toxic, moderately toxic, and very toxic, see **Figure 31**. Furthermore, the essential role of position (2) was identified. Highly hydrophilic arginine residues at position (2) were shown to impair OATP1B1-mediated microcystin uptake, but not OATP1B3-mediated uptake. Impaired transmembrane transport could be restored by transposition of the arginine residue from position (2) to (4).

Combining the *in vitro* PPP toxicodynamic dataset with the toxicokinetic data obtained in this study, the influence of transporters on microcystin toxicity appears to be much greater than the congener-specific inhibitory effects of PPPs. Therefore, it can be concluded that the congener-specific toxicity observed in *in vivo* rodent studies is due to OATP-mediated specific transport rather than PPP inhibition.

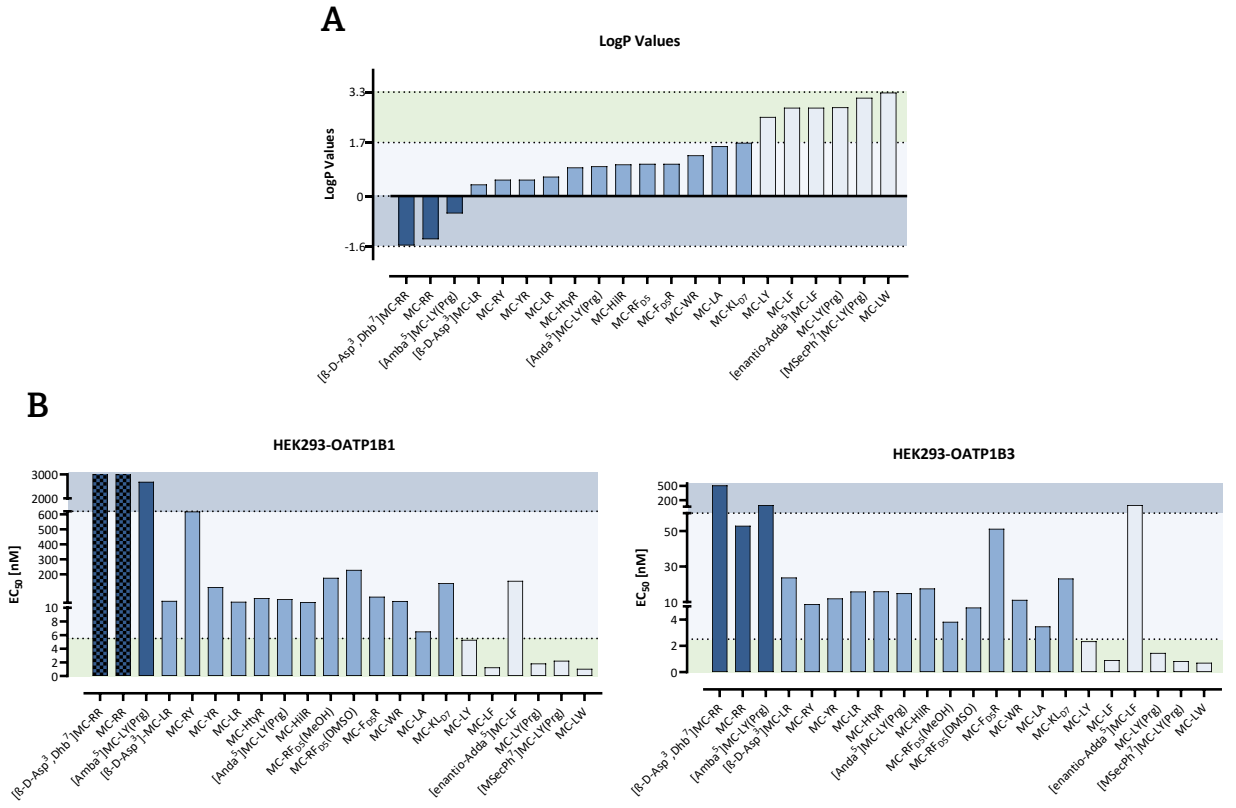

Figure 31: Correlation of Microcystin Hydrophobicity and Induced Toxicity

Shown are the correlations of **(A)** the *in silico* calculated LogP values and **(B)** measured EC_{50} values in OATP1B1- and OATP1B3-expressing cells after the exposure to all 21 microcystin congeners. The dark blue bars indicate hydrophilic congeners, whereas the white bars indicate hydrophobic congeners. Green background highlights the highly toxic microcystin congeners, while darker background indicates less toxic microcystins. The dotted bars indicate no transport.

4. Chapter III

4.1. Role of Glutathione in the Microcystin Toxicity Mechanism

4.1.1. Introduction

Cyanobacteria, a group of photosynthetic bacteria commonly found in aquatic environments, produce a variety of bioactive metabolites, including toxins. These cyanobacterial toxins comprise a wide range of structurally diverse and highly potent toxins that pose a threat not only to the environment, but also to animal and human health (Arman & Clarke, 2021; McLellan & Manderville, 2017). Cyanobacterial toxins are classified according to their target organs and mode of action. One of the most commonly detected and reported cyanotoxins worldwide are microcystins (Svirčev et al., 2019). Microcystins are classified as hepatotoxins and highly potent inhibitors of serine/threonine phosphoprotein phosphatases (PPPs) (MacKintosh et al., 1990; MacKintosh et al., 1995).

Microcystins are chemically stable and complex cyclic heptapeptides with a conserved consensus structure, including D-alanine at position (1), two variable L-amino acids at positions (2) and (4), ß-D-methylaspartate at position (3), D-glutamine at position (6), D-methyldehydroalanine (Mdha) at position (7), and a unique hydrophobic amino acid Adda (3-amino-9-methoxy-10-phenyl-2,6,8-trimethyl-deca-4(E),6(E)-dienoic acid) at position (5). Thus, specific functions can be assigned to distinct residues and positions. Despite the increasing variability resulting in over 250 microcystin congeners (Spoof & Catherine, 2016), the hypervariable positions (2) and (4) have been shown to define cellular uptake mediated by organic anion transporting polypeptides (OATPs), see Chapter II. Whereas the unique Adda side chain at position (5) has been shown to be essential for its toxicity, see Chapter I. Due to the hydrophobic Adda side chain, microcystins have been shown to display a high affinity for the hydrophobic groove of the PPP catalytic center (Goldberg et al., 1995; MacKintosh et al., 1990; MacKintosh et al., 1995). This non-covalent but highly hydrophobic interaction, albeit short-lived, has been shown to be sufficient for PPP inhibition (Craig et al., 1996; Pereira et al., 2013) and its presence, length, and orientation have been shown to be critical. At the same time, this hydrophobic interaction allows the correct positioning of the toxin in the catalytic center to form a covalent bond between the α,β-unsaturated carbonyl group of the Mdha residue at position (7) and the cysteine moiety of the PPP active site. Although the formation of the covalent bond is considered to be accessory in the context of PPP inhibition, it has been hypothesized to be associated with the elusive biological function of microcystins, allowing the conjugation to glutathione (Pereira et al., 2013).

Glutathione (GSH) is one of the most important antioxidants synthesized in cells and is a common peptide used in the phase II biotransformation in the cellular detoxification system. The tripeptide, consisting of glutamate, cysteine, and glycine, contains an unusual γ-peptide bond between glutamate and cysteine, which contributes to the protein stability and prevents it from being hydrolyzed by most peptidases (Anderson, 1998). The formation of GSH conjugates is thereby catalyzed by glutathione-S-transferase (GST) and increases the water solubility and thus the excretion of xenobiotics and toxins. Due

to its key function in detoxification and scavenging reactive oxygen species (ROS), GSH is found in high cellular concentrations ranging from 1-2 mM in the cytosol but can reach up to 10 mM in hepatocytes (Forman et al., 2009; Meister, 1988). To maintain this high concentration and thus allow for a rapid response after intoxication, GSH is not synthesized ribosomally but intracellularly via two ATP-dependent enzymatic steps, see **Figure 32**. In the first step, γ-glutamyl-cysteine ligase (GCL) catalyzes the formation of γ-glutamyl-cysteine. Thereby, the GCL activity is highly regulated by a non-allosteric feedback mechanism induced by high cellular GSH concentrations and cytosolic cysteine availability. In the second step, the addition of glycine is catalyzed by glutathione synthetase (GSS). GSS is not feedback inhibited, and since the product of GCL is present at low concentrations in the presence of GSS, only the first step of the GSH synthesis pathway is considered to be rate-limiting (Anderson, 1998; Forman et al., 2009; Lu, 2013).

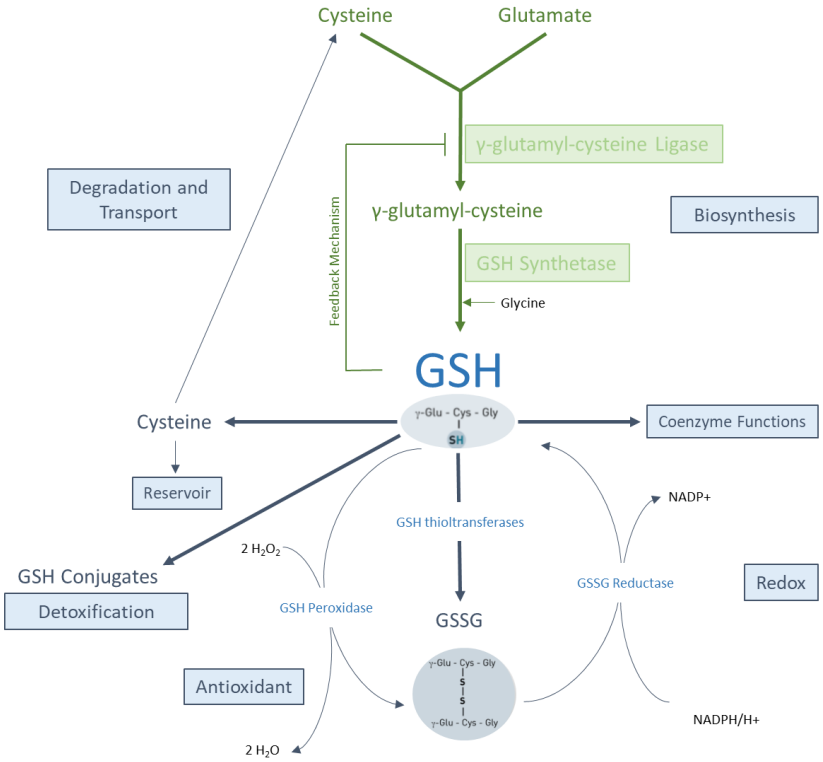

Figure 32: Glutathione Synthesis Pathway

The tripeptide glutathione (GSH) synthesis pathway is highlighted in green and includes the rate-limiting enzyme γ-glutamyl-cysteine ligase (GCL) and GSH synthetase. Besides detoxification of xenobiotics and toxins, cellular functions of GSH include coenzyme functions, reduction-oxidation (redox) reactions, antioxidant functions, and cysteine reservoir are highlighted in blue.

Similar to the covalent bond formation in the mechanism of PPP inhibition, the conjugation of GSH to microcystins is thought to be a Michael-type addition reaction of the nucleophilic sulfur atom of the cysteine moiety to the α,β-unsaturated carbonyl group of the Mdha residue. GSH conjugation to microcystins occurs either spontaneously at alkaline pH or enzymatically catalyzed via GST (Kondo et al., 1992). Thereby, GSH conjugation to microcystins has been reported for several species, including humans, although only at very low concentrations (Buratti & Testai, 2015; Kondo et al., 1992). Recent studies have

characterized GSH conjugation in human systems using recombinant GST and liver cytosol. Similar to OATPs, a congener selectivity for GST and microcystins has been reported (Buratti & Testai, 2015; Santori et al., 2020). The conjugation reaction is thereby a two-step process. In the first step, the thiol group of the cysteine residue nucleophilically attacks the α,β-unsaturated carbonyl group of the Mdha residue, resulting in the first conjugate MC-GSH. In the second step, glutamic acid is cleaved by γ-glutamyltransferase to form the intermediate microcystin-cysteine-glycine (MC-Cys-Gly), whereby the glycine residue is rapidly cleaved by dipeptidases to yield the second stable conjugate MC-Cys (Schmidt et al., 2014).

Microcystins are excreted primarily as the parent compound via urine and feces, although several studies have shown that only a small percentage of the administered dose is excreted from the body. ADME studies performed in mice showed that only 24 % of the injected microcystin dose was excreted through urine (9 %) and feces (15 %). Of these, 60 % of the excreted microcystins were present as parent compounds (Robinson et al., 1991). Since the amount of microcystin conjugates excreted is very low, the actual function of GSH conjugation to microcystins remains unclear. Moreover, the role of glutathione conjugation to microcystins in 'detoxification' is still highly controversial, as there are no valid data on MC-GSH or MC-Cys toxicities. Similarly, cellular elimination via efflux transporters is not yet fully understood. Recent studies have demonstrated microcystin-mediated export via multidrug resistance associated protein 2 (MRP2) transporters, albeit only for unbound microcystins and not for their conjugates (Kaur et al., 2019).

Aim of the Study

Although the inhibitory capacities of microcystins have been well studied, the role of glutathione conjugation in the microcystin toxicity pathway and its potential role in the detoxification have not been determined. Therefore, this study aimed to clarify the function of GSH conjugation in the mechanism of microcystin toxicity in biologically relevant systems, including toxicodynamic and toxicokinetic parameters, see **Figure 33**. To increase the analytical throughput and allow one-to-one comparison, simultaneous evaluation of phosphatase activity and glutathione response were established, allowing direct comparison of all parameters. To determine its role in microcystin detoxification, cellular glutathione levels were depleted using buthionine sulfoximine (BSO) as GCL inhibitor, see **Figure 33**. Subsequent toxicities were first determined and analyzed in simplified cellular systems (HEK293-OATP1B1 and HEK293-OATP1B3), which lack efflux transporters and thus allow the determination of potentially enhanced PPP inhibition capacities during GSH depletion, followed by physiologically more relevant and complex hepatocytes.

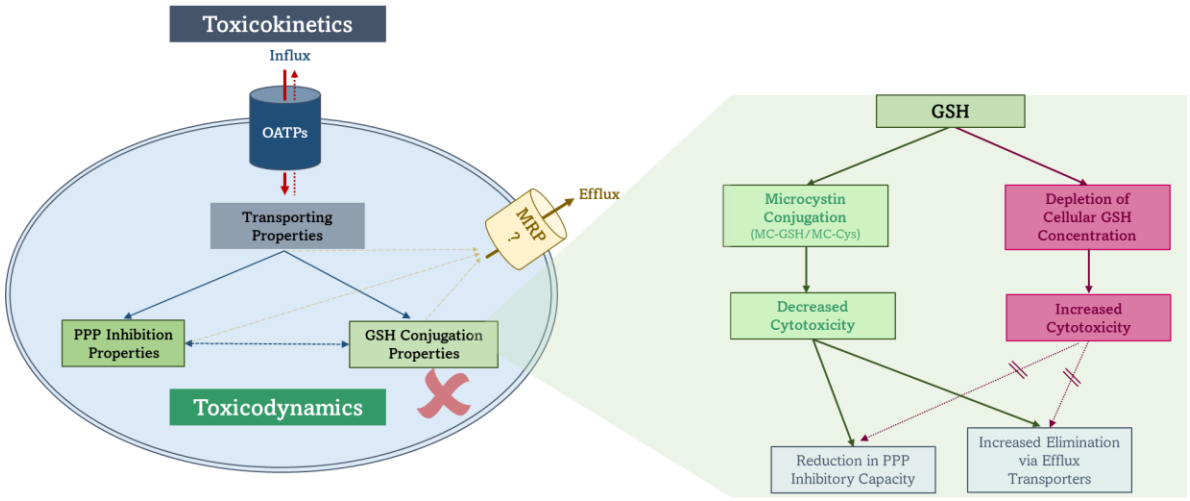

Figure 33: Chapter III Graphical Abstract

The toxicokinetic parameters of microcystins are highlighted in blue and include active uptake via organic anion transporting polypeptides (OATPs). While the cellular toxicodynamic parameters are highlighted in green, including serine/threonine phosphoprotein phosphatase (PPP) inhibition and glutathione (GSH) conjugation properties. Conjugation to GSH is theorized to reduce microcystin toxicity due to decreased PPP inhibition capacity and increased efflux transport. Therefore, in addition to OATP-expressing HEK293 cell lines lacking all efflux transporters, hepatocytes were used to study the impact of GSH in the mechanism of microcystin toxicity.

4.1.2. Results

Proof of Principle – Cell Viability, PPP Activity Assay and GSH Assay Operate Independently

To increase the analytical throughput and allow one-to-one comparison, simultaneous evaluation of cell viability, phosphatase activity and glutathione response was established, allowing direct comparison of all parameters. For multiplex establishment and assay validation OATP1B1- and OATP1B3 expressing HEK293 cells were used. Cell viability was assessed using the non-cytotoxic dye resazurin. Resazurin cell viability assay is a redox-based colorimetric assay that detects the mitochondrial metabolic activity of viable cells. The blue dye resazurin crosses the cell membrane and is reduced intracellularly to resorufin in the presence of $NADH/H^+$. This redox reaction can be quantified photometrically by monitoring absorbance at 570 nm (resazurin) and 600 nm (resorufin). Subsequently, the cells were lysed, and the cell lysates were used to determine PPP activities and cellular GSH concentrations. Since the PPP and GSH assays were performed simultaneously in the same lysate, cross-reactions had to be excluded and the independence of both assays had to be demonstrated.

Therefore, HEK293 cells were exposed to serial dilutions of buthionine sulfoximine (BSO) to deplete cellular GSH content. BSO inhibits GCL, and therefore the first and rate-limiting step in the GSH synthesis pathway. In theory, the measured cellular GSH concentrations were expected to gradually decrease with increasing BSO concentrations, whereas PPP activities were expected to remain unaffected, demonstrating the independence of the two assays. Indeed, BSO incubation resulted in a concentration-dependent decrease in cellular GSH content, while PPP activities remained fully functional (100 %), see Figure 34 A-B. Due to its key function in scavenging reactive oxygen species (ROS), BSO treatment was

performed for either 24 or 48 hours to ensure sufficient GSH depletion on the one hand and to monitor cellular viability on the other hand. Interestingly, the depletion of cellular GSH content did not reduce cell viability either for 24 or 48 hours incubation time, allowing efficient GSH depletion with simultaneous microcystin exposure for 48 hours. Surprisingly, the BSO concentration required to reduce GSH content by 50 % (EC_{50}) was similar for both incubation times and cell lines, see **Figure 34 C**. This raised the question of the actual protein stability and turnover rate of GSH.

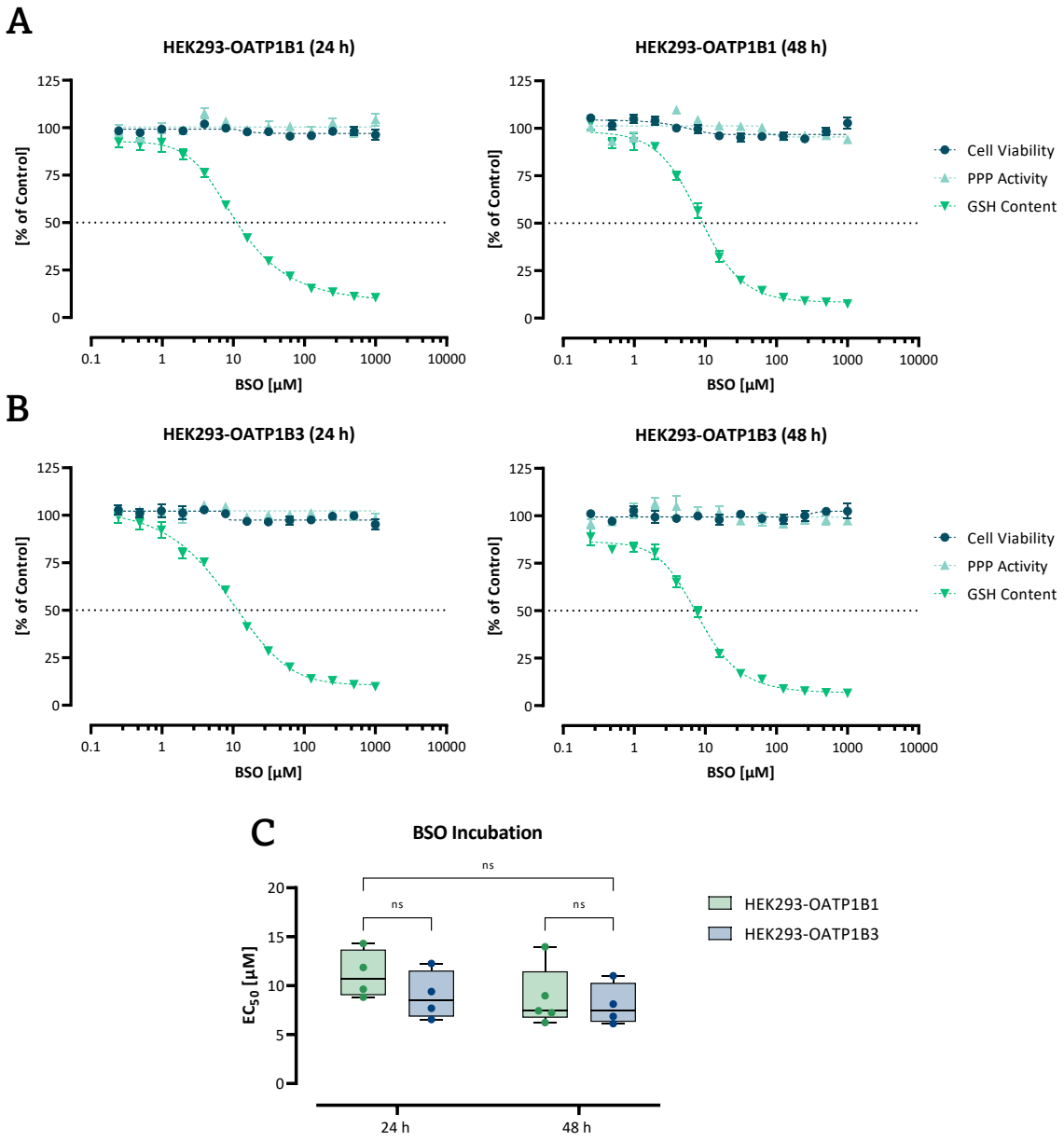

Figure 34: Validation of Multiplex Assays

Assay validation was performed using serial dilutions of buthionine sulfoximine (BSO) in **(A)** HEK293-OATP1B1 and **(B)** HEK293-OATP1B3 cells for either 24 or 48 hours. Cell viability, PPP activity and GSH content were evaluated and presented as percentages compared to the control. Each point represents the mean of 4 independent biological replicates pipetted in triplicates ± SEM (n=4). **(C)** Statistical analysis was performed for EC_{50} values using two-way ANOVA and followed by Tukey's multiple comparison post-test ($p<0.0001$); ns = not significant Each point represents an independent biological replicate.

Determination of Protein Stability and Half-Life of GSH

To ensure that all the remaining GSH proteins were completely degraded and no longer available for microcystin conjugation, the turnover rate and protein stability of GSH were determined using OATP1B1-expressing HEK293 cells. Therefore, cells were incubated with 125 µM BSO for either 1.5, 3, 6 or 10 hours before measuring GSH content, see Figure 35 A-B. Thereby, the time-dependent degradation of GSH was measured. After 1.5 hours, the cellular GSH content was already reduced to 72.6 %. With increasing time, the rate of degradation decreased, as evidenced by the fact that after 3 hours 62.4 % GSH remained and after a total of 6 hours, the cellular content was reduced to 55.2 %. As the degradation rate declined over time, it was assumed that the complete degradation of GSH would require more than 12 hours, even though the half-life ($t_{1/2}$) was approximately 6 hours. Therefore, all following experiments were performed with 24 hours preincubation of BSO prior to microcystin exposure and toxicity analyses.

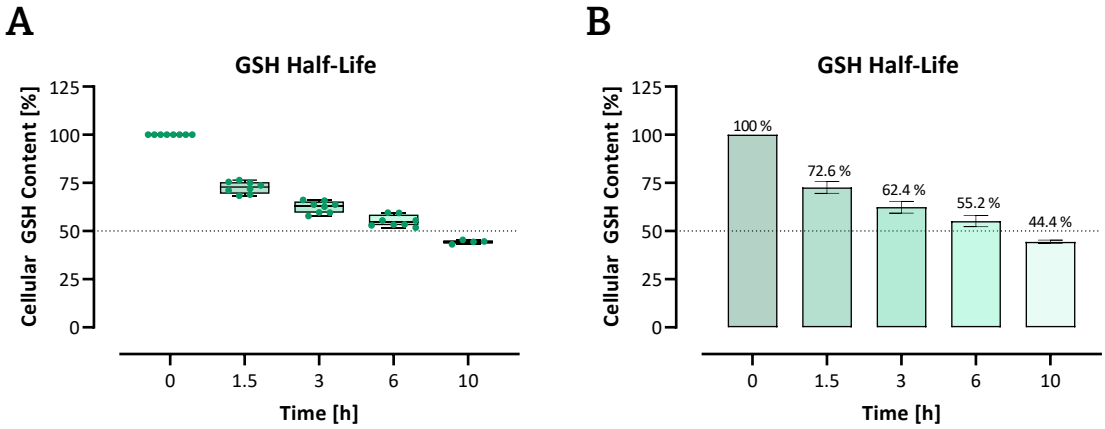

Figure 35: Glutathione Half-Life

Using OATP1B1-expressing cells, the degradation time of glutathione (GSH) was monitored after GSH depletion with BSO. Thereby, the protein half-life ($t_{1/2}$) was measured after approximately 6 hours. **(A)** Each point represents an independent biological replicate (n=8). **(B)** GSH degradation was visualized as bars and percentages, ± SD (n=8).

Impact of GSH in the Mechanism of Microcystin Toxicity

HEK293-OATP1B1 and -OATP1B3 cells were exposed to MC-LR, MC-F_{D5}R, and MC-RF_{D5}, and subsequently cell viabilities, PPP activities, and glutathione response were assessed. Additionally, the cellular GSH content was depleted prior to co-incubating with the corresponding microcystin congener, to elucidate the impact of GSH on microcystin toxicity. As already demonstrated in Chapter I and II, all three microcystin congeners induced a concentration-dependent decrease in cell viability. Likewise, PPP activities and GSH concentrations measured simultaneously, showed a similar response, see Figure 36. To efficiently compare microcystin effects in all parameters, the half-maximal effective concentrations (EC_{50}) were calculated using non-linear regression analysis. All calculated EC_{50} values and corresponding statistical analyses were summarized in Table 7. Surprisingly, GSH depletion followed by MC-LR cotreatment decreased cytotoxicity, as indicated by increased cell viability EC_{50} (39.36 nM and 55.88 nM,

respectively) in OATP1B1-expressing cells, while the corresponding PPP activities remained unaffected (28.15 nM and 20.56 nM, respectively), see **Figure 36 A**. Whereas no significant differences were observed in OATP1B3-expressing HEK293 cells exposed to MC-LR, for either cell viability or PPP activities, see **Figure 36 B**. Similar results were obtained for MC-RF_{D5}. While OATP1B1-expressing cells showed decreased cytotoxicities, as indicated in increased cell viability EC_{50} (230.0 nM and 434.8 nM, respectively), see **Figure 36 C**, OATP1B3-expressing cells showed no significant differences (4.920 nM and 4.648 nM, respectively), see **Figure 36 D**. Whereas exposure to MC-$F_{D5}R$ in both cell lines, OATP1B1- and OATP1B3-expressing cells, GSH depletion showed no significant effect on the measured cytotoxicity, neither in cell viability nor in PPP activities, see **Figure 36 E-F**.

Table 7: Summary of EC_{50} Values for HEK293 Cell Lines

EC_{50} values were calculated using asymmetric nonlinear regression. Statistical analyses were performed using two-way ANOVA, followed by Šídák post-test; ns = not significant. Analyses are visualized in **Figure 36**.

HEK293-OATP1B1												
Microcystin	Cell Viability						PPP Activities					
	No Depletion		GSH Depletion		Statistical Comparison		No Depletion		GSH Depletion		Statistical Comparison	
	EC_{50} [nM]	R^2	EC_{50} [nM]	R^2	Sign.	P-Value	EC_{50} [nM]	R^2	EC_{50} [nM]	R^2	Sign.	P-Value
MC-LR	39.36	0.9889	55.88	0.9806	*	0.0206	28.15	0.9915	20.56	0.9776	ns	0.1400
MC-$F_{D5}R$	53.96	0.9719	55.82	0.9834	ns	0.9944	40.79	0.9857	45.02	0.9716	ns	0.2949
MC-RF_{D5}	230.0	0.9624	434.8	0.9021	**	0.0017	139.0	0.9855	254.4	0.9488	ns	0.1883
HEK293-OATP1B3												
Microcystin	Cell Viability						PPP Activities					
	No Depletion		GSH Depletion		Statistical Comparison		No Depletion		GSH Depletion		Statistical Comparison	
	EC_{50} [nM]	R^2	EC_{50} [nM]	R^2	Sign.	P-Value	EC_{50} [nM]	R^2	EC_{50} [nM]	R^2	Sign.	P-Value
MC-LR	45.80	0.9899	41.80	0.9696	ns	0.9533	36.17	0.9948	25.22	0.9871	ns	0.1126
MC-$F_{D5}R$	52.05	0.9739	55.88	0.9834	ns	0.8915	30.98	0.9865	41.71	0.9813	ns	0.0666
MC-RF_{D5}	4.920	0.9812	4.648	0.9678	ns	0.8138	4.728	0.9940	4.915	0.9903	ns	>0.99

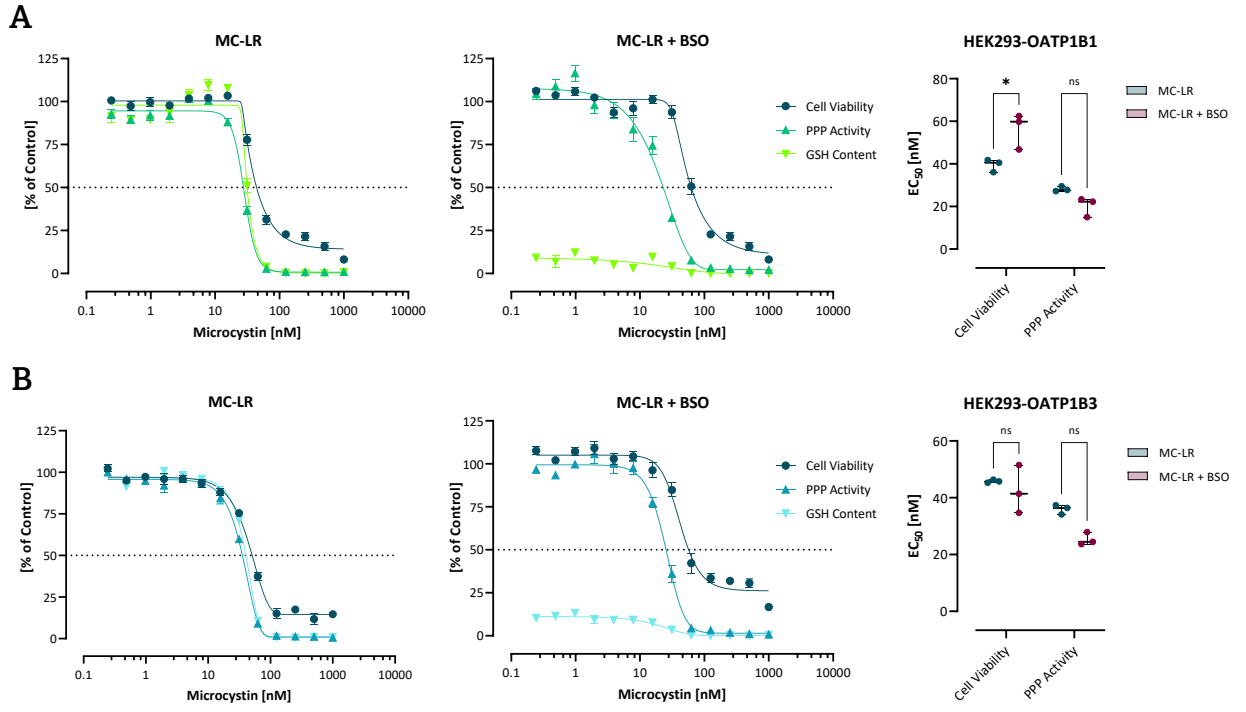

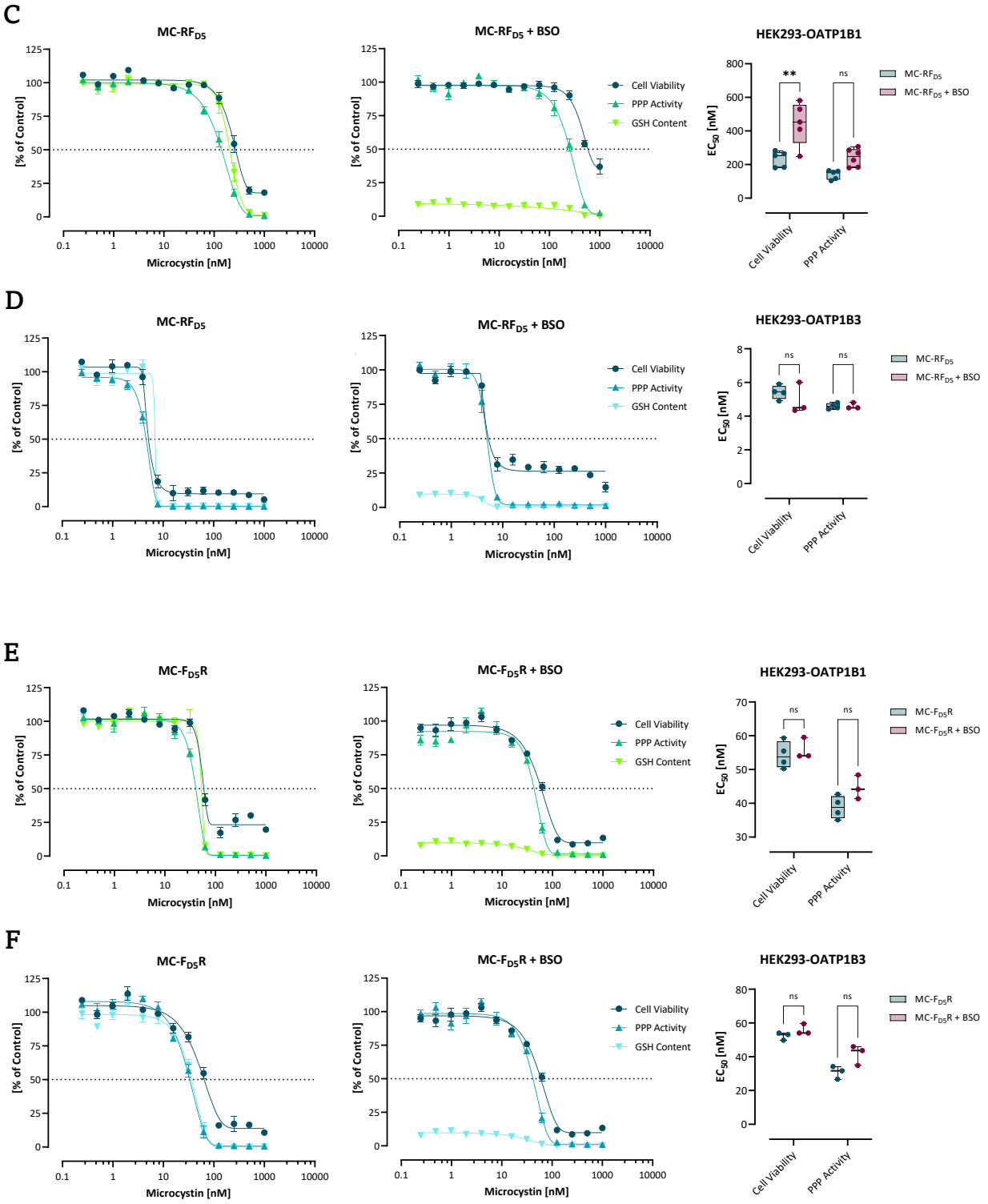

Figure 36: Impact of GSH Depletion on Microcystin Toxicity in HEK293 Cell Lines

Cell viability, PPP activity and GSH content were measured in OATP1B1- and OATP1B3-expressing cell lines exposed to **(A-B)** MC-LR, **(C-D)** MC-RF$_{D5}$, and **(E-F)** MC-F$_{D5}$R, with or without GSH depletion by BSO. Each point represents the mean of 3-5 independent biological replicates ± SEM (n=3-5). Statistical analyses were performed using two-way ANOVA, followed by Šídák post-test; ns = not significant. Only comparisons within cell line are visualized, p-values are summarized in **Table 7**.

Determination of the Effect of Glutathione on Microcystin Toxicity in Hepatocytes

Since microcystin toxicity was not affected when the total cellular GSH content was depleted, the question was raised whether this effect was due to the low GSH content of HEK293 cells. Therefore, more physiologically relevant cell lines were used, which differed significantly in their GSH content and their availability of efflux transporters (detailed expression pattern and cell line characterizations are provided in Chapter V). Due to high donor variations and immediate transporter retention of isolated primary hepatocytes, immortalized cell lines were preferred. Therefore, immortalized human hepatocytes (IHH) were used for further studies. And since the current microcystin risk assessment is entirely based on mice studies, the alpha mouse liver 12 (AML12) cell line was additionally used to determine possible differences between mouse and human responses. Indeed, IHH exhibited a cytosolic GSH concentration of 6 mM, significantly higher than HEK293-OATP1B1, -OATP1B3, and -CV cells (1.9 mM, 1.8 mM, and 1.7 mM, respectively), see **Figure 37 A.** Unfortunately, no cytosolic GSH concentration could be determined for AML12 cells, since AML12 cells are highly clumpy and difficult to dissociate. But to precisely calculate the individual cytosolic GSH concentrations, it is essential to separate each cell and measure the individual cell sizes.

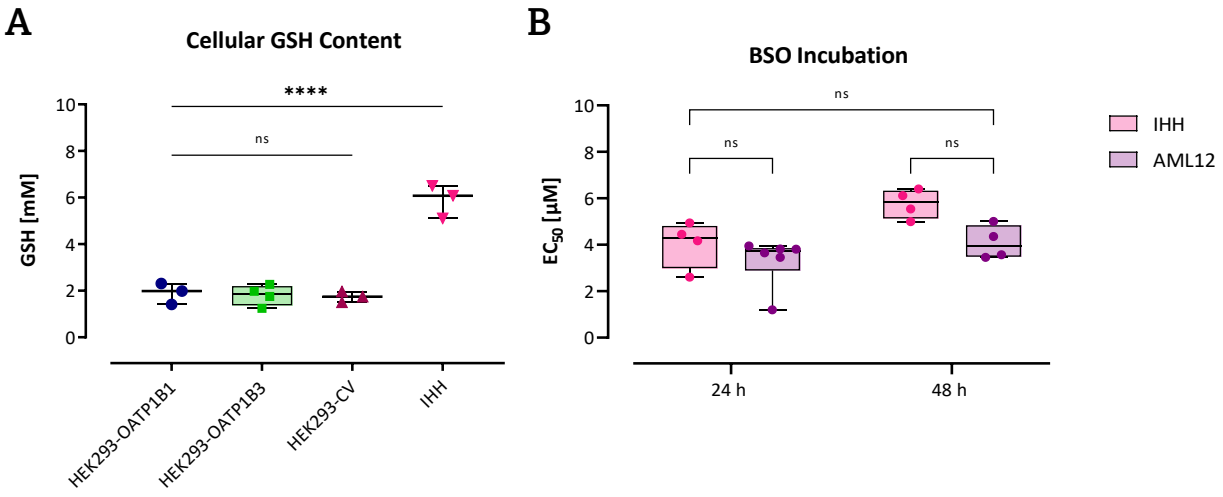

Figure 37: Cellular GSH Content of Cell Lines Used

(A) Cytosolic GSH concentrations were determined for HEK293-OATP1B1, HEK293-OATP1B3, HEK293-CV and IHH cell lines. Each point represents an independent biological replicate (n=3-4). Statistical analysis was performed using one-way ANOVA, followed by Tukey's multiple comparison post-test ($p<0.0001$). **(B)** BSO EC_{50} values measured in IHH and AML12 cells were statistically analyzed using two-way ANOVA followed by Tukey's multiple comparison post-test ($p<0.0001$). Each point represents an independent biological replicate (n=4-6).

To validate the assays and to determine an efficient but non-cytotoxic concentration of BSO for GSH depletion and toxicity testing, proof-of-principle studies similar to those shown in **Figure 34**, were performed in IHH and AML12 cells, see **Supplementary Figure 8**. Similar to the results obtained in HEK293 cells, BSO depleted GSH in a concentration-dependent manner, whereas PPP activities and cell viabilities were not affected. Comparing the BSO concentrations required to reduce cytosolic GSH levels to 50 %,

both hepatocyte cell lines, IHH and AML12, showed no significant differences either for 24 hours (4.0 µM and 3.3 µM, respectively) or 48 hours (5.8 µM and 4.1 µM, respectively) incubation time, see **Figure 37 B**. To efficiently compare microcystin effects in all parameters, the half-maximal effective concentrations (EC_{50}) were calculated using non-linear regression analysis. All calculated EC_{50} values and corresponding statistical analyses were summarized in **Table 8**. First, IHH cells were exposed to the most commonly and frequently detected MC-LR, see **Figure 38 A**. Similar to the OATP-expressing HEK293 cell lines, the exposed IHH cells showed a concentration-dependent decrease in cell viability, but at much higher concentrations (EC_{50} 16.57 µM). Similar toxicity responses were observed for the GSH content and PPP activity. Interestingly, GSH depletion with MC-LR co-treatment showed a slightly decreased cytotoxicity measured as cell viability (26.70 µM), but this was not statistically significant as the distribution of individual replicates was elevated. A similar effect was observed when IHH cells were exposed to MC-RR, see **Figure 38 B**. The highly hydrophilic congener MC-RR showed an overall lower cytotoxicity (39.59 µM) compared to MC-LR. Cytotoxicity was even lower when GSH was depleted (55.64 µM), but again no statistical significance was detected. In general, the observation that GSH depletion increased the replicate distribution was observed for all cell lines and microcystins used. Additionally, cytotoxicity appeared to be rather decreased when GSH was depleted, as evidenced by slightly increased EC_{50} values.

Table 8: Summary of EC50 Values for Hepatocyte Cell Lines

EC_{50} values were calculated using asymmetric nonlinear regression. Statistical analyses were performed using two-way ANOVA, followed by Šídák post-test; ns = not significant. Analyses are visualized in **Figure 38**.

IHH												
Microcystin	**Cell Viability**						**PPP Activities**					
	No Depletion		**GSH Depletion**		**Statistical Comparison**		**No Depletion**		**GSH Depletion**		**Statistical Comparison**	
	EC_{50} [µM]	**R^2**	**EC_{50} [µM]**	**R^2**	**Sign.**	**P-Value**	**EC_{50} [µM]**	**R^2**	**EC_{50} [µM]**	**R^2**	**Sign.**	**P-Value**
MC-LR	16.57	0.9515	26.70	0.9383	ns	0.3216	17.42	0.9705	21.66	0.9527	ns	0.9452
MC-RR	39.59	0.9352	55.64	0.9594	ns	0.5291	38.32	0.9596	36.67	0.9745	ns	0.5530
AML12												
Microcystin	**Cell Viability**						**PPP Activities**					
	No Depletion		**GSH Depletion**		**Statistical Comparison**		**No Depletion**		**GSH Depletion**		**Statistical Comparison**	
	EC_{50} [µM]	**R^2**	**EC_{50} [nM]**	**R^2**	**Sign.**	**P-Value**	**EC_{50} [µM]**	**R^2**	**EC_{50} [µM]**	**R^2**	**Sign.**	**P-Value**
MC-LR	54.45	0.9502	55.80	0.9653	ns	>0.99	45.11	0.9851	47.81	0.9834	ns	>0.99

In contrast, the mouse hepatocyte cell line AML12 showed highly different GSH responses after MC-LR exposure, compared to the results obtained for OATP-expressing HEK293 and IHH cells. While in the other cell lines used, microcystin exposure resulted in a well-fitted (R^2) sigmoidal shaped GSH response comparable to that obtained for cytotoxicity, the cytosolic GSH content showed a dramatic overshoot response, see **Figure 38 C**. With the onset of toxicity, the cytosolic GSH level increased up to 250 %. Interestingly, while BSO treatment successfully depleted cellular GSH content, as demonstrated in **Supplementary Figure 8**, albeit with lower efficiency compared to the other cell lines used, GSH depletion

followed by MC-LR co-treatment failed to deplete GSH. However, the overshoot response was reduced to 150 %. In contrast to the GSH response, PPP activities and cytotoxicities measured via cell viabilities showed well-fitted concentration-response curves.

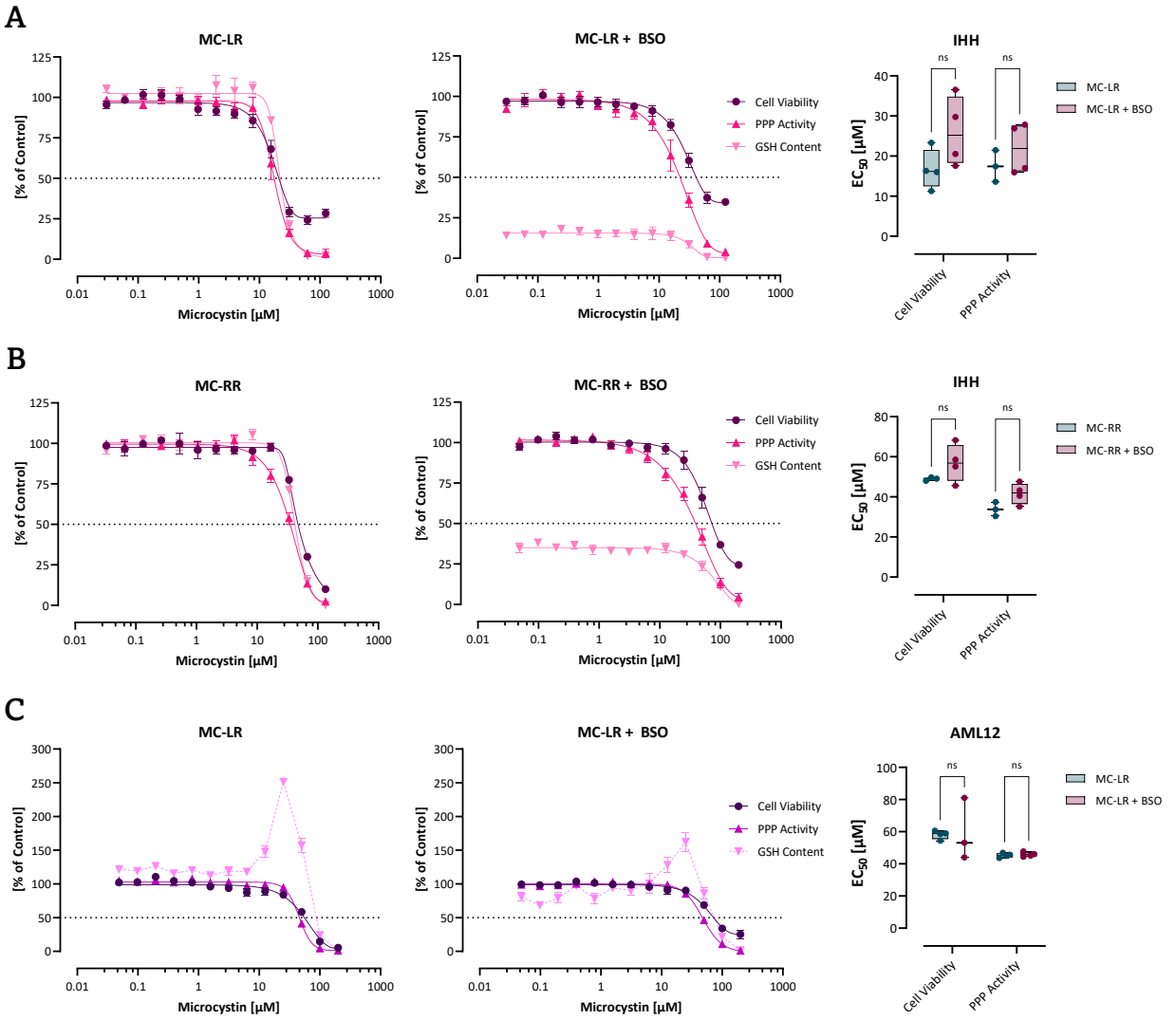

Figure 38: Impact of GSH Depletion on Microcystin Toxicity in Hepatocyte Cell Lines

Cell viability, PPP activity and GSH content were measured after exposure to MC-LR and MC-RR in **(A-B)** IHH and **(C)** AML12 cell lines, with and without GSH depletion by BSO. Each point represents the mean of 3-4 independent biological replicates ± SEM (n=3-4). Statistical analyses were performed using two-way ANOVA, followed by Šídák post-test; ns = not significant. Only comparisons within cell line are visualized, p-values are summarized in **Table 8**.

4.1.3. Discussion

GSH, a simple sulfur compound consisting of only three amino acids, but nonetheless one of the most important cellular peptides due to its function in protecting cells from oxidative damage as a reactive oxygen species (ROS) scavenger and antioxidant, while regulating the maintenance of cellular redox balance and its essential function in the cellular detoxification system. The formation of GSH conjugates catalyzed by the phase II enzyme glutathione-S-transferase (GST) increases the water solubility and thus, the excretion of xenobiotics and toxins (Forman et al., 2009). Accordingly, GSH is highly involved in the

toxicodynamics and -kinetics of various toxins. While the impact of GSH conjugation to microcystins and its potential detoxification function are not fully understood, the mode of action including its inhibitory capacity, has been studied well.

Microcystins are highly potent inhibitors of serine/threonine phosphoprotein phosphatases (PPPs), abolishing their function by binding and interacting with their catalytic subunit, thereby blocking access to their substrates (MacKintosh et al., 1990; MacKintosh et al., 1995). Owing to the hydrophobic Adda side chain, microcystins display a high affinity for the hydrophobic groove of the catalytic center. This non-covalent but highly hydrophobic interaction allows the correct positioning of the toxin to form a covalent bond between the unsaturated terminal carbonyl moiety of the Mdha group and the cysteine residue of the PPP active site (Craig et al., 1996; Goldberg et al., 1995; Pereira et al., 2013). Thereby, the inhibitory capacities of naturally occurring microcystins are comparable with similar IC_{50} values in the nanomolar range, suggesting a highly conserved molecular mode of action (Altaner et al., 2020; Fischer et al., 2010; Fontanillo & Köhn, 2018). In contrast, cellular uptake mediated by organic anion transporting polypeptides (OATPs) has been shown to be highly congener specific (Fischer et al., 2010; Fischer et al., 2005). A clear correlation between microcystin residue positions, overall hydrophobicity, and OATP-mediated uptake was demonstrated in Chapter II, although GSH conjugation was not included in the study. However, enzymatically catalyzed conjugation has also been shown to be congener dependent. Previous studies reported that MC-RR was conjugated more efficiently than MC-LR using recombinant GST and isolated cytosolic hepatocyte fractions. Moreover, it was reported that the enzymatically catalyzed conjugation via GST was predominantly observed at low cytosolic GSH concentrations (1-2 mM), whereas spontaneous GSH conjugation predominated at physiological hepatocyte concentrations (10 mM) (Buratti et al., 2011; Buratti & Testai, 2015; Santori et al., 2020).

At the same time, the actual toxicities of the resulting conjugates remain highly controversial. While initial studies claimed that microcystins conjugated to GSH exhibited approximately 3-9-fold lower toxicity (Metcalf et al., 2000), a more detailed study showed that these conjugates exhibited similar toxicities compared to the unconjugated microcystins, as evidenced by similar PPP inhibition capacities using PPP1 and PPP2A *in vitro*. Only intratracheal administration to mice *in vivo* showed that the conjugates were 1/12 as toxic as unconjugated microcystins. The authors suggested that this discrepancy between *in vitro* and *in vivo* data was more likely due to toxicokinetics, e.g., cellular uptake, rather than a reduction in PPP inhibition capacities (Ito et al., 2002). In fact, this study was one of the first to question the correlation between toxicodynamic and toxicokinetic parameters in the context of conjugates and toxicities.

Based on these results, this study aimed to elucidate the cellular role of GSH as a possible detoxification mechanism for microcystins in cell systems and thereby contribute to the understanding of microcystin cytotoxicity. The data presented in this study are unique in that they simultaneously monitor cell viability (cytotoxicity), total phosphatase activity, and glutathione response after microcystin exposure. Additionally, the role of GSH in the microcystin-induced toxicity mechanism was studied by depleting

cellular GSH levels with subsequent toxicity analyses. Therefore, two independent experimental setups were used. First, HEK293 cells stably transfected with either OATP1B1 or OATP1B3 were used to elucidate the impact of GSH in the absence of all efflux transporters, thus allowing the contextualization of the PPP inhibition capacities of the resulting conjugates. Second, physiologically more relevant hepatocytes with significantly higher GSH levels and efflux transporter expression were used to contextualize the potential increased efflux transport of the conjugates.

Contrary to the initial hypothesis that GSH depletion would result in increased microcystin toxicity due to the inability to form GSH conjugates, no significant differences in microcystin toxicity were found despite the successful depletion of cellular GSH content in HEK293 cells. If any effect at all, GSH depletion resulted in reduced cytotoxicities, at least in OATP1B1-expressing cells, as observed by higher EC_{50} values, but also clearly increased replicate distribution. Microcystin PPP inhibition is caused by i) the hydrophobic interaction of the Adda side chain with the hydrophobic groove of the PPP active site, followed by ii) the formation of a covalent bond between the terminal unsaturated carbonyl moiety of the Mdha group and a cysteine residue of the active site. Chapter I clearly demonstrated that the presence, length, and orientation of the hydrophobic Adda side chain were essential for PPP inhibition, whereas the formation of the covalent bond was not. Moreover, it was shown that steric residues (phenylselenenyl) incorporated into the Mdha group ([MSecPh^{7}]MC-LY(Prg)) showed similar PPP inhibition capacities compared to its parent microcystin molecule. This additional residue should contribute to steric effects by disrupting the interaction sites between the PPP and the Mdha group at position (7). Needless to say, that GSH as a tripeptide is larger than a phenylselenenyl residue but considering that covalent binding is not essential to induce PPP inhibition, it is not surprising that the conjugates could exhibit similar and sufficient PPP inhibition capacities. Since the Adda side chain is not affected by the GSH conjugation, its hydrophobic affinity for PPP remains unchanged. In fact, *in silico* studies have reported that microcystins are not planar, but rather flexible and twisted, allowing the molecule to dynamically change its position (Jaeger-Honz et al., 2022). Through the interaction of the hydrophobic Adda side chain with the hydrophobic groove of the PPPs, dynamic changes within the molecule could result in complete blockage of access for other substrates, regardless of the covalently bound GSH. Unfortunately, due to the unavailability of both conjugates, MC-GSH and MC-Cys, the PPP inhibition capacities could not be determined using *in vitro* PPP assays but are essential to verify the hypothesis and provide information on their toxicities directly compared to unconjugated microcystins.

However, despite the PPP inhibitory capacities, the actual formation of conjugates should be considered as well. Since the actual concentration of both conjugates inside the cells could not be measured, the formation of GSH conjugates might be very low due the rather low cellular GSH levels of HEK293 cells and therefore, no PPP inhibition and cytotoxic effects could be observed. But it is noteworthy to say that at a cytosolic concentration of approximately 2 mM and considering the cell size and volume (see Materials and Methods) and the Avogadro constant, $1.7x10^{9}$ GSH molecules are facing $3.4x10^{4}$

microcystin molecules (EC_{50} of OATP1B1-expressing cells, MC-LR) per cell, demonstrating 50,000-times more GSH than microcystin molecules. In contrast, proteomic analysis of the total protein amount of HEK293 cells identified only 0.7 % as PPPs, see Chapter II. This raises the question of whether microcystins have a significantly higher affinity for PPPs or whether the conjugation efficiency is exceptionally low. Admittedly, since the literature and this dataset are lacking the actual cellular conjugate concentrations, this study is not completely sufficient to clarify this hypothesis. But considering the complete depletion of GSH in HEK293 cells, while cytotoxicities and PPP activities remained almost unaffected, and the data obtained in Chapter I, supports the hypothesis that microcystins could indicate a dramatically higher affinity for PPPs than for GSH conjugation, explainable by the highly hydrophobic Adda side chain. Supporting this hypothesis, it was reported that at a cytosolic GSH concentration of 1-2 mM, enzymatic conjugation via GST was found to be predominant. And indeed, the authors revealed rather high K_m values for human GST ranging between 100 and 200 µM using MC-LR and MC-RR (Buratti & Testai, 2015).

Based on the results obtained in the OATP-expressing HEK293 cell lines, the initial hypothesis that GSH conjugation leads to 'detoxification' of microcystins by covalent binding, thereby abolishing their PPP inhibitory capacity, was rejected. Thus, the question was raised whether physiologically more relevant hepatocytes would provide better insights into potential detoxification via increased conjugate elimination. Interestingly, all the results were supported by those obtained in immortalized human hepatocytes (IHH), which not only indicated a significantly higher cellular GSH content but also the expression of efflux transporters. Albeit cytotoxicities were measured in significantly higher concentration ranges compared to the HEK293 cell lines (µM in IHH and nM in HEK293). In contrast to the transfected HEK293 cell lines, the hepatocyte cell line IHH does not overexpress OATP1B1 and OATP1B3 but expresses both transporters at physiological quantities. Combined with the fact that IHH cells additionally express various efflux transporters, higher microcystin concentrations were required to induce similar cytotoxic effects. *Short insertion:* IHH and AML12 transporter availability and expression were not discussed or further analyzed in this study. Detailed cell line characterization of both hepatocyte cell lines is provided in Chapter V.

Nevertheless, depletion of cellular GSH content showed no significant difference in microcystin-induced cytotoxicity in IHH, comparable to the effects observed in HEK293 cells. GSH conjugation in the BSO untreated cells showed no 'detoxification' and reduction of cytotoxicity compared to the BSO treated and GSH depleted IHH cells. Since the reduction of PPP inhibition capacity was discussed and considered rather unlikely in the HEK293 dataset, it was hypothesized that conjugation might fulfill its detoxification function by improved elimination rather than reduced PPP inhibition capacity. In fact, conjugation of xenobiotics such as toxins to GSH increases water solubility and thus affinity for efflux transport (Forman et al., 2009). Moreover, efflux transporters such as multidrug resistance (MDR) and multidrug resistance-associated protein (MRP) transporters are specialized to transport GSH conjugated endogenous and xenobiotic substances to the bile, urine, and intestinal lumen to enhance their elimination from the body

(Borst et al., 1999; Forman et al., 2009). Interestingly, unbound microcystins were reported to be exported via MRP2, whereas the MC-GSH conjugate was not (Kaur et al., 2019). Although, due to the experimental setup, possible reuptake of microcystin conjugates must be considered as a possible explanation for the lack of differences observed between BSO-treated and untreated IHH cells, reuptake of conjugates via OATPs would be impaired and significantly reduced compared to unbound microcystins. As clearly demonstrated in Chapter II, the OATP-mediated uptake of microcystins was highly dependent on the overall hydrophobicity of the toxin. While hydrophilic microcystins either failed to be transported in OATP1B1-expressing cells or showed significantly impaired transport in OATP1B3-expressing cells, hydrophobic microcystins were efficiently taken up and transported across the cell membrane (Fischer et al., 2010). Since conjugation to GSH decreases hydrophobicity and thus increases hydrophilicity, transport of conjugates is expected to be impaired and not as efficient as for unbound microcystins. In competitive uptake, unconjugated microcystins are expected to be preferentially transported. Interestingly, no data are available on OATP-mediated transport of microcystin conjugates, highlighting the lack of data on the toxicokinetic properties of conjugates. Besides testing both conjugates, MC-GSH and MC-Cys, in OATP1B1- and OATP1B3-expressing HEK293 cells to evaluate their cellular uptake, another experimental setup using IHH cells in microfluidic chip systems with continuous removal of exported conjugates and subsequent conjugate quantification should be performed, to determine the efflux and corresponding role in toxicity of these conjugates.

The current risk assessment is primarily based on a mouse study conducted in 1999 with a single microcystin congener (MC-LR) and has remained unchanged since then (Fawell et al., 1999; World Health, 2020), even though more than 250 congeners have been described (Spoof & Catherine, 2016) and congener-specific toxicity has been demonstrated. However, studies have shown that mice vary widely in the expression of OATPs, as well as in the affinity and capacity for microcystin-mediated transport (Fischer et al., 2010; Fischer et al., 2005). Therefore, mouse hepatocytes (AML12) were used and compared with human hepatocytes, to study species differences within the microcystin-induced GSH response. Indeed, differences between mouse and human hepatocytes within the GSH response after MC-LR exposure were clearly demonstrated, as the GSH response in AML12 cells resulted in a dramatic overshoot response. Furthermore, GSH could not be efficiently depleted during cotreatment with MC-LR. Experiments were repeated with two independent subjects to exclude individual or handling dependence, but this effect remained unchanged. It remains unclear whether the observed differences were due to variations in GSH turnover rates. As GSH is not a protein but a tripeptide, it cannot be ubiquitinated and degraded by the proteasome. Furthermore, the stable γ-bond can only be cleaved by γ-glutamyl transpeptidase (GGT). Therefore, GSH stability and half-life are highly dependent on the presence and activity of GGT. The GSH half-life presented in this study, were determined using HEK293 cells only. Interspecies differences between human and mouse GGT activity and levels could result in different GSH turnover rates. Indeed, previous studies reported that blocking GSH synthesis with BSO only reduced intracellular GSH levels in mice but

did not induce GGT activation, in contrast to the results obtained in rats (Gallagher et al., 1998). Moreover, interspecies differences in GST enzyme activities were additionally reported. Mice demonstrated significantly higher microcystin conjugation rates than humans, as evidenced by significantly lower K_m values, ranging from 4-12 µM, which is an order of magnitude lower than observed in human liver cytosol (Buratti & Testai, 2015). Although these are only the first steps, the results obtained comparing human and mouse hepatocytes are fundamental and only highlight the need for further analysis and evaluation towards an adapted risk assessment. It should be noted that the data presented in this study provide a valuable but preliminary insight into the role of GSH in the mechanism of microcystin toxicity, but further investigation is required to obtain comprehensive understanding.

Conclusion

In this study, preliminary results were obtained by establishing three independent assays to monitor cell viability (cytotoxicity), phosphatase activity and GSH response after microcystin toxicity exposure. Thereby, providing initial insight into the potential role of GSH conjugation to microcystins. Although the data presented in this study are preliminary and require further experimental analyses, the assumption of 'microcystin detoxification via GSH conjugation' could not be supported, at least not in *in vitro* cell experiments, see Figure 39. Rather than reducing its toxicity, it could increase the elimination. Due to the fact that ADME studies have clearly demonstrated that only 24 % of the exposed microcystin dose was excreted and of this, 60 % were excreted as unconjugated and free microcystins (Schmidt et al., 2014), leads to the assumption that cleavage via dipeptidases with subsequent recirculation of free microcystins should not be underestimated. Thereby pointing to the dramatically high affinity for PPPs, while the conjugation to GSH could be assumed to play only a minor role.

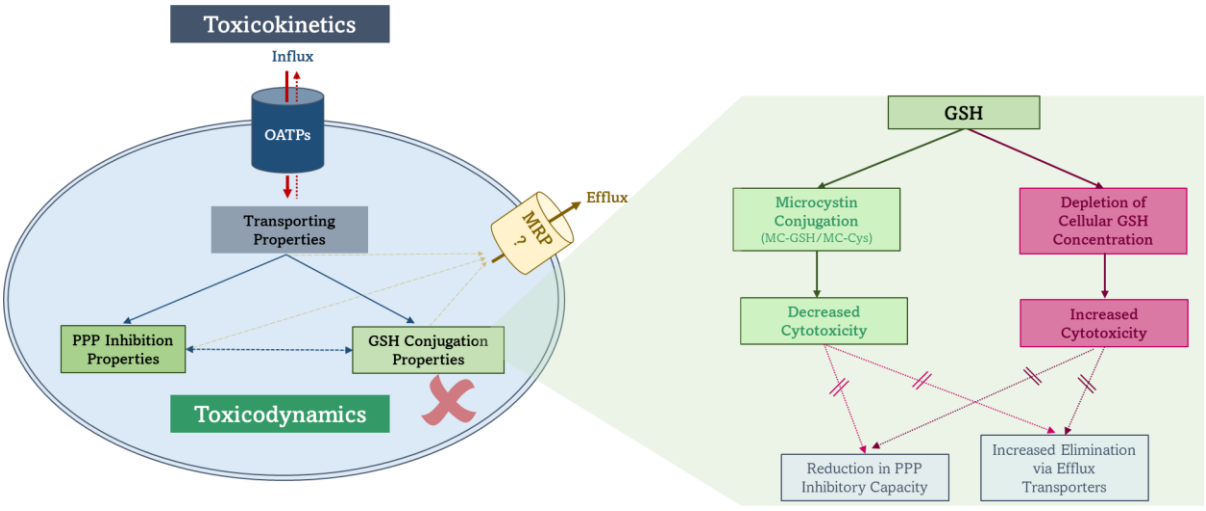

Figure 39: Role of GSH in the Microcystin Toxicity Mechanism

The initial hypothesis that GSH conjugation would result in decreased cytotoxicity and thereby 'detoxifying' microcystins was rejected. Depletion of cellular GSH did not result in increased cytotoxicity. Indeed, no significant differences in toxicity were observed in either HEK293 or both hepatocyte cell lines. Although the results of this study are preliminary and provide only first insights into this topic, conjugation of GSH to microcystins as a 'detoxification mechanism' should be critically questioned.

5. Chapter IV

5.1. Protein Half-Lives of PPPs and Glutathione Synthesizing Enzymes

5.1.1. Introduction

Proteins are the cornerstones of all cellular functions and thus of life. The process of protein synthesis is fundamental and is divided into gene expression, the transcription of DNA into RNA, and the actual synthesis, the translation of mRNA into polypeptide chains by ribosomes. These polypeptide chains are folded and activated by post-translational modifications (PTMs) to become fully functional proteins (Merrick & Pavitt, 2018; Ramazi & Zahiri, 2021). An essential PTM is thereby the attachment of phosphate groups to a protein, known as phosphorylation. Over one-third of all proteins are estimated to undergo phosphorylation (Hunter, 1995). Thereby, the balance between kinase-catalyzed phosphorylation and phosphatase-catalyzed dephosphorylation is highly regulated and acts as a molecular switch to modulate protein activity, location, conformation, and stability (Pereira et al., 2011). Due to the predominance of serine and threonine phosphorylation sites (86.4 % and 11.8 %, respectively), serine/threonine phosphoprotein phosphatases (PPPs) represent the largest class of phosphatases (Shi, 2009). In addition to the essential catalytic subunit, the general phosphatase complex may contain a scaffold subunit, responsible for enzyme confirmation, and a variable regulatory subunit, that regulates enzyme activity and provides substrate specificity (Cohen, 2004; Pereira et al., 2011; Shi, 2009). Members of the PPP family share a highly conserved catalytic subunit and based on their sequence, PPPs have been further classified into seven subtypes: PPP1, PPP2A, PPP2B (calcineurin), PPP4, PPP5, PPP6, and PPP7, see **Figure 40**.

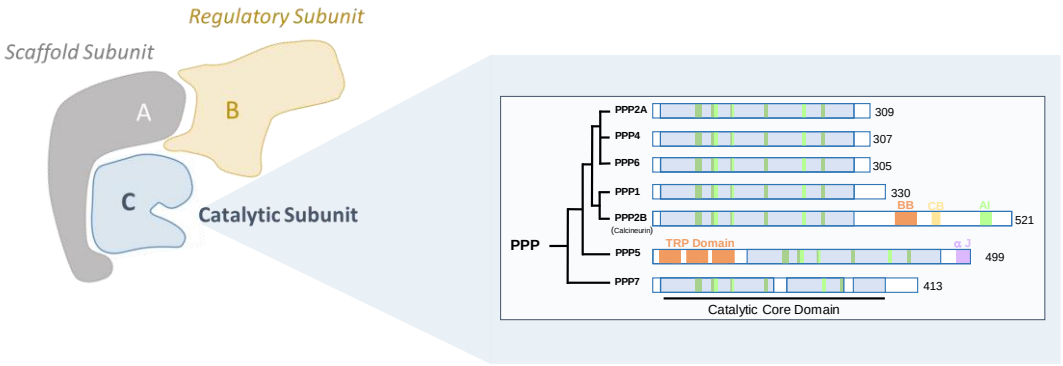

Figure 40: Serine/Threonine Phosphatase Complex

While the serine/threonine phosphatase complex may contain a scaffold subunit (enzyme conformation) or a regulatory subunit (regulation of enzymatic activity and substrate specificity), the catalytic subunit is mandatory for enzymatic activity. Thereby, all members of the PPP family share a highly conserved catalytic core domain. Figure was modified and adapted (Millward et al., 1999; Shi, 2009).

Among all phosphatases, PPP1 and PPP2A are the most essential ones, accounting for more than 90 % of protein dephosphorylation in eukaryotic cells (Bollen et al., 2010), as evidenced in their key function in the cell cycle, DNA regulation, and glycogen metabolism. PPP2A alone represents approximately 1 % of the total cellular protein amount (Ruediger et al., 1991). Besides the catalytic subunit, PPP1 requires only

a regulatory subunit to fully activate its enzymatic function, whereas PPP2A, similar to PPP4 and PPP6, requires an additional subunit for catalytic activation. In contrast to all other members of the PPP family, PPP5 is unique since no regulatory or scaffold domain is required for its enzymatic activation. PPP5 is regulated by an autoregulatory tetratricopeptide repeat (TPR) domain located on the same peptide as the catalytic subunit (Chen et al., 1994; Yang et al., 2005). Considering their essential cellular roles, it is not surprising that PPPs are the targets of several toxins such as okadaic acid, cantharidin, nodularins, or microcystins (Pereira et al., 2011). Microcystins are cyclic heptapeptides produced by various cyanobacterial species and are highly potent PPP inhibitors. These hepatotoxins interact and bind directly to the catalytic subunit of the PPPs, completely abolishing their function by blocking access to other substrates (MacKintosh et al., 1990; MacKintosh et al., 1995). Consequently, dephosphorylation is no longer catalyzed, leading to a hyperphosphorylated state of all cellular proteins and, among various cellular events, to the induction of cell death (Pereira et al., 2011; Shi, 2009).

However, eukaryotic cells are not defenseless against toxins. Glutathione (GSH) is one of the most essential peptides involved in the phase II biotransformation in the cellular detoxification system. The formation of GSH conjugates, increases the water solubility and thus the excretion of xenobiotics and toxins (Anderson, 1998). In contrast to complex proteins, the tripeptide is not synthesized ribosomally, but intracellularly via two ATP-dependent enzymatic steps. In the first step, γ-glutamyl-cysteine ligase (GCL) catalyzes the formation of γ-glutamyl-cysteine. Thereby, the GCL activity is highly regulated by a non-allosteric feedback mechanism induced by high cellular GSH concentrations and cytosolic cysteine availability. GCL is a heterodimeric enzyme that requires a catalytic (GCLC) and a modifier (GCLM) subunit for full enzymatic activation. In the second step, the addition of glycine is catalyzed by glutathione synthetase (GSS). GSS is not feedback inhibited, and since the product of GCL is present at low concentrations in the presence of GSS, only the first step of the GSH synthesis pathway is considered to be rate-limiting (Lu, 2013). The conjugation reaction of GSH with microcystins results in two stable conjugates. In the first step, GSH nucleophilically attacks microcystins, resulting in the first conjugate microcystin-GSH (MC-GSH). In a second step, glutamic acid is cleaved by γ-glutamyltransferase to form the intermediate microcystin-cysteine-glycine (MC-Cys-Gly). The glycine residue of the intermediate is rapidly cleaved by a dipeptidase to yield the second stable conjugate, microcystin-cysteine (MC-Cys) (Schmidt et al., 2014). Although both microcystin conjugates, MC-GSH and MC-Cys, have been reported for several species, including humans (Buratti & Testai, 2015; Kondo et al., 1992), their actual toxicity and potential increased elimination via efflux transporters are not fully understood and remain controversial. Nevertheless, microcystins have been shown to be excreted primarily as unconjugated compounds, although several studies have shown that only a small percentage of the administered dose is excreted from the body. ADME studies performed in mice showed that only 24 % of the injected microcystin dose was excreted through urine (9 %) and feces (15 %). Of these excreted microcystins, 60 % were present as

parent compounds (Robinson et al., 1991). Since the amount of microcystin conjugate excreted is very low, the actual function of GSH conjugation to microcystins remains unclear.

Considering that human microcystin intoxications, causing severe liver damage and cancer, has been reported mainly as a result of chronic exposure to non-lethal microcystin concentrations (Shi et al., 2021), only highlights the potential hazard of recirculating (un)conjugated microcystins. This raises the question of whether microcystins bound to PPPs could be cleaved from the enzyme, resulting in free and unbound microcystins that could recirculate and cause repeated damage to tissues and organs. However, only little is known about the degradation pathway of microcystin-bound PPPs. In eukaryotic cells, two major pathways, the ubiquitin-proteasome, and the lysosomal proteolysis pathway, mediate cellular protein degradation. Thy lysosomal degradation pathway mediates degradation though the uptake of proteins by protease-containing lysosomes and appears to be non-selective, resulting in the slow degradation of cytoplasmic proteins. In contrast, the proteasomal degradation pathway requires a 76-amino acid polypeptide called ubiquitin to mark proteins for degradation. Ubiquitinated proteins are then recognized by the proteasome and subsequently degraded by the large protease complex. This degradation pathway, although selective and rapid, requires free ubiquitination sites, such as accessible lysine residues, and degrades proteins that control fundamental cellular processes such as cell proliferation and gene expression (Cooper, 2000).

Aim of the Study

So far, microcystin toxicity studies have been limited to single exposures at relatively high microcystin concentrations. However, this does not reflect the current situation where most human intoxications have been reported as a result of chronic exposure to non-lethal microcystin concentrations. Prior to simulating chronic exposure in cell experiments, the protein half-lives, and turnover rates of the catalytic subunits of PPPs (PPP1, PPP2A, and PPP5), glutathione (GSH), and its synthesizing enzymes (GCLC and GSS) were determined, see **Figure 41**. This study aimed to provide first insights and baselines for chronic exposure studies to correlate corresponding cytotoxicity with protein availability and turnover.

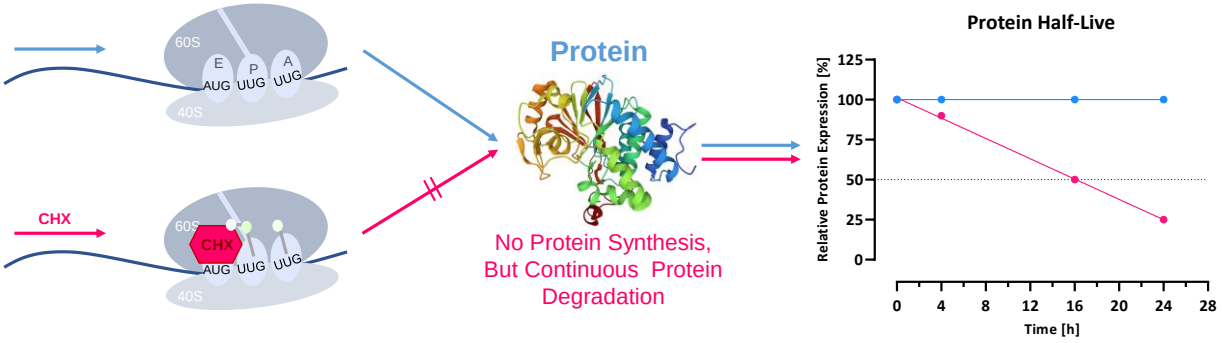

Figure 41: Chapter IV Graphical Abstract

Protein synthesis was inhibited using cycloheximide (CHX) by binding to the E-site of the 60S ribosomal unit. Protein degradation was monitored using western blot analysis, followed by linear regression to determine and calculate protein half-lives and stabilities.

5.1.2. Results

In non-tumorigenic and healthy cells, cell cycle synchronization is triggered by cell-cell contact inhibition leading to cell cycle arrest in the early G_1 phase upon formation of a confluent monolayer. As HEK293 cells are tumorigenic and not contact-inhibited cells, the stably transfected HEK293 cells were assumed to be asynchronous. Therefore, cell cycle analysis and subsequent cell cycle synchronization was performed to allow for more accurate protein expression analyses and to eliminate confounding or averaging effects due to asynchronous cell populations.

Cell Cycle Synchronization

Prior to synchronization, untreated HEK293-OATP1B1, -OATP1B3, and -CV cells were used for cell cycle analysis of non-synchronized cells using flow cytometry, see **Figure 42**. Similar to the results presented in Chapter II, no differences were observed between the cell lines. Furthermore, all HEK293 cell lines showed a similar and distinct cell cycle distribution, see **Figure 42 A**, pointing to their equivalence and comparability. Contrary to the initial assumption, the stably transfected cells already showed synchronized tendencies, see **Figure 42 B-C**. As indicated by the distinct peak, the majority of HEK293-OATP1B1, -OATP1B3, and -CV cells were found to be in G_1 phase (57.3 %, 52.5%, and 61.1 %, respectively), followed by smaller amounts in the S phase (27.1 %, 26.5 % and 22.9 %, respectively). Only 10.9 %, 12.9 % and 11.3 %, respectively, were found to be in the G_2/M phase, while only small percentages were found to be in the sub-G_1 phase of the cell cycle (4.8 %, 6.3 %, and 4.8 %, respectively).

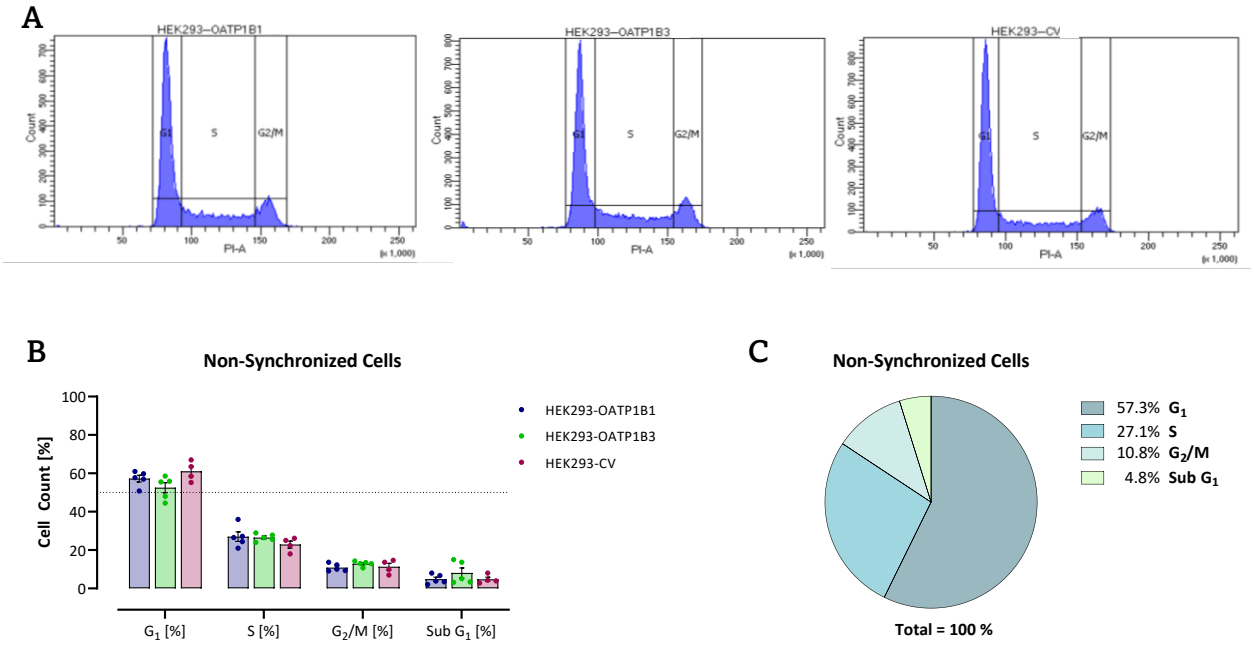

Figure 42: Cell Cycle Analysis of Non-Synchronized HEK293 Cells

Flow cytometric analyses of the cell cycle of non-synchronized HEK293-OATP1B1, -OATP1B3, and -CV cells as **(A)** a representative cell cycle histogram and **(B)** percentages of all replicates. Each point represents a biological replicate ± SEM (n=4-5). For visualization, the distribution of all cell cycle phases measured of in HEK293-OATP1B1 cells was plotted as a percentage of all counts (n=5) **(C)**.

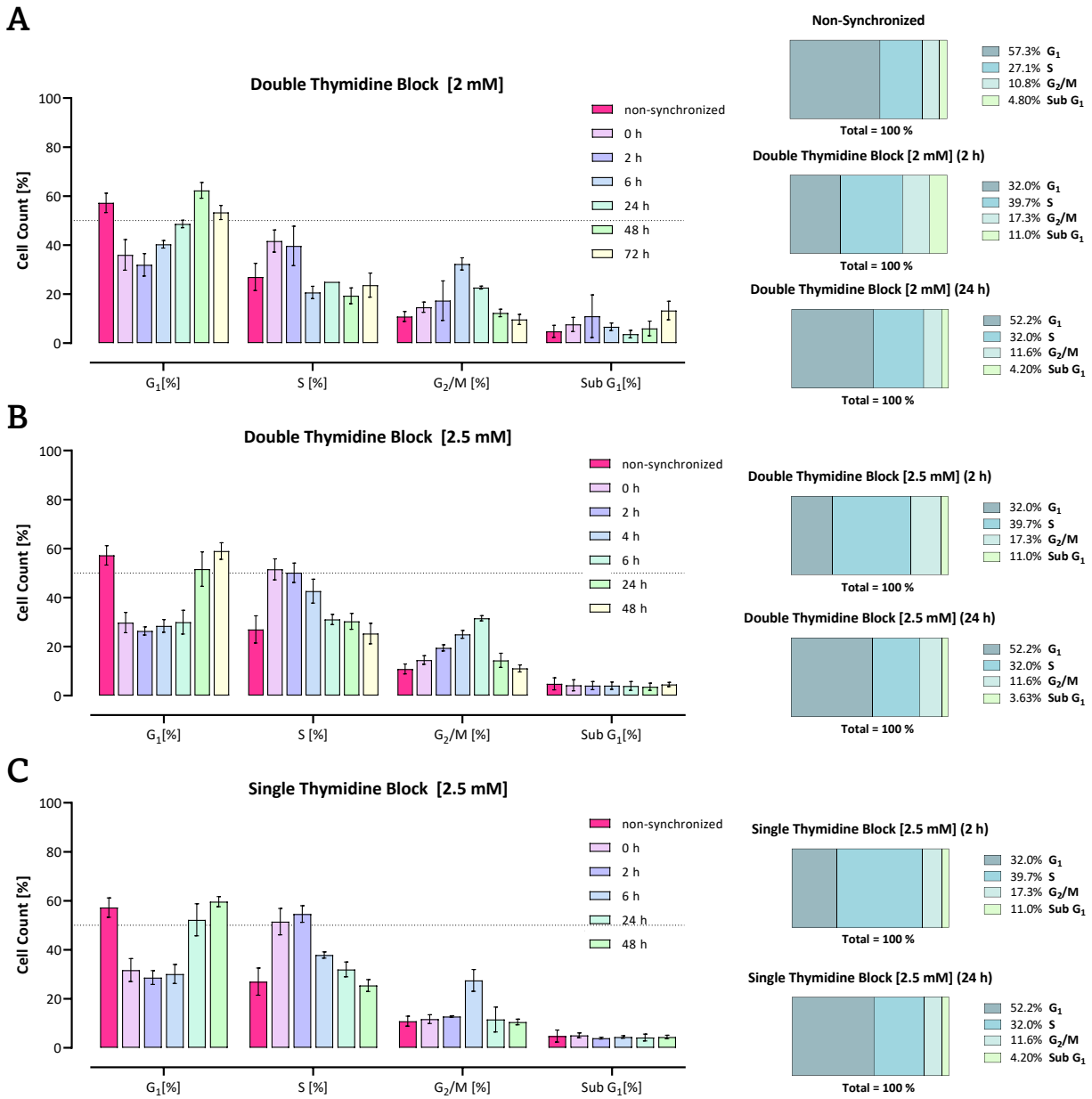

Figure 43: Cell Cycle Analysis after Synchronization Using Thymidine Block

Measured cell cycles of HEK293-OATP1B1 after **(A)** 2 mM double thymidine block (18 hours treatment, 9 hours release time between blocks), **(B)** 2.5 mM double thymidine block (18 hours treatment, 5 hours release time) and **(C)** 2.5 mM single thymidine block (18 hours treatment) with subsequent cell analysis according to the indicated timepoints ± SEM (n=3). Corresponding visualizations of the cell cycle distribution shortly after the last treatment (2 hours) and after 24 hours are shown on the right side.

Although the majority of cells were found to be in the G_1 phase, further experiments were performed to obtain cells in the same cell cycle phase. Therefore, a common and widely used experimental setup using a double thymidine block was performed to induce cell synchronization, see Figure 43. Thymidine is a DNA synthesis inhibitor and by interrupting the deoxynucleotide metabolic pathway, it induces cell cycle arrest at the G_1/S transition and inhibits DNA replication. Due to their similarity, only HEK293-OATP1B1 cells were used and incubated with 2 mM thymidine solution for 18 hours. Cells were released into the cell cycle by incubation in growth medium for 9 hours, followed by a second thymidine

incubation for 17 hours. Cells were then released into the cell cycle and monitored for 72 hours, see **Figure 43 A**. While non-synchronized cells showed a clear majority in the G_1 phase, thymidine treatment only resulted in an increased distribution in all phases instead of a single peak. Since the standard protocol failed to induce synchronization, the thymidine concentration was increased to a maximum of 2.5 mM and the release time was adjusted to 5 hours. Again, subsequent cell cycle analyses showed no induced cell cycle synchronization, but a further increased distribution within all cell cycle phases, see **Figure 43 B**. Similar results were observed when OATP1B1-transfected HEK293 cells were treated with 2.5 mM thymidine solution in a single thymidine block experiment, see **Figure 43 C**.

As cell cycle synchronization using thymidine clearly failed, but the untreated cells showed synchronized cell cycle tendencies as the majority of all cells were clearly found in the G_1 phase, further protein analyses were performed with non-synchronized cells. Rather than exposing the cells to multiple treatments simultaneously, it was decided to determine protein half-lives using the cycloheximide chase assay without any cell synchronization cotreatments.

Cycloheximide (CHX) Induces Time-Dependent Cytotoxicity

Cycloheximide (CHX) is an antibiotic produced by Streptomyces griseus that inhibits eukaryotic translation elongation by binding to the E-site of the 60S ribosomal unit. Prior determining protein half-life using CHX chase assay, an effective but non-cytotoxic concentration of CHX was determined using serial dilutions of CHX, followed by cell viability measurements in OATP1B1- and OATP1B3-expressing HEK293 cells, see **Figure 44**. Interestingly, although a wide concentration range (10 – 500 µg/ml) was used, no concentration-dependent, but therefore a highly time-dependent cytotoxicity was measured in both cell lines, see **Figure 44 A**. Irrespective of the concentrations used, already 4 hours of CHX incubation significantly decreased the average cell viability to 79.5 % in OATP1B1- and to 79.9% in OATP1B3-expressing cells. While 14 hours of CHX incubation decreased cell viability to 48.7 % and 50.8 %, respectively, hardly any viable cells remained after 24 hours (37.3 % and 32.4 %, respectively). Statistical analyses confirming significant time-dependent but not concentration-dependent cytotoxicity are provided in **Supplementary Figure 9**.

To exclude any interference or cross-reactions of the CHX treatment with the cytotoxicity assay and to further validate the results obtained, additional cellular protein content analyses were performed, see **Figure 44 B**. Indeed, a similar time-dependency was observed as already seen within the cytotoxicity screening. Therefore, further analyses using CHX as a protein synthesis inhibitor will be limited to a maximum incubation time of 24 hours.

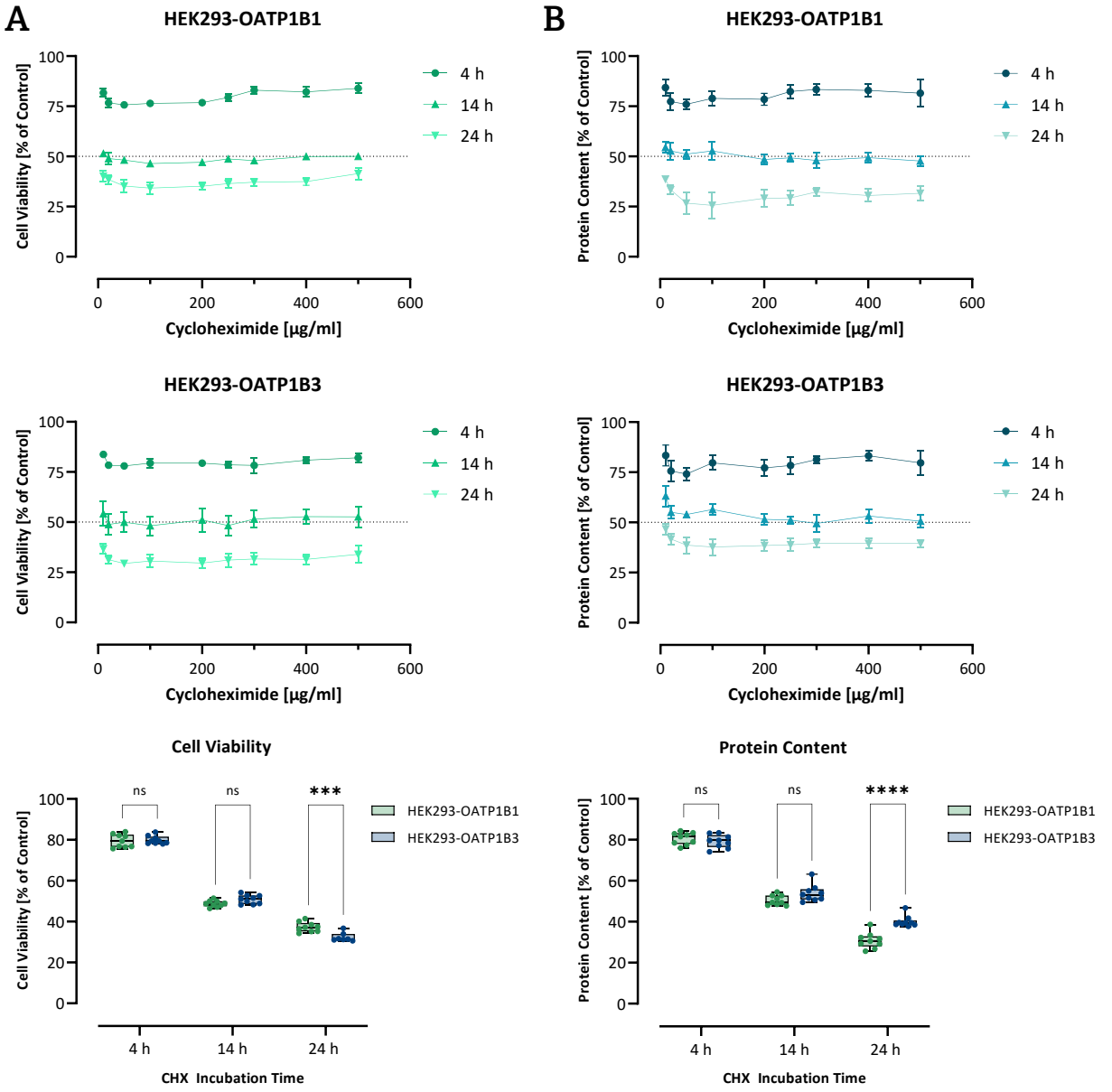

Figure 44: Cycloheximide Cytotoxicity

OATP1B1- and OATP1B3-expressing HEK293 cells were exposed to cycloheximide (CHX) for 4, 14 or 24 hours and cytotoxicity was assessed by **(A)** cell viability and **(B)** total protein content. Each point represents the mean of 4 independent biological replicates ± SEM (n=4). Corresponding statistical analyses using all concentrations per timepoint were performed using two-way ANOVA with Šídák's multiple comparison test (****p=<0.0001 ,***p=0.0003).

Protein Half-Lives of the Catalytic Subunits of PPPs

Protein synthesis was inhibited in OATP1B1-expressing HEK293 cells using 500 µg/ml CHX solution and protein degradation was monitored after 0 (control), 4, 14, and 24 hours of incubation and then visualized by western blot analyses, see **Figure 45**. All antibodies were verified using positive controls prior to half-life determination, see **Supplementary Figure 10.** Consistently, 4 hours of protein synthesis inhibition reduced the protein content of PPP1, PPP2A, and PPP5 to 90 %. After 14 hours of incubation, 74 % of PPP1 and PPP5 and only 66 % of PPP2A were detected.

Table 9: Summary of PPP Half-Lives

Calculated protein half-lives ($t_{1/2}$) and coefficients of determination (R^2) values for the corresponding linear regression in HEK293-OATP1B1 cells are summarized. Statistical analysis was performed using a one-way ANOVA followed by Tukey's multiple comparison post-test, see Figure 45.

Protein	Half-Life ($t_{1/2}$)	R^2	Statistical Comparison to PPP1	
PPP1	24 h	0.9513	-	-
PPP2A	16 h	0.9018	**	p = 0.0058
PPP5	19 h	0.8918	*	p = 0.0286

While 24 hours of incubation only reduced the PPP1 content to 50 %, PPP2A and PPP5 showed increased degradation, as indicated by barely detectable amounts of protein (20 % and 31 %, respectively), see Figure 45 A-C. Using linear regression, protein half-lives were calculated and summarized in Table 9. While the protein half-lives for PPP2A and PPP5 were comparable (16 and 19 hours, respectively) the half-life calculated for PPP1 was significantly higher (24 hours), see Figure 45 D.

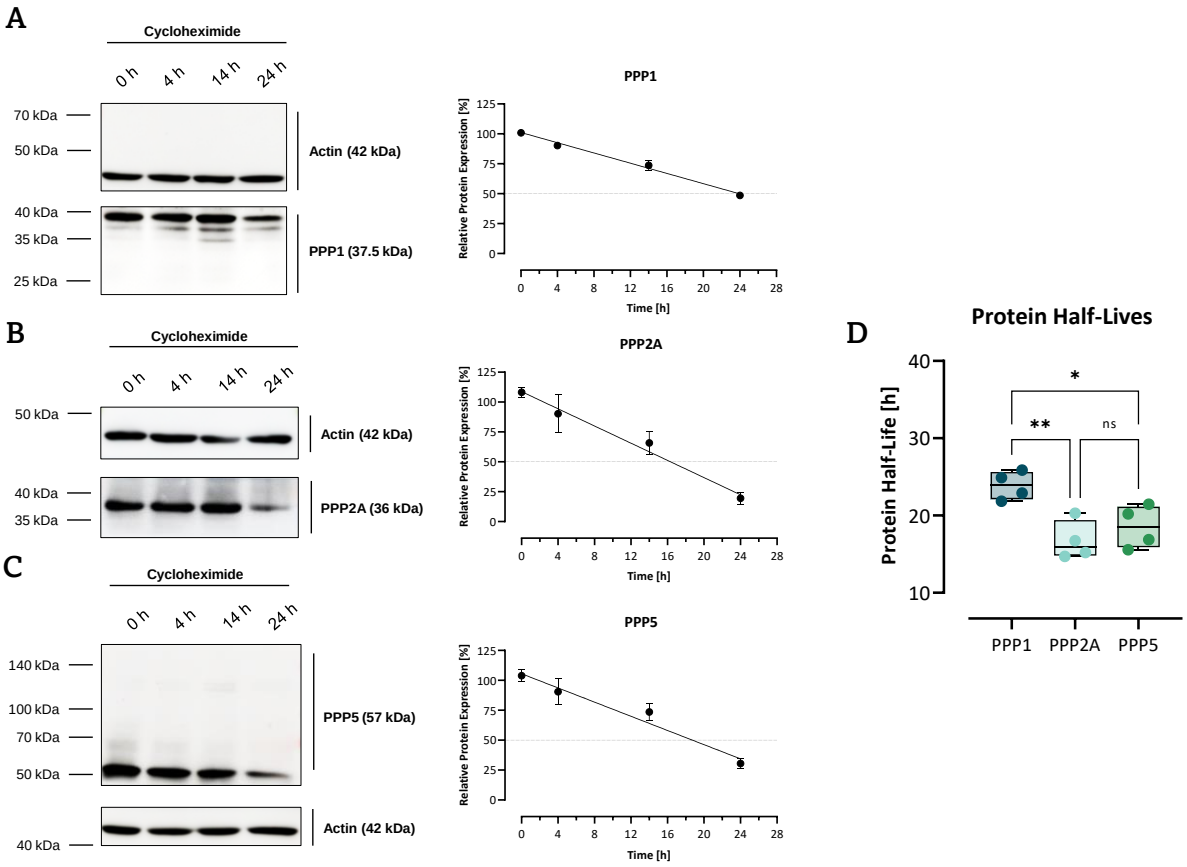

Figure 45: Cycloheximide Chase Assay for Catalytic Subunits of PPPs

HEK293-OATP1B1 cells were incubated with 500 µg/ml CHX for 0 (control), 4, 14, and 24 hours. Western blot analyses were performed using 15 µg/lane cell lysates and detected with (A) anti-PPP1c, (B) anti-PPP2Ac, and (C) anti-PPP5c. Protein degradation was monitored by blot quantification using ImageJ, each point represents the mean ± SEM (n=4). Protein half-lives were calculated using linear regression and statistically compared using a one-way ANOVA followed by Tukey's multiple comparison post-test (D). Calculated half-lives and p-values are summarized in Table 9. Only representative blots are shown, summary of all used blots is provided in Supplementary Figure 11.

Protein Half-Lives of Glutathione and its Synthesizing Enzymes

Similarly, the protein half-lives of the catalytic subunits of the GSH synthesizing enzymes GCLC and GSS were determined in HEK293-OATP1B1 cells, see **Figure 46**. While GCLC showed a linear degradation rate comparable to PPPs, see **Figure 46 A**, with a calculated protein half-life of 19 hours, GSS showed no comparable degradation. GSS appeared to be highly stable, as 84 % of GSS remained completely intact after 24 hours of CHX treatment, so that no reliable linear regression and no valid half-life could be determined, see **Figure 46 B-C**.

Although already mentioned in Chapter III, the half-life of GSH is presented here for reasons of clarity and completeness. OATP1B1-expressing HEK293 cells were incubated with 125 µM BSO, a GCL inhibitor, for either 1.5, 3, 6 or 10 hours before measuring the cellular GSH content, see **Figure 46 D-E**.

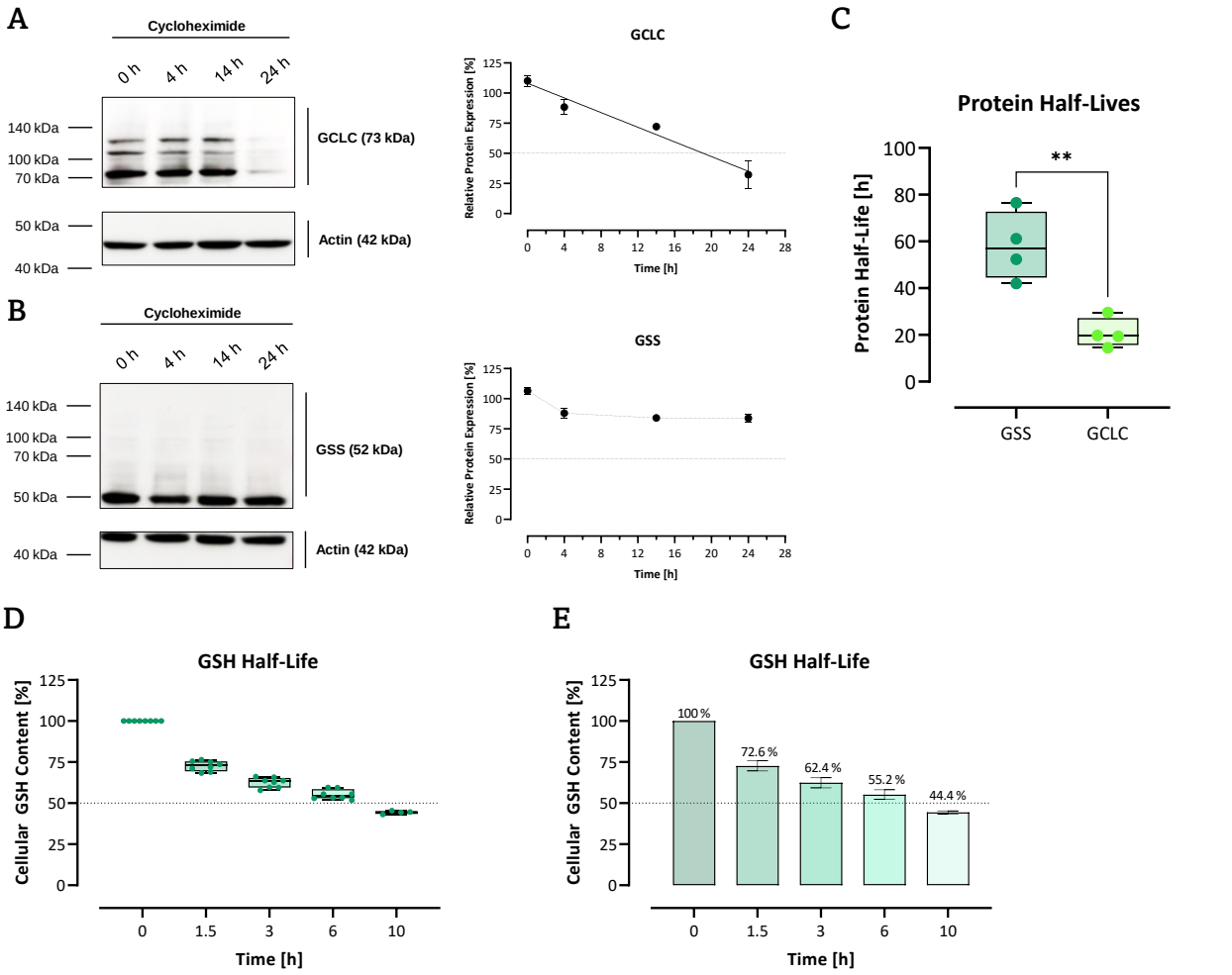

Figure 46: Determination of Half-Lives of GSH and its Synthesizing Enzymes

HEK293-OATP1B1 cells were incubated with 500 µg/ml CHX for 0 (control), 4, 14, and 24 hours. Western blot analyses were performed using 15 µg/lane cell lysates and detected with **(A)** anti-GCLC and **(B)** anti-GSS. Protein degradation was monitored by blot quantification using ImageJ, each point represents the mean ± SEM (n=4). Protein half-lives were calculated using linear regression and statistically compared using two-tailed unpaired t-test (p=0.0034), although no precise half-life for GSS could be determined **(C)**. Only representative blots are shown, summary of all blots used is provided in **Supplementary Figure 11**. Degradation time of GSH was monitored after GSH depletion with BSO. Thereby, protein half-life was measured after approximately 6 hours **(D)**. Each point represents the mean of an independent biological replicate (n=8). **(E)** GSH degradation was visualized as bars and percentages ± SD (n=8).

Thereby, the time-dependent degradation of GSH was measured. After 1.5 hours, the cellular GSH content was already reduced to 72.6 %. With increasing time, the rate of degradation decreased, as evidenced by the fact that after 3 hours 62.4 %, after 6 hours 55.2 %, and after a total of 10 hours 44.4 % of cellular GSH was still detectable. As the degradation rate declined over time, it was assumed that the complete degradation of GSH would require more than 12 hours, even though the half-life was reached at approximately 6 hours.

Proteasome Inhibition Prevents Protein Degradation of PPPs

As a proof of principle and to validate the CHX chase assay, HEK293-OATP1B1 cells were treated with MG132, a potent and cell permeable proteasome inhibitor, while protein synthesis was inhibited, see Figure 47 A-C. Indeed, cotreatment with either 10 µM, 15 µM, or 25 µM MG132 did not result in significant protein degradation of PPP1, PPP2A, or PPP5, indicating the functionality of the CHX chase assay.

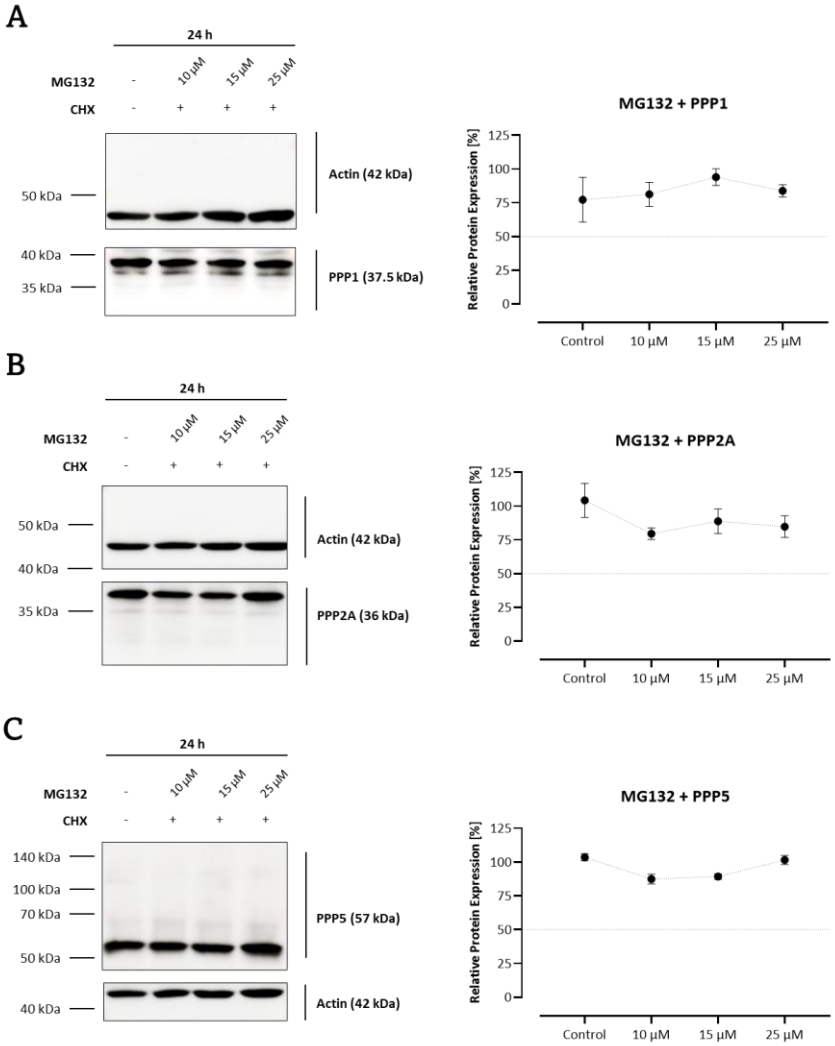

Figure 47: Cycloheximide Chase Assay While Inhibiting Proteasome Using MG132

Cycloheximide chase assay was performed while cotreated with either 10 µM, 15 µM or 25 µM proteasome inhibitor MG132. Western blot analyses were performed using 15 µg/lane cell lysate and detected with **(A)** anti-PPP1c, **(B)** anti-PPP2Ac, and **(C)** anti-PPP5c. Blots were quantified using ImageJ, each point represents the mean ± SEM (n=5). Only representative blots are shown, summary of all blots used is provided Supplementary Figure 12.

5.1.3. Discussion

Although PPPs play an essential role in cellular metabolism and contribute significantly to cell maintenance and survival, little data is available on their protein stability, turnover and half-life. Protein turnover describes the balance between protein synthesis and degradation and occurs continuously to maintain protein homeostasis and thus normal cellular function. While protein synthesis is comparatively slow, rapid protein degradation is required to allow for immediate and selective responses specific to their environment. Thereby, the turnover is highly dependent on the protein stability (Fornasiero & Savas, 2023). One measure of protein stability and corresponding turnover is the protein half-life. Depending on their cellular function and location, proteins can cover a broad range of half-lives. For example, proteins such as eye lens crystallin or collagen have exceptionally long half-lives on the order of years in humans due to their protected environment and limited metabolism (Toyama & Hetzer, 2013). On the other hand, proteins that are highly utilized and involved are theorized to have shorter half-lives. Proteomic analysis of 11,000 proteins of the human proteome revealed over 500 short-lived proteins with half-lives ranging from 20 minutes to 8 hours. Additionally, 1,400 proteins were found to be of intermediate stability with half-lives ranging from 8 to 34 hours (Li et al., 2021).

PPPs represent one of the most important and abundant enzyme families, responsible for 90 % of all protein dephosphorylation in eukaryotic cells (Bollen et al., 2010). The highly dynamic process of protein dephosphorylation regulates enzyme (de)activation, protein homeostasis and multiple signaling pathways. The balance between phosphorylation and dephosphorylation is tightly controlled, pointing to the highly selective and regulated on/off switch of PPP enzymatic activities (Brautigan, 2013; Cohen, 2004; Shi, 2009). This led to the assumption that PPPs have a rather limited lifespan and are continuously and rapidly replaced. Therefore, this study aimed to determine the protein stabilities and approximate half-lives of the enzymatically active catalytic subunits. Hence, cycloheximide (CHX) was used as a ribosomal translation elongation inhibitor to prevent protein synthesis, followed by monitoring of the degradation kinetics via western blot analyses. The CHX chase assay is a common and widely used method for measuring protein half-lives and stabilities (Darvishi & Woldemichael, 2016; Eldeeb et al., 2019; Li et al., 2021).

Prior to the determination of the protein half-lives, cell cycle analysis and cell cycle synchronization of stably transfected HEK293 cell lines was performed, to potentially improve further protein expression analyses and to eliminate confounding or averaging effects due to asynchronous cell populations. Surprisingly, non-synchronized cells showed the most distinct cell cycle distribution. The clear majority of the cells were found to be in G_1 phase, followed by S phase. Only a small fraction was found to be in G_2/M phase, consistently and irrespective of the HEK293 cell lines used. However, since by definition all cells have to be in one phase for a fully synchronized cell population, the widely used double thymidine block was performed (Chen & Deng, 2018; Ligasová & Koberna, 2021). But instead of cell synchronization, thymidine treatment resulted in increased distribution within all cell cycle phases. Regardless of the

thymidine concentrations and variations in incubation and release times, no clear cell cycle synchronization could be achieved. Cell synchronization in tumorigenic eukaryotic cells requires cell cycle inhibitors, which are by definition hazardous and cytotoxic. Effective synchronization requires repeated treatments with high concentrations of the blocking agent over a long period of time (Ligasová & Koberna, 2021). Consequently, forced, and uneven cell cycle arrest and the prolonged exposure to cytotoxic blocking agents may induce undesired cellular stress responses, and may interfere with cell growth, proliferation, and protein expression in ways that are difficult to predict. Therefore, cell cycle synchronization of whole cell cultures using blocking reagents is controversial (Cooper, 2019). Since all proteins of interest are known to be expressed continuously and independently of the cell cycle, and all synchronization experiments clearly resulted in increased cellular stress, as evidenced by increased cell death and distribution across all cell cycle phases, further protein expression analyses were performed only in non-synchronized cells to exclude any incorrect results due to cellular stress response.

Nevertheless, using the CHX chase assay without any synchronization agent resulted in a clear protein degradation. As CHX was shown to induce time-dependent rather than concentration-dependent cytotoxicity, all experiments were limited to 24 hours of exposure. Since all PPPs share a highly conserved catalytic subunit, the most abundant PPP1 and PPP2A (closely related to PPP4 and PPP6 (Shi, 2009)), and the unique PPP5 were used representatively. Thereby, the evaluation of half-lives using linear regression with strong coefficients of determination revealed higher protein stabilities as expected for all catalytic subunits. PPP1 indicated the longest half-life (24 hours), followed by comparable half-lives for PPP2A (16 hours) and PPP5 (19 hours). Even though the differences between the measured half-lives of the PPPs appear to be large (8 hours difference between PPP1 and PPP2A), it should be noted that the data obtained in this study are preliminary and provide initial insights into protein stability, allowing evaluation and classification of PPP stabilities prior to accurate turnover rates. There are many variables involved in the accurate half-life determination. In particular, quantification by western blot analysis is difficult and not as precise as analytic methods such as LC-MS/MS. Western blot quantification is highly dependent on antibody quality, which explains the high variability between PPPs and the rather high estimated half-life of PPP1. Although the PPP1 antibody was verified with a commercially available positive control prior to half-life determination, this antibody tends to have higher background noise and additional non-specific binding (double bands), while the PPP2A and PPP5 antibodies showed only a distinct and clear single band. Moreover, the quantitative accuracy is essential for the determination of the protein half-lives. Small variations in the measured protein abundance can result in pronounced effects on half-life measurement and calculation. Indeed, the variations become more apparent when the individual biological replicates were analyzed, as presented in **Figure 45 D**. The measured half-lives of the individual biological replicates (n=4) ranged from 16-24 hours for PPP1, 15-20 hours for PPP2A, and 16-22 hours for PPP5, indicating an average half-life of approximately 20 hours. This is consistent with the only previously published proteomic analysis of 11,000 proteins monitoring their 8 hour degradation kinetics using the CHX chase assay in four

different cell lines, including HEK293T cell line (Li et al., 2021). Although their study focused on short-lived proteins, they were able to identify 1,400 proteins of intermediate stability (including only those with >15 % loss of protein abundance at 8 hours) were determined with similarly strong coefficients of determination. Thereby, the catalytic subunit of PPP4 with a determined half-life of 19.47 hours (n=8) was classified as intermediately stably, underlining the results obtained in this chapter. Similar to the results obtained in this study, the authors of the proteomic analysis study claimed that the CHX assay provided accurate half-lives especially for short-lived proteins, while the half-lives of intermediately stable and long-lived proteins were more difficult to determine with greater variety. Moreover, with increasing CHX incubation time, the disruption of cellular physiology and protein response could lead to miscalculation and therefore misinterpretation of half-lives (Li et al., 2021).

Based on the data obtained from PhosphoSitePlus, an online database providing comprehensive information on all PTMs on human proteins (Hornbeck et al., 2015), various ubiquitination sites were found for all catalytic subunits analyzed and summarized in **Supplementary Figure 13** and **Supplementary Figure 14** (Dushukyan et al., 2017). Since ubiquitination sites are a clear indicator of the proteasomal degradation pathway, the proteasomal inhibitor MG132 was used as a proof of principle and to verify the CHX chase assay performed. Indeed, the proteasomal degradation of PPP1, PPP2A and PPP5 was prevented despite the CHX cotreatment, supporting the results obtained in this study.

Although the clear focus of this study was on the protein stabilities and half-lives of the catalytic subunits of PPPs, toxicodynamic parameters in the toxicity mechanism of microcystins include the conjugation to GSH (Buratti & Testai, 2015; Kondo et al., 1992). Therefore, the half-life of GSH and its synthesizing enzymes GCLC and GSS were determined. GSH itself, is not a protein but a tripeptide, it cannot be ubiquitinated and degraded by the proteasome. Furthermore, the stably γ-bond can only be cleaved by γ-glutamyl transpeptidase (GGT). Therefore, GSH stability and half-life are highly dependent on the presence and activity of GGT and can vary depending on the tissue and localization (Baudouin-Cornu et al., 2012; Gallagher et al., 1998).

Similar to the protein stability of PPPs, the highly regulated and rate-limiting enzyme GCLC was shown to have an intermediate stability with a calculated half-life of 19 hours. Interestingly, GSS showed no comparable protein degradation and appeared to be highly stably as 84 % of GSS remained completely intact after 24 hours of CHX treatment, so that no reliable linear regression and no valid half-life could be determined. Based on their cellular functions, the measured half-lives are considered to be reasonable. Similar to the highly controlled PPPs, which are not only regulated by degradation, but their enzymatic activity is additionally regulated by the attachment and dissociation of various subunits, e.g., regulatory, and scaffolding subunits, similar can be found for GCLC. GCL is a heterodimeric enzyme and requires besides the catalytic subunit (GCLC) a modifier subunit (GCLM) for full enzymatic activation, allowing for rapid and quick responses. In contrast, the enzymatic activity of GSS is not regulated, as the product of GCL is present at low concentrations in the presence of GSS, and only the first step of the GSH synthesis

pathway is considered to be rate-limiting (Anderson, 1998; Forman et al., 2009). Since the first step is highly regulated and controlled, no rapid and selective enzymatic activation or deactivation of GSS is not required. As a result, GSS may actually indicate a much higher protein stability.

Conclusion and Outlook

It can be concluded that the catalytic subunits of PPP1, PPP2A and PPP5, as well as the glutathione synthesizing and rate-limiting enzyme GCLC, can be classified as proteins of intermediate stability. Although the CHX chase assay is more suitable for short-lived proteins, the protein half-lives of the intermediate-stable proteins could be narrowed down to a range between 16 and 24 hours. For a more precise estimation, further analysis using more analytical and sensitive methods, e.g., proteasomal analysis via LC-MS/MS, should be performed. However, since this study was designed to provide initial information on the protein stability of the toxicodynamic parameters involved in the mechanism of microcystin toxicity, the data obtained seem to be sufficient and meaningful.

This study aimed to provide preliminary and first insights into the protein stabilities and half-lives of the essential PPPs and should be the basis not only for chronic exposure studies but also for microcystin-bound PPP degradation experiments to contribute to the understanding of the potential recirculation and toxicity of microcystin fragments.

6. Chapter V

6.1. Immortalized Human Hepatocyte Cell Line Characterization

6.1.1. Introduction

The liver is one of the most fascinating organs in the human body. Its ability to fully recover its structural integrity and functionality after a variety of injuries is unique and cannot be found in any other organ. In fact, this characteristic seems to be necessary given the crucial functions of the liver, including the metabolism, detoxification, and removal of various harmful substances from the body (Michalopoulos & Bhushan, 2021). All liver functions take place in the microscopic functional units, so called lobules. Each lobule consists of hepatocytes arranged in a distinctive hexagonal pattern around a central vein, with each corner of the hexagon being a portal triad consisting of a bile duct, hepatic artery, and a portal vein. Hepatocytes are the most abundant cell type found in the lobule, representing 60 % of the total cell number and 80 % of the total cell mass (Stanger, 2015). Accordingly, most of the liver-specific functions are performed within hepatocytes. Thus, hepatocytes display the highest cellular glutathione (GSH) concentration of any tissue (10 mM) (Meister, 1988), the highest amount of detoxifying enzymes (collectively termed P450 enzymes), and a wide variety of efflux and influx transporters to ensure toxin accumulation in the liver, thereby filtering the blood and protecting other organs from toxicity (Schulze et al., 2019).

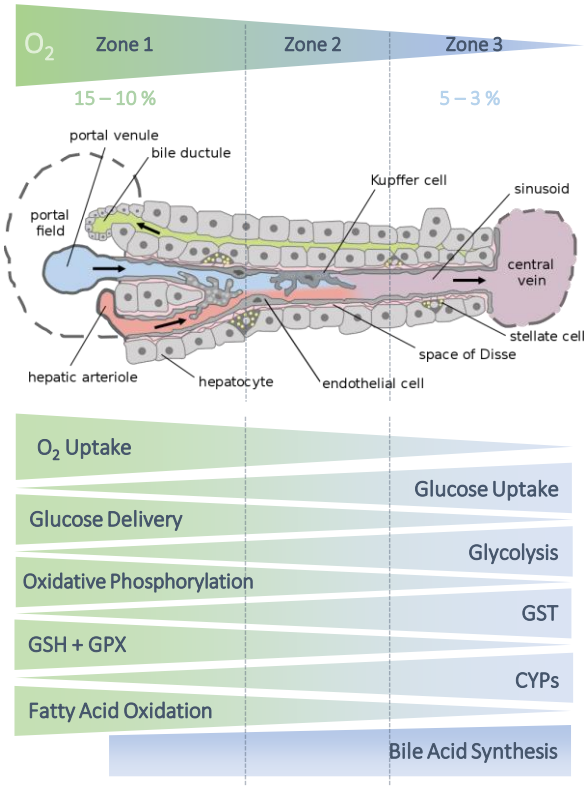

Figure 48: Liver Lobule Structure and Liver Zonation

The hepatic lobules are primarily composed of hepatocytes. Each lobule is divided into three zones based on the according oxygen levels. The hepatocytes in each zone perform different (metabolic) functions. Schematic illustration of the lobule was reproduced and adapted (Frevert et al., 2005). Information on zonation has been added (Kietzmann, 2017; Lee-Montiel et al., 2017; Stanger, 2015).

Their functions are uniquely regulated. One of the key features is their ability to exhibit functional heterogeneity. Despite similar morphology, hepatocytes located in the portal vein and central vein region have distinct functions. The division of the liver into distinct functional zones based on the distribution of blood, oxygen, nutrients, and metabolic activity is called liver zonation (Stanger, 2015). The lobule is thereby divided into three zones, see **Figure 48**. Zone 1 (or periportal zone) is located around the portal triads and is directly supplied with blood and oxygen. It has the highest oxygen content with 15-10 % oxygen. This zone includes energetically demanding functions, such as gluconeogenesis, and protein secretion. Zone 2 (or intermediary zone) is located in the midlobular zone, and its oxygen content is gradually decreased from 10 % to 5 %. Zone 3 (perivenous or centrilobular zone) is located around the central vein that drains the blood from the liver and has the lowest oxygen content (< 5 %). With decreasing oxygen, less energy-demanding processes such as xenobiotic metabolism and detoxification, bile acid and albumin biosynthesis, and glycolysis are engaged (Kietzmann, 2017; Schulze et al., 2019; Stanger, 2015).

Freshly isolated and healthy primary human hepatocytes are the gold standard for human toxicity testing and risk assessment (Kammerer & Küpper, 2018). However, the isolation and *in vitro* cultivation of primary hepatocytes is limited due to restricted accessibility, donor variability, and the retention of proliferative capacity due to cell cycle arrest, followed by rapid dedifferentiation and subsequently the rapid loss of liver-specific functions (Elaut et al., 2006; Jigorel et al., 2005; Kammerer & Küpper, 2018). Consequently, studies performed using primary hepatocytes are limited to only a few days. Hence, there have been attempts to overcome the limitations of primary cells, including various immortalization strategies of either fetal or adult hepatocytes. So far, the immortalization of healthy human hepatocytes has had only limited success (Ramboer et al., 2014). As a result, toxicity studies have been performed in in cell lines of carcinogenic origin. The most common and widely used human hepatocyte cell line is thereby HepG2.

HepG2 hepatocytes were originally isolated from a hepatoblastoma of a 15-year-old Caucasian male patient (Aden et al., 1979). Indeed, HepG2 have been shown to be highly proliferative and to exhibit hepatocyte-specific functions, such as albumin production and insulin-stimulated glycogen synthesis (Busso et al., 1990; Meier et al., 2007). However, HepG2 cells have been shown to lack human liver phase I and II enzymes (except CYP2B6) as well as essential xenobiotic influx and efflux transporters (Castell et al., 2006; Kammerer & Küpper, 2018; Louisa et al., 2016), making them rather unsuitable test systems for transporter-mediated toxicity testing, e.g., microcystins. Although HepG2 has been shown to express significantly low levels of OATPs (Louisa et al., 2016), microcystin-induced cytotoxicity studies have mainly been performed in this carcinogenic cell line. This raises the question of whether the results represent the actual mechanism of microcystin toxicity or merely the Paracelsus principle of 'the dose makes the poison'.

Aim of the Study

To date, microcystin toxicity studies have been limited to single exposures at relatively high microcystin concentrations, mostly in either rodent hepatocyte cell lines or human carcinogenic cell lines such as HepG2 with questionable OATP expression levels and therefore critical biological relevance. However, this does not reflect the current situation where most human intoxications have been reported as a result of chronic exposure to non-lethal microcystin concentrations. Prior to simulating chronic exposure in *in vitro* cell experiments, a reliable and suitable human hepatocyte cell line is required, see **Figure 49**. Therefore, immortalized human hepatocytes (IHH) were selected and characterized. IHH cells are non-tumorigenic liver epithelial cells. Primary hepatocytes were originally isolated from a healthy liver tissue of a 59-year-old male patient. The cells were immortalized by stable transfection with a recombinant plasmid containing the early region of the simian virus (SV) 40 (Schippers et al., 1997).

This study is divided into several parts:

(i) Characterization and identification of hepatocyte-specific properties of the IHH cell line.

(ii) Identification of microcystin relevant influx and efflux transporters (OATP1B1, OATP1B3, and MRP2).

(iii) Evaluation of microcystin toxicity and potential suitability of IHH cells for experimental studies of chronic microcystin exposure.

As a side project, the characterization of the IHH cell line was performed under standard atmospheric oxygen conditions (AtmOx, 21 % O_2), but also under physiological oxygen conditions (PhysOx, 5 % and 10 % O_2) to simulate liver zonation *in vitro*.

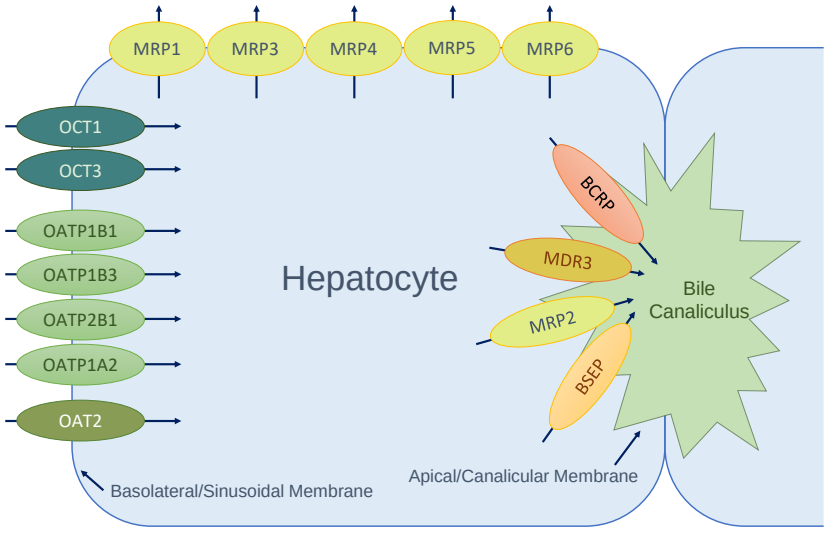

Figure 49: Chapter V Graphical Abstract

Human hepatocytes express a variety of essential transporters that regulate the uptake of xenobiotics into the hepatocyte, where they are immediately metabolized, detoxified, and eliminated. Therefore, the expression of transporters is highly regulated and expressed only at specific membranes (polarization) and responsible for hepatocyte-specific functions. To determine whether IHH cells are a suitable cell line for microcystin toxicity studies, the presence and expression of OATP1B1, OATP1B3, and MRP2 are critical and need to be identified. Schematic illustration was reproduced and adapted (Krajcsi, 2013).

6.1.2. Results

Although the clear aim of this study was to characterize IHH cells for microcystin toxicity testing under conventional culture conditions (AtmOx, 21 % O_2), an additional experimental setup was performed simultaneously to study whether liver zonation could be induced *in vitro*. Therefore, the cells were adapted to PhysOx conditions (5 % and 10 % O_2) for at least 14 days prior to measurements.

Morphology and Growth Characteristics

In vivo, healthy primary human hepatocytes have a polarized and epithelial-like structure, as indicated by their regular dimensions and polygonal shape. Human hepatocytes are rather large cells with a diameter ranging between 20 and 25 µm and are often found to be binucleated (Vinken & Hengstler, 2018). Adhesion of IHH cells to the culture dish was observed within a few hours under conventional culture conditions. Depending on the seeding density, IHH cells were either prolonged or polygonal in shape. While at low confluence, IHH cells appeared to be more elongated to form intercellular contacts with neighboring cells, see **Figure 50 A**, higher confluence resulted in a highly dense cell layer, but the polygonal shape was maintained. Unlike tumorigenic cell lines such as HEK293, IHH cells did not appear to overgrow and form tumor-like structures. A confluent monolayer could be maintained for at least 14 days. Interestingly, when a fully confluent and highly dense monolayer was reached, vacuole-like structures were formed evenly distributed throughout the monolayer, see **Figure 50 B**.

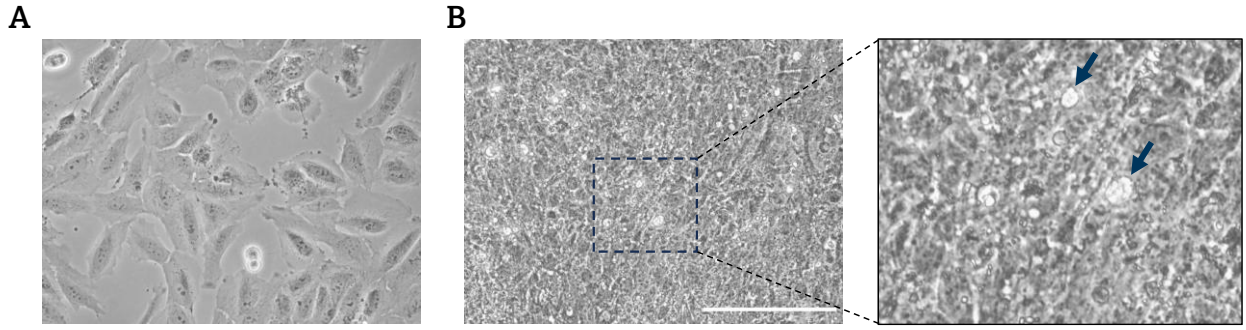

Figure 50: IHH Morphology

Cell monolayer of IHH showing **(A)** a rather prolonged but epithelial-like morphology at low confluence, while **(B)** at maximum confluence the cells became dense with increased formation of vacuole-like structures (see arrows). Scale bar indicates 150 µm.

In vitro cultured cells indicate a characteristic sigmoidal proliferation pattern, including a lag phase (cells do not divide and adapt to culture conditions) a logarithmic phase (cells start to proliferate and cell numbers increase exponentially), followed by a stationary phase (cell proliferation slows down due to confluency), and consequently a decline phase due to increased cell death. To study cell growth and potential contact inhibition properties of IHH, cell proliferation was monitored by daily cell counting. Morphological changes as well as cell densities were assessed, see **Figure 51**. Simultaneously, potential differences in morphology, cell growth and doubling times under both PhysOx conditions were evaluated.

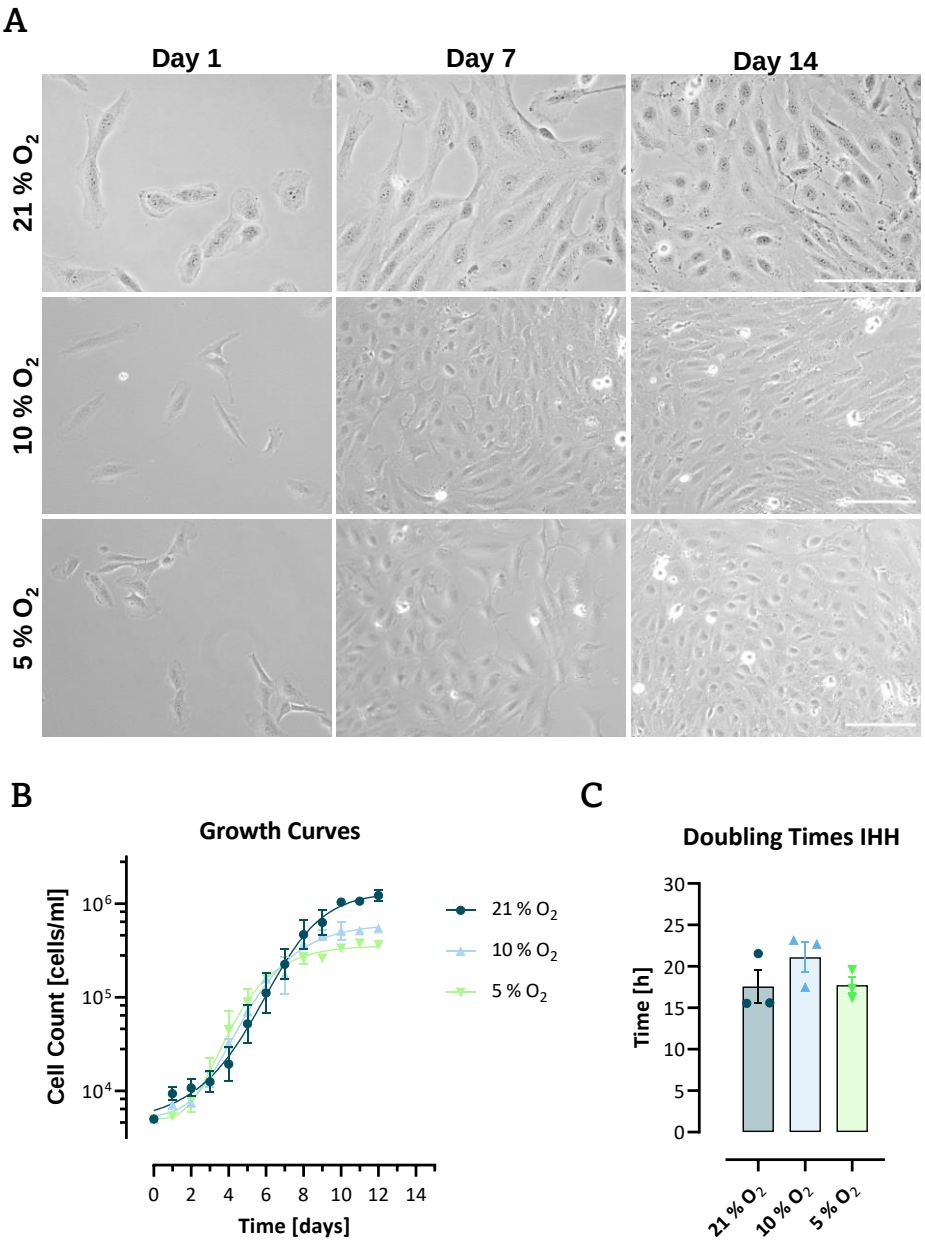

Figure 51: IHH Cell Growth Curves and Doubling Times

(A) No morphological differences were observed for either AtmOx or both PhysOx culture conditions over time (days 1-14), scale bars indicate 150 µm. (B) Growth curves were plotted for all conditions. Each point represents the mean of 3 independent biological replicates ± SEM (n=3). (C) Corresponding doubling times were statistically analyzed using one-way ANOVA, followed by Tukey's multiple comparison post-test. No significant differences were found.

No striking morphological changes were observed for either AtmOx or both PhysOx culture conditions, see Figure 51 A. The same was true for the cell growth curves. IHH proliferation displayed a sigmoidal shaped growth curve with a stable stationary plateau phase at approximately 10 days after seeding for all culture conditions, see Figure 51 B. Interestingly, the cell density in the stationary plateau phase was significantly higher under AtmOx culture conditions ($1.1x10^6$ cells/ml) compared to both PhysOx culture conditions. IHH cells grown at 10 % and 5 % oxygen, reached the stationary plateau phase with comparable cell densities of $5.2x10^5$ cells/ml and $3.6x10^5$ cells/ml, respectively, raising the question

whether these culture conditions lead to an increase in cell size. Nevertheless, no significant differences were observed in the corresponding doubling times under AtmOx (18 hours) or 10 % and 5 % PhysOx conditions (21 hours and 18 hours, respectively), see Figure 51 C.

IHH Do Not Undergo Epithelial-To-Mesenchymal Transition (EMT)

The epithelial-to-mesenchymal transition (EMT) is a highly dynamic process in which epithelial cells lose their cell polarity, cell-cell adhesion and, consequently, their typical morphological structure. The cells gain migratory and invasive properties and become mesenchymal cells. In healthy organisms, this process is crucial for embryonic development, tissue regeneration and wound healing. In *in vitro* cell culture, however, this process leads to the loss of characteristic cell functions.

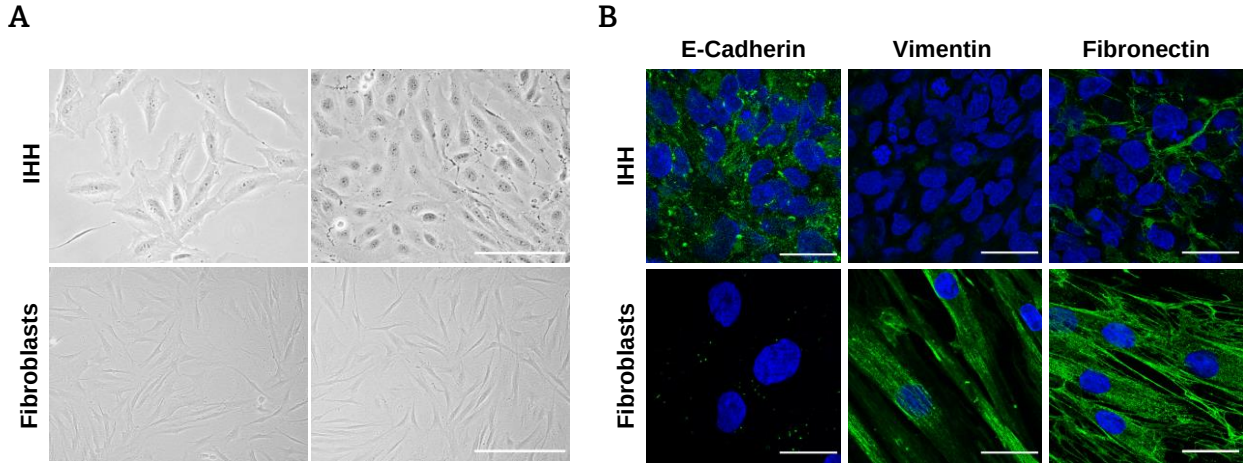

Figure 52: Epithelial-to-Mesenchymal Transition of IHH

(A) IHH cells showed prolonged but epithelial-like polygonal shaped morphology, whereas fibroblasts showed a significantly more elongated cell shape without many cell-cell attachments; scale bars indicate 150 µm. (B) IHH showed the expression of the epithelial marker E-cadherin and lacked the expression of the mesenchymal marker vimentin. Only low levels of fibronectin were detected. Fibroblasts were used as control. Nuclei were visualized with Hoechst; scale bars indicate 30 µm.

Hepatocytes are known to be highly susceptible and sensitive to EMT, especially under standard *in vitro* culture conditions. Therefore, IHH cells were compared to fibroblasts, the most common cell type in connective tissue and highly involved in wound healing. Although at first glance IHH cells appeared to have a more prolonged shape, especially at lower cell densities, compared to the clearly elongated fibroblasts with reduced cell-cell attachments, the IHH cells exhibited a clearly epithelial-like morphology, see Figure 52 A. Indeed, the epithelial marker E-cadherin was present only in IHH but not in fibroblasts, see **Figure 52** B. Vice versa, the mesenchymal maker was absent in IHH. Fibronectin expression was low in IHH cells but significantly higher in fibroblasts.

Since previous studies reported that PhysOx culture conditions significantly reduced hepatocyte dedifferentiation *in vitro* (Guo et al., 2017), EMT markers were simultaneously monitored under both PhysOx conditions, see **Figure 53**. Surprisingly, the expression of the epithelial marker E-cadherin was slightly reduced in both PhysOx conditions compared to AtmOx, see Figure 53 A. While only a very low

signal was detected in 10 % but not in 5 % oxygen culture conditions, see **Figure 53 B**. Whereas fibronectin expression was completely depleted in both PhysOx conditions, see **Figure 53 C**.

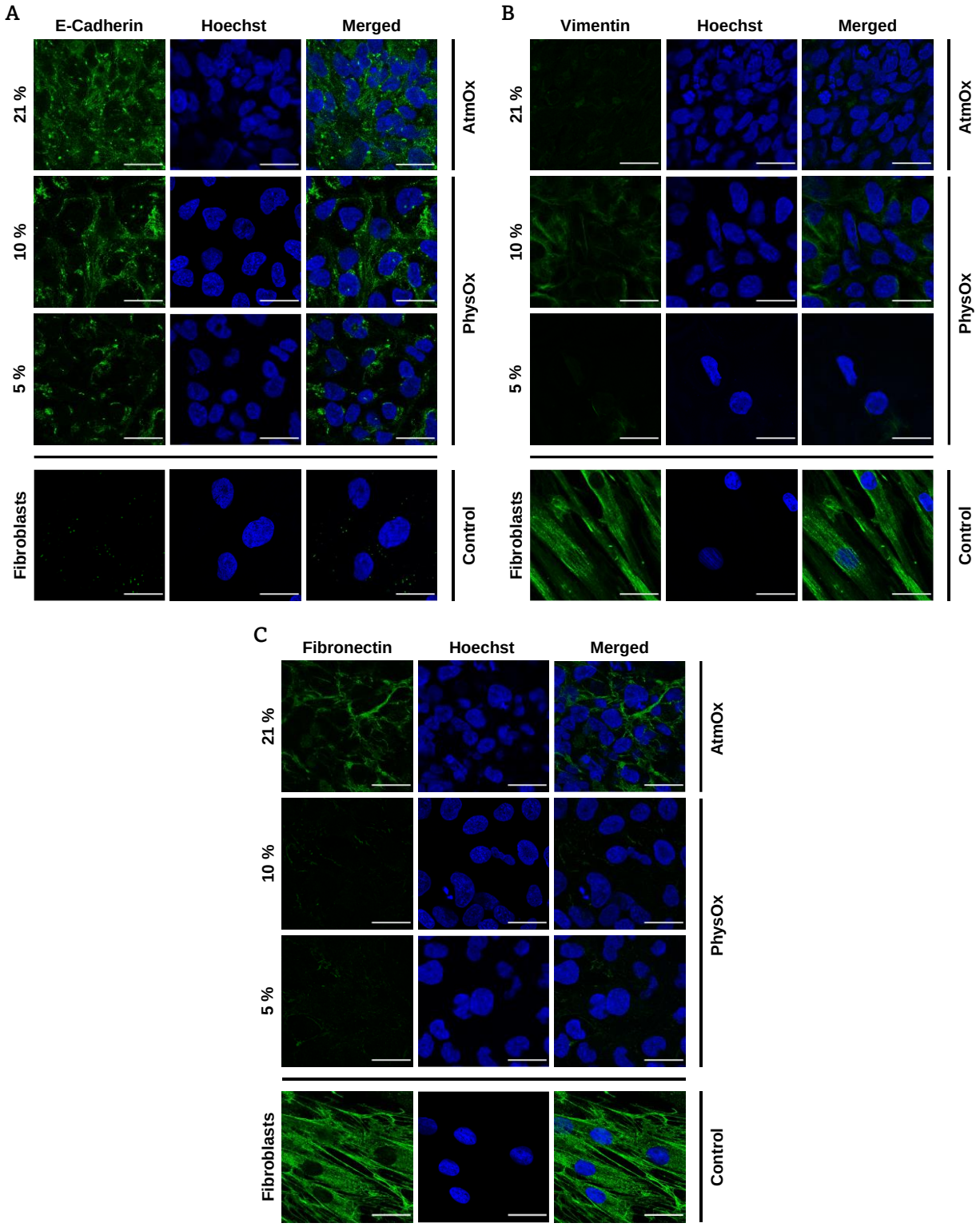

Figure 53: Immunocytochemistry of EMT Markers AtmOx vs. PhysOx

Immunocytochemistry was used to study changes within the protein expression of **(A)** the epithelial marker E-cadherin and the mesenchymal markers **(B)** vimentin and **(C)** fibronectin in AtmOx and both PhysOx culture conditions. As positive control for EMT, protein expressions were compared to fibroblasts. Nuclei were stained with Hoechst; all scale bars indicate 30 µm.

IHH Express Microcystin Relevant Influx and Efflux Transporters

Unfortunately, the parental and original primary hepatocytes used to establish the IHH cell line were not available to study the potential retention of transporters after immortalization. Therefore, IHH gene expression of essential hepatic influx and efflux transporters, including the microcystin-relevant transporters OATP1B1, OATP1B3, and MRP2, characteristic detoxifying enzymes and hepatic markers were identified using commercially available whole human liver lysate (WHLL). It should be noted that the WHLL includes all cell types found in the human liver and therefore a direct one-to-one comparison of expression levels was not intended, but rather the identification of the presence or absence of gene expression. However, since hepatocytes are the predominant cell type found in the human liver (60 %) WHLL was considered suitable for primer validation and identification of the IHH gene expression pattern.

According to the graphical abstract (see **Figure 49**), MDR1, MDR3, and MRP4 were used as characteristic hepatic efflux transporters. One the other hand, OCT1, OATP1B1, OATP1B3, OATP2B1, and OAT2 were used as characteristic hepatic influx transporters , which are typically expressed on the basolateral side of hepatocytes. While the efflux transporters BCRP, MDR3, MRP2, BSEP as well as the P-type ATPase ATP8B1 were used as transporters directed to the apical, i.e., canalicular, side of hepatocytes. In fact, except for OAT2 and OATP2B1, all analyzed transporters were found to be expressed in the IHH cell line, see **Figure 54**. While MRP1, MRP4, BCRP, and ATP8B1 were significantly higher expressed in IHH cells, MDR3, BSEP, and OCT1 genes showed a rather low gene expression compared to WHLL. Strikingly, the OATP1B3 gene was more abundant than OATP1B1 in the IHH cell line. Indeed, immunocytochemistry using anti-OATP1B1 and -OATP1B3 antibodies confirmed the significantly lower expression of OATP1B1, see **Figure 54 A**. Similarly, the rather low expression of BSEP was confirmed, see **Figure 54 B**. Interestingly, MRP2 antibody staining revealed the concentration of MRP2 at specific sites, cautiously suggesting a potential polarity of IHH.

Surprisingly, the gene expression of the hepatocyte-specific detoxification enzymes CYP2C9 was rather low, while CYP3A4 could not be detected. Likewise, the prominent hepatic marker HNF1A was absent in IHH, while HNF4 was detectable, albeit only at low levels. To test whether CYPs other than CYP3A4 and CYP2C9 are expressed in IHH cells, immunocytochemistry was performed using anti-CYP7A1 and -CYP8B1. Unfortunately, hardly any signal could be detected for both cytochrome P450 enzymes, see **Figure 54 B**, suggesting a rather reduced detoxification potential of IHH.

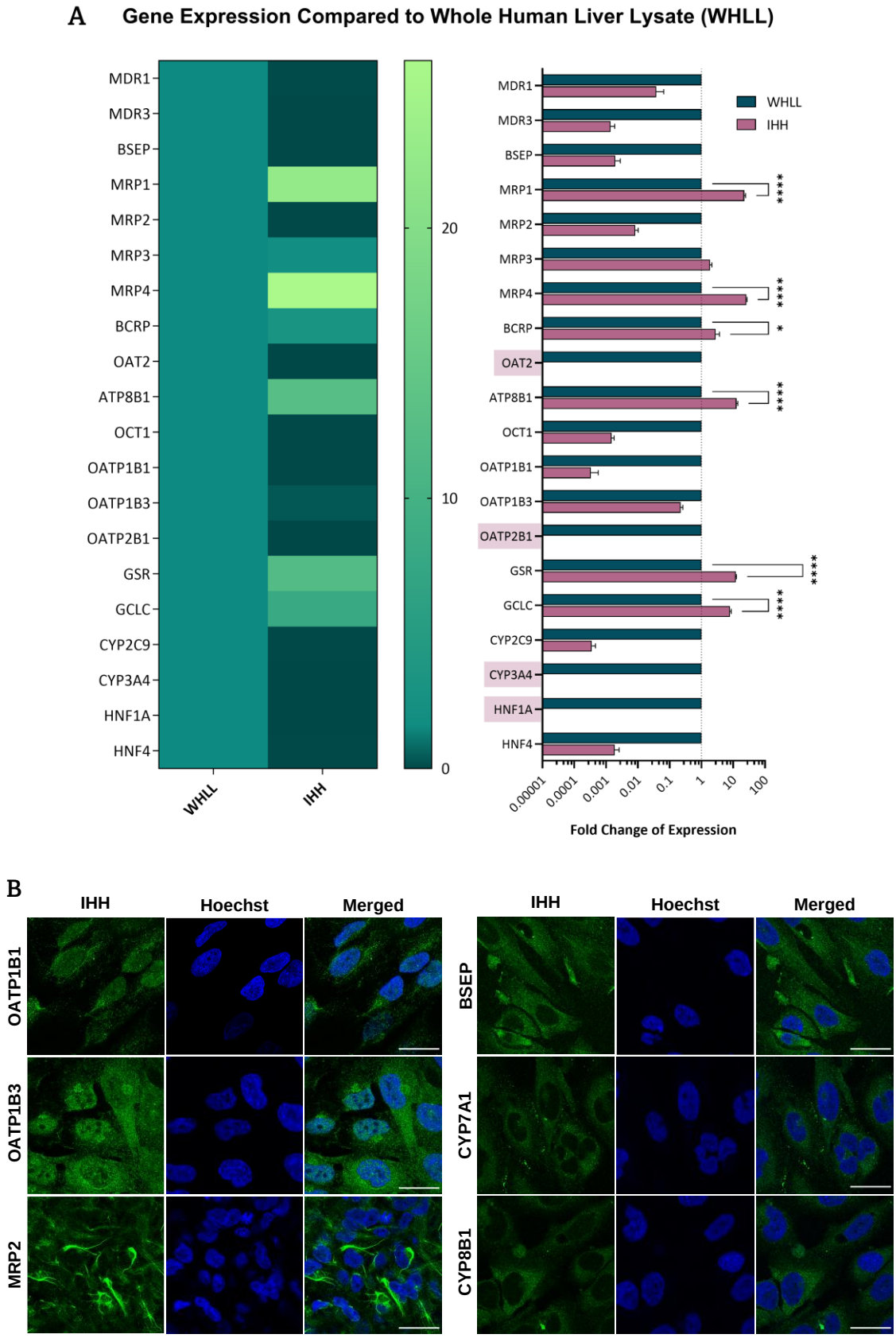

Figure 54: Gene Expression Pattern of IHH

(A) Gene expression was expressed as fold change relative to commercially available whole human liver lysate (WHLL) and visualized as a heatmap and bar graph (SEM, n=3). Statistical analysis was performed using a two-way ANOVA, followed by Šídák post-test (*p=0.0376; ****p<0.0001). **(B)** Immunocytochemistry using anti-OATP1B1, -OATP1B3, -MRP2, -BSEP, -CYP7A1 and -CYP8B1 was performed to visualize the corresponding protein expression. Nuclei were stained with Hoechst; all scale bars indicate 30 µm.

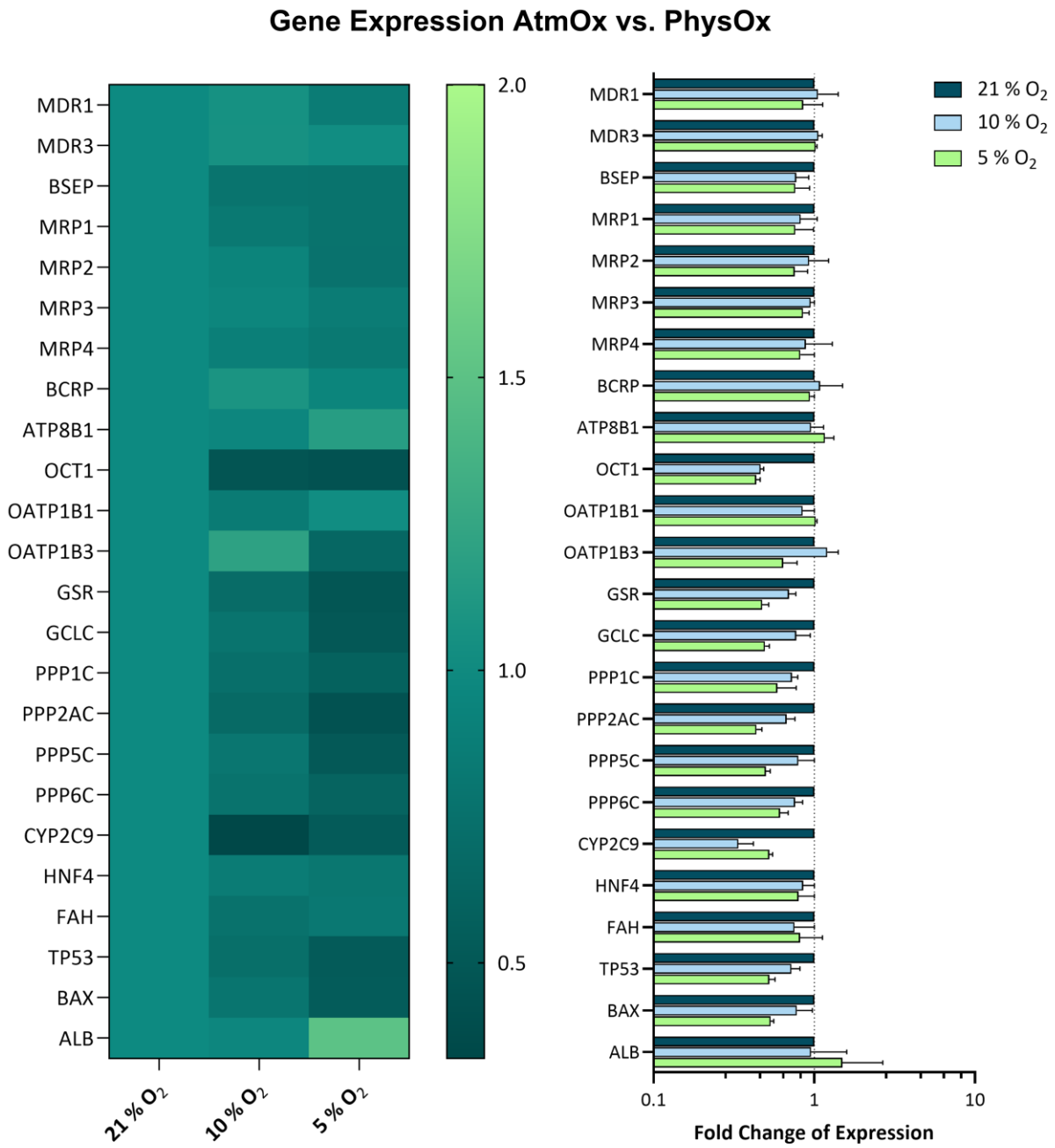

Figure 55: Gene Expression AtmOx vs. PhysOx

Gene expression measured for both PhysOx culture conditions (10 % and 5 % O_2) was expressed as fold change relative to AtmOx (21 % O_2) and visualized as a heatmap and bar graph (SEM, n=3). Statistical analysis was performed using a two-way ANOVA, followed by Šídák post-test. No statistically significant differences were found between AtmOx and PhysOx gene expression patterns.

At the same time, changes within the gene expression pattern under both PhysOx culture conditions were evaluated and compared to AtmOx, see **Figure 55**. Therefore, in addition to hepatocyte-specific transporters, gene expression of microcystin-relevant enzymes (PPP1C, PPP2AC, PPP5C, and PPP6C), apoptotic markers (TP53 and BAX), and liver-specific markers (HNF4, FAH, and ALB) were analyzed and compared. Although slight variations in gene expression were observed, no statistically significant up- or downregulation could be detected. Note: Significant differences in gene expression are only conclusive if at least a 2-fold change in expression can be detected.

Functionality and Metabolic Activity

To evaluate the functionality and metabolic activity of IHH, the gene expression of albumin (ALB) was further analyzed. Albumin production is an important indicator of healthy hepatocyte function. In some hepatocyte cell lines, such as AML12, the expression of liver-specific proteins decreases over time but can be reactivated by culturing the cells in serum-free medium. Therefore, albumin gene expression was analyzed not only under AtmOx and PhysOx culture conditions, but additionally using normal growth medium (supplemented with 10 % FCS) and serum-free medium (no FCS), see **Figure 56**. While no differences in albumin gene expression were observed using culture medium under AtmOx and PhysOx conditions, treatment of cells with serum-free medium resulted in significantly upregulated albumin gene expression under both 10 % and 5 % PhysOx conditions compared to AtmOx (3.4-fold and 3.2-fold, respectively). Nevertheless, to confirm the results obtained, further analysis of the actual protein expression levels should be performed to validate the gene expression data.

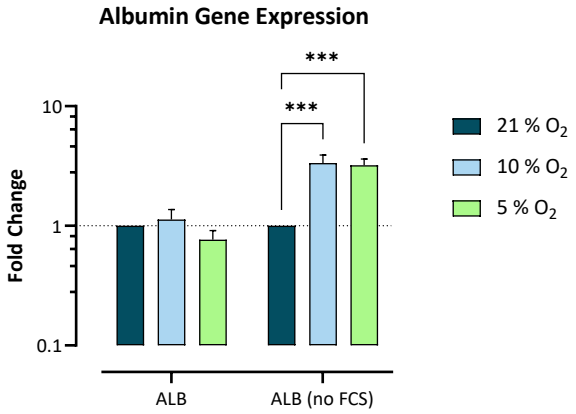

Figure 56: Albumin Gene Expression

Albumin (ALB) gene expression was expressed as fold change relative to AtmOx (21 % O_2). IHH cultured using standard growth medium, supplemented with 10 % FCS, resulted in comparable ALB gene expression under AtmOx and both PhysOx (10 % and 5 % O_2) conditions. In contrast, IHH cultured in serum-free (no FCS) medium, showed significantly upregulated ALB gene expression in both PhysOx conditions. The fold change in gene expression was visualized as a bar graph (SEM, n=3). Statistical analysis was performed using two-way ANOVA, followed by Tukey's multiple comparison post-test (***p=0.001).

To assess the potential induction of liver zonation under PhysOx culture conditions, the Seahorse XF real-time ATP rate assay kit was used to quantify the rate of ATP production from either mitochondria (oxidative phosphorylation, OXPHOS) or glycolysis. And indeed, differences within the source of ATP production could be clearly induced, see **Figure 57**. While the difference between glycolysis and OXPHOS was only barely observable under AtmOx culture conditions (53 % and 47 %, respectively), the differences were significant under PhysOx conditions. When cells were cultured at 10 % oxygen, corresponding to zone 1 (periportal zone), OXPHOS was clearly favored over glycolysis (75 % and 25 %, respectively). In contrast, when cells were cultured at 5 % oxygen, corresponding to zone 3 (perivenous/centrilobular zone), glycolysis was preferentially used to produce ATP over glycolysis (69 % and 31 %, respectively), clearly representing the potential induction of liver zonation.

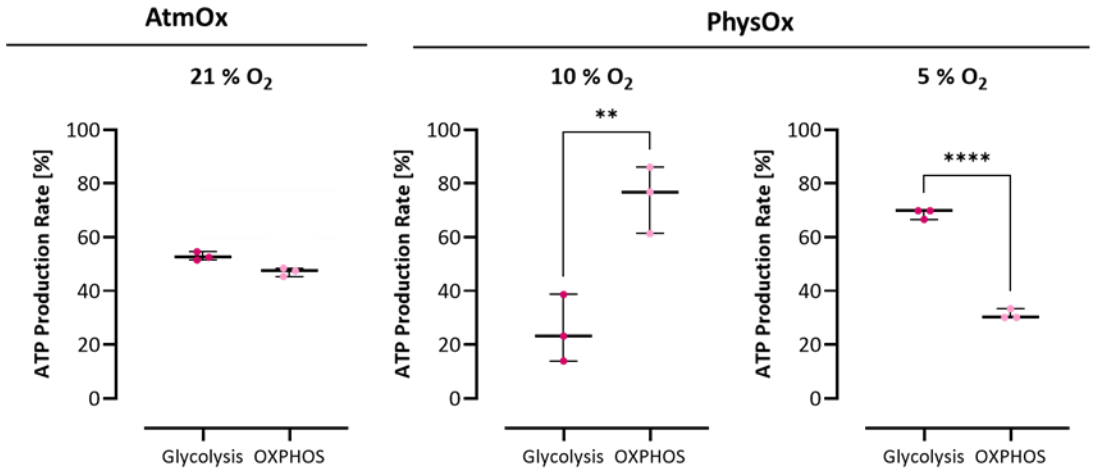

Figure 57: ATP Production Rate AtmOx vs. PhysOx

ATP production rate was measured using the Seahorse XF real-time ATP rate assay kit. Assay was performed in the corresponding oxygen condition. Each point represents one biological replicate consisting of 5 technical replicates (n=3). Statistical analysis was performed using a two-tailed unpaired t-test (**p=0.0083, ****p<0.0001).

Microcystin-Induced Cytotoxicity

Since both microcystin-relevant influx transporters OATP1B1 and OATP1B3 were detected at the gene and protein expression level, microcystin-induced cytotoxic effects were investigated. To this end, IHH cells were exposed to either MC-LR or MC-RR for 48 hours and cell viability was subsequently measured, see **Figure 58**. Indeed, both microcystin congeners induced a sigmoidal concentration-dependent decrease in cell viability, although with different toxicities, see **Figure 58 A**. A concentration of 16.57 µM of the most abundant and predominant congener MC-LR was required to reduce hepatocyte cell viability by 50 %. In contrast, one of the most hydrophobic congeners MC-RR, was less toxic, requiring a statistically significant 2.4-fold higher concentration to induce a similar effect (39.59 µM), see **Figure 58 B**.

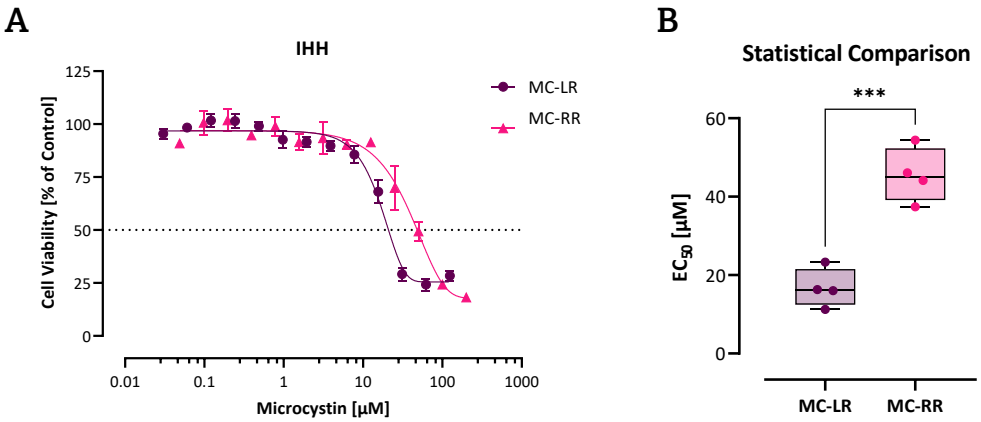

Figure 58: Microcystin-Induced Cytotoxicity in IHH

(A) Measured cell viability after MC-LR and MC-RR exposure in IHH. Each point represents 4 independent biological replicates, pipetted in triplicates ± SEM (n=4). EC_{50} values were calculated using asymmetric nonlinear regression. **(B)** Individual EC_{50} value of each biological replicate was statistically compared using a two-tailed unpaired t-test (***p=0.0005).

Comparison of Immortalized Human Hepatocytes (IHH) and Mouse Hepatocytes (AML12)

Since microcystin toxicity studies were mostly performed using rodent, moreover, mouse hepatocytes and the whole human microcystin risk assessment provided by the World Health Organization (WHO) is based on a mice study, IHH were compared to a frequently used mouse hepatocyte cell line (alpha mouse liver 12, AML12). The differences in morphology and cell structure were striking, see Figure 59 A. Compared to IHH, AML12 cells showed an increased formation of vacuole-like structures of unknown function. To test whether these vacuole-like structures are lipid or glycogen storages, Oil-Red-O and Periodic-Acid-Schiff (PAS) staining kits were used. While glycogen accumulations could be visualized in IHH, vacuole-like structures could not be identified as either glycogen or lipid storages, see Supplementary Figure 15. In fact, MC-LR exposure led to the typical features of cell rounding, loss of cell-cell adhesion and finally to the formation of apoptotic bodies comparable for both cell lines, see **Figure 59 B**. Similar to the results observed in IHH, MC-LR exposure resulted in a concentration-dependent decrease in cell viability in AML12, albeit with different toxicities. AML12 appeared to be significantly less sensitive to MC-LR, with a 3-fold higher EC_{50} of 53.66 µM compared to the human hepatocytes, see Figure 59 C.

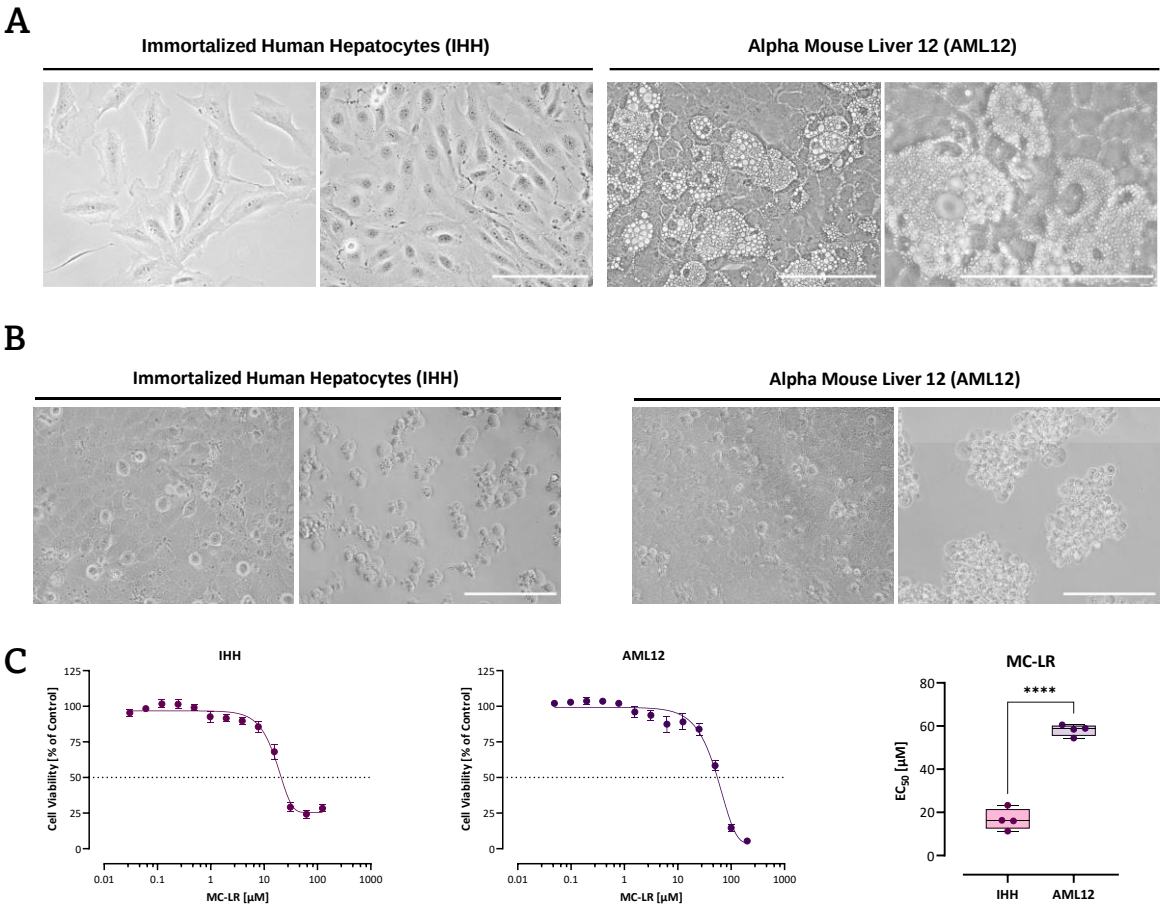

Figure 59: Microcystin-Induced Cytotoxicity in Human Hepatocytes vs. Mouse Hepatocytes

(A) Normal cellular morphology of IHH and AML12; all scale bars indicate 150 µm. **(B)** Morphological changes induced after the exposure of either 15 µM (left) or 100 µM (right) MC-LR; all scale bars indicate 150 µm. **(C)** Comparison of the cytotoxicity curves of IHH and AML12. Each point represents 4 independent biological replicates, pipetted in triplicates ± SEM (n=4). Individual EC_{50} value of each biological replicate was statistically compared using a two-tailed unpaired t-test (****p<0.0001).

6.1.3. Discussion

For human toxicity studies, freshly isolated and healthy human hepatocytes are a valuable tool and the gold standard for accurate risk assessment and evaluation. However, the isolation and *in vitro* cultivation of these primary cells is limited by restricted accessibility, donor variability, and the retention of proliferative capacity due to cell cycle arrest, followed by rapid dedifferentiation and subsequent loss of liver-specific functions. Consequently, long-term experiments, such as chronic toxicity studies, are not possible due to the rapid loss of function and their short-term viability (Kammerer & Küpper, 2018). Hence, alternatives have been attempted to overcome the limitations of primary cells, including various immortalization strategies.

To successfully establish a fully functional hepatocyte cell line, the following problems have to be overcome: i) isolated hepatocytes are typically in G_0 cell cycle arrest and must be forced back into the cell cycle to reactivate their proliferative properties; ii) hepatocyte-specific functions, such as the production of albumin and bile acid and the expression of detoxifying enzymes, such as cytochrome P450 (CYPs), must be maintained; iii) dedifferentiation associated with EMT must be prevented; and iv) essential influx and efflux transporters responsible for xenobiotic uptake/elimination and associated cellular polarity must be maintained (Elaut et al., 2006; Jigorel et al., 2005; Kammerer & Küpper, 2018).

Schippers et al. reported the successful establishment of a non-carcinogenic immortalized human hepatocyte (IHH) cell line. Therefore, primary hepatocytes, originally isolated from a healthy liver tissue of a 59-year-old male patient, were immortalized by stable transfection with a recombinant plasmid containing the early region of SV40. Cells were selected for proliferative colonies, secreting high levels of albumin, while proliferating but metabolically inactive cells were excluded (Schippers et al., 1997). This resulted in the establishment of a functional cell line that was shown to respond properly to external stimuli comparable to freshly isolated primary hepatocytes, as measured by secretion of fibrinogen, apolipoprotein B, and albumin. Interestingly, IHH cells were shown to form bile canaliculi-like structures as evidenced by microscopic evaluation and accumulation of glutathione methylfluorescein. However, not all cells showed a similar ability to form bile canalicular-like structures with associated cell polarization (Schippers et al., 1997). And indeed, similar observations were seen in this study, consistent with the reported data. Vacuole-like structures were formed only when an exceptionally full confluent monolayer was maintained for several days. These vacuole-like structures were initially thought to be glycogen storage compartments. However, because these vacuole-like structures differed in size and distribution from glycogen storages stained with PAS, and because these formations were present only at very high cell densities, it is reasonable to assume that these formations may be bile canalicular-like structures as described in the original paper by Schippers et al., (1997). This is also supported by the fact that the ATP8B1 gene, which encodes an ATPase highly present in the canalicular membrane (Cai et al., 2009; Paulusma et al., 2006), showed a 13-fold upregulation compared to WHLL, indicating the potential for bile canaliculi formation.

In addition, growing the cells under both PhysOx conditions appeared to be potentially beneficial for the formation of bile canaliculi-like structures. Although it appeared to be difficult to grow cells at this high cell densities, as cells stopped growing at cell densities of $5.2x10^5$ cells/ml (10 %) and $3.6x10^5$ cells/ml (5 %) at PhysOx culture conditions. But nevertheless, an increase and accumulation of CD10 expression, a marker of biliary canaliculi membrane (Shousha et al., 2004), was observed in both PhysOx conditions compared to the standard AtmOx culture conditions, see **Supplementary Figure 16**. Similarly, immunocytochemical staining with anti-MRP2 antibody suggested a possible polarization of IHH cells. However, these data provide only initial insights into the formation of bile canaliculi-like structures and are preliminary in nature and should therefore be treated with caution. Further validation using transport assays and electron microscopic analyses are required to confirm the reported observations.

In fact, Schippers et al. similarly reported the expression of MRP2, which is known to be expressed at the apical/canalicular site of hepatocytes and is associated with cell polarization. But so far, despite the confirmed expression of MRP2 and MRP1 (Schippers et al., 1997), no data on the presence or possible retention of transporters are available for the IHH cell line. Therefore, the gene expression of the essential and hepatocyte-specific transporters was analyzed prior to using the IHH cell line for toxicity studies. And indeed, except for OAT2 and OATP2B1, the expression of all analyzed transporters was confirmed. Interestingly, OATP1B1 appeared to be expressed at lower levels than OATP1B3, as evidenced by gene expression and confirmed by protein expression using immunocytochemical staining. In general, OATPs were shown to have high interindividual specificity and donor variability (Fischer et al., 2010; König et al., 2000a). Moreover, the expression of OATPs in primary human hepatocytes was shown to differ depending on the location of the hepatocytes within the liver. Thereby, hepatocytes located in the central vein region were shown to express significantly more OATP1B3 than hepatocytes located in the portal vein region, indicating that the location of isolation plays a role in the transporter expression pattern (König et al., 2000a). Since the primary hepatocytes used for immortalization were isolated from adult tissue and are not derived from hepatic stem cells, the loss of liver-specific transporters, such as OATPs or sodium-dependent transporters, prior to immortalization cannot be excluded (Schippers et al., 1997). The same holds true for the loss of liver-specific functions, which were shown to be significantly reduced already within three days (Liang et al., 1993; Schippers et al., 1997), making it almost impossible to maintain full primary hepatocyte function in an immortalized cell line. Therefore, a special experimental setup using PhysOx instead of conventional standard culture conditions might be an interesting and useful tool to restore or at least maintain physiological function for a longer period of time. And indeed, by culturing primary human hepatocytes under both PhysOx conditions, dedifferentiation associated with EMT could be delayed and primary cells could be cultured for a longer period of time (Guo et al., 2017). Thus, it is reasonable to expect similar beneficial effects on metabolic activities. Therefore, changes in metabolic activity as well as gene and protein expression were analyzed under 10 % and 5 % PhysOx culture conditions in an attempt to mimic liver zonation *in vitro*. The fact that the PhysOx conditions did not show clear effects on EMT was

not surprising, since IHH have been shown not to undergo EMT in general. More interestingly, both PhysOx culture conditions showed no effect on gene expression levels, even though the cells had been adapted to the corresponding oxygen condition for at least 14 days prior to the measurement. Since most of the available data investigating the correlation between liver zonation and gene expression patterns focused on whole liver sections (Cunningham & Porat-Shliom, 2021; Hildebrandt et al., 2021; Zhang et al., 2023), it is difficult to draw conclusions for an immortalized cell line.

Moreover, since this study focused mainly on the identification of transporters and only analyzed a few metabolic genes, including CYPs, which were not detected in IHH cells, no clear conclusion can be drawn. It could be theorized that IHH cells, which have been immortalized and maintained under conventional standard culture conditions for a longer period of time, require more time to adapt to the corresponding culture condition (> 14 days) than used in this experimental setup, or that the liver zonation induced within an established cell line is manifested by changes in the metabolic activity rather than in (transporter) expression levels. Indeed, the first indications of successful induction of liver zonation were seen in the ATP production rate, measured at the corresponding oxygen concentration using the Seahorse XF real-time ATP rate assay kit. While the differences between glycolysis and OXPHOS were only barely observable under AtmOx culture conditions, the differences were significant under PhysOx conditions. Cells cultured at 10 % oxygen, corresponding to zone 1 (periportal zone), clearly favored OXPHOS over glycolysis. In contrast, cells cultured at 5 % oxygen, corresponding to zone 3 (perivenous/centrilobular zone), preferentially used glycolysis to produce ATP, in agreement with data presented in the literature and thus clearly demonstrating the first steps towards the induction of liver zonation *in vitro* (Kietzmann, 2017). Needless to say, that the data presented here are preliminary and clearly should be further validated and analyzed for a complete picture. Metabolic liver zonation is not only manifested in the glycolysis and OXPHOS ratio, but also the fatty acid oxidation or bile acid synthesis should be significantly different in zone 1 and zone 3 and could be further analyzed to validate the potentially induced zonation (Cunningham & Porat-Shliom, 2021; Kietzmann, 2017). Nevertheless, the data obtained in this study suggest the potential beneficial use of the PhysOx culture condition *in vitro*, and IHH as a useful immortalized human hepatocyte cell line.

Conclusion and Evaluation of IHH Cell as Cell System For Microcystin Toxicity Testing

The aim of this study was to characterize an immortalized but non-carcinogenic human hepatocyte cell line as a suitable cell system for chronic microcystin exposure. Therefore, the not widely known IHH cell line was used. The IHH cell line was found to be easy to maintain, exhibited healthy and normal cell growth, as well as contact inhibitory properties that allowed the maintenance of a confluent cell monolayer over time, which is critical for chronic exposure studies. Moreover, IHH cells exhibited essential hepatocyte-specific properties as the potential induction of bile canaliculi-like structure and polarity, as well as typical epithelial-like morphology and no EMT-associated dedifferentiation.

Indeed, microcystin-relevant influx and efflux transporters (OATP1B1, OATP1B3, and MRP2) were positively identified at both gene and protein expression levels, see **Figure 60**. Although IHH cells lacked liver-specific CYPs, glutathione-related enzymes (GSR, GSS, GCLC; and GSH itself, see Chapter III) were expressed in the expected quantities. Since microcystins are known not to be involved in CYP-related biotransformation (Arman & Clarke, 2021; Buratti et al., 2011; Vichi et al., 2016), the lack of CYPs expression was not considered critical. The same holds true for the lack of expression of OATP2B1, as previous studies clearly demonstrated no OATP2B1-mediated uptake of microcystins (Fischer et al., 2005). Similarly, the lower expression of OATP1B1 compared to OATP1B3 is considered to be due to donor variability and is therefore assumed to mirror the expression ratio in adult human hepatocytes and therefore not considered to be critical.

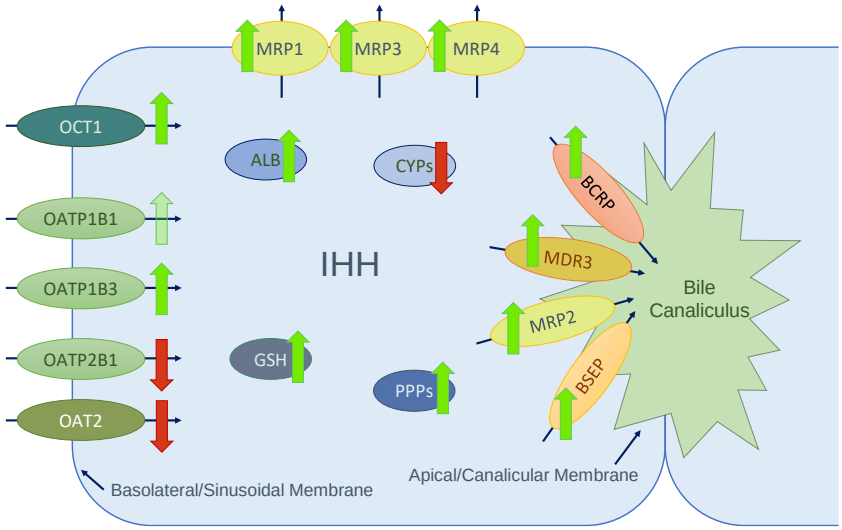

Figure 60: Schematic Overview of Immortalized Human Hepatocyte (IHH)

Characterization of immortalized human hepatocytes (IHH) revealed the presence of the critical hepatocyte-specific transporters OCT1, OATP1B1, OATP1B3, MRP1, MRP2, MRP3, MPR4, BCRP, MDR3 and BSEP. Moreover, IHH were shown to produce albumin (ALB), demonstrated the presence of glutathione (GSH) relevant enzymes (GSR, GSS, GCLC, and GSH itself), and the presence of all PPPs, as indicated by green arrows. While the expression of CYPs and the transporters OATP2B1 and OAT2 was not confirmed, as indicated by red arrows. Since neither CYPs, OATs nor OATP2B1 play a role in the mechanism of microcystin toxicity, the IHH cell line appeared to be a suitable cell model for (chronic) microcystin exposure studies.

Initial microcystin toxicity analysis using MC-LR and MC-RR confirmed OATP-mediated uptake, as indicated by the sigmodal concentration curve. However, cytotoxicities were measured in significantly higher concentration ranges compared to the previously used HEK293 cell lines (µM instead of nM, see Chapters II and III). In contrast to the stably transfected HEK293 cell lines, the hepatocyte cell line IHH does not overexpress OATPs, but expresses both transporters at physiologically relevant quantities. Combined with the fact that IHH cells additionally express several efflux transporters, including MRP2, higher microcystin concentrations were required to reduce cell viability by 50 %. Nevertheless, similar effects as observed in the HEK293 cell lines were observed in the IHH cells. Although OATP1B1 was expressed at lower levels, the hydrophobic congener MC-RR demonstrated significantly less cytotoxicity compared to the more hydrophilic MC-LR. To validate a similar pattern as shown in Chapter II, further

analysis with more congeners is recommended. Overall, however, the functionality and suitability of IHH cells as a test system for (chronic) microcystin exposure studies can be confirmed.

The current microcystin risk assessment is primarily based on a mouse study performed in 1999 with a single microcystin congener (MC-LR) and has remained unchanged since then (Fawell et al., 1999; World Health, 2020), even though more than 250 congeners have been described (Spoof & Catherine, 2016) and congener-specific toxicity have been demonstrated (Altaner et al., 2020; Fischer et al., 2010). However, studies have shown that mice vary widely in the expression of OATPs, as well as in the affinity and capacity for microcystin-mediated transport (Fischer et al., 2010; Fischer et al., 2005). Therefore, mouse hepatocytes (AML12) were used and compared to the IHH cells. The AML12 cell line is a widely used mouse hepatocyte cell line, particularly used in in the field of toxicology, and is a suitable test system for microcystin research (McLellan & Manderville, 2017). Although significant differences in morphology were observed, a similar microcystin-induced response was observed, as indicated by the loss of cell-cell contacts, cell rounding and induction of apoptotic bodies (note: prior to microcystin exposure, the availability and expression levels of mouse specific Oatps were confirmed and compared to mouse whole liver lysates, data were not shown). Strikingly, the observed cytotoxicities of the most common microcystin MC-LR, on which also the WHO guideline is based on, indicated significant differences in cytotoxicity in mouse compared to human hepatocytes. AML12 appeared to be significantly less sensitive to MC-LR, with a 3-fold higher EC_{50} concentration (53.66 µM) compared to the human hepatocytes (16.57 µM). Combined with the striking results obtained in Chapter III, this raises the question of a potential underestimation of microcystin toxicity.

7. Concluding Discussion

Despite the fact that more than 250 microcystin congeners have been described so far (Spoof & Catherine, 2016), the understanding of their toxic mechanism remains incomplete since their toxicities have been assessed using only a few congeners, including limited aspects of toxicity. However, the mechanism of microcystin toxicity can only be fully understood by evaluating and combining its toxicodynamic (e.g., PPP inhibition but also GSH conjugation capabilities) and toxicokinetic (e.g., cellular influx/efflux) properties. Consequently, the primary aim of this dissertation was to identify the characteristics responsible for the induction of toxicity and their respective contributions to either toxicodynamic or -kinetic properties. Thereby, each chapter addressed specific questions and aspects of toxicity, starting with the basic understanding of its mode of action, followed by studies in simplified cell systems (OATP-expressing HEK293 cell lines), and subsequently progressing to more complex but biologically more relevant cell systems (human and mouse hepatocytes). Since all chapters of this dissertation included in-depth discussions with cross-references to all chapters, this concluding discussion is aimed to summarize and emphasize the distinctive findings, thereby incorporating all chapters into a comprehensive overview of the microcystin toxicity mechanism, see Figure 61.

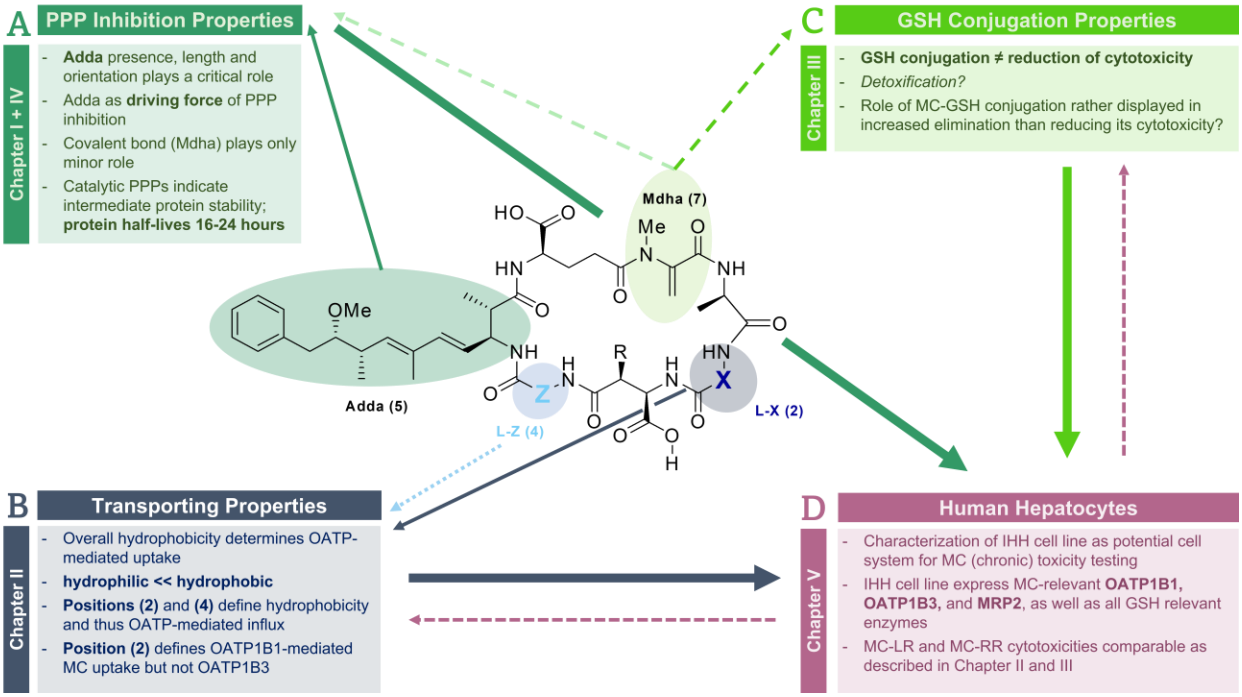

Figure 61: Concluding Summary of the Dissertation

Graphical summary of the main aspects and results obtained in this study. While toxicodynamic aspects are highlighted in green, toxicokinetic aspects are highlighted in blue and the combination of both is emphasized in dark pink. **(A)** summarizes the main results obtained from the analysis of the PPP inhibition mechanism mainly involving positions (5) and (7). **(B)** summarizes OATP-mediated uptake involving the hypervariable positions (2) and (4), while **(C)** concludes the role of GSH conjugation facilitated by covalent binding at position (5). Finally, all parameters were combined and **(D)** human hepatocytes were used to evaluate and analyze all results in a more biologically relevant context.

As the toxicity of microcystins is based on their ability to bind and inhibit PPPs, the initial step of this study was to pinpoint the microcystin characteristics and properties that are essential and critical for their PPP inhibition capability. Based on the initial insights from *in silico* and crystallization studies (Goldberg et al., 1995; Pereira et al., 2013; Xing et al., 2006), microcystin-induced PPP inhibition was theorized to be facilitated by two steps, involving the interaction of the hydrophobic Adda side chain, followed by the formation of a covalent bond between the Mdha group and the cysteine moiety of the PPP active site (Craig et al., 1996; Fontanillo & Köhn, 2018). Thus, instead of using naturally occurring microcystins, which vary mainly in their hypervariable l-amino acid positions (2) and (4), this study focused on synthetic microcystin derivates with specific modifications at either the Adda or Mdha group to analyze and evaluate their explicit role in PPP inhibition. And indeed, this study clearly demonstrated that the presence, length, and orientation of the hydrophobic Adda side chain at position (5) played a critical role in the microcystin-induced PPP inhibition mechanism. While the formation of the covalent bond facilitated by the Mdha group at position (7), despite inducing irreversibility, only played a minor role. However, the correct positioning of the microcystin molecule, which is controlled by the hydrophobic affinity of the Adda side chain, was more important for PPP inhibition, as demonstrated and observed by the detailed study of the Adda side chain length. Thereby, the length of the Adda backbone was shown to be critical for providing sufficient hydrophobic interaction sites and shortening the Adda backbone induced a significant loss of affinity, see Figure 61 A.

Notably, only purified and enzymatically active rPPP1 and hPPP5 were used in this study. Given that the catalytic subunits of the PPP family are highly conserved (Shi, 2009), it can be assumed that the microcystin-induced inhibition mechanism also applies to other PPP members. Indeed, a previous study performed in our laboratory demonstrated similarity between rPPP1 and hPPP2A, as evidenced by the highly comparable IC_{50} values observed for 18 different microcystin congeners (Altaner et al., 2020). Only hPPP5 was reported to be slightly less sensitive to microcystins, as the IC_{50} values were shown to be elevated. However, since PPP1 and PPP2A account for more than 90 % of the total protein dephosphorylation and are involved in essential cellular functions (e.g., cell cycle) (Cohen, 2004; Shi, 2009), and PPP5 is the most unique PPP since no regulatory or scaffolding subunit is required for its activation (Yang et al., 2005), the most critical PPPs were selected for this study. Consistently, proteomic analysis of HEK293 cell lines identified PPP2A and PPP1 as the most abundantly expressed PPPs (54.7 % and 29.6 %, respectively), whereas only lower expression levels of PPP4, PPP5 and PPP6 were detected (4.1 %, 4.3 %, and 5.9 %, respectively). Interestingly, among all proteins, 1.5 % were identified as phosphatases, of which only 0.02 % were tyrosine phosphatases, and 0.7 % were serine/threonine phosphatases. Remarkably, the inhibition of a rather low abundance group of enzymes results in severe cellular consequences, further emphasizing their essential and critical role in cell survival. This was also reflected in their relatively high protein stability, as this study narrowed their protein half-lives to approximately 16-24 hours, classifying PPPs as intermediately stable proteins. This raises the question of

whether their high protein stability is potentially beneficial for microcystins due to their higher turnover rates, or whether the proteasomal degradation of microcystin-bound PPPs results in the release of free toxins, thereby contributing to their cytotoxic effects. This question should be further investigated and clarified, especially before designing chronic exposure studies.

However, returning to the *in vitro* toxicodynamic properties of microcystins. Analysis of the IC_{50} values reported for 18 different microcystins in rPPP1, hPPP2A, and hPPP5 did not reveal a clear pattern or trend. In addition, the IC_{50} values obtained for naturally occurring microcystins indicated similar concentration ranges in the low nanomolar range, particularly for rPPP1 and hPPP2A (Altaner et al., 2020). In contrast, *in vivo* rodent studies reported distinct congener specificity (Chernoff et al., 2020; Sivonen & Jones, 1999), raising the question whether this discrepancy is due to toxicokinetic rather than toxicodynamic aspects. Initial studies that contributed significantly to this hypothesis used *Xenopus laevis* oocytes as an expression system and identified OATP1B1 and OATP1B3 as the main microcystin influx transporters (Fischer et al., 2005). Following, the authors proposed an OATP congener specific uptake using MC-LR, MC-LF, and MC-RR in OATP1B1- and OATP1B3-expressing HEK293 cells (Fischer et al., 2010). To further evaluate this hypothesis, the next step in this study was to pinpoint the microcystin characteristics responsible for sufficient OATP-mediated uptake. Therefore, the stably transfected HEK293 expression system was used as a simplified cell system to study toxicokinetics including toxicodynamic parameters, with the clear advantage of the absence of all other efflux and influx transporters, thus ensuring the causality of OATP-mediated uptake with associated cytotoxicity. And indeed, the study performed in this thesis, using a total of 21 microcystin congeners, showed a clear correlation between the overall hydrophobicity of the microcystin molecule and its OATP-mediated uptake. Based on their hydrophobicity (LogP values) and the resulting EC_{50} values, microcystins were classified into three groups: less toxic, moderately toxic, and very toxic. Thereby, the so far underestimated roles of the hypervariable positions (2) and (4) were determined. Both positions were shown to define the OATP-mediated uptake by determining the overall hydrophobicity of the molecule. It can be concluded that as the hydrophobicity of the microcystin molecule increases, OATP-mediated uptake, and thus the cytotoxicity, increases and vice versa. Furthermore, the critical role of position (2) was identified. Highly hydrophilic arginine residues incorporated at position (2) were shown to drastically impair OATP1B1-mediated microcystin uptake, while OATP1B3-mediated transport was not affected. Interestingly, the impaired transmembrane transport could be restored by transposition of the arginine residue from position (2) to (4), while maintaining the overall hydrophobicity of the toxin. One open question remains in terms of microcystin toxicokinetic properties. So far, the cellular elimination of microcystins via efflux transporters has not been fully understood. Recent studies have demonstrated microcystin-mediated export via MRP2 transporters, albeit only for unbound microcystins and not for their GSH conjugates (Kaur et al., 2019). Therefore, future studies are highly needed to identify all involved microcystin efflux transporters, as well as their potential congener-specificity to accurately assess and contextualize microcystin toxicokinetic properties.

In conclusion, position (5) was identified as the driving force of the PPP inhibition mechanism, see **Figure 61 A**, while the variable positions (2) and (4) were shown to be negligible in this toxicodynamic context. However, this study identified their critical roles in the OATP-mediated uptake, see **Figure 61 B**. Since position (7) appeared to be accessory for PPP inhibition, it was hypothesized to play a more important part in the biological role of microcystins, including its function in the conjugation to GSH (Pereira et al., 2013). Consequently, the next step of this study was to identify the role of cellular GSH conjugation in the mechanism of microcystin toxicity. Therefore, three independent assays were established to simultaneously monitor cytotoxicity, PPP activity, and GSH response after microcystin exposure. Although the data presented in this study are preliminary and require further in-depth analysis (e.g., LC-MS/MS analysis of cellular MC-GSH conjugate concentrations after exposure), the commonly accepted and proposed hypothesis of 'microcystin detoxification via GSH conjugation' could not be supported, as cellular GSH availability did not result in the reduction of cytotoxicity compared to completely depleted GSH contents. This raised the question of whether microcystins have a significantly higher affinity for PPPs or whether the conjugation efficiency is exceptionally low. Keeping in mind that the covalent bond as well as steric residues at position (7) did not affect the PPP inhibition capacity, this study strongly suggests that the conjugates still exhibit PPP inhibitory properties, that should not be underestimated. To verify this assumption, further analysis to determine the PPP inhibition capacities of both stable conjugates (MC-GSH and MC-Cys) is strongly recommended. Nevertheless, considering the complete GSH depletion in HEK293 cells, while cytotoxicities and PPP activities remained nearly unchanged, combined with the toxicodynamic study regarding the subordinate role of the covalent bond in the PPP inhibition mechanism, strongly supports the hypothesis that microcystins may have a dramatically higher affinity for PPPs than for GSH conjugation. This hypothesis is supported by reports indicating that at a cytosolic GSH concentration of 1-2 mM (as found in the HEK293 cells), the enzymatic conjugation via GST was predominant. In fact, the authors reported rather high K_m values for human GST (100-200 µM) using MC-LR and MC-RR (Buratti & Testai, 2015). Although no actual measured K_m values are available for PPPs, it is reasonable to assume that these values would be much lower than those measured for GST, since the EC_{50} values in HEK293 cells were determined in the nanomolar range, and in human and mouse hepatocytes in the lower micromolar range. This led to the assumption that GSH conjugation might enhance the elimination of microcystins via efflux transporters rather than reducing their cytotoxicity. Since hepatocytes generally indicate higher cytosolic GSH concentrations and express various efflux transporters, the question was raised whether physiologically more relevant hepatocytes would provide better insights into the role of GSH conjugation in the microcystin toxicity mechanism, see **Figure 61 C**.

Thus, as a next step in this study, a functional but non-carcinogenic human hepatocyte cell line that most closely resembles human *in vivo* exposure was required. Therefore, the immortalized human hepatocyte (IHH) cell line was selected and characterized prior to microcystin toxicity and conjugation

studies. And indeed, microcystin-relevant influx and efflux transporters were positively identified. Despite the absence of liver-specific CYPs, the IHH cells expressed all GSH-related enzymes in the anticipated quantities. As microcystins are not involved in CYP-related biotransformation pathways, the absence of CYPs expression was not considered to be critical. The same is true for the absence of OATP2B1 transporter, as previous studies clearly demonstrated no OATP2B1-mediated microcystin uptake (Fischer et al., 2005). Similarly, the lower expression of OATP1B1 compared to OATP1B3 is considered to be due to donor variability (Fischer et al., 2010; König et al., 2000a) and is therefore assumed to reflect the expression ratio in adult human hepatocytes. In conclusion, the IHH cell line was considered to be an appropriate and suitable cell system to study the mechanism of microcystin toxicity. This is where all the toxicodynamic and toxicokinetic studies performed in this thesis come together, see **Figure 61 D**. Combined with the fact that IHH cells do not overexpress the OATP transporters and additionally express various efflux transporters (e.g., MRPs) higher microcystin concentrations were required to induce similar cytotoxic effects, as evidenced by higher EC_{50} values compared to the overexpressing HEK293 cell lines. However, it is reasonable to assume that overall hydrophobicity plays a similar role in microcystin uptake in IHH cells, as the highly hydrophilic MC-RR exhibited significantly reduced cytotoxicity compared to the more hydrophobic MC-LR. Needless to say, further studies with additional microcystin congeners are required. Nevertheless, depletion of cellular GSH content showed no significant difference in microcystin-induced cytotoxicity in IHH, comparable to the effects observed in HEK293 cells. However, coming back to the initial hypothesis that GSH conjugation might fulfill its detoxification function through improved elimination rather than reduced PPP inhibition ability, no definitive answer can be provided. Due to the experimental setup, potential reuptake of the conjugates cannot be excluded. But since conjugation to GSH decreases hydrophobicity and thus increases hydrophilicity, reuptake of conjugates is expected to be impaired and not as efficient as for unbound microcystins.

The current risk assessment is primarily based on a mouse study conducted in 1999 with a single microcystin congener (MC-LR) and has remained unchanged since then (Fawell et al., 1999; World Health, 2020), even though exceptionally high numbers of congeners have been described and identified (Spoof & Catherine, 2016) and congener-specific toxicity has been demonstrated (Fischer et al., 2010). However, studies have shown that mice vary widely in the expression of OATPs, as well as in their affinity and capacity for microcystin-mediated transport (Fischer et al., 2005). While human hepatocytes have been shown to express both OATP1B1 and OATP1B3 transporters, both of which contribute significantly to microcystin uptake, mouse hepatocytes have been shown to express only one OATP transporter capable of transporting microcystins, namely Oatp1b2 (Fischer et al., 2005). Consequently, as a final step of this thesis, a commonly used toxicity test cell line of mouse hepatocytes (AML12) was used and compared with a human hepatocyte cell line (IHH) to study species differences within the microcystin toxicity mechanism and the corresponding GSH response. And indeed, significant differences were found between mouse and human hepatocytes. Thereby alarmingly, the observed cytotoxicity of the most common

microcystin MC-LR, on which the WHO guideline is based, indicated significant differences in cytotoxicity in mouse compared to human hepatocytes. AML12 cells appeared to be significantly less sensitive to MC-LR, with a 3-fold higher EC_{50} concentration compared to the human hepatocytes. Moreover, differences became more apparent when observing the GSH response after MC-LR exposure, as the GSH response in AML12 cells resulted in a dramatic overshoot reaction. The role of the dramatically increased GSH content remains unclear and requires further analysis and investigation. Taken together, these results raise the question of a potential underestimation of microcystin toxicity and highlight the need for an updated risk assessment.

It is important to note that this study was not focused or designed to assess the risk of microcystins but rather to understand and determine their toxic mechanism by studying their toxicodynamic and toxicokinetic properties. Nevertheless, the significant differences found in human hepatocytes compared to mouse hepatocytes, combined with the identified high congener-specificity of OATPs, revealing that MC-LR is not one of the most toxic microcystin variants, challenge the current risk assessment and underline the need for revision, as has already been requested by other researchers (Altaner et al., 2020; Buratti et al., 2011; Dietrich & Hoeger, 2005). This study was not designed to propose exact guideline values but could provide potential aspects and concepts for an updated and more precise risk assessment. As the HEK293 cell lines overexpress the microcystin-relevant transporters, it is not recommended to use these EC_{50} data (low nanomolar range) without extrapolation. This extrapolation is assumed to be by a factor of 1000. Since the EC_{50} values for OATP1B1- and OATP1B3-expressing HEK293 cells exposed to MC-LR were found to be 17 nM and 16 nM, respectively, and the corresponding EC_{50} for IHH cells was found to be 17 µM. The same is true for MC-RR. In the OATP1B3-expressing cells a EC_{50} of 52 nM was measured (no transport in OATP1B1-expressing cells), while in IHH an EC_{50} of 40 µM was determined. Obviously, further evaluation with more congeners is required. It is recommended that different representatives of each class identified in this study should be used, with particular emphasis on the very toxic class of microcystins involving MC-LF, MC-LY, and MC-LW. That data could then be used to train *in silico* prediction models, as suggested by Altaner et al. and thus contribute to a revised risk assessment evaluation.

8. Materials and Methods

8.1. Cell Systems

8.1.1. Cell Lines

Stably Transfected Human Embryonic Kidney 293 (HEK293) Cell Lines

Human embryonic kidney 293 (HEK293) cells stably transfected with recombinant human organic anion transporting polypeptide 1B1 (HEK293-OATP1B1), 1B3 (HEK293-OATP1B3) or control vector (HEK293-CV) were kindly provided by Prof. Dr. Dietrich Keppler (Division of Tumor Biochemistry, German Research Center, Heidelberg, Germany). Cells were cultured in growth medium consisting of Dulbecco's Minimal Essential Medium (DMEM, Cat.# C4324, Genaxxon) supplemented with 10 % FCS, 100 Units/ml Penicillin/Streptomycin (Cat.# M3140, Genaxxon) and 400 µg/ml G418-sulfate (Cat.# M3118, Genaxxon) at 37 °C and 5 % CO_2. Growth medium was replaced every second to third day and cells were subcultured using Trypsin/EDTA solution (Cat.# C4261, Genaxxon) and 5 min of centrifugation at 500 rcf. Owing to the high binding affinity of microcystins to serum albumin, microcystin treatments were performed in toxin exposure medium consisting of DMEM supplemented with 1 % FCS, 100 Units/ml Penicillin/Streptomycin and 400 µg/ml G418-sulfate. Cycloheximide (CHX) treatments were performed in serum-free DMEM but including all other supplements. All cell culture plates were precoated with 1 mg/ml Poly-D-Lysine (Cat.# P0899, Sigma-Aldrich) to facilitate cell attachment. Seeding densities according to the assay and analysis method, are summarized in Table 10.

Table 10: Seeding Densities for HEK293 Cells

Assay	Cell Culture Plates	Seeding Density			Medium	
		[cells/well]	[cells/ml]	[ml/well]	Seeding	Treatment
Cell Cycle Analysis	6-well-plate	$7x10^5$	$3.5x10^5$	2.0	10 % FCS	10 % FCS
Cycloheximide Chase	6-well-plate	$8x10^5$	$4x10^5$	2.0	10 % FCS	0 % FCS
GSH Half-Life	96-well-plate	$6x10^4$	$3x10^5$	0.2	10 % FCS	1 % FCS
Immunocytochemistry	24-well-plate	$3x10^5$	$6x10^5$	0.5	10 % FCS	-
Multiplex Assays	96-well-plate	$6x10^4$	$3x10^5$	0.2	10 % FCS	1 % FCS
Toxin Exposure	96-well-plate	$6x10^4$	$3x10^5$	0.2	10 % FCS	1 % FCS

Immortalized Human Hepatocytes (IHH)

Immortalized human hepatocytes (IHH) were kindly provided by Prof. Dr. Thomas Brunner (Department of Biochemical Pharmacology, University of Konstanz, Germany). IHH are non-tumorigenic liver epithelial cells (59-years-old, male). Primary hepatocytes were isolated from healthy liver tissue and immortalized by stably transfection with recombinant plasmid containing the early region of the simian virus (SV) 40 (Schippers et al., 1997).

IHH were cultured in growth medium consisting of Dulbecco's Modified Eagle's Medium/Nutrient Mixture F-12 Ham (DMEM:F12) with 15 mM HEPES (Cat.# D6421, Sigma-Aldrich) and supplemented

with 10 % FCS, 100 Units/ml Penicillin/Streptomycin, 2 mM GlutaMax™ (Cat.# 35050061, Thermo Fisher), 10 mg/ml gentamicin (Cat.# G1272, Sigma-Aldrich), 40 ng/ml dexamethasone and Insulin-Transferrin-Selenium (ITS-G) solution (Cat.# 41400045, Thermo Fisher) at 37 °C and 5 % CO_2. Growth medium was renewed every second to third day and cells were subcultured using Trypsin/EDTA solution and 5 min of centrifugation at 500 rcf. As the expression of liver-specific proteins decreased over time, serum-free DMEM:F12 medium, including all other supplements, was used to reactivate hepatocyte function and protein expression. Cells were cultured either at standard cell culture conditions (AtmOx: atmospheric oxygen ≈ 21 % O_2, 5 % CO_2, 37 °C and 95 % humidity) or physiological conditions (PhysOx: either 10 % or 5 % O_2, 5 % CO_2, 37 °C and 75 % humidity, SCI-tie Baker Ruskinn Low-Ox chamber, medium equilibrated to atmosphere for 24 h), with medium exchange every second or third day. Seeding densities according to the assay and analysis methods are summarized in Table 11.

Table 11: Seeding Densities for Immortalized Human Hepatocytes

Assay	Cell Culture Plates	Seeding Density			Medium	
		[cells/well]	[cells/ml]	[ml/well]	Seeding	Treatment
Growth Curve	24-well-plate	$5.0x10^3$	$5.0x10^3$	1.0	10 % FCS	-
Immunocytochemistry	24-well-plate	$1.5x10^5$	$1.5x10^5$	1.0	0 % FCS	-
Multiplex Assays	96-well-plate	$1.5x10^4$	$7.5x10^4$	0.2	10 % FCS	0 % FCS
Seahorse	24-well-plate	$3.0x10^5$	$3.0x10^5$	1.0	10 % FCS	0 % FCS
Toxin Exposure	96-well-plate	$1.5x10^4$	$7.5x10^4$	0.2	10 % FCS	0 % FCS

Alpha Mouse Liver 12 (AML12)

Alpha mouse liver 12 (AML12) hepatocytes were purchased from ATCC (Cat.# CRL-2254). The AML12 cell line was established from isolated hepatocytes of a mouse (3 months old, male CD1 strain, line MT42) transgenic for human transforming growth factor alpha (TGF- α). AML12 cells were cultured in growth medium consisting of Dulbecco's Modified Eagle's Medium/Nutrient Mixture F-12 Ham (DMEM:F12) with 15 mM HEPES supplemented with 10 % FCS, 100 Units/ml Penicillin/Streptomycin, 2 mM GlutaMax™, 40 ng/ml dexamethasone and ITS-G solution at 37 °C and 5 % CO_2. Growth medium was replaced every second to third day and cells were subcultured using Trypsin/EDTA solution and 5 min of centrifugation at 500 rcf. Similar to IHH cells, hepatocyte-specific protein expression was reactivated by culturing the cells in serum-free DMEM:F12 medium, including all other supplements. Seeding densities are summarized in Table 12.

Table 12: Seeding Densities for Alpha Mouse Liver 12 (AML12)

Assay	Cell Culture Plates	Seeding Density			Medium	
		[cells/well]	[cells/ml]	[ml/well]	Seeding	Treatment
Growth Curve	24-well-plate	$5.0x10^3$	$5.0x10^3$	1.0	10 % FCS	-
Immunocytochemistry	24-well-plate	$2.0x10^5$	$2.0x10^5$	1.0	0 % FCS	-
Multiplex Assays	96-well-plate	$2.5x10^4$	$1.25x10^5$	0.2	10 % FCS	0 % FCS
Toxin Exposure	96-well-plate	$2.5x10^4$	$1.25x10^5$	0.2	10 % FCS	0 % FCS

8.1.2. Microscopic Assessment

Brightfield

Cellular morphology was assessed by microscopy at AtmOx using the ECLIPSE TS100/TS100-F (Nikon) and at PhysOx (10 % and 5 % O_2) using the EVOS M5000 (Invitrogen). Images were adjusted for display using ImageJ software.

Immunocytochemistry

HEK293-OATP1B1, -OATP1B3 and -CV cells were seeded on Poly-D-Lysine coated coverslips, whereas IHH and AML12 cells were seeded on non-coated coverslips in 24-well-plates. Plates were incubated at 37 °C and 5 % CO_2 until 80 % confluency was reached. Cells were washed once with PBS and fixed for 10 min with 4 % paraformaldehyde (PFA)/0.1 % Triton X-100. After fixation, the cells were washed twice with PBS and blocked with 1 % BSA in PBS for 1 h at room temperature. The primary antibodies, listed in ***Table 13***, were diluted in blocking buffer, and incubated overnight at 4 °C.

Table 13: Primary Antibodies Used for Immunocytochemistry

Cell Line	Protein	Supplier	Cat.#	Species	Dilution
HEK293 Cell Lines	OATP1B1	Kindly provided by Prof. Dr. Bruno Stieger (University of Zurich, Switzerland)		Rabbit	1:100
	OATP1B3			Rabbit	1:100
IHH and AML12	ABCB11	Invitrogen	PA5-114800	Rabbit	1:100
	ATP8B1	Abcam	ab234761	Rabbit	1:100
	CD10	Abcam	ab256494	Rabbit	1:500
	CYP8B1	Bioss	BS-14165R	Rabbit	1:100
	CYP7A1	Invitrogen	PA5-119862	Rabbit	1:500
	E-Cadherin	Abcam	ab287970	Mouse	1:250
	Fibronectin	Abcam	ab2413	Rabbit	1:250
	MRP2	Abcam	ab172630	Rabbit	1:100
	OATP1B1	Abcam	ab254575	Rabbit	1:100
	OATP1B3	Abcam	ab222900	Rabbit	1:100
	Vimentin	Sigma-Aldrich	V6630	Mouse	1:40

Cells were washed three times with PBS before incubation with the secondary antibody, listed in Table 14, for 1 h at room temperature. The cells were washed three times with PBS for 5 min and counterstained with Phalloidin iFluor488 (Cat.# ab176753, Abcam, 1:2000 in 1 % BSA) for 2 h, followed by Hoechst33342 counterstaining for 7 min at room temperature. With the cells facing downwards, the coverslips were transferred onto microscopic glass slides, mounted using a fluorescence mounting medium (Cat.# S3023, Dako) and sealed with nail polish. Microscopic slides were stored at 4 °C in a humidity chamber until imaging. Cells were imaged using a laser scanning confocal microscope (LSM 700, Zeiss). Images were adjusted for display using ImageJ software.

Table 14: Secondary Antibodies Used for Immunocytochemistry

Antibody	Supplier	Cat.#
Goat anti-mouse AlexaFluor™647	Invitrogen	A21235
Goat anti-rabbit AlexaFluor™647	Invitrogen	A21244
Goat anti-rabbit AlexaFluor™532	Invitrogen	A-11009
Goat anti-mouse AlexaFluor™532	Invitrogen	A-11002

8.1.3. Growth Analysis

In vitro cultured cells display a sigmoidal pattern of proliferation, including a lag phase (cells do not divide and adapt to culture conditions), a logarithmic phase (cells start to proliferate and exponentially increase in cell number), followed by a stationary phase (cellular proliferation slows down due to confluency), and consequently a decline phase (increased cell death).

Growth Curves

IHH and AML12 growth curves were generated under AtmOx and both PhysOx conditions. Cell proliferation was studied by counting cells every 24 h for 12 days. Therefore, cells were seeded in 24-well-plates with medium exchange every second to third day. Cells were detached using Trypsin/EDTA solution and cell nuclei were stained using 0.4 % trypan blue solution. Cell numbers were determined using a hemocytometer.

Calculation of Doubling Times

Cell line and oxygen condition-specific doubling times were calculated using cells in the logarithmic phase. Therefore, the following equation was used:

$$Doubling\ Time = \frac{Duration\ (h) * \log(2)}{\log(t_2\ cell\ number) - \log(t_1\ cell\ number)}$$

Here, t_1 indicates the start and t_2 indicates the end of the logarithmic growth phase.

Contact Inhibition

Contact Inhibition is a regulatory mechanism of non-tumorigenic cells that keeps cells growing as a monolayer in a cell culture dish. Nevertheless, cell immortalization can lead to the loss of cell-cell induced contact inhibition, leading to cell overgrowth and tumor-like formation. To investigate whether the used hepatocyte cell lines displayed contact inhibition properties, cells were seeded in 6-well-plates. Growth medium was exchanged every second to third day. Microscopic images were obtained daily for 14 days.

8.2. Microcystins

Microcystin congeners were purchased either from Enzo Life Sciences (MC-LR, -RR, -LF, -LY, -YR, -LW, -WR, -LA, [β-D-Asp^3]MC-LR, -HilR and -HtYR) or were synthesized ([Amba^5]MC-LY(Prg), [Anda^5]MC-LY(Prg), [enantio-Adda^5]MC-LF, MC-LY(Prg), [MSecPh^7]MC-LY(Prg), MC-RY, MC-KL$_{D7}$, MC-F$_{D5}$R, MC-RF$_{D5}$, [Apda^5]MC-LF, [Apha^5]MC-LF, [Ala^7]MC-L(DAz)-Y(Prg)) in the Bioorganic Chemistry Department of Prof. Dr. Valentin Wittmann (University of Konstanz, Germany) using previously published procedures (Fontanillo et al., 2016; Zemskov et al., 2017). [β-D-Asp^3, Dhb^7]MC-RR was kindly provided by Dr. Judith Blom (University of Zurich, Switzerland). All microcystins, except MC-F$_{D5}$R, were dissolved in pure methanol. Due to solubility, the synthesized congener MC-F$_{D5}$R was dissolved in DMSO. For the commercially available microcystins as well as MC-LY(Prg), [MSecPh^7]MC-LY (Prg), MC-RY, MC-RF$_{D5}$ and MC-KL$_{D7}$, the actual concentrations were determined by UV spectroscopy at 238 nm using the extinction coefficient of MC-LR (ε = 39800 mol L-1 cm-1). Stocks dissolved in DMSO and Adda variants ([Amba^5]MC-LY(Prg), [Anda^5]MC-LY(Prg) and [enantio-Adda^5]MC-LF, [Apda^5]MC-LF, [Apha^5]MC-LF) were quantified by dissolving precisely weighed amounts of the congener in an appropriate volume of solvent, as no photometric measurement was possible. Stocks were stored in sealed glass vials at -20 °C until use.

8.3. Assays

8.3.1. Cytotoxicity Assays

Toxin Exposure Assay

Toxin exposure assay was adapted and modified according to already published procedures (Fischer et al., 2010). Cells were seeded in 96-well-plates and incubated overnight for at least 15 h. Microcystin stocks were serially diluted to concentrations ranging from 0.17 nM to 3750 nM for stably transfected HEK293 cell lines and from 0.03 µM to 200 µM for the hepatocytes. As a control, cells were only treated with solvent (0.25 % for HEK293 cell lines and 1 % for IHH and AML12 cell). Each concentration was pipetted in triplicates. Cells were incubated with the corresponding toxin concentration for 48 h at 37 °C and 5 % CO_2.

Glutathione Depletion and Toxicity Testing

Prior to performing the toxin exposure assay, cellular glutathione (GSH) was depleted using buthionine sulfoximine (BSO). Therefore, cells were seeded in 96-well-plates and incubated overnight for at least 15 h. Cells were incubated for 24 h with 125 µM BSO in toxin exposure medium (HEK293 cells) or serum-free medium (IHH and AML12). As GSH depletion control, cells were treated with solvent only. Subsequently, the toxin exposure and multiplexing assays were performed.

Resazurin Cell Viability Assay

Resazurin cell viability assay is a redox-based colorimetric assay that detects the mitochondrial metabolic activity of viable cells. The blue dye resazurin passes through the cell membrane and is reduced intracellularly to resorufin in the presence of mitochondrial $NADH/H^+$. This redox reaction can be quantified photometrically by monitoring the absorbance at 570 nm (resazurin) and 600 nm (resorufin) or by fluorescence measurements. Unlike the MTT (3-(4,5-dimethylthiazol-2-yl)-2,5-diphenyltetrazolium bromide) assay, resazurin is not cytotoxic and the cell viability assay can be combined with multiple other assays. After toxin exposure, the supernatant of the 96-well-plates was replaced with medium containing 45 µM resazurin. The plates were incubated for 3 h (HEK293 cell lines) or 2 h (IHH and AML12 cells) at 37 °C and 5 % CO_2. For stably transfected HEK293-OATP1B1, -OATP1B3 or -CV cells, the absorption was measured at 570 nm and 600 nm using a microplate reader (Infinite 200 Pro, Tecan). Due to the rather acidic hepatocytes, the viability of IHH and AML12 cells was measured using fluorescence (excitation: 530 nm, emission: 590 nm). Viability data were expressed as percentage of solvent control cells. The half-maximal effective concentrations (EC_{50}) were calculated using GraphPad Prism 9 software via five-parameter asymmetric nonlinear regression without anchoring points.

Sulforhodamine B Cytotoxicity Screening

Sulforhodamine B (SRB) is a pink aminoxanthene dye that allows the determination of the protein content of cells fixed to tissue culture plates by trichloroacetic acid (TCA) precipitation. Under mildly acidic conditions, SRB binds to the basic amino acid residues of proteins through its sulfonic groups, whereas under basic conditions, SRB dissociates from proteins and solubilizes. Since the binding of SRB is stoichiometric and completely independent of cellular metabolic activity, the amount of dye extracted from stained cells is directly proportional to the protein content within the cells. To support the cycloheximide (CHX) cytotoxicity data measured using resazurin, SRB cytotoxicity screening was performed as previously described (Vichai & Kirtikara, 2006). After resazurin cell viability measurements, CHX exposed cells were treated with 100 µl/well of ice-cold 10 % TCA solution. The plates were then incubated for 1 h at 4 °C. Subsequently, the plates were washed with deionized water and air dried for at least 48 h. After adding 100 µl of 0.057 % SRB solution per well, the plates were incubated for 30 min at room temperature. Plates were rinsed four times with 1 % acetic acid to remove unbound SRB dye, before 200 µl of 10 mM Tris base solution per well was added. Plates were incubated for 5 min while shaking. The absorbance was measured at 510 nm using a microplate reader (Infinite 200 Pro, Tecan). Protein content was calculated by first subtracting the background (cells treated with 0.1 % Triton X-100) and then comparing it to the solvent control. Calculations were performed using Microsoft Excel, and data visualization and analyses were performed using GraphPad Prism 9 software.

8.3.2. Metabolic Assays

Seahorse XF Real-Time ATP Rate Assay

The Seahorse XF Real-Time ATP Rate Assay Kit (Cat.# 103592-100, Agilent) was used to quantify the production rate of adenosine triphosphate (ATP) from the mitochondria and glycolysis in IHH cells. The real-time ATP rate assay was performed using a Seahorse Analyzer (XFe24, Agilent) under both AtmOx and PhysOx conditions, according to the manufacturer's instructions. Cells were seeded in 24-well seahorse XFe24 culture plates (Cat.# 100882-004, Agilent) and cultured for 2 days in serum-free medium. Assay was conducted in Seahorse XF DMEM assay medium (Cat.# 103680-100, Agilent), supplemented with 17.8 mM glucose (Seahorse XF 1.0 M Glucose Solution, Cat.# 103577-100, Agilent), 0.625 mM pyruvate (Seahorse XF 100 mM Pyruvate Solution, Cat.# 103578-100, Agilent) and 2 mM glutamine (Seahorse XF 200 mM Glutamine Solution, Cat.# 103579-100, Agilent). After the measurements, cells were fixed using 4 % PFA, stained with Hoechst33342 and counted using a cell counter (Cellomics) to normalize the obtained values. Data were processed using Agilent Seahorse WAVE software and exported to Microsoft Excel and GraphPad Prism 9 for statistical analysis and data representation.

8.3.3. Phosphatase Assays

All used phosphatase assays were based on the ability of phosphatases to dephosphorylate p-nitrophenyl phosphate (pNPP) into yellow luminous p-nitrophenol. Upon phosphatase inhibition by microcystins (serine/threonine protein phosphatases), sodium orthovanadate (tyrosine protein phosphatases) and sodium fluoride (serine/threonine protein phosphatases), p-nitrophenol is no longer formed. The enzymatically catalyzed reaction can be measured photometrically at 405 nm. For this dissertation, different variations based on this chemical reaction were developed and adapted. All buffer compositions are listed in Table 15.

Table 15: Phosphatase Assay Buffer Composition

Buffer	Composition
Enzyme Buffer	52 mM Tris (pH 7), 2 mM $MnCl_2$, 0.5 mg/ml BSA, 1 mM DTT, 0.5 mM NaOAc, 123.5 µM EGTA, 3 U rPPP1 or hPPP5
Enzyme Dilution Buffer	52 mM Tris (pH 7), 2 mM $MnCl_2$, 0.5 mg/ml BSA, 1 mM DTT, 0.5 mM NaOAc, 123.5 µM EGTA
Substrate Solution	62.5 mM Tris (pH 8.1), 26 mM $MgCl_2$, 0.2 mM $MnCl_2$, 0.5 mg/ml BSA, 2 mM DTT, 24 mM p-nitrophenyl phosphate (pNPP, Cat.# 4165.9, Roth), 1 mM NaOAc
Lysis Enzyme Buffer	52 mM Tris (pH 7), 0.1% Triton X-100

Phosphatases

Enzymatically active rPPP1 (rabbit skeletal muscle) was purchased from New England Biolabs (Cat.# P0754L, product discontinued), while hPPP5 was produced in the lab as already published (Altaner et al., 2020). The enzymatic activity of the purified phosphatases was calculated and expressed in units. One unit (U) was thereby defined as the amount of enzyme needed to dephosphorylate 1 nmol of pNPP in 1 min at 30 °C (rPPP1: 2.5 U/µl).

Colorimetric Protein Phosphatase Inhibition Assay (Using Purified PPPs)

To validate the functionality of the synthesized microcystin congeners, their inhibitory properties were measured using purified and enzymatically active phosphatases (rPPP1 and hPPP5), based on previously described methods (Altaner et al., 2020; Fischer et al., 2010; Heresztyn & Nicholson, 2001). Serial dilutions of MC-LF (0.00007 nM – 20 µM), [Apda^{5}]MC-LF (0.08 nM – 40 µM), [Apha^{5}]MC-LF (0.08 nM – 2 mM), [Amba^{5}]MC-LY(Prg) (76.2 nM – 1.5 mM), [Anda^{5}]MC-LY(Prg) (0.76 nM – 200 µM) and MC-LY(Prg) (0.02 nM – 5,000 nM) were dissolved in Milli-Q water and stored in LC-vials at -20 °C, whereby the solvent content of the highest concentration never exceeded 5 % MeOH. All pipetting steps were performed on ice. Each microcystin congener (20 µl/well) was pipetted in triplicates into a 96-well-plate. Three U of either rPPP1 or hPPP5 were diluted in 2,120 µl enzyme dilution buffer and 20 µl of the solution was pipetted into each well, corresponding to 0.07 U/well enzyme activity. As a 100 % enzyme activity control, 20 µl/well of the enzyme solution was added to 20 µl/well of Milli-Q water. In contrast, 20 µl/well enzyme dilution buffer lacking the PPPs but supplemented with 20 µl/well Milli-Q water served as the no-enzyme activity control. The plates were incubated at 37 °C for 5 min to ensure the enzymatic activation and interaction of PPPs with microcystins. Substrate solution (200 µl/well) was added, and the absorbance was measured at 405 nm using a microplate reader (Infinite 200 Pro, Tecan). Plates were further incubated for 3 h at 37 °C before the absorbance was measured again. The measured start value (0 h) was subtracted from the end value (3 h) and phosphatase inhibition data were expressed as percentage of the enzyme activity control. The half-maximal inhibitory concentrations (IC_{50}) were calculated using GraphPad Prism 9 software via five-parameter asymmetric nonlinear regression with constraints between 0 % and 100 %.

Colorimetric Protein Phosphatase Activity Assay (Using Cells)

The colorimetric protein phosphatase inhibition assay was adapted and modified to determine phosphatase activities in cells. HEK293-OATP1B1 and HEK293-OATP1B3 cells were lysed in lysis enzyme buffer and protein amounts were quantified using the Pierce™ BCA Protein Assay Kit (Cat.# 23225, Thermo Fisher). Serial dilutions of cell lysates (highest concentration: 40 µg protein/well, lowest concentration: 0.08 µg protein/well) using the enzyme diluent buffer were prepared and 20 µl/well was pipetted into each well of a 96-well-plate. After 5 min of incubation at 37 °C, 200 µl of substrate solution

was added to each well. Kinetic measurements were performed by measuring the absorbance at 405 nm every 10 min over a period of 4 h at 37 °C. Enzyme activity in the cell lysates was determined by linear regression for each dilution over time. The resulting slopes were compared to the corresponding slopes of rPPP1. Experiments using phosphatase inhibitors (10 mM sodium orthovanadate or 50 mM sodium fluoride) were performed using defined enzyme activity of HEK293-OATP1B1 or HEK293-OATP1B3 cell lysates. Enzyme activity (3 U) corresponded to 70 µg protein diluted in 2120 µl enzyme diluent buffer.

8.3.4. Glutathione Assays

All used glutathione assays were based on the reaction of glutathione (GSH) with 5,5'-dithio-bis-(2-nitrobenzoic acid (DTNB), resulting in a TNB chromophore with an absorbance measured at 412 nm. Thereby, the formation of TNB is proportional to the GSH concentration in the sample. Simultaneously, the disulfide product (GS-TNB) is reduced by glutathione reductase, recycling GSH back into the reaction ($[GSH]_{Total}$ = [GSH] + 2[GSSG]). To calculate the GSH concentration of an unknown sample, GSH standards ranging from 0.78 µM to 100 µM were used. Several variants based on this chemical reaction have been developed and modified for this dissertation. Buffer compositions are listed in Table 16.

Table 16: Glutathione Assay Buffer Composition

Buffer	Composition
DTNB Solution	1.5 mg/ml 5,5′-Dithiobis(2-nitrobenzoic acid)(M: 396.4 g/mol)
Enzyme Solution	6 Units/ml Glutathione Reductase (Cat.# G3664, Sigma-Aldrich)
Extraction Buffer	0.1 % Triton X-100, 0.6 % sulfosalicylic acid in KPE buffer
KPE Buffer	0.1 M Potassium Phosphate (KP) Buffer, 5 mM EDTA
NADPH Solution	0.16 mg/ml NADPH (Cat.# AE14.2, Roth) in Extraction Buffer
Potassium Phosphate (KP) Buffer	16 ml Potassium Phosphate Buffer A + 84 ml Potassium Phosphate Buffer B, pH 7.5
Potassium Phosphate Buffer A	100 mM KH_2PO_4 (M: 136.1 g/mol)
Potassium Phosphate Buffer B	100 mM K_2HPO_4 (M: 174.2 g/mol)
Working Solution	1:1 Enzyme Solution and DTNB solution

Quantitative Determination of Glutathione Using Enzymatic Recycling Method

For the quantitative determination of the cellular GSH concentration, a previously published protocol (Rahman et al., 2006) was modified and adapted. Cells were detached from culture plates and washed once with PBS. The cells were centrifuged for 5 min at 500 rcf. Cell pellets were resuspended in PBS. Cell numbers and sizes were determined using CASY Cell Analyzer (OMNI Life Science). All following steps were performed on ice. Samples ($2x10^6$ cells/sample) were aliquoted and centrifuged for 5 min at

5,000 rcf at 4 °C. Cell pellets were resuspended in 200 µl extraction buffer. For efficient cell lysis, all samples were vortexed for 1 min and homogenized using a 27 G syringe. Cell lysates were centrifuged for 10 min at 10,000 rcf. Supernatant was transferred to an Eppendorf tube and 10 µl/well were pipetted into a 96-well-plate in triplicates. To ensure that the samples remained within the standard linear concentration range, serial dilutions of the samples were prepared. As background control, 10 µl/well extraction buffer was used. After pipetting 10 µl/well of each GSH standard concentration, 150 µl of the working mixture was added to each well and the plates were incubated light protected for 5 min at room temperature. Next, 500 µl of NADPH solution was pipetted into each well and the absorbance was immediately measured in a preheated (37 °C) microplate reader (Infinite 200 Pro, Tecan) at 412 nm with a kinetic read (1 min intervals for 10 min).

Calculation of the Cytosolic GSH Concentration

The total cellular GSH concentration was measured indirectly using the known enzymatic activity of the glutathione reductase within the known GSH standard concentrations. The GSH concentration was calculated by subtracting the start values from all measured points, followed by the subtraction of the background. GSH standard concentrations were plotted as a function of the reaction time ($\Delta abs/min$). The obtained slopes were plotted against the standard GSH concentration. The GSH concentration of an unknown sample was calculated using the following equation:

$$GSH\ [\mu M] = \frac{\Delta abs/_{min}\,(Sample)}{\frac{\Delta abs/_{min}}{\mu M}\,(GSH\ Standard)}$$

Since the cellular cytosol is highly diluted when cells are lysed in 200 µl of extraction buffer, the cellular GSH concentration was calculated by applying a mathematically simplified approximation of cells as spheres:

$$Cell\ volume\ [\mu m^3] = \frac{4}{3} * \pi * r^3$$

Thereby, a mean diameter of 14 µm (r = 7 µm) was measured in HEK293 cells and 16 µm (r = 8 µm) was measured in both hepatocyte cell lines (IHH and AML12). Using HEK293 cells as an example, the following calculations were performed:

$$Cell\ volume\ [\mu m^3] = \frac{4}{3} * \pi * (7\ \mu m)^3 = 1436.8\ \mu m^3 = 1.4368 * 10^{-9} ml$$

By converting µm^3 to ml, the following volume for a single cell was obtained:

$$Cell\ volume\ [ml] = 1436.8\ \mu m^3 * 1 * 10^{-12} = 1.4368 * 10^{-9} ml$$

To obtain the total cell volume within the sample, single cell volume was multiplied with the cell number:

$$Cell\ volume_{total}[\mu l] = 1.4368 * 10^{-9}\ ml * (2 * 10^{6}\ cells) = 0.00287\ ml = 2.87\ \mu l$$

Consequently, by lysing the cells in 200 µl of extraction buffer, the cytosolic GSH concentration was diluted by a factor of 70. This dilution factor was multiplied with the measured GSH concentration to obtain the cytosolic GSH concentration.

8.3.5. Multiplexing of Assays

To increase the analytical throughput by increasing the toxin concentrations tested and working as sustainably as possible, simultaneous evaluation of cell viability, phosphatase activity, glutathione response, and protein quantification using a single toxin exposure plate was established as a multiplexing assay.

Cell Lysis

After obtaining cell viability data via resazurin assay, the 96-well-plates were washed once with PBS. Cells were lysed using 50 µl/well (HEK293 cell lines) or 40 µl/well (IHH and AML12 cells) extraction buffer. To ensure sufficient cell lysis, cells were additionally lysed by freeze-thawing at -80 °C and thawing while shaking at 4 °C.

Colorimetric Protein Phosphatase Activity Assay for Multiplexing Assays

Immediately after cell lysis, 20 µl/well of the cell lysates were transferred into fresh 96-well-plates and mixed with 20 µl/well enzyme dilution buffer. As a background control, 20 µl/well of extraction buffer and 20 µl/well of enzyme dilution buffer were mixed. The plates were incubated at 37 °C for 5 min to enzymatically activate the phosphatases. Next, 200 µl of substrate solution was added to each well. Absorbance was measured at 405 nm every 10 min for 4 h. Phosphatase activities were calculated by subtracting the start value (0 h) and the background from all measured points. Phosphatase activities were expressed as percentage of solvent control cells or normalized to the protein content. The half-maximal effective concentrations (EC_{50}) were calculated using GraphPad Prism 9 software via five-parameter asymmetric nonlinear regression without anchoring points.

Quantitative Determination of Glutathione For Multiplexing Assays

The quantitative GSH assay was performed simultaneously with the colorimetric protein phosphatase activity assay. Therefore, 10 µl/well of the cell lysates were transferred into 96-well-plates. After pipetting 10 µl/well of each GSH standard concentration and 10 µl/well extraction buffer as a background control, 150 µl of the working mixture was added to each well and the plates were incubated light protected for 5 min at room temperature. Next, 500 µl/well NADPH solution was added, and the absorbance was immediately measured in a preheated (37 °C) microplate reader (Infinite 200 Pro, Tecan) with a kinetic read at 1 min intervals for 10 min.

Sulforhodamine B for Protein Quantification After Multiplexing Assays

After using 20 µl/well for the phosphatase assay and 10 µl/well for the GSH assay, only 20 µl/well (HEK293 cells) and 10 µl/well (IHH and AML12 cells) remained. Since protein quantification in 96-well-plates was not reliably using Pierce™ BCA Protein Assay Kit, the SRB assay was adapted to quantify the protein amounts in each sample. BSA standards ranging from 25 to 2000 µg/ml were prepared using Pierce™ Bovine Serum Albumin Standard Ampules (Cat.# 23209, Thermo Fisher) diluted in extraction buffer. Standards were prepared for analysis of either 10 µl/well or 20 µl/well samples. Proteins within the samples were precipitated using 50 µl/well of 10 % TCA solution. The plates were then incubated for 1 h at 4 °C, followed by centrifugation for 15 min at 2,000 rcf (Megafuge™ 8, Thermo Fisher). The supernatant was slowly aspirated, and the plates were air-dried for 48 h. Subsequently, 50 µl/well of 0.057 % SRB solution was added and the plates were incubated for 30 min at room temperature. The SRB solution was slowly aspirated, and the plates were rinsed twice with 1 % acetic acid to remove the unbound SRB dye. Next, 100 µl/well of 10 mM Tris base solution was added and the plates were incubated for 5 min at room temperature while shaking. The absorbance was measured at 510 nm using a microplate reader (Infinite 200 Pro, Tecan). Linear regression of the standards was calculated by plotting the measured absorbance against the BSA concentration. Calculations were performed using Microsoft Excel, and data visualization and analyses were performed using GraphPad Prism 9 software.

8.4. Protein Half-Life Analysis

8.4.1. Cycloheximide Chase Assay

The cycloheximide (CHX) chase assay allows the visualization of the protein degradation kinetics of steady-state proteins. CHX is an antibiotic produced by Streptomyces griseus, which inhibits eukaryotic translation elongation by binding to the E-site of the 60S ribosomal unit. HEK293-OATP1B1 cells were seeded in Poly-D-Lysine coated 6-well-plates and incubated overnight. The following day, growth medium was replaced with serum-free medium, and the plates were incubated for 24 h at 37 °C and 5 % CO_2. Cells were treated with 500 µg/ml CHX dissolved in DMSO and incubated for 0, 4, 14 or 24 h at 37 °C and 5 % CO_2. The plates were washed once with ice-cold PBS, and the cells were lysed in RIPA buffer using a cell scraper. Cell lysates were homogenized using a 26 G syringe and centrifuged for 20 min at 4 °C and 16,000 rcf. The supernatant was transferred into a pre-chilled Eppendorf tube and the proteins were quantified using the Pierce™ BCA Protein Assay Kit. Samples were prepared by mixing cell lysates with 5x SDS sample buffer, heated to 95 °C for 10 min, and aliquots were stored at -20 °C. Protein degradation was measured using SDS PAGE and western blot analyses.

Cycloheximide Chase Assay with MC-132 Co-Treatment

To check whether the proteins of interest were degraded via the ubiquitin-proteasome pathway, a cycloheximide chase assay was performed with MG-132 co-treatment. MG-132 is a cell-permeable

proteasome inhibitor that reduces the degradation of ubiquitin-conjugated proteins. HEK293-OATP1B1 cells were seeded in Poly-D-Lysine coated 6-well-plates and incubated for at least 15 h. Growth medium was replaced with serum-free medium, and the plates were incubated for 24 h at 37 °C and 5 % CO_2. Cells were treated with 500 µg/ml CHX, 10 µM and 25 µM MG-132 (Cat.# M7449, Sigma-Aldrich) for 24 h at 37 °C and 5 % CO_2. Cell lysis was performed as previously described for the cycloheximide chase assay.

8.4.2. Determination of Glutathione Half-Life and Protein Stability

Since GSH is a non-ribosomal but enzymatically produced protein, the half-life of GSH could not be determined using the CHX chase assay. Therefore, the rate-limiting enzyme of GSH synthesis (γ-glutamyl-cysteine synthetase) was inhibited by BSO in a time-dependent manner, and cellular GSH levels were measured using the GSH assay. HEK293-OATP1B1 cells were seeded in Poly-D-Lysine coated 96-well-plates and incubated for 15 h at 37 °C and 5 % CO_2. Cells were treated with 125 µM BSO for 0, 1.5, 3, 6 or 10 h. Cells were lysed using 50 µl/well extraction buffer. To ensure sufficient cell lysis, cells were additionally lysed by freeze-thawing at -80 °C and thawing while shaking at 4 °C. Cellular GSH content was measured using the quantitative GSH assay for multiplexing assays.

8.5. Protein Analysis

8.5.1. Membrane Protein Isolation

Membrane proteins were isolated by differential centrifugation, according to a previously published protocol (Huber et al., 2007). All following steps were performed at 4 °C. Confluent T_{75} cell culture flasks were rinsed three times with 0.9 % NaCl and once with 250 mM sucrose solution. Cells were scraped and resuspended in 5 mM sucrose solution containing 1 mM phenylmethylsulfonyl fluoride (PMSF). Cell suspension was homogenized using a glass Teflon potter. The homogenate was centrifuged for 10 min at 900 rcf. The supernatant was transferred into a fresh Eppendorf tube and centrifuged for 20 min at 8,400 rcf, followed by ultracentrifugation for 1 h at 100,000 rcf (Optima L70, Beckman). The final pellet was resuspended in 250 mM sucrose solution containing 1 mM PMSF. The protein concentration of the membrane fraction was determined using Pierce™ BCA Protein Assay Kit. Samples were aliquoted and mixed with 5x SDS sample buffer, heated to 65 °C for 10 min, and stored at -80 °C.

8.5.2. SDS PAGE

Sodium dodecyl sulfate polyacrylamide gel electrophoresis (SDS PAGE) was used to separate the proteins according to their molecular weights. All samples were supplemented with 5x SDS sample buffer and heated to 95 °C (cytosolic proteins) or 65 °C (membrane proteins). Equal amounts of proteins (15 µg/lane for cytosolic proteins and 30 µg/lane for membrane proteins) were loaded onto 8-12 % SDS gels, depending on the protein size. To estimate the size of proteins within the samples, Spectra™ Multicolor Broad Range Protein Ladder, 10-260 kDa (Cat.# 26634, Thermo Fisher) or PageRuler™

Prestained Protein Ladder, 10-180 kDa (Cat.# 26616, Thermo Fisher) was used. The gels were run at 200 V. Gels were either stained with Coomassie for proteomic analysis or used for western blot analysis.

8.5.3. Western Blot Analysis

Proteins were transferred onto 0.2 µm PVDF membranes (Cat.# 10600021, Cytiva) by blotting for 2 h at 50 V while cooling. Membranes were blocked either with 5 % non-fat dried milk or 5 % BSA diluted in TBST for 3-4 h to reduce unspecific antibody binding. Primary antibodies (listed in **Table 17**) were diluted in blocking solution and membranes were incubated overnight at 4 °C. Membranes were washed three times with TBST for 15 min to remove excess antibodies.

Table 17: Primary Antibodies Used for Western Blot Analysis

Protein	Supplier	Cat.#	Species	Dilution	Blocking Solution
ABCB11	Invitrogen	PA5-114800	Rabbit	1:1,000	5 % milk
Actin	Sigma-Aldrich	A2228	Mouse	1:10,000	5 % BSA
CD10	Abcam	ab256494	Rabbit	1:1,000	5 % BSA
CYP3A4	Abcam	ab124921	Rabbit	1:1,000	5 % BSA
CYP7A1	Invitrogen	PA5-119862	Rabbit	1:1,000	5 % BSA
CYP8B1	Bioss	bs-14165R	Rabbit	1:5,000	5 % BSA
E-Cadherin	Abcam	ab287970	Mouse	1:1,000	5 % BSA
Fibronectin	Abcam	ab2413	Rabbit	1:1,000	5 % BSA
GAPDH	Santa Cruz	sc-25778	Rabbit	1:1,000	5 % BSA
GCLC	Thermo Fisher	PA5-19702	Rabbit	1:900	5 % BSA
GSS	Thermo Fisher	PA5-49598	Rabbit	1:1,000	5 % BSA
GSTM1	Bio-Techne	MAB6894	Mouse	1:5,00	5 % BSA
MRP2	Abcam	ab172630	Rabbit	1:1,000	5 % BSA
OATP1B1	Kindly provided by Bruno Stieger		Rabbit	1:1,000	5 % milk
OATP1B3	Kindly provided by Bruno Stieger		Rabbit	1:1,000	5 % milk
PPP1Cα	Bio-Techne	MAB6105	Mouse	1:500	5 % BSA
PPP2AC	Bio-Techne	AF1653	Rabbit	1:2,000	5 % BSA
PPP4C	Bio-Techne	MAB5074	Mouse	1:500	5 % BSA
PPP5	Thermo Fisher	PA5-17339	Rabbit	1:1,000	5 % BSA
PPP6C	Thermo Fisher	PA5-84040	Rabbit	1:250	5 % BSA
Vimentin	Sigma-Aldrich	V6630	Mouse	1:200	5 % BSA

Subsequently, membranes were incubated with secondary antibodies (listed in **Table 18**) diluted in the corresponding blocking solution for 2 h at room temperature. Membranes were washed three times with TBST for 15 min and immuno-positive bands were detected by enhanced chemiluminescence (ECL ultra, Cat.# TMA-100, Lumingen). Blots were imaged using Amersham ImageQuant 800 (Cytiva). Blots were adjusted using Microsoft PowerPoint and quantified using ImageJ software.

Table 18: Secondary Antibodies Used for Western Blot Analysis

Antibody	Supplier	Cat.#
Anti-Mouse IgG-HRP	Sigma-Aldrich	A9044
Anti-Rabbit IgG-HRP	Sigma-Aldrich	A0545

Since the readout of the cycloheximide chase assay is highly dependent on the antibodies used, PPP and glutathione relevant enzyme antibodies were verified using either overexpression lysates or purified proteins, as listed in Table 19.

Table 19: Positive Controls Used for Western Blot Analysis

Positive Control	Supplier	Cat.#	Size [kDa]	Concentration
GCLC Human Recombinant Protein	Abcam	ab112293	96.0	300 ng/lane
GSS Human Overexpression Lysate	Origene	LY424876	52.4	20.0 µg/lane
GSTM1 Human Overexpression Lysate	Origene	LY424640	25.5	5.00 µg/lane
PPP1Cα Human Recombinant Protein	Origene	TP760285	37.3	500 ng/lane
PPP2A Human Recombinant Protein	Abcam	ab114424	60.0	300 ng/lane
PPP4C Human Recombinant Protein	Origene	TP760519	34.9	250 ng/lane
PPP5 Human Recombinant Protein	Produced in the lab according to Altaner et al. (2020)			
PPP6C Human Overexpression Lysate	Origene	LY426607	38.8	20.0 µg/lane

8.5.4. Proteomics

Proteomic analyses were performed at the Proteomic Facility Center (University of Konstanz). Stably transfected HEK293 cells were lysed in RIPA buffer and 175 µg/lane of the lysate was loaded onto a 10 % SDS gel. Staining solution was prepared by mixing 100 ml of Solution A (10 % (w/v) ammonium sulfate and 2 % (w/v) phosphoric acid in Milli-Q water) with 2.5 ml of Solution B (5 % (w/v) Coomassie Brilliant Blue G-250 in Milli-Q water). The staining solution was mixed thoroughly for 20 min, and 25 ml pure methanol was added and mixed again for 30 min. Gels were stained overnight while gently shaking. The gels were washed with 25 % methanol for 1 h, followed by washing with Milli-Q water until protein bands were clearly visible. Subsequently, the loaded lane was cut into 10 equal pieces and analyzed at the Proteomic Facility Center using nano-LC-MS/MS and shotgun analysis.

8.6. Gene Expression Analysis

8.6.1. Primer

Primer Design

Primers were designed using the Nucleotide Database of the National Center for Biotechnology Information (NCBI). Optimal primers were considered to have a length of approximately 20 base pairs (bp) and melting temperatures between 59 °C and 61 °C. On the corresponding genomic DNA, the primers should span an exon-exon junction or be separated by at least one intron. All primers were synthesized by Eurofins. Lyophilized primer pairs were dissolved in nuclease-free water to a stock concentration of 100 µM.

Primer Validation and Efficiency

For primer validation, standard PCR with thermostable Taq polymerase (as summarized in Table 20), designed primer pairs, and cDNA from either whole human liver lysate (total RNA, Cat.# AM7960, Invitrogen) or whole mouse liver lysate (total RNA, Cat.# QS0634, Invitrogen) were used.

Table 20: Taq Polymerase PCR Template

Cycle	Temperature	Time
1 cycle	95 °C	2 min
30 cycles	95 °C	30 sec
	59 °C	30 sec
1 cycle	68 °C	60 sec
1 cycle	68 °C	5 min
	12 °C	hold

PCR products were visualized using a 2 % agarose gel (120 V for 1 h). Gel was stained using ethidium bromide. Only PCR products with clear amplicons were purified using the QIAquick PCR Purification Kit (Cat.# 28104, Qiagen), according to the manufacturer's instructions, followed by Sanger sequencing (Eurofins). Validated primer efficiencies were determined by quantitative real-time PCR using dilutions of cDNA from either whole human or mouse liver lysate. The resulting primer pairs are listed in Table 21 and Table 22.

Table 21: Human Primer Sequences

	Protein	Gene	NCBI	Sequence
Apoptosis Marker	BAX	BAX	NM_004324.4	GCCCTTTTGCTTCAGGGTTTC
				TGAGACACTCGCTCAGCTTC
	p53	TP53	NM_001276761.3	TTCCGAGAGCTGAATGAGGC
				TTTGGACTTCAGGTGGCTGG
Bile Canaliculi	ATP8B1	ATP8B1	NM_001374386.1	AACAGCAGAACTGGACGGAG
				AGAGGAATTGCCCACCTGTG
	BAR	NR1H4	NM_001206977	TGCAAAGAGATGGGAATGTTGG
				GCTAGACCCCTCCCCTGTAA
	PXR	NR1I2	NG_011856.2	CGGCTCCTTGGTAAAGCTACT
				CGATGGGCAAGTCCCTGAAG
Dedifferentiation	E-Cadherin	CDH1	NM_001317185.2	GCCTCCTGAAAAGAGAGTGGAAG
				TGGCAGTGTCTCTCCAAATCCG
	SNAI2	SNAI2	NM_003068.5	ATCTGCGGCAAGGCGTTTTCCA
				GAGCCCTCAGATTTGACCTGTC
Hepatic Marker	HNF1A	HNF1A	NM_000545	CAGTAAGGTCCACGGTGTGC
				CACTTGGTGGAGGGGTGTAG
	HNF4	HNF4	NM_178849.3	CATAGCTTGACCTTCGAGTGC
				CGTGGTGGACAAAGACAAGA

Housekeeping Genes	Actin	ACTB	NM_001101	GTTGTCGACGACGAGCG
				GCACAGAGCCTCGCCTT
	GAPDH	GAPD	NM_001357943.2	AATCCCATCACCATCTTCCAGGAG
				CATGGTTCACACCCATGACGAACA
	HPRT1	HPRT1	NM_000194.3	TGACACTGGCAAAACAATGCA
				GGTCCTTTTCACCAGCAAGCT
	RPL13A	RPL13A	NG_010172.2	CCTGGAGGAGAAGAGGAAAGAGA
				TTGAGGACCTCTGTGTATTTGTCAA
	SDHA	SDHA	NM_004168.4	TGGGAACAAGAGGGCATCTG
				CCACCACTGCATCAAATTCATG
Metabolism/ Detoxification	Albumin	ALB	NM_000477.7	GATGAGATGCCTGCTGACTTGC
				CACGACAGAGTAATCAGGATGCC
	CYP2C9	CYP2C9	NM_000771.4	CTATTGAAAGCTTGGAAAACACTGC
				TCCTGGACTTTAGCTGTGACC
	CYP3A4	CYP3A4	NM_001202855.3	CCAAGCTATGCTCTTCACCG
				TCAGGCTCCACTTACGGTGC
	FAH	FAH	NM_000137.4	CCAACCCGAAGCAGGACC
				TTGCATATGGTAGCCGCCTG
	GCLC	GCLC	NM_001498.4	ACGGAGGAACAATGTCCGAG
				CAGGACAGCCTAATCTGGGAA
	GR	GSR	NM_000637.5	CAATGATCAGCACCAACTGCAC
				TTAACCTCCTTGACCTGGGAGA
	PAH	PAH	NM_001354304.2	CATTGGTGCCACTGTCCATGAG
				TCAGCATCCAGTTCCGCTCCAT
Serine/Threonine Phosphatases	PPP1CA	PPP1	NM_002708.4	CCTTGGAGACCATCTGCCTG
				TCCTCCACAAGCACGACTTG
	PPP2CA	PPP2C	NM_002715.4	GCCTCTGCGAGAAGGCTAAA
				CCCATGCACATCTCCACAGA
	PPP5C	PPP5	NM_006247.4	AAACCACACTCAAAGAGACAGAGA
				CCTCGGTCCACAAAGTCACC
	PPP6C	PPP6	NM_002721.5	CCTGAAGCGGCTATGTGACT
				TCAGGAACCTGACCTCCAGT
Bile Canaliculi Transporter	BCRP	ABCG2	NM_004827.3	GGGTAATCCCCAGGCCTCTAT
				AGAAGAGAACCCCAGCTCTGT
	BSEP	ABCB11	NM_003742.4	GAACACGTTGTGGGTTGCTG
				CTGTATCTGACGAGCTGCGG
	MRP2	ABCC2	NM_000392.5	CCAAGAGTAAGACCATTCAGGTCA
				TGAATGAAGGTTCCCAGGCA
Efflux Transporter	MDR1	ABCB1	NM_001348946.2	GCCAAAGCCAAAATATCAGC
				TTCCAATGTGTTCGGCATTA
	MDR3	ABCB4	NM_000443.4	CAAAGAACGGAACAGCCTGG
				GCCAATCGGAGTATCGAAACAATG
	MRP1	ABCC1	NM_004996.3	CTGGACTGATGACCCCATCG
				GCGATCCCTTGTGAAATGCC
	MRP3	ABCC3	NM_001144070.2	GTCCCATTCCGCTCCAAGAT
				TCAGGGTAGGGGTTAGGGTC
	MRP4	ABCC4	NM_005845.5	TCTCCGTTTATGGCCAATTT
				CCGTGTACCAGGAGGTGAAG

Influx Transporter	OAT1	SLC22A6	NM_004790	CCATCGTGACTGAGTGGGAC
				TCTGCAAGGTAGCCGAACAC
	OAT2	SLC22A7	NM_006672.3	TTGCAACTGAGTGGGATCTGG
				GCGAAGAAGAAAGTGGACGC
	OAT4	SLC22A11	NM_018484	CCGCAGTAGATGACGAATGTT
				ATCCTGGTGGGCTCCTTTAT
	OATP1B1	SLCO1B1	NM_006446.4	TTGCACTGGGTTTCCACTCA
				AAGCCCAAGTAGACCCTTGAAA
	OATP1B3	SLCO1B3	NM_019844.3	TTGTTCTCTGCAACAGGAGGT
				GAGCTAGAATTCCTCCTAGTGTTCT
	OATP2B1	SLCO2B1	NM_001145212.3	ACCCACACACCCTCCTTCAT
				CTGGGCATCCAGGCCAAAAT
	OCT1	SLC22A1	NM_000531.6	CCCCTCATTTTGTTTGCGGT
				TTTCTCCCAAGGTTCTCGGC
	OCT2	SLC22A2	NM_003058	TGCATATTTTCGGCTTCCTC
				ACCGGCTCACTAACATCTGG

Table 22: Mouse Primer Sequences

	Protein	Gene	NCBI	Sequence
Dedifferentiation	Afamin	Afm	NM_145146	AGGGATCACGGATGAGGAGT
				GACTCAGGCTCCTGCACTTC
Housekeeping	Actin	Actb	NM_007393	GGCTGTATTCCCCTCCATCG
				CCAGTTGGTAACAATGCCATGT
Metabolism/ Detoxification	Albumin	Alb	NM_009654	TGTAGTGGATCCCTGGTGGA
				ACAAGGTTTGGACCCTCAGTC
	Gclc	Gclc	NM_010295	GTGCTCAAGTGGGGTGACG
				GAGGGTCGGATGGTTGGG
	Gss	Gss	NM_008180	CGAGCTGCTAGACAGGAAGAT
				CTCGGAAGTACACCACAGCA
	Gstm1	Gstm1	NM_001374678	GCACCACCTGGATGGAGAG
				GCAAAGGGTTTGGCAATGGA
Serine/Threonine Phosphatases	Ppp2ca	Ppp2ca	NM_019411	CTCACGTTGGTGTCCAGAGC
				CTGGGTCAAACTGCAAGAAAGAATA
	Ppp4c	Ppp4c	NM_001360464	GCAGATCGAGCAGCTACGG
				GACATCGCCACCTACTCTGAAC
	Ppp5c	Ppp5c	NM_011155	GACGCTCTGTCGTGGACTC
				TTCACCTGTACTAGGATCTGGTAGG
Transporter	Mrp2	Abcc2	NM_013806	GCTTTGTTCTGTCCAACGCC
				CCCACGGCGCCTCATTA
	Mrp4	Abcc4	NM_001033336	CTGCTCGCGCGTGTTCT
				AGTTCTTTATCCCAGTACCGTTGA
	Oatp1a1	Slco1a1	NM_013797	ACGCAAGATCCAACAGAGTGT
				GGGCCAACAATCTTCCCCAT
	Slc22a7	Slc22A7	NM_144856	CATCATTGTACTTCCGTTGGAGTT
				CACGACCCTGGGTTAGAAGC

8.6.2. Quantitative Real-Time PCR (RT-qPCR)

Total RNA was isolated from the samples using the RNeasy Mini Kit (Cat.# 74104, Qiagen) according to the manufacturer's instructions. Reverse transcription was performed using a qScript cDNA Synthesis Kit (Cat.# 733-1175, VWR) according to the manufacturer's instructions. Quantitative real-time PCR (RT-qPCR) was performed using 40 ng cDNA per sample (in duplicates) in KAPA SYBR FAST Master Mix (Cat.# KK4601, Sigma-Aldrich) with 10 µM of each forward and reverse primer. RT-qPCR was performed using the CFX Connect Real-Time PCR Detection System (Bio-Rad) according to the template described in Table 23.

Table 23: Quantitative Real-Time PCR Template

Step	Temperature	Time	Cycles
Initial Denaturation	95 °C	3 min	
Denaturation	95 °C	3 sec	} 40 x
Annealing/Elongation	59 °C	20 sec	
Melting Curve	65 – 95 °C	5 min	

Gene expression was normalized to the mean expression of housekeeping genes according to the following formula:

$$\Delta C_q(GOI) = \frac{\sum C_q(Housekeeping\ Genes)}{n\ (Housekeeping\ Genes)} - C_q(GOI)$$

The fold change was calculated in relation to the respective standard using following formula:

$$Fold\ Change\ (Sample) = 2^{\Delta C_q(Sample) - \Delta C_q(Standard)}$$

8.7. Cell Cycle Analysis

In non-tumorigenic cells, cell cycle synchronization is triggered by cell-cell contact inhibition, leading to cell cycle arrest in the early G_1 phase when forming a confluent monolayer. Cell cycle arrest can be reversed by subculturing the cells at a lower density, causing them to reenter the cell cycle simultaneously. As HEK293 cells are tumorigenic and not contact inhibited cells, HEK293 cells are considered to be asynchronous. Therefore, different methods such as serum starvation or double thymidine block are used to synchronize cells, leading to more precise protein expression analyses.

8.7.1. Cell Cycle Synchronization

Cell Cycle Synchronization by Double Thymidine Block

Thymidine is commonly used as a DNA synthesis inhibitor. By interrupting the deoxynucleotide metabolic pathway, thymidine induces cell cycle arrest at the G_1/S boundary and inhibits DNA replication. Stably transfected HEK293 cells were seeded on poly-D-lysine coated 6-well plates and incubated for 15 h at 37 °C and 5 % CO_2. Medium was replaced with 2.5 mM thymidine solution dissolved in growth

medium. Plates were incubated for 18 h at 37 °C and 5 % CO_2. Cells were washed once with PBS to remove excess thymidine. Cells were released into the cell cycle by incubation for either 5 h or 9 h in growth medium, followed by a second thymidine incubation for 17 h. Medium containing thymidine was aspirated, cells were washed once with PBS, and again released into the cell cycle by incubation in growth medium. Samples for cell cycle analysis were collected at 0 h, 2 h, 6 h, 24 h and 48 h after cell synchronization. Cell cycle analysis was performed using flow cytometry.

Cell Cycle Analysis Using Flow Cytometry

Cells were detached from culture plates using Trypsin/EDTA solution, followed by centrifugation for 5 min at 500 rcf at 4 °C. The supernatant was discarded, and the cell pellets were washed twice with ice-cold PBS. Cell density was measured using CASY Cell Analyzer (OMNI Life Science). Samples containing $2x10^6$ cells were aliquoted and permeabilized for 30 min by dropwise addition of 70 % ice-cold ethanol while vortexing. Samples were centrifuged for 5 min at 500 rcf and washed twice with PBS, followed by RNase A (100 µg/ml) digestion. DNA was stained with 50 µg/ml propidium iodide (PI). Dead cells were stained using SYTOX™ Blue Dead Cell Stain (Cat.# S34857, Invitrogen). Samples were analyzed using a flow cytometer (LSRFortessa™, BD Biosciences) at the Flow Cytometry Center (University of Konstanz).

9. Supplementary

9.1. Chapter I

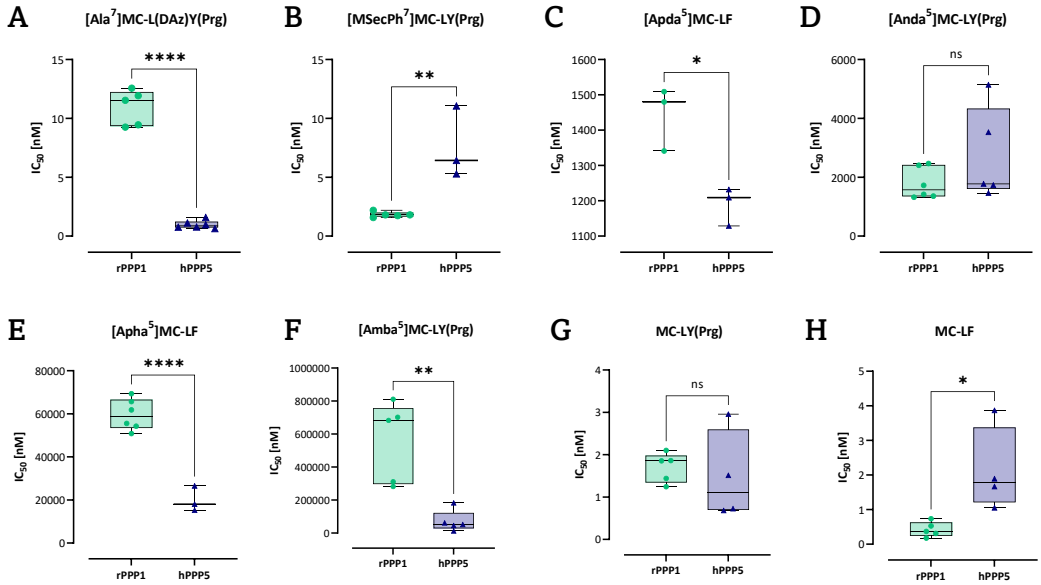

Supplementary Figure 1: Statistical Comparison of rPPP1 and hPPP5

The IC_{50} values obtained for rPPP1 and hPPP5 were compared and statistically analyzed. Each point represents an independent biological replicate (n=3-6). Individual statistical analysis was performed using a two-tailed unpaired t-test (****p<0.0001, **p<0.004, *p<0.02, ns = not significant).

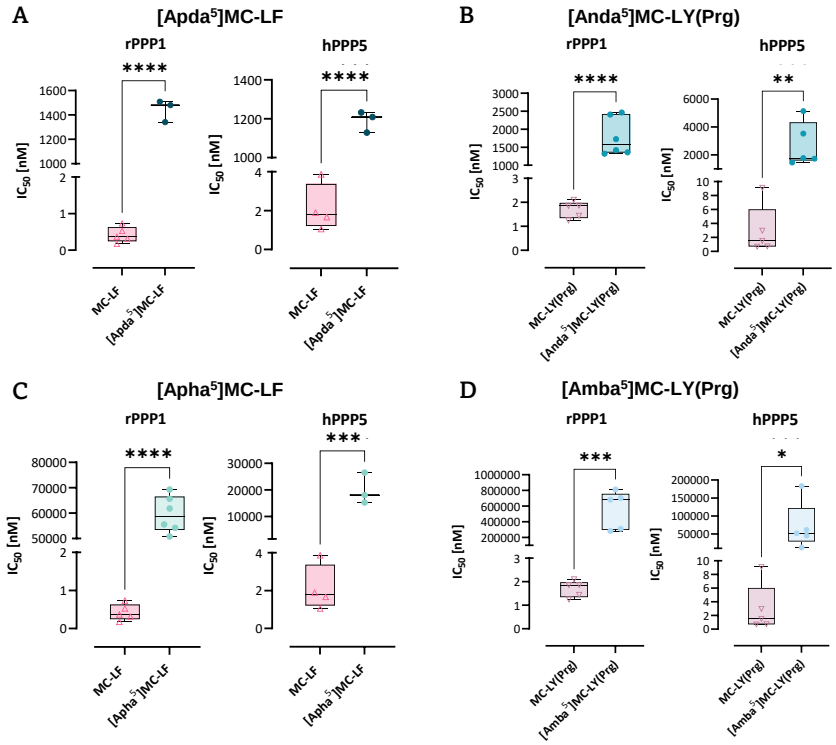

Supplementary Figure 2: Statistical Analyses of Adda Derivates in rPPP1 and hPPP5

The IC_{50} values of Adda derivates obtained in either rPPP1 or hPPP5 were compared to their parent microcystin molecule and statistically analyzed. Each point represents an independent biological replicate (n=3-6). Individual statistical analysis was performed using a two-tailed unpaired t-test (****p<0.0001, ***p=0.0009, **p=0,.0048, *p=0.0419).

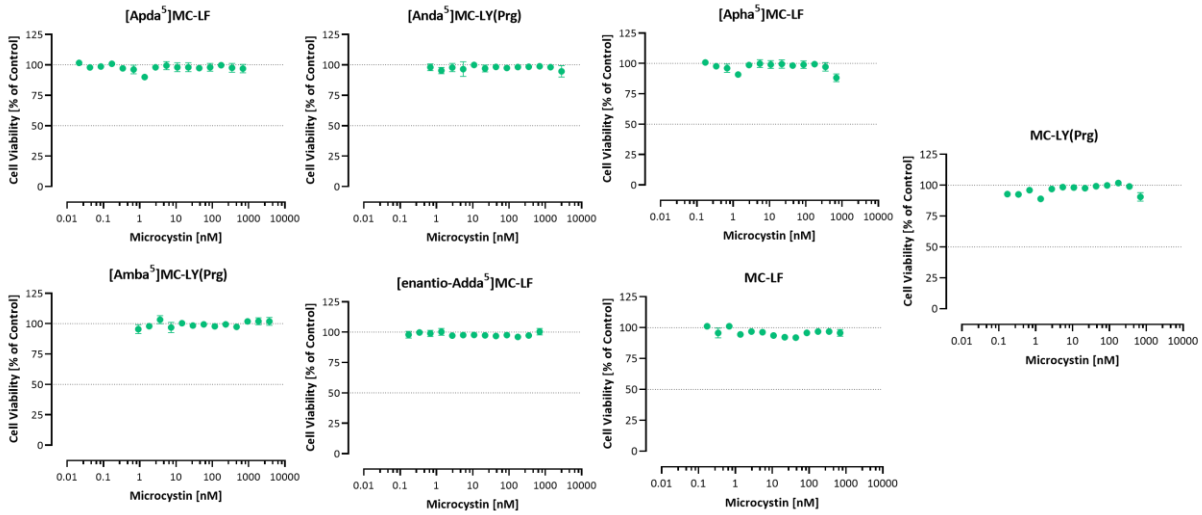

Supplementary Figure 3: HEK293-CV and Adda Derivates

Cell viability measured in HEK293-CV cells after 48 h exposure to the five Adda derivates are graphed. No reduction in cell viability was measured, therefore no EC_{50} values were determined. Each point represents the mean of 5-6 independent biological replicates, pipetted in triplicates ± SEM (n=5-6).

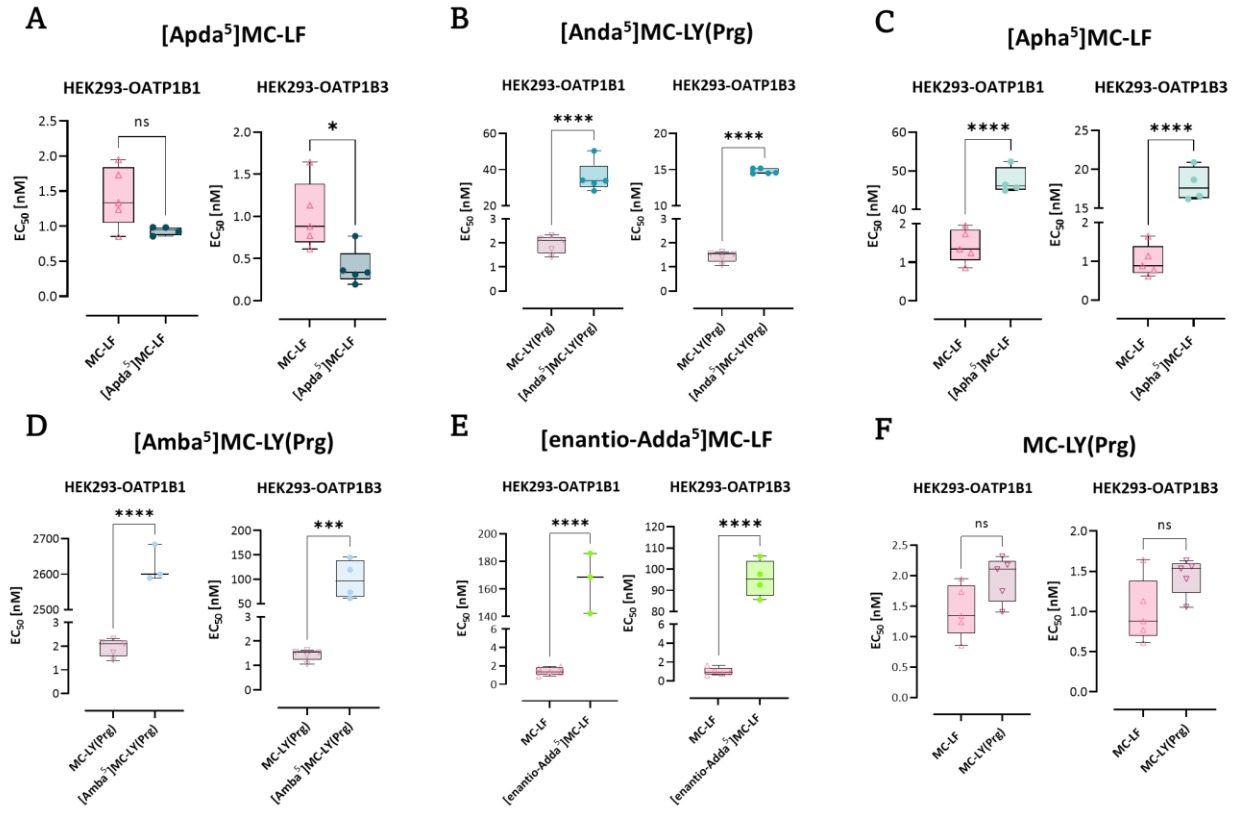

Supplementary Figure 4: Statistical Analyses of Adda Derivates in HEK293-OATP1B1 and -OATP1B3 Cells

The IC_{50} values obtained in either HEK293-OATP1B1 or -OATP1B3 for the synthetic microcystin derivates were compared to their parent microcystin molecule and statistically analyzed. Each point represents an independent biological replicate (n=3-5). Individual statistical analysis was performed using a two-tailed unpaired t-test (****p<0.0001, ***p=0.0007, *p=0.0169, ns = not significant).

9.2. Chapter II

Supplementary Table 1: Congener Specific Modifications

The individual residues and modifications of the microcystin congeners used are summarized. Table was adapted and expanded from Altaner et al. (2020).

Microcystin	Position (2)	Position (4)	Position (3)	Position (7)	Position (5)
MC-LR	Leucine	Arginine	β-D-MeAsp	Mdha	Adda
MC-RR	Arginine	Arginine	β-D-MeAsp	Mdha	Adda
MC-LF	Leucine	Phenylalanine	β-D-MeAsp	Mdha	Adda
MC-LW	Leucine	Tryptophan	β-D-MeAsp	Mdha	Adda
MC-YR	Tyrosine	Arginine	β-D-MeAsp	Mdha	Adda
MC-HilR	Homoisoleucine	Arginine	β-D-MeAsp	Mdha	Adda
MC-LA	Leucine	Alanine	β-D-MeAsp	Mdha	Adda
MC-WR	Tryptophan	Arginine	β-D-MeAsp	Mdha	Adda
MC-LY	Leucine	Tyrosine	β-D-MeAsp	Mdha	Adda
MC-HtyR	Homotyrosine	Arginine	β-D-MeAsp	Mdha	Adda
[ß-D-Asp^3]MC-LR	Leucine	Arginine	β-D-Asp	Mdha	Adda
[ß-D-Asp^3, Dhb^7]MC-RR	Arginine	Arginine	β-D-Asp	Dhb	Adda
[MSecPh^7]MC-LY(Prg)	Leucine	Tyrosine (Prg)	β-D-MeAsp	MSecPh	Adda
MC-LY(Prg)	Leucine	Tyrosine (Prg)	β-D-MeAsp	Mdha	Adda
[enantio-Adda^5]MC-LF	Leucine	Phenylalanine	β-D-MeAsp	Mdha	*enantio*-Adda
[Anda^5]MC-LY(Prg)	Leucine	Tyrosine (Prg)	β-D-MeAsp	Mdha	Anda
[Amba^5]MC-LY(Prg)	Leucine	Tyrosine (Prg)	β-D-MeAsp	Mdha	Amba
MC-RY	Arginine	Tyrosine	β-D-MeAsp	Mdha	Adda
MC-KL$_{D7}$	Lysine	Leucine (deuterated)	β-D-MeAsp	Mdha	Adda
MC-RF$_{D5}$	Arginine	Phenylalanine (deuterated)	β-D-MeAsp	Mdha	Adda
MC-F$_{D5}$R	Phenylalanine (deuterated)	Alanine	β-D-MeAsp	Mdha	Adda

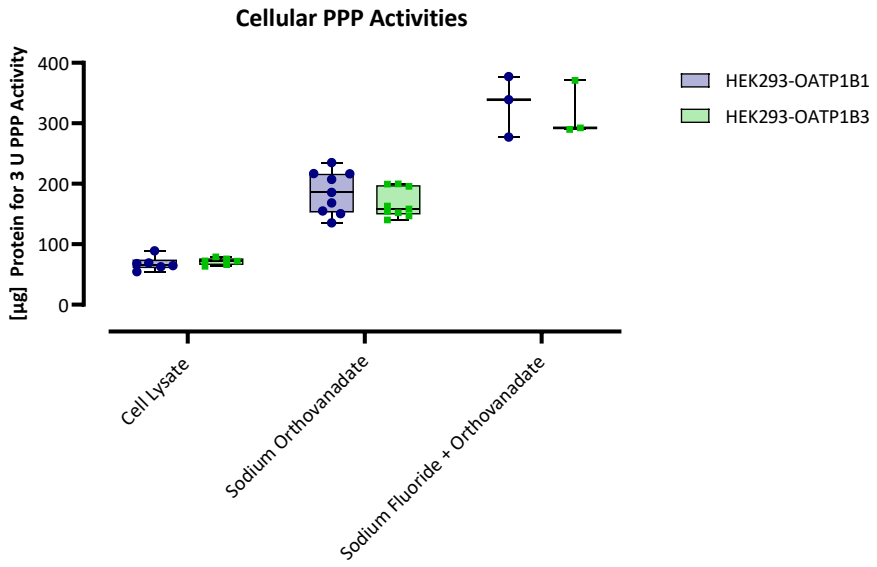

Supplementary Figure 5: Cellular PPP Activities in Stably Transfected HEK Cell Lines

Total cellular phosphatase activity in HEK293-OATP1B1 and -OATP1B3 cells was measured and compared with 3 U enzyme activity of commercially available rPPP1. Sodium orthovanadate was used as tyrosine phosphatase inhibitor (10 mM), while sodium fluoride was used as PPP inhibitor (50 mM). Each point represents an independent biological replicate (n=3-9).

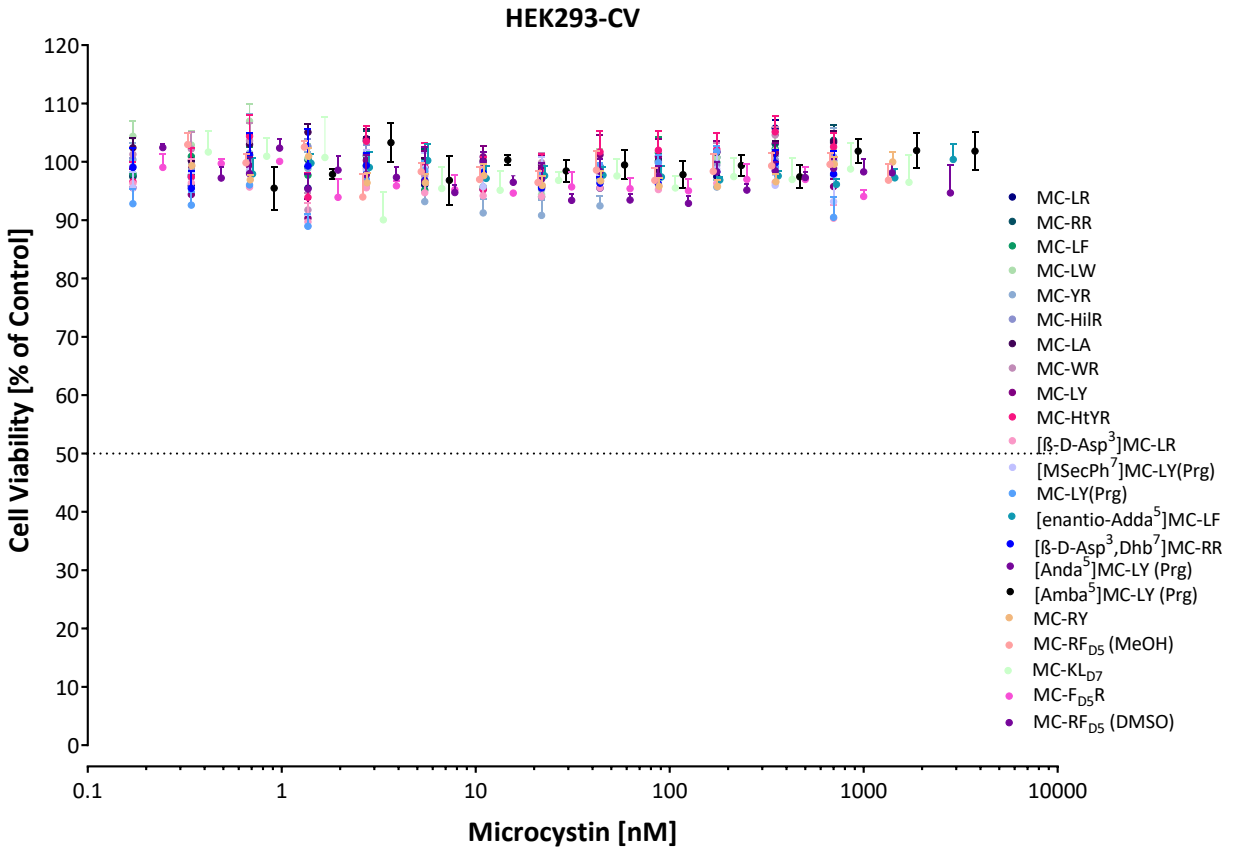

Supplementary Figure 6: Microcystin Exposure in HEK293-CV Cells

Cell viability was measured in HEK293-CV cells after the exposure to all used microcystin congeners. Each point represents the mean of 5 independent biological replicates, pipetted in triplicates ± SEM (n=5). No reduction in cell viability was measured, therefore no EC_{50} values were determined. Only upper error bars are shown for reasons of clarity.

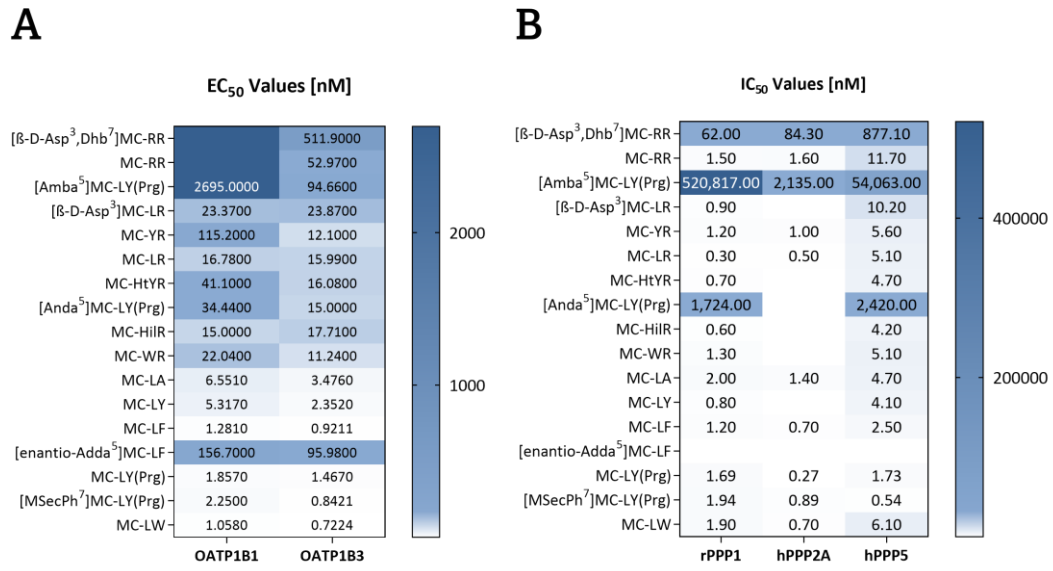

Supplementary Figure 7: Heatmaps of all Congeners Used

Visualized are the comparison of **(A)** EC_{50} values measured in OATP1B1- and OATP1B3-expressing HEK293 cells and **(B)** IC_{50} values determined for rPPP1, hPPP2A and hPPP5 after the exposure to all microcystins used. IC_{50} values were obtained from Altaner et al. (2020). Empty boxes indicate missing data due to product discontinuation (hPPP2A) or no inhibitory effect ([enantio-Adda^5]MC-LF).

9.3. Chapter III

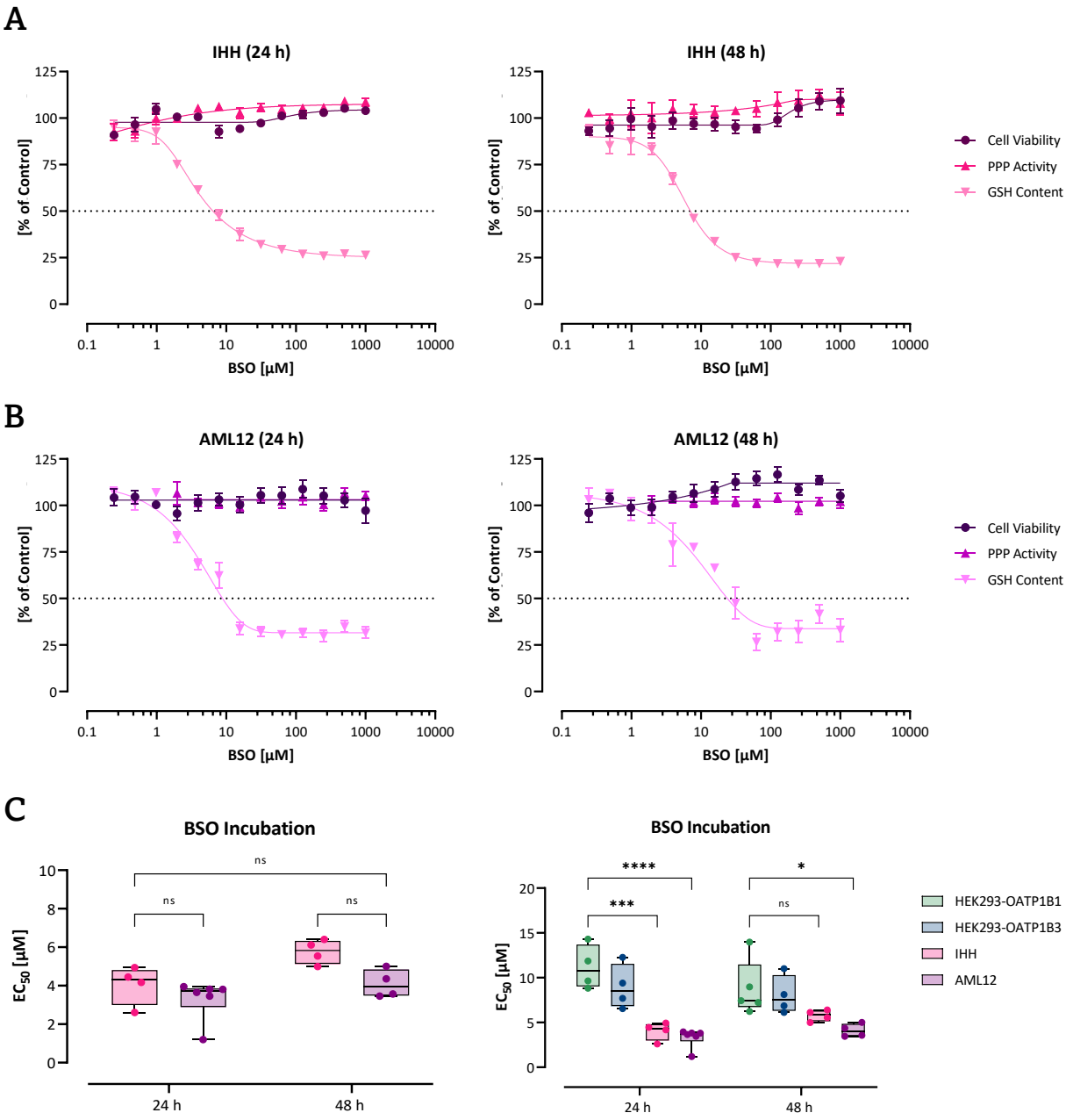

Supplementary Figure 8: Assay Validation Using Immortalized Hepatocyte Cell Lines

Assay validation was performed using serial dilutions of buthionine sulfoximine (BSO) in **(A)** immortalized human hepatocytes (IHH) and **(B)** alpha mouse liver 12 (AML12) cells for either 24 or 48 hours. Cell viability, PPP activity and GSH content were evaluated and presented as percentages compared to the control. Each point represents the mean of 4-5 independent biological replicates, pipetted in triplicates ± SEM (n=4-5). **(C)** Statistical analysis was performed for the obtained EC_{50} in both hepatocyte cell lines (left side) and compared to the transfected HEK293 cell lines (right side). Two-way ANOVA followed by Tukey's multiple comparison post-test was performed for both statistical analyses (****p<0.0001, ***p=0.0004, *p=0.0225, ns = not significant).

9.4. Chapter IV

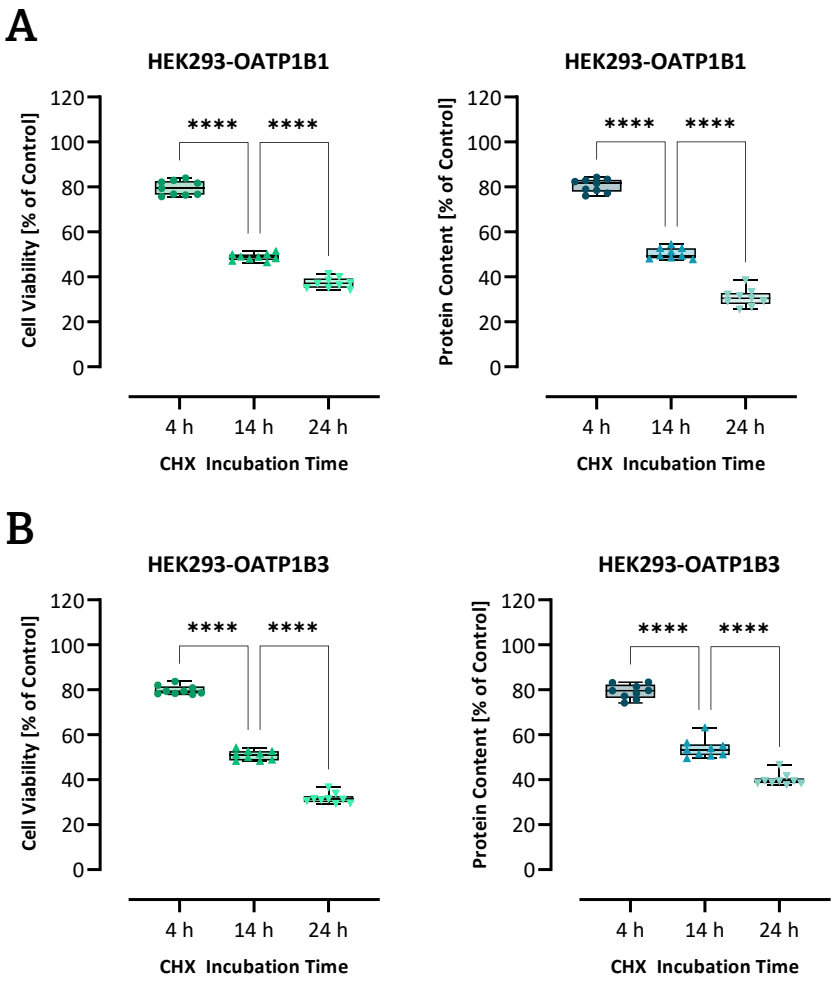

Supplementary Figure 9: Statistical Analysis of Cycloheximide Cytotoxicity

(A) OATP1B1- and **(B)** OATP1B3-expressing HEK293 cells were exposed to cycloheximide (CHX) for either 4, 14 or 24 hours and the corresponding cytotoxicities were assessed by either cell viability (left side) or protein content (right side). Each point represents an independent biological replicate (n=4). Corresponding statistical analyses were performed using a one-way ANOVA followed by Tukey's multiple comparison post-test (****p<0.0001).

Supplementary Figure 10: Antibody Verification

All antibodies used were previously established and verified using positive controls prior to half-life determination using cycloheximide chase assay. Antibody establishment and verification was performed by Elena Schönfeld as part of her master's thesis. Figure was adapted from (Schoenfeld, 2022).

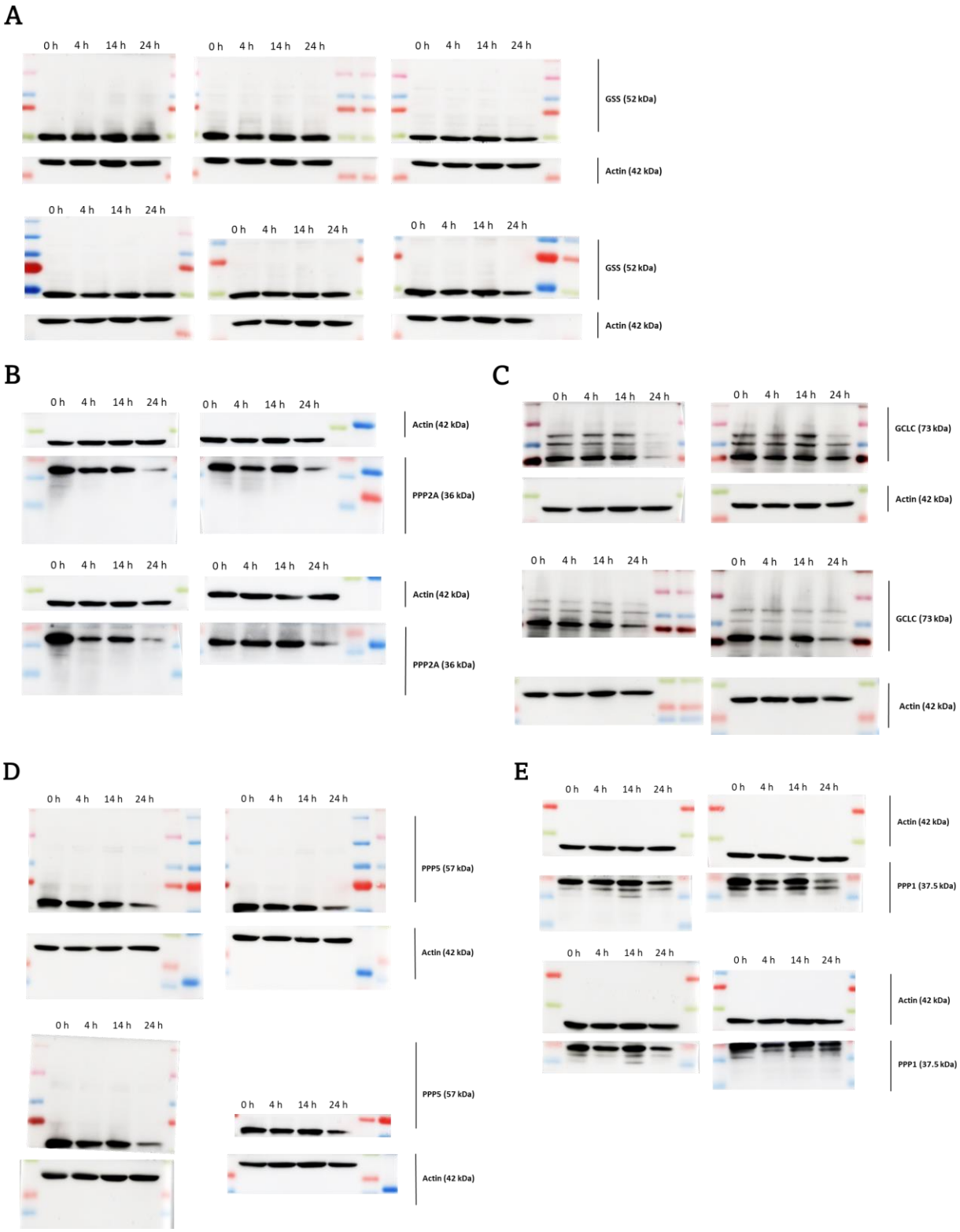

Supplementary Figure 11: Cycloheximide Chase Assay

HEK293-OATP1B1 cells were incubated with 500 µg/ml CHX for 0 (control), 4, 14, and 24 hours. Western blot analyses were performed using 15 µg/lane cell lysate and detected with **(A)** anti-GSS, **(B)** -PPP2A, **(C)** -GCLC, **(D)** -PPP5c, and **(E)** -PPP1c. All replicates used to calculate the protein half-lives are shown.

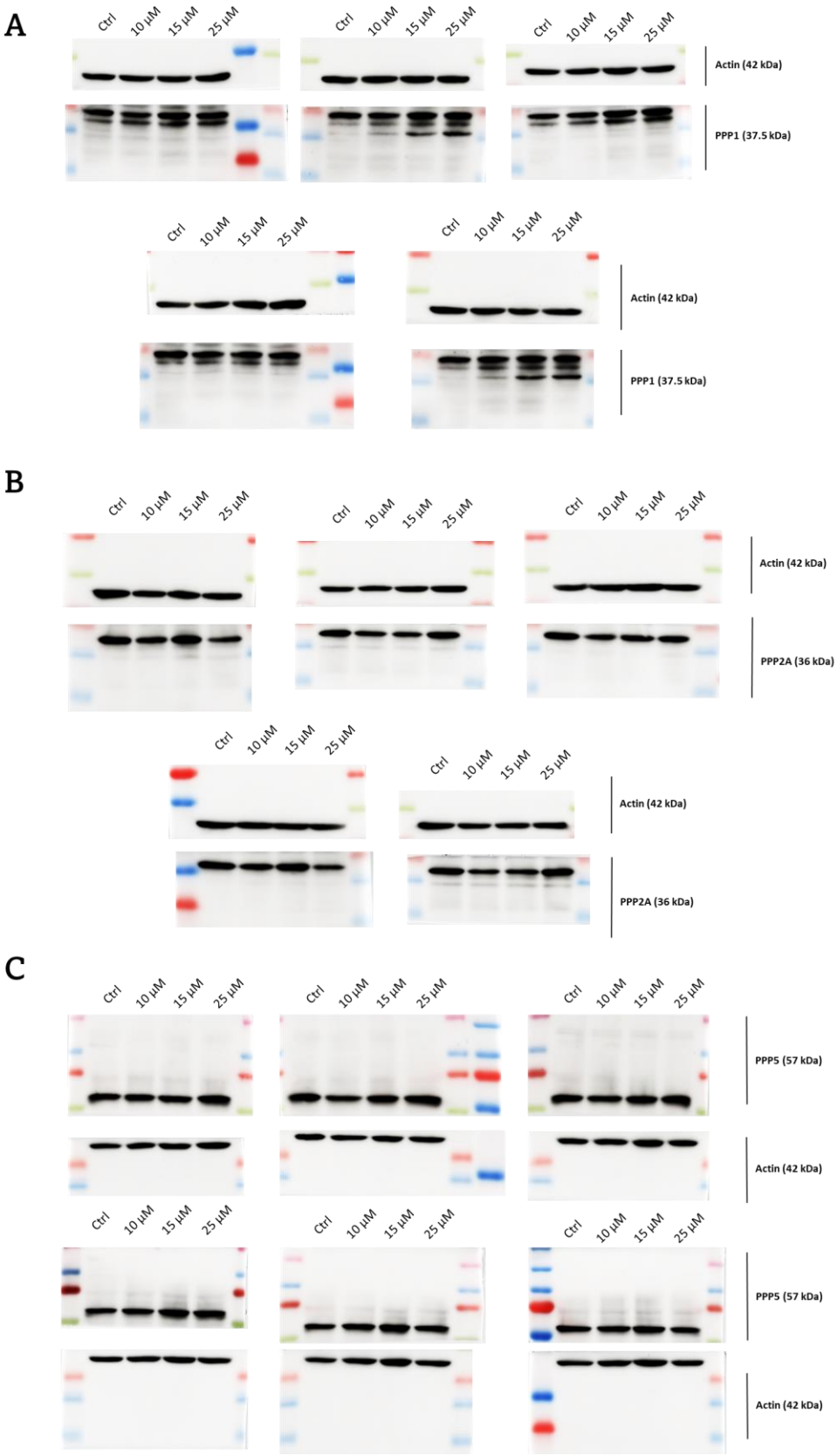

Supplementary Figure 12: Cycloheximide Chase Assay While Proteasome Inhibition (MG132)

Cycloheximide chase assay was performed while cotreated with either 10 µM, 15 µM or 25 µM proteasome inhibitor MG132. Western blot analyses were performed using 15 µg/lane cell lysate and detected with **(A)** anti-PPP1c, **(B)** -PPP2Ac, and **(C)** -PPP5c. All replicates used to calculate protein the half-lives are shown.

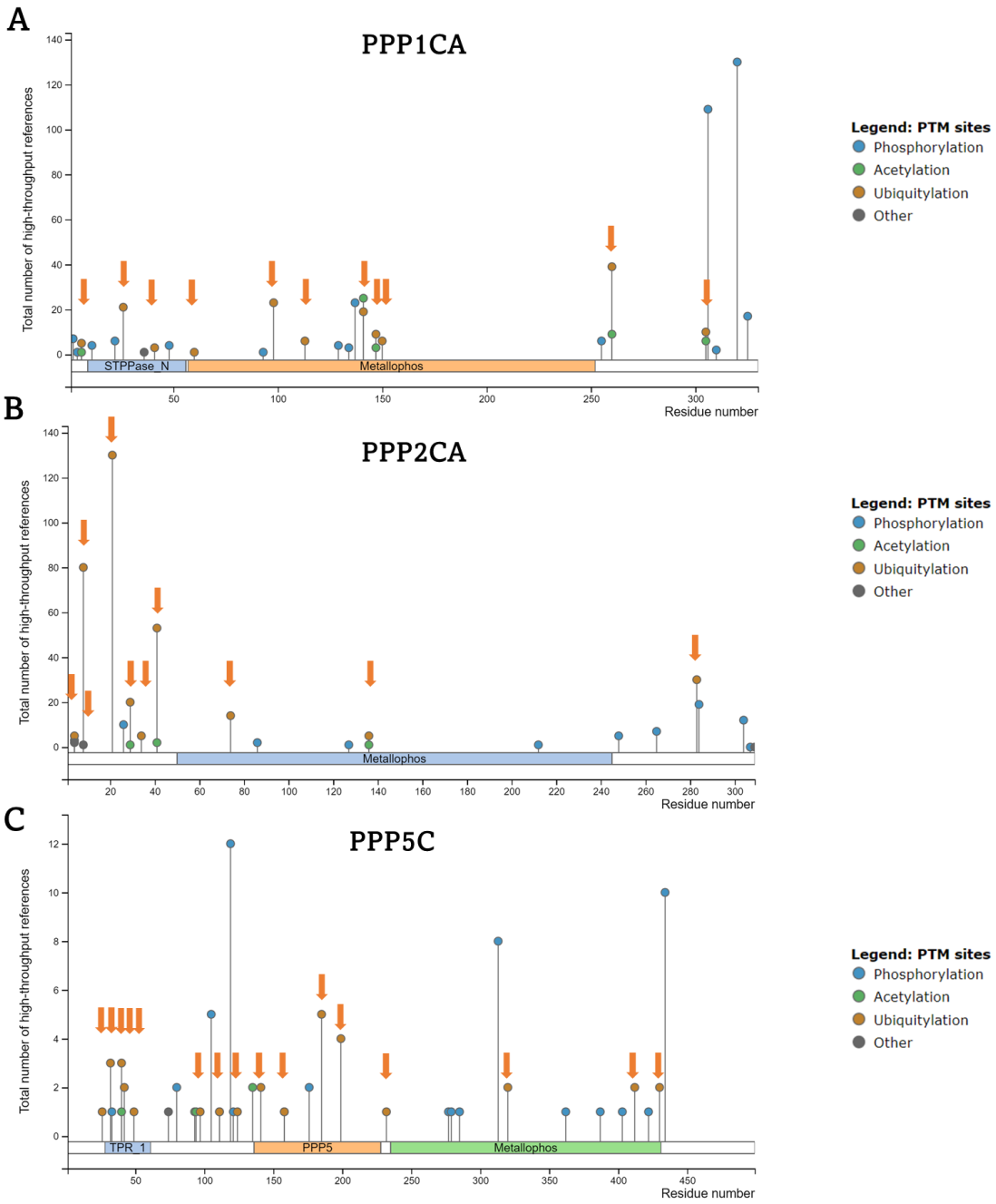

Supplementary Figure 13: Ubiquitination Sites of PPPs (PhosphoSitePlus)

Shown are the post-translational modification (PTM) sites of **(A)** PPP1CA, **(B)** PPP2CA, and **(C)** PPP5C found in high-throughput references. Graphs were obtained from PhosphoSitePlus, an online database that provides comprehensive information on all PTMs on human proteins (Hornbeck et al., 2015). Ubiquitination sites were highlighted with orange arrows.

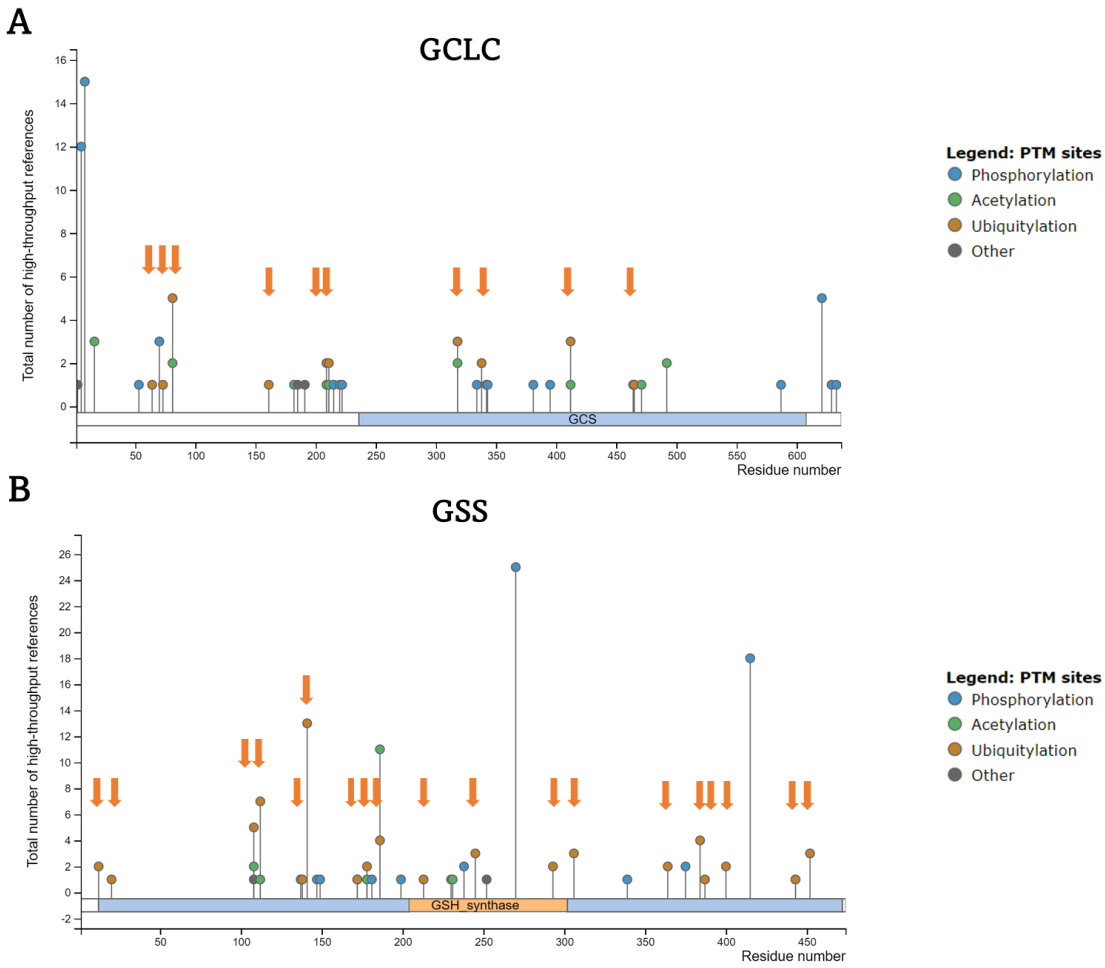

Supplementary Figure 14: Ubiquitination Sites of GSH Enzymes (PhosphoSitePlus)

Shown are the post-translational modification (PTM) sites of **(A)** GCLC and **(B)** GSS found in high-throughput references. Graphs were obtained from PhosphoSitePlus, an online database that provides comprehensive information on all PTMs on human proteins (Hornbeck et al., 2015). Ubiquitination sites were highlighted with orange arrows.

9.5. Chapter V

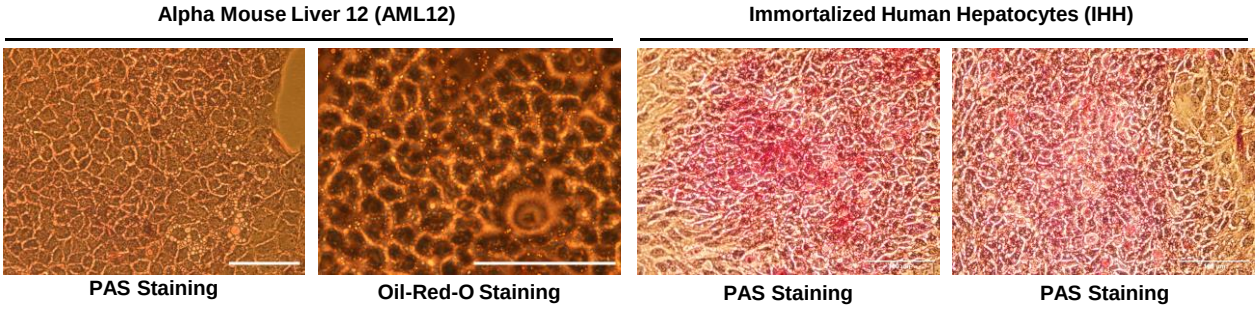

Supplementary Figure 15: Lipid and Glycogen Staining

No lipid (Oil-Red-O) or glycogen (PAS) staining confirmed the origin of the vacuole-like structures in the AML12 cell line. While positive PAS staining, indicated by the accumulation of red color, was observed in IHH cells. Staining and visualization was performed by Julia Dressler as a part of her master's thesis. Figure was adapted from (Dressler, 2022).

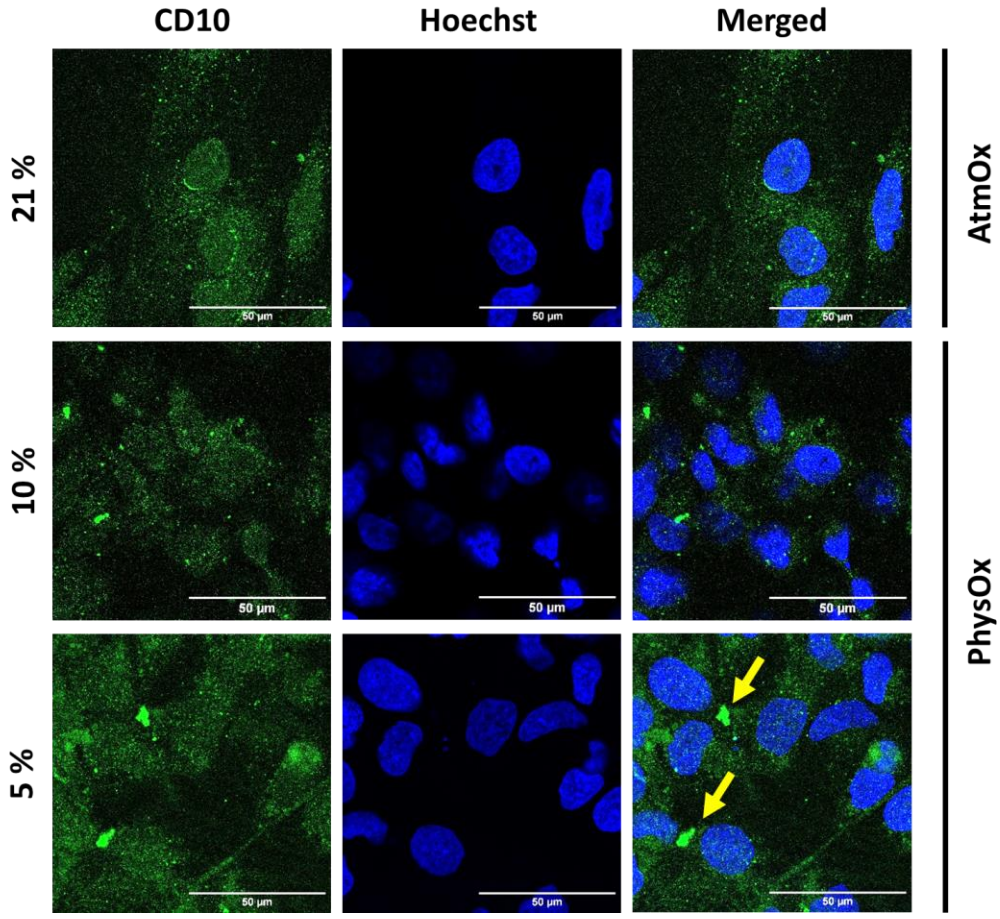

Supplementary Figure 16: Immunocytochemistry of Bile Canaliculi Marker CD10

Immunocytochemistry was used to visualize the expression of the bile canaliculi marker CD. Nuclei were stained with Hoechst; all scale bars indicate 50 µm. Yellow arrows point to the accumulation of CD10 and potential formation of bile canaliculi-like structures in IHH cells. Immunocytochemistry was performed by Julia Dressler as a part of her master's thesis. Figure was adapted from (Dressler, 2022).

10. Authors Contributions

Chapter I: Hydrophobic Adda Determines Toxicity

This study was a collaboration between Regina Fotler (Prof. Dr. Daniel Dietrich, Human and Environmental Toxicology Department, University of Konstanz) and Marius Wrona (Prof. Dr. Valentin Wittmann, Bioorganic Chemistry Department, University of Konstanz). Microcystin derivates were synthesized by Marius Wrona ([Apda^{5}]MC-LF, [Apha^{5}]MC-LF, and [Ala^{7}]MC-L(DAz)-Y(Prg)) and Ivan Zemskov ([Anda^{5}]MC-LY(Prg), [Amba^{5}]MC-LY(Prg), [enantio-Adda^{5}]MC-LF, [MSecPh^{7}]MC-LY(Prg) and MC-LY(Prg)). Biological experiments with phosphatases (rPPP1 and hPPP5) and cell systems (HEK293-OATP1B1, -OATP1B3, and -CV) were performed by Regina Fotler. Conceptual design of Chapter I as a manuscript, data analysis and interpretation, and statistical analyses were performed by Regina Fotler. Chapter I was solely written by Regina Fotler.

Chapter II: L-Amino Acid at Position (2) Determines OATP-Mediated Uptake

The study was designed by Regina Fotler and Prof. Dr. Daniel Dietrich (Human and Environmental Toxicology, University of Konstanz). Biological experiments with HEK293-OATP1B1, -OATP1B3, and -CV cells were performed by Regina Fotler. Membrane isolation and western blot analyses with corresponding quantification were performed by Julia Dressler (bachelor thesis supervised by Regina Fotler). Immunocytochemistry and preparation of the proteomic samples with subsequent data analyses were performed by Elena Schönfeld (master thesis supervised by Regina Fotler). Synthetic microcystins were provided by Prof. Dr. Valentin Wittmann (Bioorganic Chemistry Department, University of Konstanz) and synthesized by Marius Wrona and Ivan Zemskov. *In silico* calculation of LogP values was performed by Sabrina Jaeger-Honz (Prof. Dr. Falk Schreiber, Life Science Informatics, University of Konstanz). The conception of Chapter II, data analysis and statistical evaluation were performed by Regina Fotler. Chapter II was solely written by Regina Fotler.

Chapter III: Role of Glutathione in the Microcystin Toxicity Mechanism

The study was designed by Regina Fotler and Prof. Dr. Daniel Dietrich (Human and Environmental Toxicology, University of Konstanz). Multiplex assays (PPPs, GSH, cytotoxicity, and protein quantification) were established by Regina Fotler. Biological experiments with HEK293-OATP1B1, -OATP1B3 and -CV cells were performed by Regina Fotler, while biological experiments with IHH and AML12 cell lines were performed by Julia Dressler (master thesis supervised by Regina Fotler). Synthetic microcystin derivates were provided by Prof. Dr. Valentin Wittmann (Bioorganic Chemistry Department, University of Konstanz) and synthesized by Marius Wrona. The conception of Chapter III, assay establishment, data analysis and interpretation, and statistical analyses were performed by Regina Fotler. Chapter III was solely written by Regina Fotler.

Chapter IV: Protein Half-Lives of PPPs and Glutathione Synthesizing Enzymes

The study was designed by Regina Fotler and Prof. Dr. Daniel Dietrich (Human and Environmental Toxicology, University of Konstanz). Cell cycle analyses with subsequent data analysis and antibody verification and establishment was performed by Elena Schönfeld (master thesis supervised by Regina Fotler). Cytotoxicity analysis, cycloheximide chase assays and following western blot analyses with subsequent quantifications were performed by Regina Fotler. The conception of Chapter IV, protein half-life determination, statistical evaluation and interpretation were performed by Regina Fotler. Chapter IV was solely written by Regina Fotler.

Chapter V: Immortalized Human Hepatocyte Cell Line Characterization

The study was designed by Regina Fotler and Prof. Dr. Daniel Dietrich (Human and Environmental Toxicology, University of Konstanz). Experiments using IHH and AML12 cell lines were performed by Julia Dressler (master thesis supervised by Regina Fotler) The conception of Chapter V, data analysis and interpretation, and statistical analysis were performed by Regina Fotler. Chapter V was solely written by Regina Fotler.

11. List of Figures

Figures

Figure 1: Cyanobacterial Blooms 1
Figure 2: Geographical Distribution of Cyanotoxin Reports 3
Figure 3: Consensus Structure of Microcystins 4
Figure 4: Phosphatase Classification 6
Figure 5: PPP Catalytic Domains 6
Figure 6: Cellular Consequences of Microcystin-Induced PPP2A Inhibition 9
Figure 7: Toxicokinetics of Microcystins 10
Figure 8: Hepatic Lobule 12
Figure 9: Systemic Circulation and Organ Distribution of Microcystins 14
Figure 10: Schematic Structure of Organic Anion Transporting Polypeptides 18
Figure 11: Glutathione Conjugation to Microcystin-LR 19
Figure 12: Graphical Abstract of the Dissertation 22
Figure 13: Interaction Sites of Microcystins and Catalytic Subunit of PPPs 24
Figure 14: Graphical Abstract of Chapter I 25
Figure 15: Phosphatase Inhibition Properties of Mdha Derivates 27
Figure 16: OATP-mediated Uptake of Mdha Derivates 28
Figure 17: Phosphatase Inhibition Properties of Adda Derivates 30
Figure 18: OATP-mediated Uptake of Adda Derivates 32
Figure 19: Comparison of Adda Derivates 33
Figure 20: Chapter II Graphical Abstract 39
Figure 21: Summary of the Used Microcystin Variants 40
Figure 22: Immunocytochemistry Staining 41
Figure 23: Transporter Expression, GSH Content and PPP Activities 42
Figure 24: Proteomic Analysis of PPP Expression Levels 43
Figure 25: OATP1B1- and OATP1B3-Mediated Microcystin Cytotoxicity 44
Figure 26: Correlation Between Microcystin Hydrophobicity and OATP-Mediated Uptake 47
Figure 27: Comparison of Positions (2) and (4) in OATP-Mediated Microcystin Uptake 48
Figure 28: Statistical Analysis of Transposed Positions 49
Figure 29: Toxicokinetics vs. Toxicodynamics 50
Figure 30: Role of Microcystin Positions in the Toxicity Mechanism 55
Figure 31: Correlation of Microcystin Hydrophobicity and Induced Toxicity 56
Figure 32: Glutathione Synthesis Pathway 58
Figure 33: Chapter III Graphical Abstract 60
Figure 34: Validation of Multiplex Assays 61
Figure 35: Glutathione Half-Life 62
Figure 36: Impact of GSH Depletion on Microcystin Toxicity in HEK293 Cell Lines 64
Figure 37: Cellular GSH Content of Cell Lines Used 65
Figure 38: Impact of GSH Depletion on Microcystin Toxicity in Hepatocyte Cell Lines 67
Figure 39: Role of GSH in the Microcystin Toxicity Mechanism 72
Figure 40: Serine/Threonine Phosphatase Complex 73
Figure 41: Chapter IV Graphical Abstract 75
Figure 42: Cell Cycle Analysis of Non-Synchronized HEK293 Cells 76
Figure 43: Cell Cycle Analysis after Synchronization Using Thymidine Block 77
Figure 44: Cycloheximide Cytotoxicity 79
Figure 45: Cycloheximide Chase Assay for Catalytic Subunits of PPPs 80
Figure 46: Determination of Half-Lives of GSH and its Synthesizing Enzymes 81
Figure 47: Cycloheximide Chase Assay While Inhibiting Proteasome Using MG132 82
Figure 48: Liver Lobule Structure and Liver Zonation 87
Figure 49: Chapter V Graphical Abstract 89
Figure 50: IHH Morphology 90

Figure 51: IHH Cell Growth Curves and Doubling Times 91
Figure 52: Epithelial-to-Mesenchymal Transition of IHH 92
Figure 53: Immunocytochemistry of EMT Markers AtmOx vs. PhysOx 93
Figure 54: Gene Expression Pattern of IHH 95
Figure 55: Gene Expression AtmOx vs. PhysOx 96
Figure 56: Albumin Gene Expression 97
Figure 57: ATP Production Rate AtmOx vs. PhysOx 98
Figure 58: Microcystin-Induced Cytotoxicity in IHH 98
Figure 59: Microcystin-Induced Cytotoxicity in Human Hepatocytes vs. Mouse Hepatocytes 99
Figure 60: Schematic Overview of Immortalized Human Hepatocyte (IHH) 103
Figure 61: Concluding Summary of the Dissertation 105

Supplementary Figures

Supplementary Figure 1: Statistical Comparison of rPPP1 and hPPP5 131
Supplementary Figure 2: Statistical Analyses of Adda Derivates in rPPP1 and hPPP5 131
Supplementary Figure 3: HEK293-CV and Adda Derivates 132
Supplementary Figure 4: Statistical Analyses of Adda Derivates in HEK293-OATP1B1 and -OATP1B3 Cells 132
Supplementary Figure 5: Cellular PPP Activities in Stably Transfected HEK Cell Lines 133
Supplementary Figure 6: Microcystin Exposure in HEK293-CV Cells 134
Supplementary Figure 7: Heatmaps of all Congeners Used 134
Supplementary Figure 8: Assay Validation Using Immortalized Hepatocyte Cell Lines 135
Supplementary Figure 9: Statistical Analysis of Cycloheximide Cytotoxicity 136
Supplementary Figure 10: Antibody Verification 136
Supplementary Figure 11: Cycloheximide Chase Assay 137
Supplementary Figure 12: Cycloheximide Chase Assay While Proteasome Inhibition (MG132) 138
Supplementary Figure 13: Ubiquitination Sites of PPPs (PhosphoSitePlus) 139
Supplementary Figure 14: Ubiquitination Sites of GSH Enzymes (PhosphoSitePlus) 140
Supplementary Figure 15: Lipid and Glycogen Staining 141
Supplementary Figure 16: Immunocytochemistry of Bile Canaliculi Marker CD10 141

12. List of Tables

Tables

Table 1: Members and Functions of PPP Family 7
Table 2: OATP1 Subfamily Members 18
Table 3: Summary of the IC_{50} Values and Statistical Analyses 31
Table 4: Summary of the EC_{50} Values and Statistical Analyses 31
Table 5: Summary of EC_{50} Values and Statistical Analyses 45
Table 6: Summary of EC_{50} Values of Transposed Microcystin Pairs 49
Table 7: Summary of EC_{50} Values for HEK293 Cell Lines 63
Table 8: Summary of EC50 Values for Hepatocyte Cell Lines 66
Table 9: Summary of PPP Half-Lives 80
Table 10: Seeding Densities for HEK293 Cells 111
Table 11: Seeding Densities for Immortalized Human Hepatocytes 112
Table 12: Seeding Densities for Alpha Mouse Liver 12 (AML12) 112
Table 13: Primary Antibodies Used for Immunocytochemistry 113
Table 14: Secondary Antibodies Used for Immunocytochemistry 114
Table 15: Phosphatase Assay Buffer Composition 117
Table 16: Glutathione Assay Buffer Composition 119
Table 17: Primary Antibodies Used for Western Blot Analysis 124
Table 18: Secondary Antibodies Used for Western Blot Analysis 124
Table 19: Positive Controls Used for Western Blot Analysis 125
Table 20: Taq Polymerase PCR Template 126
Table 21: Human Primer Sequences 126
Table 22: Mouse Primer Sequences 128
Table 23: Quantitative Real-Time PCR Template 129

Supplementary Tables

Supplementary Table 1: Congener Specific Modifications 133

13. List of Abbreviations

Adda	3-amino-9-methoxy-10-phenyl-2,6,8-trimethyl-deca-4(E),6(E)-dienoic acid
ADME	Absorption, distribution, metabolism, and excretion
AF	Allocation factor
ALB	Albumin
ALT	Alanine aminotransferase
Amba	(2S,3S)-3-amino-2-methylbutanoic acid
AML12	Alpha mouse liver 12
Anda	(2S,3S,4E,6E)-3-amino-2-methylnona-4,6-dienoic acid
Apda	(2S,3S)-3-amino-2-methyl-10-phenyldecanoic acid
Apha	(2S,3S)-3-amino-2-methyl-7-phenylheptanoic acid
AST	Aspartate aminotransferase
AtmOx	Atmospheric oxygen, ≈ 21 % O_2, 5 % CO_2, 37 °C and 95 % humidity
ATP	Adenosine triphosphate
ATP8B1	ATPase phospholipid transporting 8B1
BAX	Bcl2 associated X
BBB	Blood-brain-barrier
BCRP	Breast cancer resistance protein
BSA	Bovine serum albumin
BSEP	Bile salt export pump
BSO	Buthionine sulfoximine
BSP	Bromosulfophthalein
CamKII	Ca^{2+}/calmodulin-dependent protein kinase II
CHX	Cycloheximide
CV	Control vector
CYP2C9	Cytochrome P450 2C9
CYP3A4	Cytochrome P450 3A4
Dhb	(E)-2-amino-2-butenoic acid
DMSO	Dimethyl sulfoxide
DTNB	5,5'-dithio-bis-(2-nitrobenzoic acid
EC_{50}	Half-maximal effective concentration
EMT	Epithelial-to-mesenchymal transition
FAH	Fumarylacetoacetate hydrolase
FCP/SCP	Aspartate-based protein phosphatases
FCS	Fetal calf serum
GGT	Glutamyl transaminase
GSH	Glutathione, thiol-reduced form
GSK3ß	Glycogen synthase kinase-3ß
GSR	Glutathione reductase
GSSG	Glutathione, disulfide-oxidized form
GST	Glutathione-S-transferase
GV	Guideline value
HABs	Harmful algal blooms
HEK293	Human embryonic kidney 239

HEPES	4-(2-hydroxyethyl)-1-piperazineethanesulfonic acid
HNF1A	Hepatocyte nuclear factor 1 homeobox A
HNF4	Hepatocyte nuclear factor 4
IARC	International Agency for Research on Cancer
IC_{50}	Half-maximal inhibitory concentration
IHH	Immortalized human hepatocytes
K_m	Michaelis-Menten Constant
MAPK	Mitogen-activated kinase
MC	Microcystin
MC-Cys	Microcystin-Cysteine conjugate
MC-Cys-Gly	Microcystin-Cysteine-Glycine intermediate
MC-GSH	Microcystin-GSH conjugate
Mdha	D-methyldehydroalanine
MDR	Multidrug resistance transporters
MG132	Proteasome Inhibitor
MRP2	Multidrug resistance-associated protein 2
MSecPh	N-methyl-Se-phenyl-L-selenocysteine
NADPH	Nicotinamide adenine dinucleotide phosphate
NCBI	National Center for Biotechnology Information (NCBI)
NOEL	No-observed-effect-level
OATPs	Organic anion transporting polypeptides
OCT1	Organic cation transporter 1
OXPHOS	Oxidative phosphorylation
PBS	Phosphate-buffered saline
PFA	Paraformaldehyde
PhysOx	Physiological oxygen; either 10 % or 5 % O_2, 5 % CO_2, 37 °C and 75 % humidity
pNPP	P-nitrophenyl phosphate
PPM	Metal-dependent phosphatases
PPPs	Serine/threonine phosphoprotein phosphatases
Prg	Propargylated
ROS	Reactive oxygen species
RT-qPCR	Quantitative real-time PCR
SDS PAGE	Sodium dodecyl sulfate polyacrylamide gel electrophoresis
SLCO	Salute carrier organic anion
SRB	Sulforhodamine B
$t_{1/2}$	Protein half-life
TCA	Trichloroacetic acid
TDI	Tolerable daily intake
TP53	Tumor protein p53
TPR	Tetratricopeptide repeat domain
UF	Uncertainty factor
VFDF	Fast death factor
WHLL	Whole human liver lysate
WHO	World Health Organization

14. Bibliography

Aden, D. P., Fogel, A., Plotkin, S., Damjanov, I., & Knowles, B. B. (1979, Dec 6). Controlled synthesis of HBsAg in a differentiated human liver carcinoma-derived cell line. *Nature, 282*(5739), 615-616. https://doi.org/10.1038/282615a0

Alam, K., Crowe, A., Wang, X., Zhang, P., Ding, K., Li, L., & Yue, W. (2018, Mar 14). Regulation of Organic Anion Transporting Polypeptides (OATP) 1B1- and OATP1B3-Mediated Transport: An Updated Review in the Context of OATP-Mediated Drug-Drug Interactions. *Int J Mol Sci, 19*(3). https://doi.org/10.3390/ijms19030855

Altaner, S. (2019). *Cyanobacterial microcystins and human health : First steps towards a congener dependent risk assessment of microcystins*

Altaner, S., Jaeger, S., Fotler, R., Zemskov, I., Wittmann, V., Schreiber, F., & Dietrich, D. R. (2020). Machine learning prediction of cyanobacterial toxin (microcystin) toxicodynamics in humans. *ALTEX, 37*(1), 24-36. https://doi.org/10.14573/altex.1904031

Anderson, M. E. (1998, Apr 24). Glutathione: an overview of biosynthesis and modulation. *Chem Biol Interact, 111-112*, 1-14. https://doi.org/10.1016/s0009-2797(97)00146-4

Arman, T., & Clarke, J. D. (2021, Jul 29). Microcystin Toxicokinetics, Molecular Toxicology, and Pathophysiology in Preclinical Rodent Models and Humans. *Toxins (Basel), 13*(8). https://doi.org/10.3390/toxins13080537

Aubrey, B. J., Kelly, G. L., Janic, A., Herold, M. J., & Strasser, A. (2018, 2018/01/01). How does p53 induce apoptosis and how does this relate to p53-mediated tumour suppression? *Cell Death & Differentiation, 25*(1), 104-113. https://doi.org/10.1038/cdd.2017.169

Azevedo, S. M. F. O., Carmichael, W. W., Jochimsen, E. M., Rinehart, K. L., Lau, S., Shaw, G. R., & Eaglesham, G. K. (2002). Human intoxication by microcystins during renal dialysis treatment in Caruaru—Brazil. *Toxicology, 181-182*, 441-446. https://doi.org/10.1016/s0300-483x(02)00491-2

Backer, L. C., Landsberg, J. H., Miller, M., Keel, K., & Taylor, T. K. (2013, Sep 24). Canine cyanotoxin poisonings in the United States (1920s-2012): review of suspected and confirmed cases from three data sources. *Toxins (Basel), 5*(9), 1597-1628. https://doi.org/10.3390/toxins5091597

Barford, D., Das, A. K., & Egloff, M. P. (1998). The structure and mechanism of protein phosphatases: insights into catalysis and regulation. *Annu Rev Biophys Biomol Struct, 27*, 133-164. https://doi.org/10.1146/annurev.biophys.27.1.133

Baudouin-Cornu, P., Lagniel, G., Kumar, C., Huang, M. E., & Labarre, J. (2012, Feb 10). Glutathione degradation is a key determinant of glutathione homeostasis. *J Biol Chem, 287*(7), 4552-4561. https://doi.org/10.1074/jbc.M111.315705

Bautista, A. C., Moore, C. E., Lin, Y., Cline, M. G., Benitah, N., & Puschner, B. (2015, 2015/06/19). Hepatopathy following consumption of a commercially available blue-green algae dietary supplement in a dog. *BMC Veterinary Research, 11*(1), 136. https://doi.org/10.1186/s12917-015-0453-2

Benet, L. Z., Hosey, C. M., Ursu, O., & Oprea, T. I. (2016, Jun 1). BDDCS, the Rule of 5 and drugability. *Adv Drug Deliv Rev, 101*, 89-98. https://doi.org/10.1016/j.addr.2016.05.007

Besant, P. G., & Attwood, P. V. (2005, Dec 30). Mammalian histidine kinases. *Biochim Biophys Acta, 1754*(1-2), 281-290. https://doi.org/10.1016/j.bbapap.2005.07.026

Bollen, M., Peti, W., Ragusa, M. J., & Beullens, M. (2010, Aug). The extended PP1 toolkit: designed to create specificity. *Trends Biochem Sci, 35*(8), 450-458. https://doi.org/10.1016/j.tibs.2010.03.002

Borst, P., Evers, R., Kool, M., & Wijnholds, J. (1999, 1999/12/06/). The multidrug resistance protein family. *Biochimica et Biophysica Acta (BBA) - Biomembranes, 1461*(2), 347-357. https://doi.org/https://doi.org/10.1016/S0005-2736(99)00167-4

Botha, N., van de Venter, M., Downing, T. G., Shephard, E. G., & Gehringer, M. M. (2004, Mar 1). The effect of intraperitoneally administered microcystin-LR on the gastrointestinal tract of Balb/c mice. *Toxicon, 43*(3), 251-254. https://doi.org/10.1016/j.toxicon.2003.11.026

Bouaïcha, N., & Maatouk, I. (2004, Mar 14). Microcystin-LR and nodularin induce intracellular glutathione alteration, reactive oxygen species production and lipid peroxidation in primary cultured rat hepatocytes. *Toxicol Lett, 148*(1-2), 53-63. https://doi.org/10.1016/j.toxlet.2003.12.005

Brautigan, D. L. (2013). Protein Ser/Thr phosphatases - the ugly ducklings of cell signalling. *FEBS Journal, 280*(2), 324-325. https://doi.org/10.1111/j.1742-4658.2012.08609.x

Broda, E., & Peschek, G. A. (1983, 1983/01/01/). Nitrogen fixation as evidence for the reducing nature of the early biosphere. *Biosystems, 16*(1), 1-8. https://doi.org/https://doi.org/10.1016/0303-2647(83)90021-7

Buratti, F. M., Manganelli, M., Vichi, S., Stefanelli, M., Scardala, S., Testai, E., & Funari, E. (2017). Cyanotoxins: producing organisms, occurrence, toxicity, mechanism of action and human health toxicological risk evaluation. *Archives of Toxicology, 91*(3), 1049-1130. https://doi.org/10.1007/s00204-016-1913-6

Buratti, F. M., Scardala, S., Funari, E., & Testai, E. (2011). Human Glutathione Transferases Catalyzing the Conjugation of the Hepatoxin Microcystin-LR. *Chemical Research in Toxicology, 24*(6), 926-933. https://doi.org/10.1021/tx2000976

Buratti, F. M., & Testai, E. (2015). Species- and congener-differences in microcystin-LR and -RR GSH conjugation in human, rat, and mouse hepatic cytosol. *Toxicology Letters, 232*(1), 133-140. https://doi.org/10.1016/j.toxlet.2014.10.020

Busso, N., Chesne, C., Delers, F., Morel, F., & Guillouzo, A. (1990, Sep 14). Transforming growth-factor-beta (TGF-beta) inhibits albumin synthesis in normal human hepatocytes and in hepatoma HepG2 cells. *Biochem Biophys Res Commun, 171*(2), 647-654. https://doi.org/10.1016/0006-291x(90)91195-x

Cai, S. Y., Gautam, S., Nguyen, T., Soroka, C. J., Rahner, C., & Boyer, J. L. (2009, Mar). ATP8B1 deficiency disrupts the bile canalicular membrane bilayer structure in hepatocytes, but FXR expression and activity are maintained. *Gastroenterology, 136*(3), 1060-1069. https://doi.org/10.1053/j.gastro.2008.10.025

Campos, A., & Vasconcelos, V. (2010). Molecular Mechanisms of Microcystin Toxicity in Animal Cells. *International Journal of Molecular Sciences, 11*(1), 268-287. https://doi.org/10.3390/ijms11010268

Carmichael, W. W., Azevedo, S. M., An, J. S., Molica, R. J., Jochimsen, E. M., Lau, S., Rinehart, K. L., Shaw, G. R., & Eaglesham, G. K. (2001, Jul). Human fatalities from cyanobacteria: chemical and biological evidence for cyanotoxins. *Environ Health Perspect, 109*(7), 663-668. https://doi.org/10.1289/ehp.01109663

Carmichael, W. W., Biggs, D. F., & Gorham, P. R. (1975, Feb 14). Toxicology and pharmacological action of anabaena flos-aquae toxin. *Science, 187*(4176), 542-544. https://doi.org/10.1126/science.803708

Carmichael, W. W., Biggs, D. F., & Peterson, M. A. (1979). Pharmacology of anatoxin-a, produced by the freshwater cyanophyte Anabaena flos-aquae NRC-44-1. *Toxicon, 17*(3), 229-236. https://doi.org/10.1016/0041-0101(79)90212-5

Castell, J. V., Jover, R., Martínez-Jiménez, C. P., & Gómez-Lechón, M. J. (2006, Apr). Hepatocyte cell lines: their use, scope and limitations in drug metabolism studies. *Expert Opin Drug Metab Toxicol, 2*(2), 183-212. https://doi.org/10.1517/17425255.2.2.183

Chen, G., & Deng, X. (2018, Sep 5). Cell Synchronization by Double Thymidine Block. *Bio Protoc, 8*(17). https://doi.org/10.21769/BioProtoc.2994

Chen, J., Xie, P., Li, L., & Xu, J. (2009, Mar). First identification of the hepatotoxic microcystins in the serum of a chronically exposed human population together with indication of hepatocellular damage. *Toxicol Sci, 108*(1), 81-89. https://doi.org/10.1093/toxsci/kfp009

Chen, L., Chen, J., Zhang, X., & Xie, P. (2016, 2016/01/15/). A review of reproductive toxicity of microcystins. *Journal of Hazardous Materials, 301*, 381-399. https://doi.org/https://doi.org/10.1016/j.jhazmat.2015.08.041

Chen, M. X., McPartlin, A. E., Brown, L., Chen, Y. H., Barker, H. M., & Cohen, P. T. (1994, Sep 15). A novel human protein serine/threonine phosphatase, which possesses four tetratricopeptide repeat motifs and localizes to the nucleus. *Embo j, 13*(18), 4278-4290. https://doi.org/10.1002/j.1460-2075.1994.tb06748.x

Chernoff, N., Hill, D., Lang, J., Schmid, J., Le, T., Farthing, A., & Huang, H. (2020, Jun 18). The Comparative Toxicity of 10 Microcystin Congeners Administered Orally to Mice: Clinical Effects and Organ Toxicity. *Toxins (Basel), 12*(6). https://doi.org/10.3390/toxins12060403

Chorus, I., & Welker, M. (2021). *Toxic cyanobacteria in water: a guide to their public health consequences, monitoring and management*. Taylor & Francis.

Clarke, J. D., Dzierlenga, A., Arman, T., Toth, E., Li, H., Lynch, K. D., Tian, D. D., Goedken, M., Paine, M. F., & Cherrington, N. (2019, Apr 15). Nonalcoholic fatty liver disease alters microcystin-LR toxicokinetics and acute toxicity. *Toxicon, 162*, 1-8. https://doi.org/10.1016/j.toxicon.2019.03.002

Codd, G. A., Lindsay, J., Young, F. M., Morrison, L. F., & Metcalf, J. S. (2005). Harmful Cyanobacteria. In J. Huisman, H. C. P. Matthijs, & P. M. Visser (Eds.), *Harmful Cyanobacteria* (pp. 1-23). Springer Netherlands. https://doi.org/10.1007/1-4020-3022-3_1

Cohen, P. T. W. (2004). Overview of protein serine/threonine phosphatases. In J. n. Ariño & D. R. Alexander (Eds.), *Protein Phosphatases* (pp. 1-20). Springer Berlin Heidelberg. https://doi.org/10.1007/978-3-540-40035-6_1

Colyer, C. L., Kinkade, C. S., Viskari, P. J., & Landers, J. P. (2005, Jun). Analysis of cyanobacterial pigments and proteins by electrophoretic and chromatographic methods. *Anal Bioanal Chem, 382*(3), 559-569. https://doi.org/10.1007/s00216-004-3020-4

Cooper, G. M. (2000). *The Cell: A Molecular Approach. 2nd edition*. Sinauer Associates 2000. http://lib.ugent.be/catalog/ebk01:3450000000002155

Cooper, S. (2019, Dec). The synchronization manifesto: a critique of whole-culture synchronization. *Febs j, 286*(23), 4650-4656. https://doi.org/10.1111/febs.15050

Craig, M., Luu, H. A., McCready, T. L., Williams, D., Andersen, R. J., & Holmes, C. F. (1996). Molecular mechanisms underlying he interaction of motuporin and microcystins with type-1 and type-2A protein phosphatases. *Biochem Cell Biol, 74*(4), 569-578. https://doi.org/10.1139/o96-061

Cunningham, R. P., & Porat-Shliom, N. (2021, 2021-September-09). Liver Zonation – Revisiting Old Questions With New Technologies [Review]. *Frontiers in Physiology, 12*. https://doi.org/10.3389/fphys.2021.732929

Daina, A., Michielin, O., & Zoete, V. (2017, 2017/03/03). SwissADME: a free web tool to evaluate pharmacokinetics, drug-likeness and medicinal chemistry friendliness of small molecules. *Scientific Reports, 7*(1), 42717. https://doi.org/10.1038/srep42717

Darvishi, E., & Woldemichael, G. M. (2016, Dec). Cycloheximide Inhibits Actin Cytoskeletal Dynamics by Suppressing Signaling via RhoA. *J Cell Biochem, 117*(12), 2886-2898. https://doi.org/10.1002/jcb.25601

Davis, T., Berry, D., Boyer, G., & Gobler, C. (2009, 06/01). The Effects of Temperature and Nutrients on the Growth and Dynamics of Toxic and Non-Toxic Strains of Microcystis during Cyanobacteria Blooms. *Harmful Algae, 8*, 715-725. https://doi.org/10.1016/j.hal.2009.02.004

Dawson, R. M. (1998, 1998/07/01/). the toxicology of microcystins. *Toxicon, 36*(7), 953-962. https://doi.org/https://doi.org/10.1016/S0041-0101(97)00102-5

Dietrich, D., & Hoeger, S. (2005, 2005/03/15/). Guidance values for microcystins in water and cyanobacterial supplement products (blue-green algal supplements): a reasonable or misguided approach? *Toxicology and Applied Pharmacology, 203*(3), 273-289. https://doi.org/https://doi.org/10.1016/j.taap.2004.09.005

Dressler, J. (2022). *Characterization of Human and Mouse Hepatocytes under Physiological Oxygen Conditions and their Cellular Response to the Cyanobacterial Toxin Microcystin* [Master's Thesis Univeristy of Konstanz].

Drobac, D., Tokodi, N., Simeunović, J., Baltić, V., Stanić, D., & Svirčev, Z. (2013, Jun). Human exposure to cyanotoxins and their effects on health. *Arh Hig Rada Toksikol, 64*(2), 119-130. https://doi.org/10.2478/10004-1254-64-2013-2320

Dushukyan, N., Dunn, D. M., Sager, R. A., Woodford, M. R., Loiselle, D. R., Daneshvar, M., Baker-Williams, A. J., Chisholm, J. D., Truman, A. W., Vaughan, C. K., Haystead, T. A., Bratslavsky, G., Bourboulia, D., & Mollapour, M. (2017, Nov 14). Phosphorylation and Ubiquitination Regulate Protein Phosphatase 5 Activity and Its Prosurvival Role in Kidney Cancer. *Cell Rep, 21*(7), 1883-1895. https://doi.org/10.1016/j.celrep.2017.10.074

Egloff, M. P., Cohen, P. T., Reinemer, P., & Barford, D. (1995, Dec 15). Crystal structure of the catalytic subunit of human protein phosphatase 1 and its complex with tungstate. *J Mol Biol, 254*(5), 942-959. https://doi.org/10.1006/jmbi.1995.0667

Elaut, G., Henkens, T., Papeleu, P., Snykers, S., Vinken, M., Vanhaecke, T., & Rogiers, V. (2006, Aug). Molecular mechanisms underlying the dedifferentiation process of isolated hepatocytes and their cultures. *Curr Drug Metab, 7*(6), 629-660. https://doi.org/10.2174/138920006778017759

Eldeeb, M. A., Siva-Piragasam, R., Ragheb, M. A., Esmaili, M., Salla, M., & Fahlman, R. P. (2019). A molecular toolbox for studying protein degradation in mammalian cells. *Journal of Neurochemistry, 151*(4), 520-533. https://doi.org/https://doi.org/10.1111/jnc.14838

Falconer, I., B, J., Langley, B. J., & Runnegar, M. (1980, 11/30). Liver Pathology in Mice in Poisoning by the Blue-Green Alga Microcystis Aeruginosa. *Australian Journal of Biological Sciences, 34*, 179-188. https://doi.org/10.1071/BI9810179

Falconer, I. R., Burch, M. D., Steffensen, D. A., Choice, M., & Coverdale, O. R. (1994). Toxicity of the blue-green alga (cyanobacterium) Microcystis aeruginosa in drinking water to growing pigs, as an animal model for human injury and risk assessment. *Environmental Toxicology and Water Quality, 9*(2), 131-139. https://doi.org/https://doi.org/10.1002/tox.2530090209

Fawell, J. K., Mitchell, R. E., Everett, D. J., & Hill, R. E. (1999, Mar). The toxicity of cyanobacterial toxins in the mouse: I microcystin-LR. *Hum Exp Toxicol, 18*(3), 162-167. https://doi.org/10.1177/096032719901800305

Feurstein, D., Holst, K., Fischer, A., & Dietrich, D. R. (2009). Oatp-associated uptake and toxicity of microcystins in primary murine whole brain cells. *Toxicology and Applied Pharmacology, 234*(2), 247-255. https://doi.org/10.1016/j.taap.2008.10.011

Feurstein, D., Kleinteich, J., Heussner, A. H., Stemmer, K., & Dietrich, D. R. (2010). Investigation of Microcystin Congener–Dependent Uptake into Primary Murine Neurons. *Environmental Health Perspectives, 118*(10), 1370-1375. https://doi.org/10.1289/ehp.0901289

Feurstein, D., Stemmer, K., Kleinteich, J., Speicher, T., & Dietrich, D. R. (2011). Microcystin Congener– and Concentration-Dependent Induction of Murine Neuron Apoptosis and Neurite Degeneration. *Toxicological Sciences, 124*(2), 424-431. https://doi.org/10.1093/toxsci/kfr243

Fischer, A., Hoeger, S. J., Stemmer, K., Feurstein, D. J., Knobeloch, D., Nussler, A., & Dietrich, D. R. (2010). The role of organic anion transporting polypeptides (OATPs/SLCOs) in the toxicity of different microcystin congeners in vitro: A comparison of primary human hepatocytes and OATP-transfected HEK293 cells. *Toxicology and Applied Pharmacology, 245*(1), 9-20. https://doi.org/10.1016/j.taap.2010.02.006

Fischer, W. J., Altheimer, S., Cattori, V., Meier, P. J., Dietrich, D. R., & Hagenbuch, B. (2005). Organic anion transporting polypeptides expressed in liver and brain mediate uptake of microcystin. *Toxicology and Applied Pharmacology, 203*(3), 257-263. https://doi.org/10.1016/j.taap.2004.08.012

Fladmark, K. E., Brustugun, O. T., Mellgren, G., Krakstad, C., Boe, R., Vintermyr, O. K., Schulman, H., & Doskeland, S. O. (2002, Jan 25). Ca2+/calmodulin-dependent protein kinase II is required for microcystin-induced apoptosis. *J Biol Chem, 277*(4), 2804-2811. https://doi.org/10.1074/jbc.M109049200

Fontanillo, M., & Köhn, M. (2018, 2018/03/15/). Microcystins: Synthesis and structure–activity relationship studies toward PP1 and PP2A. *Bioorganic & Medicinal Chemistry, 26*(6), 1118-1126. https://doi.org/https://doi.org/10.1016/j.bmc.2017.08.040

Fontanillo, M., Zemskov, I., Häfner, M., Uhrig, U., Salvi, F., Simon, B., Wittmann, V., & Köhn, M. (2016). Synthesis of Highly Selective Submicromolar Microcystin-Based Inhibitors of Protein Phosphatase (PP)2A over PP1. *Angewandte Chemie, 128*(45), 14191-14195. https://doi.org/10.1002/ange.201606449

Forman, H. J., Zhang, H., & Rinna, A. (2009, Feb-Apr). Glutathione: overview of its protective roles, measurement, and biosynthesis. *Mol Aspects Med, 30*(1-2), 1-12. https://doi.org/10.1016/j.mam.2008.08.006

Fornasiero, E. F., & Savas, J. N. (2023). Determining and interpreting protein lifetimes in mammalian tissues. *Trends in Biochemical Sciences, 48*(2), 106-118. https://doi.org/10.1016/j.tibs.2022.08.011

Frevert, U., Engelmann, S., Zougbédé, S., Stange, J., Ng, B., Matuschewski, K., Liebes, L., & Yee, H. (2005). Intravital Observation of Plasmodium berghei Sporozoite Infection of the Liver. *PLOS Biology, 3*(6), e192. https://doi.org/10.1371/journal.pbio.0030192

Gallagher, B. C., Rudolph, D. B., Hinton, B. T., & Hanigan, M. H. (1998, Jul). Differential induction of gamma-glutamyl transpeptidase in primary cultures of rat and mouse hepatocytes parallels induction during hepatocarcinogenesis. *Carcinogenesis, 19*(7), 1251-1255. https://doi.org/10.1093/carcin/19.7.1251

Gilroy, D. J., Kauffman, K. W., Hall, R. A., Huang, X., & Chu, F. S. (2000, May). Assessing potential health risks from microcystin toxins in blue-green algae dietary supplements. *Environ Health Perspect, 108*(5), 435-439. https://doi.org/10.1289/ehp.00108435

Goldberg, J., Huang, H.-b., Kwon, Y.-g., Greengard, P., Nairn, A. C., & Kuriyan, J. (1995, 1995/08/01). Three-dimensional structure of the catalytic subunit of protein serine/threonine phosphatase-1. *Nature, 376*(6543), 745-753. https://doi.org/10.1038/376745a0

Guo, R., Xu, X., Lu, Y.-t., & Xie, X. (2017). Physiological oxygen tension reduces hepatocyte dedifferentiation in in vitro culture. *Scientific Reports, 7*.

Hagenbuch, B., & Meier, P. J. (2003). The superfamily of organic anion transporting polypeptides. *Biochimica et Biophysica Acta (BBA) - Biomembranes, 1609*(1), 1-18. https://doi.org/10.1016/s0005-2736(02)00633-8

Hagenbuch, B., & Meier, P. J. (2004). Organic anion transporting polypeptides of the OATP/ SLC21 family: phylogenetic classification as OATP/ SLCO superfamily, new nomenclature and molecular/functional properties. *Pflugers Archiv European Journal of Physiology, 447*(5), 653-665. https://doi.org/10.1007/s00424-003-1168-y

Harada, K.-I., Murata, H., Qiang, Z., Suzuki, M., & Kondo, F. (1996, 1996/06/01/). Mass spectrometric screening method for microcystins in cyanobacteria. *Toxicon, 34*(6), 701-710. https://doi.org/https://doi.org/10.1016/0041-0101(95)00163-8

Harada, K., Ogawa, K., Matsuura, K., Murata, H., Suzuki, M., Watanabe, M. F., Itezono, Y., & Nakayama, N. (1990, Sep-Oct). Structural determination of geometrical isomers of microcystins LR and RR from cyanobacteria by two-dimensional NMR spectroscopic techniques. *Chem Res Toxicol, 3*(5), 473-481. https://doi.org/10.1021/tx00017a014

Heresztyn, T., & Nicholson, B. C. (2001, Sep). Determination of cyanobacterial hepatotoxins directly in water using a protein phosphatase inhibition assay. *Water Res, 35*(13), 3049-3056. https://doi.org/10.1016/s0043-1354(01)00018-5

Heussner, A. H., Mazija, L., Fastner, J., & Dietrich, D. R. (2012, Dec 1). Toxin content and cytotoxicity of algal dietary supplements. *Toxicol Appl Pharmacol, 265*(2), 263-271. https://doi.org/10.1016/j.taap.2012.10.005

Hildebrandt, F., Andersson, A., Saarenpää, S., Larsson, L., Van Hul, N., Kanatani, S., Masek, J., Ellis, E., Barragan, A., Mollbrink, A., Andersson, E. R., Lundeberg, J., & Ankarklev, J. (2021, 2021/12/02). Spatial Transcriptomics to define transcriptional patterns of zonation and structural components in the mouse liver. *Nature Communications, 12*(1), 7046. https://doi.org/10.1038/s41467-021-27354-w

Hoeger, S. J., Dietrich, D. R., & Hitzfeld, B. C. (2002, Nov). Effect of ozonation on the removal of cyanobacterial toxins during drinking water treatment. *Environ Health Perspect, 110*(11), 1127-1132. https://doi.org/10.1289/ehp.021101127

Hoeger, S. J., Schmid, D., Blom, J. F., Ernst, B., & Dietrich, D. R. (2007). Analytical and Functional Characterization of Microcystins [Asp3]MC-RR and [Asp3,Dhb7]MC-RR: Consequences for Risk Assessment? *Environmental Science & Technology, 41*(7), 2609-2616. https://doi.org/10.1021/es062681p

Hohmann, T., & Dehghani, F. (2019, Apr 18). The Cytoskeleton-A Complex Interacting Meshwork. *Cells, 8*(4). https://doi.org/10.3390/cells8040362

Holland, A., & Kinnear, S. (2013, Jun 27). Interpreting the possible ecological role(s) of cyanotoxins: compounds for competitive advantage and/or physiological aide? *Mar Drugs, 11*(7), 2239-2258. https://doi.org/10.3390/md11072239

Hornbeck, P. V., Zhang, B., Murray, B., Kornhauser, J. M., Latham, V., & Skrzypek, E. (2015, Jan). PhosphoSitePlus, 2014: mutations, PTMs and recalibrations. *Nucleic Acids Res, 43*(Database issue), D512-520. https://doi.org/10.1093/nar/gku1267

Huber, R. D., Gao, B., Sidler Pfändler, M. A., Zhang-Fu, W., Leuthold, S., Hagenbuch, B., Folkers, G., Meier, P. J., & Stieger, B. (2007, Feb). Characterization of two splice variants of human organic anion transporting polypeptide 3A1 isolated from human brain. *Am J Physiol Cell Physiol, 292*(2), C795-806. https://doi.org/10.1152/ajpcell.00597.2005

Hunter, T. (1995, Jan 27). Protein kinases and phosphatases: the yin and yang of protein phosphorylation and signaling. *Cell, 80*(2), 225-236. https://doi.org/10.1016/0092-8674(95)90405-0

Iarc. (2010). *Ingested nitrate and nitrite, and cyanobacterial peptide toxins* [IARC Monograph](IARC Monographs on the Evaluation of Carcinogenic Risks to Humans, vol. 94, Issue. http://monographs.iarc.fr/ENG/Monographs/vol94/mono94.pdf

Ito, E., Takai, A., Kondo, F., Masui, H., Imanishi, S., & Harada, K. (2002, Jul). Comparison of protein phosphatase inhibitory activity and apparent toxicity of microcystins and related compounds. *Toxicon, 40*(7), 1017-1025. https://doi.org/10.1016/s0041-0101(02)00099-5

Jaeger-Honz, S., Nitschke, J., Altaner, S., Klein, K., Dietrich, D. R., & Schreiber, F. (2022, 2022/01/05/). Investigation of microcystin conformation and binding towards PPP1 by molecular dynamics simulation. *Chemico-Biological Interactions, 351*, 109766. https://doi.org/https://doi.org/10.1016/j.cbi.2021.109766

Jigorel, E., Le Vee, M., Boursier-Neyret, C., Bertrand, M., & Fardel, O. (2005, Oct). Functional expression of sinusoidal drug transporters in primary human and rat hepatocytes. *Drug Metab Dispos, 33*(10), 1418-1422. https://doi.org/10.1124/dmd.105.004762

Kammerer, S., & Küpper, J.-H. (2018). Human hepatocyte systems for in vitro toxicology analysis. *Journal of Cellular Biotechnology, 3*, 85-93. https://doi.org/10.3233/JCB-179012

Kaur, G., Fahrner, R., Wittmann, V., Stieger, B., & Dietrich, D. R. (2019, 2019/09/25/). Human MRP2 exports MC-LR but not the glutathione conjugate. *Chemico-Biological Interactions, 311*, 108761. https://doi.org/https://doi.org/10.1016/j.cbi.2019.108761

Kietzmann, T. (2017, 2017/04/01/). Metabolic zonation of the liver: The oxygen gradient revisited. *Redox Biology, 11*, 622-630. https://doi.org/https://doi.org/10.1016/j.redox.2017.01.012

Kleinteich, J., Wood, S. A., Küpper, F. C., Camacho, A., Quesada, A., Frickey, T., & Dietrich, D. R. (2012, 2012/05/01). Temperature-related changes in polar cyanobacterial mat diversity and toxin production. *Nature Climate Change, 2*(5), 356-360. https://doi.org/10.1038/nclimate1418

Kondo, F., Ikai, Y., Oka, H., Okumura, M., Ishikawa, N., Harada, K., Matsuura, K., Murata, H., & Suzuki, M. (1992, Sep-Oct). Formation, characterization, and toxicity of the glutathione and cysteine conjugates of toxic heptapeptide microcystins. *Chem Res Toxicol, 5*(5), 591-596. https://doi.org/10.1021/tx00029a002

König, J., Cui, Y., Nies, A. T., & Keppler, D. (2000a, Jul 28). Localization and genomic organization of a new hepatocellular organic anion transporting polypeptide. *J Biol Chem, 275*(30), 23161-23168. https://doi.org/10.1074/jbc.M001448200

König, J., Cui, Y., Nies, A. T., & Keppler, D. (2000b, Jan). A novel human organic anion transporting polypeptide localized to the basolateral hepatocyte membrane. *Am J Physiol Gastrointest Liver Physiol, 278*(1), G156-164. https://doi.org/10.1152/ajpgi.2000.278.1.G156

Krajcsi, P. t. (2013). Drug-transporter interaction testing in drug discovery and development.

Lee-Montiel, F. T., George, S. M., Gough, A. H., Sharma, A. D., Wu, J., DeBiasio, R., Vernetti, L. A., & Taylor, D. L. (2017, Oct). Control of oxygen tension recapitulates zone-specific functions in human liver microphysiology systems. *Exp Biol Med (Maywood), 242*(16), 1617-1632. https://doi.org/10.1177/1535370217703978

Li, G., Cai, F., Yan, W., Li, C., & Wang, J. (2012, Jun). A proteomic analysis of MCLR-induced neurotoxicity: implications for Alzheimer's disease. *Toxicol Sci, 127*(2), 485-495. https://doi.org/10.1093/toxsci/kfs114

Li, G., Yan, W., Dang, Y., Li, J., Liu, C., & Wang, J. (2015, Jun 10). The role of calcineurin signaling in microcystin-LR triggered neuronal toxicity. *Sci Rep, 5*, 11271. https://doi.org/10.1038/srep11271

Li, J., Cai, Z., Vaites, L. P., Shen, N., Mitchell, D. C., Huttlin, E. L., Paulo, J. A., Harry, B. L., & Gygi, S. P. (2021, Nov 18). Proteome-wide mapping of short-lived proteins in human cells. *Mol Cell, 81*(22), 4722-4735.e4725. https://doi.org/10.1016/j.molcel.2021.09.015

Li, Y., Li, J., Huang, H., Yang, M., Zhuang, D., Cheng, X., Zhang, H., & Fu, X. (2016, Aug). Microcystin-LR induces mitochondria-mediated apoptosis in human bronchial epithelial cells. *Exp Ther Med, 12*(2), 633-640. https://doi.org/10.3892/etm.2016.3423

Liang, D., Hagenbuch, B., Stieger, B., & Meier, P. J. (1993, Nov). Parallel decrease of Na(+)-taurocholate cotransport and its encoding mRNA in primary cultures of rat hepatocytes. *Hepatology, 18*(5), 1162-1166.

Ligasová, A., & Koberna, K. (2021, Oct 5). Strengths and Weaknesses of Cell Synchronization Protocols Based on Inhibition of DNA Synthesis. *Int J Mol Sci, 22*(19). https://doi.org/10.3390/ijms221910759

Lin, H., Liu, W., Zeng, H., Pu, C., Zhang, R., Qiu, Z., Chen, J. A., Wang, L., Tan, Y., Zheng, C., Yang, X., Tian, Y., Huang, Y., Luo, J., Luo, Y., Feng, X., Xiao, G., Feng, L., Li, H., Wang, F., Yuan, C., Wang, J., Zhou, Z., Wei, T., Zuo, Y., Wu, L., He, L., Guo, Y., & Shu, W. (2016, May 17). Determination of Environmental Exposure to Microcystin and Aflatoxin as a Risk for Renal Function Based on 5493 Rural People in Southwest China. *Environ Sci Technol, 50*(10), 5346-5356. https://doi.org/10.1021/acs.est.6b01062

Louisa, M., Suyatna, F. D., Wanandi, S. I., Asih, P. B., & Syafruddin, D. (2016). Differential expression of several drug transporter genes in HepG2 and Huh-7 cell lines. *Adv Biomed Res, 5*, 104. https://doi.org/10.4103/2277-9175.183664

Lu, S. C. (2013, May). Glutathione synthesis. *Biochim Biophys Acta, 1830*(5), 3143-3153. https://doi.org/10.1016/j.bbagen.2012.09.008

MacKintosh, C., Beattie, K. A., Klumpp, S., Cohen, P., & Codd, G. A. (1990). Cyanobacterial microcystin-LR is a potent and specific inhibitor of protein phosphatases 1 and 2A from both mammals and higher plants. *FEBS Letters, 264*(2), 187-192. https://doi.org/10.1016/0014-5793(90)80245-e

MacKintosh, R. W., Dalby, K. N., Campbell, D. G., Cohen, P. T., Cohen, P., & MacKintosh, C. (1995, Sep 11). The cyanobacterial toxin microcystin binds covalently to cysteine-273 on protein phosphatase 1. *FEBS Lett, 371*(3), 236-240. https://doi.org/10.1016/0014-5793(95)00888-g

Mahagita, C., Grassl, S. M., Piyachaturawat, P., & Ballatori, N. (2007, Jul). Human organic anion transporter 1B1 and 1B3 function as bidirectional carriers and do not mediate GSH-bile acid cotransport. *Am J Physiol Gastrointest Liver Physiol, 293*(1), G271-278. https://doi.org/10.1152/ajpgi.00075.2007

Maidana, M., Carlis, V., Galhardi, F. G., Yunes, J. S., Geracitano, L. A., Monserrat, J. M., & Barros, D. M. (2006, Feb 25). Effects of microcystins over short- and long-term memory and oxidative stress generation in hippocampus of rats. *Chem Biol Interact, 159*(3), 223-234. https://doi.org/10.1016/j.cbi.2005.12.001

Makower, A. K., Schuurmans, J. M., Groth, D., Zilliges, Y., Matthijs, H. C., & Dittmann, E. (2015, Jan). Transcriptomics-aided dissection of the intracellular and extracellular roles of microcystin in Microcystis aeruginosa PCC 7806. *Appl Environ Microbiol, 81*(2), 544-554. https://doi.org/10.1128/aem.02601-14

Malik, J. K., Bharti, V. K., Rahal, A., Kumar, D., & Gupta, R. C. (2020). Chapter 31 - Cyanobacterial (blue-green algae) toxins. In R. C. Gupta (Ed.), *Handbook of Toxicology of Chemical Warfare Agents (Third Edition)* (pp. 467-478). Academic Press. https://doi.org/https://doi.org/10.1016/B978-0-12-819090-6.00031-3

Marnett, L. J. (2000, Mar). Oxyradicals and DNA damage. *Carcinogenesis, 21*(3), 361-370. https://doi.org/10.1093/carcin/21.3.361

Marquardt, H., Schäfer, S. G., Barth, H., & Stuttgart, W. V. (2019). *Toxikologie*. Wissenschaftliche Verlagsgesellschaft Stuttgart. https://books.google.de/books?id=YT5KzQEACAAJ

Martin, W. F., Garg, S., & Zimorski, V. (2015). Endosymbiotic theories for eukaryote origin. *Philosophical Transactions of the Royal Society B: Biological Sciences, 370*(1678), 20140330. https://doi.org/doi:10.1098/rstb.2014.0330

Massey, I. Y., Yang, F., Ding, Z., Yang, S., Guo, J., Tezi, C., Al-Osman, M., Kamegni, R. B., & Zeng, W. (2018, Sep 1). Exposure routes and health effects of microcystins on animals and humans: A mini-review. *Toxicon, 151*, 156-162. https://doi.org/10.1016/j.toxicon.2018.07.010

McLellan, N. L., & Manderville, R. A. (2017). Toxic mechanisms of microcystins in mammals. *Toxicology Research, 6*(4), 391-405. https://doi.org/10.1039/c7tx00043j

Meier, M., Klein, H. H., Kramer, J., Drenckhan, M., & Schütt, M. (2007, Apr). Calpain inhibition impairs glycogen syntheses in HepG2 hepatoma cells without altering insulin signaling. *J Endocrinol, 193*(1), 45-51. https://doi.org/10.1677/joe.1.07087

Meister, A. (1988, Nov 25). Glutathione metabolism and its selective modification. *J Biol Chem, 263*(33), 17205-17208.

Merrick, W. C., & Pavitt, G. D. (2018, Dec 3). Protein Synthesis Initiation in Eukaryotic Cells. *Cold Spring Harb Perspect Biol, 10*(12). https://doi.org/10.1101/cshperspect.a033092

Metcalf, J. S., Beattie, K. A., Pflugmacher, S., & Codd, G. A. (2000). Immuno-crossreactivity and toxicity assessment of conjugation products of the cyanobacterial toxin, microcystin-LR. *FEMS Microbiology Letters, 189*(2), 155-158. https://doi.org/10.1111/j.1574-6968.2000.tb09222.x

Michalopoulos, G. K., & Bhushan, B. (2021, 2021/01/01). Liver regeneration: biological and pathological mechanisms and implications. *Nature Reviews Gastroenterology & Hepatology, 18*(1), 40-55. https://doi.org/10.1038/s41575-020-0342-4

Miller, M. A., Kudela, R. M., Mekebri, A., Crane, D., Oates, S. C., Tinker, M. T., Staedler, M., Miller, W. A., Toy-Choutka, S., Dominik, C., Hardin, D., Langlois, G., Murray, M., Ward, K., & Jessup, D. A. (2010). Evidence for a Novel Marine Harmful Algal Bloom: Cyanotoxin (Microcystin) Transfer from Land to Sea Otters. *PLOS ONE, 5*(9), e12576. https://doi.org/10.1371/journal.pone.0012576

Millward, T. A., Zolnierowicz, S., & Hemmings, B. A. (1999, 1999/05/01/). Regulation of protein kinase cascades by protein phosphatase 2A. *Trends in Biochemical Sciences, 24*(5), 186-191. https://doi.org/https://doi.org/10.1016/S0968-0004(99)01375-4

Milutinović, A., Sedmak, B., Horvat-Znidarsic, I., & Suput, D. (2002). Renal injuries induced by chronic intoxication with microcystins. *Cell Mol Biol Lett, 7*(1), 139-141.

Namikoshi, M., Rinehart, K. L., Dahlem, A. M., Beasley, V. R., & Carmichael, W. W. (1989, 1989/01/01/). Total synthesis of Adda, the unique C20 amino acid of cyanobacterial hepatotoxins. *Tetrahedron Letters, 30*(33), 4349-4352. https://doi.org/https://doi.org/10.1016/S0040-4039(00)99357-2

Niedermeyer, T. H., Daily, A., Swiatecka-Hagenbruch, M., & Moscow, J. A. (2014). Selectivity and potency of microcystin congeners against OATP1B1 and OATP1B3 expressing cancer cells. *PLOS ONE, 9*(3), e91476. https://doi.org/10.1371/journal.pone.0091476

Ohta, T., Nishiwaki, R., Yatsunami, J., Komori, A., Suganuma, M., & Fujiki, H. (1992, Dec). Hyperphosphorylation of cytokeratins 8 and 18 by microcystin-LR, a new liver tumor promoter, in primary cultured rat hepatocytes. *Carcinogenesis, 13*(12), 2443-2447. https://doi.org/10.1093/carcin/13.12.2443

Olsen, J. V., Blagoev, B., Gnad, F., Macek, B., Kumar, C., Mortensen, P., & Mann, M. (2006, Nov 3). Global, in vivo, and site-specific phosphorylation dynamics in signaling networks. *Cell, 127*(3), 635-648. https://doi.org/10.1016/j.cell.2006.09.026

Olson, J. M. (2006, 2006/05/01). Photosynthesis in the Archean Era. *Photosynthesis Research, 88*(2), 109-117. https://doi.org/10.1007/s11120-006-9040-5

Paerl, H. W., & Huisman, J. (2008). Blooms Like It Hot. *Science, 320*(5872), 57-58. https://doi.org/doi:10.1126/science.1155398

Paerl, H. W., & Otten, T. G. (2013, May). Harmful cyanobacterial blooms: causes, consequences, and controls. *Microb Ecol, 65*(4), 995-1010. https://doi.org/10.1007/s00248-012-0159-y

Paulusma, C. C., Groen, A., Kunne, C., Ho-Mok, K. S., Spijkerboer, A. L., Rudi de Waart, D., Hoek, F. J., Vreeling, H., Hoeben, K. A., van Marle, J., Pawlikowska, L., Bull, L. N., Hofmann, A. F., Knisely, A. S., & Oude Elferink, R. P. (2006, Jul). Atp8b1 deficiency in mice reduces resistance of the canalicular membrane to hydrophobic bile salts and impairs bile salt transport. *Hepatology, 44*(1), 195-204. https://doi.org/10.1002/hep.21212

Pearson, L., Mihali, T., Moffitt, M., Kellmann, R., & Neilan, B. (2010). On the Chemistry, Toxicology and Genetics of the Cyanobacterial Toxins, Microcystin, Nodularin, Saxitoxin and Cylindrospermopsin. *Marine Drugs, 8*(5), 1650-1680.

Pereira, S. R., Vasconcelos, V. M., & Antunes, A. (2011, 2011/02/01). The phosphoprotein phosphatase family of Ser/Thr phosphatases as principal targets of naturally occurring toxins. *Critical Reviews in Toxicology, 41*(2), 83-110. https://doi.org/10.3109/10408444.2010.515564

Pereira, S. R., Vasconcelos, V. M., & Antunes, A. (2013). Computational study of the covalent bonding of microcystins to cysteine residues - a reaction involved in the inhibition of the PPP family of protein phosphatases. *FEBS Journal, 280*(2), 674-680. https://doi.org/10.1111/j.1742-4658.2011.08454.x

Pilotto, L. S., Douglas, R. M., Burch, M. D., Cameron, S., Beers, M., Rouch, G. J., Robinson, P., Kirk, M., Cowie, C. T., Hardiman, S., Moore, C., & Attewell, R. G. (1997, Oct). Health effects of exposure to cyanobacteria (blue-green algae) during recreational water-related activities. *Aust N Z J Public Health, 21*(6), 562-566. https://doi.org/10.1111/j.1467-842x.1997.tb01755.x

Pouria, S., de Andrade, A., Barbosa, J., Cavalcanti, R. L., Barreto, V. T., Ward, C. J., Preiser, W., Poon, G. K., Neild, G. H., & Codd, G. A. (1998, Jul 4). Fatal microcystin intoxication in haemodialysis unit in Caruaru, Brazil. *Lancet, 352*(9121), 21-26. https://doi.org/10.1016/s0140-6736(97)12285-1

Prakash, G., Paul, N., Oliver, G. A., Werz, D. B., & Maiti, D. (2022). C–H deuteration of organic compounds and potential drug candidates [10.1039/D0CS01496F]. *Chemical Society Reviews, 51*(8), 3123-3163. https://doi.org/10.1039/D0CS01496F

Rahman, I., Kode, A., & Biswas, S. K. (2006). Assay for quantitative determination of glutathione and glutathione disulfide levels using enzymatic recycling method. *Nat Protoc, 1*(6), 3159-3165. https://doi.org/10.1038/nprot.2006.378

Ramazi, S., & Zahiri, J. (2021, Apr 7). Posttranslational modifications in proteins: resources, tools and prediction methods. *Database (Oxford), 2021*. https://doi.org/10.1093/database/baab012

Ramboer, E., De Craene, B., De Kock, J., Vanhaecke, T., Berx, G., Rogiers, V., & Vinken, M. (2014, 2014/10/01/). Strategies for immortalization of primary hepatocytes. *Journal of Hepatology, 61*(4), 925-943. https://doi.org/https://doi.org/10.1016/j.jhep.2014.05.046

Ren, Y., Yang, M., Chen, M., Zhu, Q., Zhou, L., Qin, W., & Wang, T. (2017, Jan 4). Microcystin-LR promotes epithelial-mesenchymal transition in colorectal cancer cells through PI3-K/AKT and SMAD2. *Toxicol Lett, 265*, 53-60. https://doi.org/10.1016/j.toxlet.2016.11.004

Rinehart, K. L., Harada, K., Namikoshi, M., Chen, C., Harvis, C. A., Munro, M. H. G., Blunt, J. W., Mulligan, P. E., Beasley, V. R., & et al. (1988, 1988/12/01). Nodularin, microcystin, and the configuration of Adda. *Journal of the American Chemical Society, 110*(25), 8557-8558. https://doi.org/10.1021/ja00233a049

Robinson, N. A., Pace, J. G., Matson, C. F., Miura, G. A., & Lawrence, W. B. (1991, Jan). Tissue distribution, excretion and hepatic biotransformation of microcystin-LR in mice. *J Pharmacol Exp Ther, 256*(1), 176-182.

Ruediger, R., Van Wart Hood, J. E., Mumby, M., & Walter, G. (1991, Aug). Constant expression and activity of protein phosphatase 2A in synchronized cells. *Mol Cell Biol, 11*(8), 4282-4285. https://doi.org/10.1128/mcb.11.8.4282-4285.1991

Runnegar, M. T. C., Andrews, J., Gerdes, R. G., & Falconer, I. R. (1987, 1987/01/01/). Injury to hepatocytes induced by a peptide toxin from the cyanobacterium Microcystis aeruginosa. *Toxicon, 25*(11), 1235-1239. https://doi.org/https://doi.org/10.1016/0041-0101(87)90142-5

Santori, N., Buratti, F. M., Scardala, S., Dorne, J.-L. C. M., & Testai, E. (2020, 2020/04/01/). In vitro detoxication of microcystins in human samples: variability among variants with different hydrophilicity and structure. *Toxicology Letters, 322*, 131-139. https://doi.org/https://doi.org/10.1016/j.toxlet.2020.01.007

Schippers, I. J., Moshage, H., Roelofsen, H., Müller, M., Heymans, H. S., Ruiters, M., & Kuipers, F. (1997, Jul). Immortalized human hepatocytes as a tool for the study of hepatocytic (de-)differentiation. *Cell Biol Toxicol, 13*(4-5), 375-386. https://doi.org/10.1023/a:1007404028681

Schmidt, J., Wilhelm, S., & Boyer, G. (2014). The Fate of Microcystins in the Environment and Challenges for Monitoring. *Toxins, 6*(12), 3354-3387. https://doi.org/10.3390/toxins6123354

Schoenfeld, E. (2022). *Determination of Protein Half-lives and Protein Stabilites of Human Serine/Threonine Phosphatases and Glutathione Relevant Enzymes* [Master Thesis University of Konstanz].

Schulze, R. J., Schott, M. B., Casey, C. A., Tuma, P. L., & McNiven, M. A. (2019, Jul 1). The cell biology of the hepatocyte: A membrane trafficking machine. *J Cell Biol, 218*(7), 2096-2112. https://doi.org/10.1083/jcb.201903090

Shi, L., Du, X., Liu, H., Chen, X., Ma, Y., Wang, R., Tian, Z., Zhang, S., Guo, H., & Zhang, H. (2021, Apr). Update on the adverse effects of microcystins on the liver. *Environ Res, 195*, 110890. https://doi.org/10.1016/j.envres.2021.110890

Shi, Y. (2009). Serine/Threonine Phosphatases: Mechanism through Structure. *Cell, 139*(3), 468-484. https://doi.org/10.1016/j.cell.2009.10.006

Shousha, S., Gadir, F., Peston, D., Bansi, D., Thillainaygam, A. V., & Murray-Lyon, I. M. (2004, Oct). CD10 immunostaining of bile canaliculi in liver biopsies: change of staining pattern with the development of cirrhosis. *Histopathology, 45*(4), 335-342. https://doi.org/10.1111/j.1365-2559.2004.01927.x

Sivonen, K., & Jones, G. (1999). Cyanobacterial toxins. *Toxic cyanobacteria in water: a guide to their public health consequences, monitoring and management, 1*, 43-112.

Smith, J. L., Schulz, K. L., Zimba, P. V., & Boyer, G. L. (2010, 2010/07/01/). Possible mechanism for the foodweb transfer of covalently bound microcystins. *Ecotoxicology and Environmental Safety, 73*(5), 757-761. https://doi.org/https://doi.org/10.1016/j.ecoenv.2009.12.003

Soares, R. M., Yuan, M., Servaites, J. C., Delgado, A., Magalhães, V. F., Hilborn, E. D., Carmichael, W. W., & Azevedo, S. M. (2006, Apr). Sublethal exposure from microcystins to renal insufficiency patients in Rio de Janeiro, Brazil. *Environ Toxicol, 21*(2), 95-103. https://doi.org/10.1002/tox.20160

Spoof, L., & Catherine, A. (2016). Appendix 3: Tables of Microcystins and Nodularins. In *Handbook of Cyanobacterial Monitoring and Cyanotoxin Analysis* (pp. 526-537). https://doi.org/https://doi.org/10.1002/9781119068761.app3

Stanger, B. Z. (2015). Cellular homeostasis and repair in the mammalian liver. *Annu Rev Physiol, 77*, 179-200. https://doi.org/10.1146/annurev-physiol-021113-170255

Stieger, B., & Hagenbuch, B. (2014). Organic anion-transporting polypeptides. *Curr Top Membr, 73*, 205-232. https://doi.org/10.1016/b978-0-12-800223-0.00005-0

Stotts, R. R., Namikoshi, M., Haschek, W. M., Rinehart, K. L., Carmichael, W. W., Dahlem, A. M., & Beasley, V. R. (1993, 1993/06/01/). Structural modifications imparting reduced toxicity in microcystins from Microcystis spp. *Toxicon, 31*(6), 783-789. https://doi.org/https://doi.org/10.1016/0041-0101(93)90384-U

Svirčev, Z., Drobac, D., Tokodi, N., Mijović, B., Codd, G. A., & Meriluoto, J. (2017, 2017/02/01). Toxicology of microcystins with reference to cases of human intoxications and epidemiological investigations of exposures to cyanobacteria and cyanotoxins. *Archives of Toxicology, 91*(2), 621-650. https://doi.org/10.1007/s00204-016-1921-6

Svirčev, Z., Lalić, D., Bojadžija Savić, G., Tokodi, N., Drobac Backović, D., Chen, L., Meriluoto, J., & Codd, G. A. (2019, 2019/09/01). Global geographical and historical overview of cyanotoxin distribution and cyanobacterial poisonings. *Archives of Toxicology, 93*(9), 2429-2481. https://doi.org/10.1007/s00204-019-02524-4

Takumi, S., Komatsu, M., Furukawa, T., Ikeda, R., Sumizawa, T., Akenaga, H., Maeda, Y., Aoyama, K., Arizono, K., Ando, S., & Takeuchi, T. (2010, Sep). p53 Plays an important role in cell fate determination after exposure to microcystin-LR. *Environ Health Perspect, 118*(9), 1292-1298. https://doi.org/10.1289/ehp.1001899

Thompson, J. J., & Williams, C. S. (2018, Feb 26). Protein Phosphatase 2A in the Regulation of Wnt Signaling, Stem Cells, and Cancer. *Genes (Basel), 9*(3). https://doi.org/10.3390/genes9030121

Tomitani, A., Knoll, A. H., Cavanaugh, C. M., & Ohno, T. (2006). The evolutionary diversification of cyanobacteria: Molecular–phylogenetic and paleontological perspectives. *Proceedings of the National Academy of Sciences, 103*(14), 5442-5447. https://doi.org/doi:10.1073/pnas.0600999103

Toyama, B. H., & Hetzer, M. W. (2013, Jan). Protein homeostasis: live long, won't prosper. *Nat Rev Mol Cell Biol, 14*(1), 55-61. https://doi.org/10.1038/nrm3496

Vermaas, W. F. J. (2001). Photosynthesis and Respiration in Cyanobacteria.

Vichai, V., & Kirtikara, K. (2006). Sulforhodamine B colorimetric assay for cytotoxicity screening. *Nat Protoc, 1*(3), 1112-1116. https://doi.org/10.1038/nprot.2006.179

Vichi, S., Buratti, F. M., & Testai, E. (2016). Microcystins: Toxicological Profile. In P. Gopalakrishnakone, V. Haddad Jr, A. Tubaro, E. Kim, & W. R. Kem (Eds.), *Marine and Freshwater Toxins* (pp. 219-238). Springer Netherlands. https://doi.org/10.1007/978-94-007-6419-4_24

Vichi, S., Lavorini, P., Funari, E., Scardala, S., & Testai, E. (2012, Dec). Contamination by Microcystis and microcystins of blue-green algae food supplements (BGAS) on the Italian market and possible risk for the exposed population. *Food Chem Toxicol, 50*(12), 4493-4499. https://doi.org/10.1016/j.fct.2012.09.029

Vidal, F., Sedan, D., D'Agostino, D., Cavalieri, M. L., Mullen, E., Parot Varela, M. M., Flores, C., Caixach, J., & Andrinolo, D. (2017). Recreational Exposure during Algal Bloom in Carrasco Beach, Uruguay: A Liver Failure Case Report. *Toxins, 9*(9), 267. https://www.mdpi.com/2072-6651/9/9/267

Vinken, M., & Hengstler, J. G. (2018, 2018/10/01). Characterization of hepatocyte-based in vitro systems for reliable toxicity testing. *Archives of Toxicology, 92*(10), 2981-2986. https://doi.org/10.1007/s00204-018-2297-6

Wang, J., Lin, F., Cai, F., Yan, W., Zhou, Q., & Xie, L. (2013, Sep). Microcystin-LR inhibited hippocampal long-term potential via regulation of the glycogen synthase kinase-3 β pathway. *Chemosphere, 93*(2), 223-229. https://doi.org/10.1016/j.chemosphere.2013.04.069

Wang, J., Zhang, C., Zhu, J., Ding, J., Chen, Y., & Han, X. (2019, Nov 1). Blood-brain barrier disruption and inflammation reaction in mice after chronic exposure to Microcystin-LR. *Sci Total Environ, 689*, 662-678. https://doi.org/10.1016/j.scitotenv.2019.06.387

Wang, Q., Xie, P., Chen, J., & Liang, G. (2008, Nov). Distribution of microcystins in various organs (heart, liver, intestine, gonad, brain, kidney and lung) of Wistar rat via intravenous injection. *Toxicon, 52*(6), 721-727. https://doi.org/10.1016/j.toxicon.2008.08.004

Whitton, B., & Potts, M. (2007). The Ecology of Cyanobacteria. *Springer Dordrecht, 1*, XVIII, 669. https://doi.org/https://doi.org/10.1007/0-306-46855-7

Wildman, S. A., & Crippen, G. M. (1999). Prediction of Physicochemical Parameters by Atomic Contributions. *J. Chem. Inf. Comput. Sci., 39*, 868-873.

Wood, S. A., & Dietrich, D. R. (2011, Jun). Quantitative assessment of aerosolized cyanobacterial toxins at two New Zealand lakes. *J Environ Monit, 13*(6), 1617-1624. https://doi.org/10.1039/c1em10102a

World Health, O. (2020). *Cyanobacterial toxins: microcystins* CC BY-NC-SA 3.0 IGO). https://apps.who.int/iris/handle/10665/338066

Xing, Y., Xu, Y., Chen, Y., Jeffrey, P. D., Chao, Y., Lin, Z., Li, Z., Strack, S., Stock, J. B., & Shi, Y. (2006, Oct 20). Structure of protein phosphatase 2A core enzyme bound to tumor-inducing toxins. *Cell, 127*(2), 341-353. https://doi.org/10.1016/j.cell.2006.09.025

Xu, S., Yi, X., Liu, W., Zhang, C., Massey, I. Y., Yang, F., & Tian, L. (2020). A Review of Nephrotoxicity of Microcystins. *Toxins, 12*(11), 693. https://www.mdpi.com/2072-6651/12/11/693

Yang, J., Roe, S. M., Cliff, M. J., Williams, M. A., Ladbury, J. E., Cohen, P. T., & Barford, D. (2005, Jan 12). Molecular basis for TPR domain-mediated regulation of protein phosphatase 5. *Embo j, 24*(1), 1-10. https://doi.org/10.1038/sj.emboj.7600496

Yoshida, T., Makita, Y., Tsutsumi, T., Nagata, S., Tashiro, F., Yoshida, F., Sekuima, M., Tamura, S.-I., Harada, T., Maita, K., & Ueno, Y. (1998). Immunohistochemical Localization of Microcystin-LR in the Liver of Mice: A Study on the Pathogenesis of Microcystin-LR-Induced Hepatotoxicity. *Toxicologic Pathology, 26*(3), 411-418. https://doi.org/10.1177/019262339802600316

Yu, S. Z. (1995, Nov-Dec). Primary prevention of hepatocellular carcinoma. *J Gastroenterol Hepatol, 10*(6), 674-682. https://doi.org/10.1111/j.1440-1746.1995.tb01370.x

Zegura, B. (2016). An Overview of the Mechanisms of Microcystin-LR Genotoxicity and Potential Carcinogenicity. *Mini Rev Med Chem, 16*(13), 1042-1062. https://doi.org/10.2174/1389557516666160308141549

Zemskov, I., Altaner, S., Dietrich, D. R., & Wittmann, V. (2017). Total Synthesis of Microcystin-LF and Derivatives Thereof. *The Journal of Organic Chemistry, 82*(7), 3680-3691. https://doi.org/10.1021/acs.joc.7b00175

Zhang, T., Gu, J., Wang, X., Lu, Y., Cai, K., Li, H., Nie, Y., Chen, X., & Wang, J. (2023, 2023-March-02). A novel liver zonation phenotype-associated molecular classification of hepatocellular carcinoma [Original Research]. *Frontiers in Immunology, 14*. https://doi.org/10.3389/fimmu.2023.1140201

Zhang, W., Liang, G., Wu, L., Tuo, X., Wang, W., Chen, J., & Xie, P. (2013, Aug). Why mammals more susceptible to the hepatotoxic microcystins than fish: evidences from plasma and albumin protein binding through equilibrium dialysis. *Ecotoxicology, 22*(6), 1012-1019. https://doi.org/10.1007/s10646-013-1086-5

Zhang, Y., Zhang, J., Wang, E., Qian, W., Fan, Y., Feng, Y., Yin, H., Li, Y., Wang, Y., & Yuan, T. (2018). Microcystin-Leucine-Arginine Induces Tau Pathology Through Bα Degradation via Protein Phosphatase 2A Demethylation and Associated Glycogen Synthase Kinase-3β Phosphorylation. *Toxicological Sciences, 162*(2), 475-487. https://doi.org/10.1093/toxsci/kfx271

Zhou, L., Yu, H., & Chen, K. (2002, Jun). Relationship between microcystin in drinking water and colorectal cancer. *Biomed Environ Sci, 15*(2), 166-171.

Zhou, M., Tu, W.-w., & Xu, J. (2015, 2015/07/01/). Mechanisms of microcystin-LR-induced cytoskeletal disruption in animal cells. *Toxicon, 101*, 92-100. https://doi.org/https://doi.org/10.1016/j.toxicon.2015.05.005